Université de Liège

Doctoral Thesis

Low-dimensional *d*-states electron systems: insights from first-principles

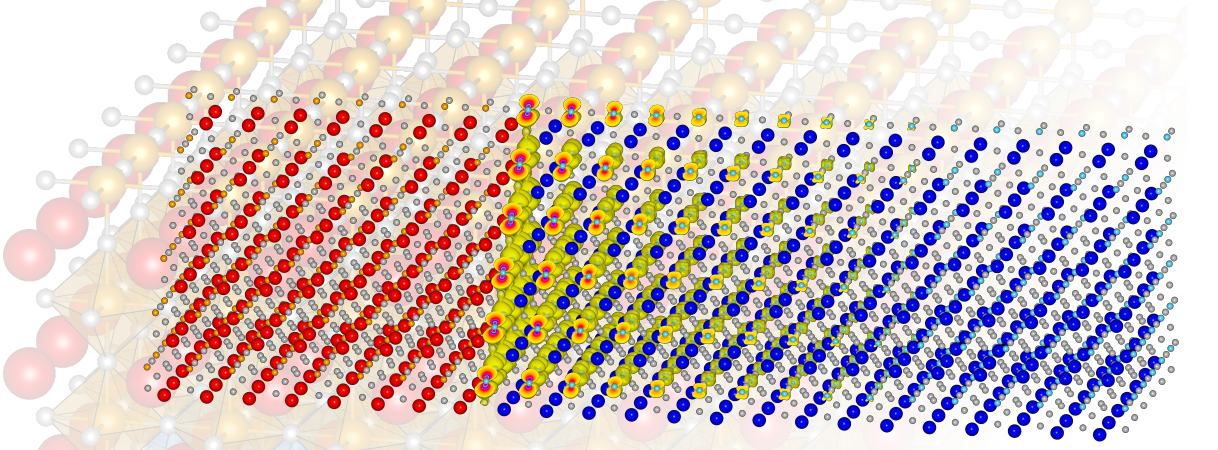

Thesis submitted in fulfilment of the requirements
for the degree of Doctor of Sciences
by

Sébastien Lemal

Physique Théorique des Matériaux
Unité de Recherche CESAM
Faculté des Sciences

Jury:

Dr. Eric Bousquet (secretary)	Université de Liège
Dr. Nicholas C. Bristowe	University of Kent
Pr. Alessio Filippetti	University of Cagliari
Pr. Philippe Ghosez (supervisor)	Université de Liège
Dr. Jean-Yves Raty	Université de Liège
Pr. Jean-Marc Triscone	Université de Genève
Pr. Matthieu J. Verstraete (president)	Université de Liège

September 2019

Abstract

The present thesis focuses on the physics of various solid-state systems sharing the common feature of involving $3d$ electrons with a low-dimensional aspect for transport, and studied using Density Functional Theory. Exploiting an original hybrid functional approach for the exchange-correlation energy, with improved accuracy compared to local/semi-local functionals, we present the seminal two-dimensional electron system (2DES) at the (001) interface of band insulators $SrTiO_3$ and $LaAlO_3$, and review two of the most popular hypotheses about its origin, namely the electric-field driven Zener breakdown model and polarity-induced surface oxygen vacancies model. This analysis is extended to the interface between $SrTiO_3$ and the $(Sr_{1-x}La_x)(Ti_{1-x}Al_x)O_3$ alloy. We also study, based on experiments and theoretical modelling, how the composition of the alloy overlayer affects the charge density of the 2DES. We then address the effect of structural confinement on the 2DES when the host layer thickness is reduced toward the very-thin limit, and how such effects are witnessed in angle-resolved photo-emission spectroscopy experiments. We study the effects of capping the $SrTiO_3/LaAlO_3$ heterostructures with $SrTiO_3$, highlighting how experiments may be interpreted from the aforementioned electric-field driven models. This work also focuses on the thermoelectric properties of layered oxides, specifically $Ca_3Co_4O_9$ and $SrTiO_3$-based superlattices, discussing the relevance of their layered structure for improving the thermoelectric properties. Importing the concepts of low-dimensional transport found in $SrTiO_3$-based systems to the iron-based Heusler Fe_2YZ family, we explore the effect of electron doping, highlighting magnetic instabilities related to their Fe $3d$ orbitals, which impact significantly the thermoelectric properties. Finally, shifting our attention on Fe_2TiSn, we rationalize experimental results provided by collaborators from first-principles, addressing the role of native defects and their relevance for tailoring transport.

Résumé

Les travaux de recherche présentés dans cette thèse concernent la physique de différents composés solides qui partagent comme point commun des états électroniques $3d$ avec un caractère basse dimensionnalité, étudiée *via* la théorie de la fonctionnelle de la densité. Ce travail trouve son originalité dans l'exploitation d'une fonctionnelle hybride pour la modélisation de l'énergie d'échange-corrélation, qui améliore sensiblement la précision de nos calculs. Nous présentons d'abord le système électronique bi-dimensionnel à l'interface (001) des isolants $SrTiO_3$ et $LaAlO_3$, et examinons en détail deux des hypothèses les plus populaires concernant son origine, à savoir un claquage Zener ou la stabilisation de lacunes d'oxygène à la surface du $LaAlO_3$, les deux étant provoqués par le champs électrostatique de la couche $LaAlO_3$. Cette étude est étendue à l'interface entre $SrTiO_3$ et l'alliage $(Sr_{1-x}La_x)(Ti_{1-x}Al_x)O_3$. Nous étudions également, en combinant expériences et modèles numériques, comment la composition de cet alliage influence la densité du système électronique bi-dimensionnel. De plus, nous étudions l'effet du confinement structurel et son impact sur les propriétés de ce système électronique et comparons nos résultats à des expériences de spectroscopie photoélectronique résolue en angle. Enfin, nous étudions également des hétérostructures $SrTiO_3/LaAlO_3$ couvertes par une fine couche de $SrTiO_3$, et relativisons les résultats expérimentaux au regard des hypothèses susmentionnées concernant les mécanismes à l'origine du système d'électron bi-dimensionnel. Ce travail contient également des résultats de recherche portant sur les propriétés thermoélectriques d'oxydes à structure stratifiée, spécifiquement $Ca_3Co_4O_9$ ainsi que des super-réseaux à base de $SrTiO_3$. Nous explorons de la pertinence de leur nature stratifiée pour l'amélioration des propriétés thermoélectriques. Important les concepts de transport basse dimensionnalité des composés à base de $SrTiO_3$ à la famille des Heusler Fe_2YZ, nous étudions l'effet du dopage en électrons, mettant en évidence des instabilités électroniques et magnétiques liées aux orbitales $3d$ des atomes de fer, avec un effet significatif sur les propriétés thermoélectriques. Enfin, nous focalisons notre attention sur Fe_2TiSn, nous rationalisons des résultats expérimentaux fournis par nos collaborateurs à partir sur base de simulations numériques, en abordant le rôle des défauts natifs dans les échantillons, et de leurs effets sur le transport électronique.

Acknowledgements

It took time, but this manuscript is finally brought to completion. In principle, a doctoral thesis is supposed to be an individual work, but such a simplistic picture would ignore all the help and interactions that I received and which contributed directly or indirectly to this work. Hence, it is necessary for me to acknowledge and thank all the people involved in the development of the present work.

First, I would like to express my deepest gratitude to my supervisor Pr. Philippe Ghosez for the opportunity to work in his laboratory, his precious advices, as well as his patience. His passion has always manifested during his lectures, and it is amongst the main reasons behind my motivation to pursue a doctoral degree in the field of solid state physics. Moreover, I will always be impressed by his spot-on insights.

My thanks also go to Julien Varignon, for introducing me to the CRYSTAL code and helping me at the very beginning of this adventure. I would also like to thank my first direct collaborators, Matthieu J. Verstraete and Daniel I. Bilc for introducing me to the world of thermoelectricity and for many other things as well. Then, I would like to express my deepest gratitude to Fabio Ricci, who has been an exceptional collaborator, with an exquisite taste in beers, and skilled in coffee management. I would also like to thank Nick B. Bristowe, who took the time to introduce me to the most intricate theoretical aspects of electron systems at oxide interfaces.

Of course, I would like to thank everyone in the PhyTheMa research group, including former members: Eric, Henu, Naihua, Alina, Ruihao, Begüm, Denis, Karan Deep, Julien, Safari, Hania, Jordan, Yajun, Marcus, Alain, Danila, Wen-Yi, Alexandre, He, and Camilo. Also, from the NanoMat group: Antoine, Nick (P.), Gabriele, Momar, Bin, and Micael. I would also like to thank Jean-Yves and Wilfredo, who both shared my enthusiasm on thermoelectrics. Many thanks to the executive secretary Florence Gemine as well. Overall, great personalities contributing to an exceptionally nice working environment.

Then, I would like to thank my collaborators, starting from the people from the DQMP Group of Pr. Jean-Marc Triscone (University of Geneva). My thanks goes to Denver, Stefano, Zhenping, Margherita and of course Pr. Jean-Marc Triscone, for the opportunity to collaborate on one of the most stimulating topic in the field of oxide interfaces. My thanks also go to Pr. Marc Gabay and his former student Manali Vivek for the interesting discussions we had. I would also like to thanks my collaborators from CNR-SPIN and CNR-IOM, namely Ilaria Pallecchi as well as Alessio Filippetti. Finally, I would also like to thank Marco Caputo and Vladimir N. Strocov of the Swiss Light Source (Paul Scherrer Institute) for the opportunity to collaborate on their spectroscopy experiments.

I would also like to pay homage to Brahim Belhadji, as a former colleague, but also as a friend. I also want to pay homage to Roberto Orlando: we only exchanged e-mails, yet he fixed a code without which several results in this manuscript would never have been computed.

I also want to thank Peter Schlagheck as well as all the folks from the IPNAS Coffee Club. Special thanks to Alexandre (for the beers, the noisily debated polemics and for his C++ coding tips), Florence, Cyril, Guillaume and Céline.

To be able to perform the intensive calculations necessary to produce the results presented in this manuscript, I needed access to powerful supercomputers. Calculations have been performed on the Belgian CÉCI facilities funded by F.R.S-FNRS Belgium (Grant No. 2.5020.1) and Tier-1 supercomputer of the Fédération Wallonie-Bruxelles funded by the Walloon Region (Grant No. 1117545). I acknowledge Sunil Patel and Steven Gunn for the LaTeX template used for this manuscript.

Now is the time to thank all the people from outside the lab, starting with my parents Mirella and Antoine, my brothers Ludovic and Axel, and my grandparents Luigi and Santina. I would also like to thank all of my friends: Bernard, Antony, Victoria, Rémy, Simon, Ghilan, Burhan, Milan, Gaël, Robin, and many others as well !

Last but not least, I would like to thank my dear Alice, for her love and support during all these years. Of course, many thanks to her family as well.

Contents

List of Figures

List of Tables

Abbreviations

2DES	**2**-**D**imensional **E**lectron **S**ystem
2DHS	**2**-**D**imensional **H**ole **S**ystem
ARPES	**A**ngle **R**esolved **P**hoto**E**mission **S**pectroscopy
CBM	**C**onduction **B**and **M**inimum
CCO	$\mathbf{Ca_3Co_4O_9}$
CRTA	**C**onstant **R**elaxation **T**ime **A**pproximation
DFT	**D**ensity **F**unctional **T**heory
DOS	**D**ensity **O**f **S**tate
EDC	**E**nergy **D**istribution **C**urve
EDX	**E**nergy **D**ispersive **X**-ray
IBZ	**I**rreducible **B**rillouin **Z**one
LAO	$\mathbf{LaAlO_3}$
MBE	**M**olecular **B**eam **E**pitaxy
MIT	**M**etal-**I**nsulator phase **T**ransition
PF	**P**ower **F**actor
PLD	**P**ulsed **L**aser **D**eposition
RBS	**R**utherford **B**ackscattering **S**pectroscopy
RHEED	**R**election **H**igh-**E**nergy **E**lectron **D**iffraction
SOC	**S**pin **O**rbit **C**oupling
SQUID	**S**uperconducting **Q**uantum **I**nterference **D**evice
STO	$\mathbf{SrTiO_3}$
TE	**T**hermo**E**lectric
VBM	**V**alence **B**and **M**aximum
XRD	**X**-**R**ay **D**iffraction

Physical Constants

Speed of Light	c	=	$2.997\ 924\ 58 \times 10^{8}\ \mathrm{m\,s^{-1}}$
Planck constant	$\hbar$	=	$1.054\ 571\ 80 \times 10^{-31}\ \mathrm{J\,s^{-1}}$
Boltzmann constant	k_B	=	$1.380\ 648\ 52 \times 10^{-23}\ \mathrm{J\,K^{-1}}$
Vacuum permittivity	ε_0	=	$8.854\ 187\ 82 \times 10^{-12}\ \mathrm{C\,V^{-1}\,m^{-1}}$
Bohr magneton	μ_B	=	$9.274\ 009\ 99 \times 10^{-24}\ \mathrm{J\,T^{-1}}$
Lorenz number	L	=	$2.443\ 002\ 88 \times 10^{-8}\ \mathrm{W\,\Omega\,K^{-1}}$

Dedicated to my beloved Alice;
and my parents, Mirella and Antoine...

Chapter 1

Introduction

It is usual for a thesis work to focus on a specific theme. However, the present manuscript covers different topics in the field of material science; specifically, it is about the 2-dimensional electron gas system appearing at the interface between band insulators oxides (namely $LaAlO_3$ and $SrTiO_3$), as well as thermoelectricity in oxides and iron-based Heusler systems. *A priori*, these two topics are seemingly unrelated. This is not necessarily the case: on one hand, even if the underlying materials discussed in the following Chapters have different compositions, they share some features in the form of low-dimensional transport that are related to the nature atomic orbitals at the origin of their transport properties. On another hand, all the compounds of interest in this work are studied by the means of first-principles calculations, which are the state-of-the-art methods for modelling materials at the nanoscopic scale. We aim to show how the versatility of first-principles methods can help to build bridges between these thematics.

1.1 Material science and modelling

Controlling matter has always been a prerequisite to the development of technology. From an historical point of view, materials science has mostly progressed empirically, based of experiments with the aim to address the emerging macroscopic properties from a phenomenological point of view, without necessarily understanding the underlying natural laws behind.

In this regards, the advent of the theory of quantum mechanics in the early 20th century, elaborated to provide a consistent explanation to various physical phenomena (black body radiation, photoelectric effect, quantized energy transfer between light and matter...), shed light to a fundamental issue regarding as to why the nuclei and electrons forming matter actually "stick" together, forming molecules, liquid or solid and ordered matter, based on new laws of physics occurring at their scale. In a methodological reductionist fashion, quantum mechanics and the laws of electromagnetism lay what we call the first principles ruling the material world, and based on these first principles, it is therefore possible to understand why some material conduct electricity while some not, why some crystals undergo structural phase transitions with pressure or temperature, and so on.

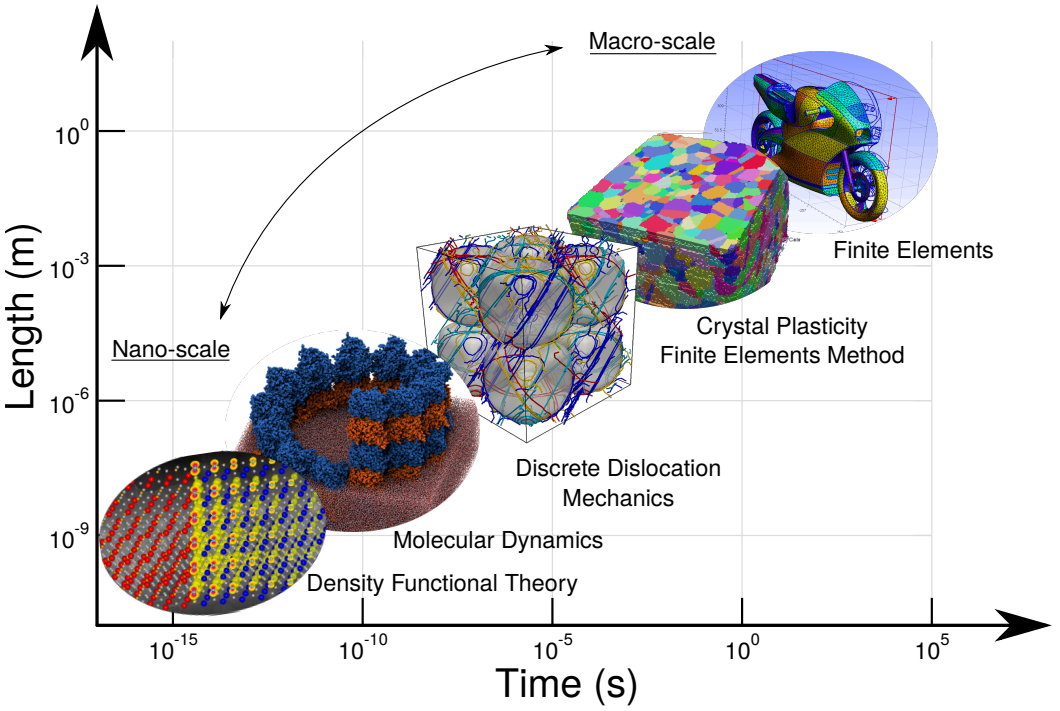

FIGURE 1.1: A small and non-exhaustive representation of numerical methods in the field of material sciences, placed on logarithmic scales in size and time.

Concomitantly with these conceptual advances, tremendous progress in technologies led to the development of calculators with the abilities to solve mathematical problems beyond a human brain capacity, opening new methodologies for scientific enquiries: numerical simulations. Simulations are often performed to study the behaviour of complex systems based on the knowledge of the properties underlying sub-systems. Materials science as a whole profited from this new way of performing research, half-way between virtual experimental methods and pure theoretical developments. Depending on the scale of the problem (in size and in time), several methods have been developed relying on theory adapted to the scale, some examples being given in Figure 1.1: from the macroscopic scale where the macroscopic properties of materials are modelled to see how they interact with each other, down to the nanoscopic scale where atoms and electrons interactions are purposely modelled. Of course, between these two limits, there is a handful of other scales, and usually, the corresponding methods are not exclusive, often bridged together in order to get an understanding of the properties' interplay between the different scales. Often, the multi-scale modelling is done through a bottom-up approach, by exploiting the properties determined at the lower scale, as in "second principles" approaches.

In this work, the theoretical framework is based on Density Functional Theory (DFT), whose principles are described in Chapter 2. The practical implementation of this theory has been formalized by Lu Jeu Sham and Walter Kohn [1] in 1965, who obtained the 1998 Nobel Prize in Chemistry (conjointly with John Pople) for this work. At the time, due to the low computational power available, the theory was mainly used for small systems. As the computational power increased, larger and more complex systems became accessible to DFT, and the method grew in popularity, as can be seen by the increasing number of citations per years of the original article [1], shown in Figure 1.2. One of the main

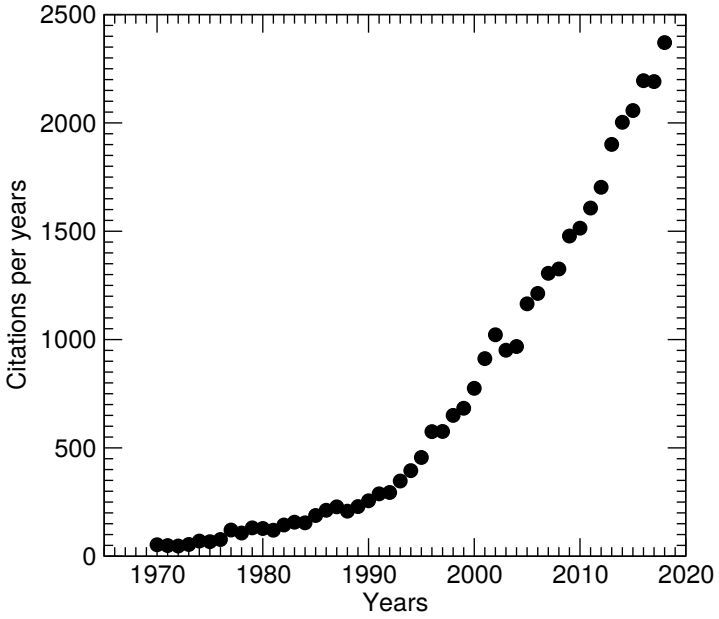

FIGURE 1.2: Number of citations per year of the original DFT paper by Kohn and Sham [1]. The data has been extracted from the Scopus database.

advantages of DFT is the transferability of the method, and it can be used to study all kind of materials, independently of the composition or the dimensionality.

1.2 Low-dimensional systems

In the vast field of material science, a particular sub-field concerns low-dimensional systems. Low-dimensional is a generic terminology to designate systems where the motion of the particles is limited in a given direction of space compared to their mean-free-path. An example is given in Figure 1.3.(a) and (b): if we consider a hallway, a bee in that hallway is free to move in all directions of space, and it can be considered as a 3-dimensional system. However, if a hippopotamus were to move in the same hallway, its motion would be restricted in a single direction, and therefore it can be considered as a 1-dimensional system. In these very specific examples, the dimensionality of the system is determined by the relative size between the bee or the hippopotamus and the hallway. The low dimensionality in the hippopotamus case is a consequence of confinement, yet, this is not the only strategy to achieve a low dimensional system. Another example would be the motion of pedestrians on a flat surface: in this case, the combined effects of the gravitational and the normal reaction forces compel the pedestrians to move along the plane of the surface, and such a system would be a 2-dimensional system, as shown in Figure 1.3.(c). In this case however, the low-dimensional aspect is not just determined by confinement, but is also a consequence of the forces applied to the pedestrians. These examples show that the relationship between confinement and dimensionality is not always straightforward.

This is especially true in solid state physics, where the particles are usually electrons, and there exists several strategies to achieve low-dimensional electron systems, by reducing the thickness of a given compound to the atomic limit (graphene, silicene) for example. However, it is not the only way to achieve a low-dimensional electron system.

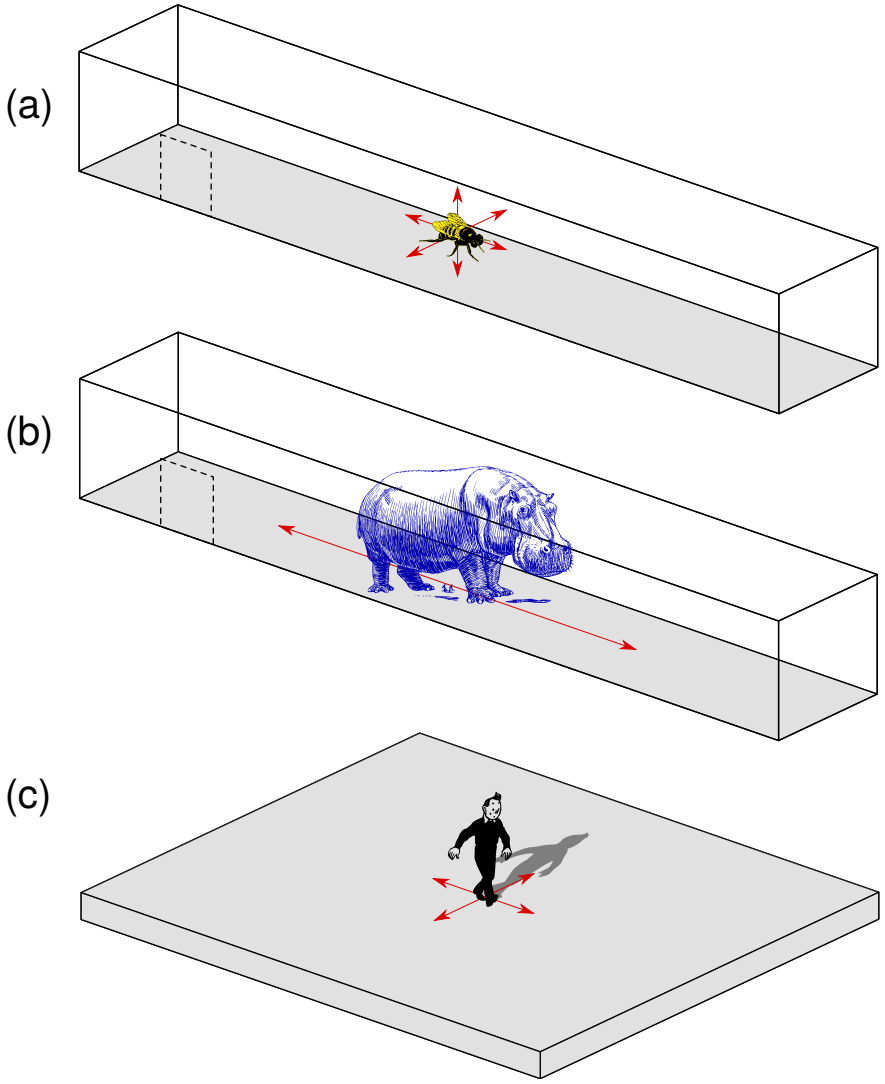

FIGURE 1.3: (a) a bee in a hallway; (b) a hippopotamus in the same hallway and (c), a pedestrian walking on a flat surface.

Indeed, it is possible to find low-dimensional systems in structures with a bulk-like character. For example, the topical 2-dimensional electron gas near the interface between $SrTiO_3$ and $LaAlO_3$ is located in the $SrTiO_3$ side of the junction, but remains confined within only a few nanometres of the interface whereas the electrons are highly mobile in the plane of the interface. Another example can be found in the topical iron-based full Heusler compounds, where the electronic carriers have highly anisotropic effective masses, constraining their motions under an applied electric field. The underlying mechanisms behind the confinement effects in these examples are related to the symmetry of the quantum states holding the carriers: the states in the vicinity of the conduction band arises from transition metal (Ti or Fe in these examples) $3d$ orbitals, which have a highly directional character due to their symmetry (shown in Figure 1.4). It is therefore possible to exploit these $3d$ orbitals to achieve low-dimensional electron systems.

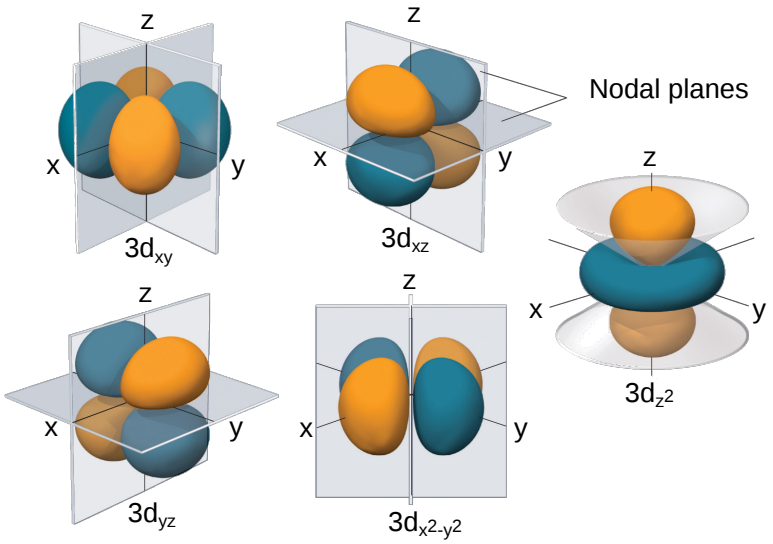

FIGURE 1.4: Representation of the wavefunction isosurfaces for 3*d* orbitals within the hydrogen-like atomic model, with the nodal planes where the wave function is null. Figure adapted from Reference [2]

1.3 Purpose of the present work

The present manuscript focuses on the physics of various systems sharing the common feature of involving 3*d* electrons for transport with a low-dimensional aspect, and studied from first-principles. It is organized as follows: in Chapter 2, we present the methodology upon which the studies are performed, introducing the basics of DFT, its practical implementation and the Boltzmann transport theory used to calculate transport coefficients. The manuscript is then split in two parts: Chapters 3, 4 and 5 are about the peculiar conducting interface between band insulators $LaAlO_3$ and $SrTiO_3$, and we will discuss its possible origins and its properties based on first-principles calculations. Then, in Chapter 6, we present a small introduction to thermoelectricity, and how low-dimensional systems can potentially increases the performance of thermoelectric materials. We present insights on the thermoelectric properties of layered oxides in Chapter 7, specifically calcium cobaltite $Ca_3Co_4O_9$ and $SrTiO_3$-based layered compounds. Finally, going beyond oxides, we investigate how low-dimensional transport can be achieved in iron-based bulk Heusler compounds in Chapter 8, how they may be exploited to reach high thermoelectric properties, and their properties if chemically doped with donors.

Chapter 2

Methodology

The objective of the present Chapter is to review the different aspects of the *ab initio* techniques used in this work. We will present the purpose of first-principles methods, the basic theoretical principles of DFT, its practical implementation within the CRYSTAL simulation package, as well as the semi-classical Boltzmann transport theory and its implementation in the BoltzTraP code to obtain the thermoelectric properties of the compounds, based on their electronic and structural properties as determined from first-principles. The following Sections are inspired by several References [3–5] that the interested reader may look at to get a more complete understanding of the methods from which the results of this manuscript are calculated.

2.1 Introduction to first-principles methods

A crucial element of any scientific inquiry is a robust methodology to highlight the different properties of a given system. This can be quite complicated in material sciences, specifically in the fields related to the atomic scale physics, which target the understanding of the microscopic mechanisms behind emergent phenomena observed at human scale.

Tremendous progress has been done during the past decades in both experimental and theoretical methodologies which can often be used concomitantly: indeed, experiments often provides a specific information of a system, which need to be interpreted within a given model. For example, one can perform X-Ray diffraction spectroscopy (XRD), and the obtained data can interpreted in terms of Bragg's law, to assess the structure, symmetry and the constituents of a given crystalline compound. However XRD cannot provide an explanation as to why the atoms are arranged as they are; theoretical methods can provide such an information.

Historically, theoretical studies in physics are associated with the finding of the analytical solution to the equation associated with a given problem (for example, two bodies in interaction). However, equations can quickly become impossible to solve as the complexity of a problem increases (three, four, ... bodies in interaction), which is typically the case in material sciences. One is then left with two possibilities: either to simplify the problem, by modelling the system as simpler entities in interaction, or to solve the equations numerically. Sometime, both are necessary.

In this regard, the development of numerical methods, concomitant with the development of computer technologies, has been quickly adopted in the field of material sciences. Atomistic simulations can for instance be performed by modelling the interactions between the atoms, usually by Lennard-Jones potentials adjusted to experiments.

Ab initio or first-principles methods are characterized by the fact that they treat explicitly the interactions between electrons and nuclei, using the basic laws of quantum mechanics and electromagnetism. In a sense, because they do not require any experimental input, they are predictive. One of the most successful *ab initio* technique is Density Functional Theory (DFT). The majority of the developments and results in this manuscript are based on DFT.

2.2 Ground state properties

2.2.1 The many-body problem

A crystal consists in a primitive unit cell containing atoms and repeated periodically in all spatial directions, forming the Bravais lattice. The Bravais lattice, containing the interacting nuclei and electrons, constitutes the problem to solve from the equations of quantum mechanics.

Let us consider a quantum system which contains N^0 nuclei, and N electrons in interactions. Such a system can be characterized by a wave function which can be obtained by solving the static Schrödinger equation:

$$H(\mathbf{r},\mathbf{R})\,|\Psi(\mathbf{r},\mathbf{R})\rangle \;=\; E\,|\Psi(\mathbf{r},\mathbf{R})\rangle \tag{2.1}$$

where $|\Psi(\mathbf{r},\mathbf{R})\rangle$ is the eigenfunction and H is the hamiltonian operator, which is the sum of distinct operators related to the kinetic and interaction energies between electrons and nuclei:

$$H(\mathbf{r},\mathbf{R}) \;=\; T_{\text{core}}(\mathbf{R}) + U_{\text{core}-\text{core}}(\mathbf{R}) + T_{\text{e}}(\mathbf{r}) + U_{\text{ee}}(\mathbf{r}) + U_{\text{core}-\text{e}}(\mathbf{r},\mathbf{R}) \tag{2.2}$$

The mathematical expressions in this Chapter will make use of the following notations:

- N^0 is the total number of nuclei in the system,
- N is the total number of electrons in the system,
- the indices κ and κ' refer to the nuclei,
- the indices i and j refer to the electrons,
- $\mathbf{r}_i$ is the position of the electron i,
- $\mathbf{R}_\kappa$ is the position of the nucleus κ,
- Z_κ is the charge of the nucleus κ.

If we work in atomic units[1], we have:

$$\begin{array}{lll} \dfrac{1}{4\pi\epsilon_0} = 1 & \hbar = 1 & e = 1 \\ m_{e^-} = 1 & & c = 137.036 \end{array}$$

[1] From this point and onward, we will make use of atomic units, unless specified.

and the different terms in Equation 2.2 can be written as:

$$T_{\text{core}}(\mathbf{R}) = -\sum_{\kappa=1}^{N^0} \frac{1}{2M_\kappa} \Delta_{\mathbf{R}_\kappa} \tag{2.3}$$

$$U_{\text{core-core}}(\mathbf{R}) = +\sum_{\kappa<\kappa'} \frac{Z_\kappa Z_{\kappa'}}{|\mathbf{R}_\kappa - \mathbf{R}'_\kappa|} \tag{2.4}$$

$$T_{\text{e}}(\mathbf{r}) = -\sum_{i=1}^{N} \frac{1}{2} \Delta_{\mathbf{r}_i} \tag{2.5}$$

$$U_{\text{ee}}(\mathbf{r}) = +\sum_{i<j} \frac{1}{|\mathbf{R}_i - \mathbf{R}_j|} \tag{2.6}$$

$$U_{\text{core-e}}(\mathbf{r}, \mathbf{R}) = -\sum_{\kappa,i} \frac{Z_\kappa}{|\mathbf{r}_i - \mathbf{R}_\kappa|} \tag{2.7}$$

These terms are identified as follows:

- (2.3) is the operator related to the kinetic energy of the nuclei,
- (2.4) is the operator related to the interaction energy between the nuclei,
- (2.5) is the operator related to the kinetic energy of the electrons,
- (2.6) is the operator related to the interaction energy between electrons,
- (2.7) is the operator related to the interaction energy between the nuclei and the electrons.

In practice, such a Schrödinger equation is impossible to solve analytically. Moreover, it is computationally difficult to obtain a numerical solution. It is therefore necessary to make use of a few approximations in order to simplify the problem.

We notice that the nuclei have masses that are large compared to the mass of the electrons ($M_\kappa \approx 10^3\, m_e$). So, the $T_{\text{core}}(\mathbf{R})$ term is very small compared to T_{e}, and we can consider it as a small perturbation. It means that the electrons are more mobile than the cores and follow adiabatically the ionic motions. In other words, the inertia of the electrons is considered negligible compared to that of the ions. This is the Born-Oppenheimer approximation [6], which constitute the first hypothesis to simplify the problem.

The unperturbed Hamiltonian is the Born-Oppenheimer Hamiltonian:

$$H_{\text{BO}}(\mathbf{r}, \mathbf{R}) = U_{\text{core-core}}(\mathbf{R}) + T_{\text{e}}(\mathbf{r}) + U_{\text{ee}}(\mathbf{r}) + U_{\text{core-e}}(\mathbf{r}, \mathbf{R}) \tag{2.8}$$

and the Born-Oppenheimer energy can be obtained by solving the Born-Oppenheimer Schrödinger equation:

$$H_{\text{BO}}(\mathbf{r}, \mathbf{R}) \, |\psi(\mathbf{r}, \mathbf{R})\rangle = E_{\text{BO}}(\mathbf{R}) \, |\psi(\mathbf{r}, \mathbf{R})\rangle \tag{2.9}$$

Since the Born-Oppenheimer hamiltonian does not have any differential operator on $\mathbf{R}$, $\mathbf{R}$ can be considered as a simple parameter of the hamiltonian. By fixing $\mathbf{R}$, $U_{\text{core-core}}(\mathbf{R})$ becomes a global shift of the electronic energy, thus that we can further write:

$$H_{\text{BO}}(\mathbf{r}, \mathbf{R}) = H_{\text{el}}(\mathbf{r}, \mathbf{R}) + U_{\text{core-core}}(\mathbf{R}) \tag{2.10}$$

with

$$H_{\mathrm{el}}(\mathbf{r},\mathbf{R}) \quad = \quad T_{\mathrm{e}}(\mathbf{r}) + U_{\mathrm{ee}}(\mathbf{r}) + U_{\mathrm{core-e}}(\mathbf{r},\mathbf{R}) \tag{2.11}$$

In practice, the Born-Oppenheimer approximation permits to treat the electrons and the nuclei problems separately :

1. the electronic ground state can be found for any given geometrical configuration of the nuclei by solving

$$H_{\mathrm{el}}(\mathbf{r},\mathbf{R})\,|\Psi(\mathbf{r},\mathbf{R})\rangle = E_{\mathrm{el}}(\mathbf{R})\,|\Psi(\mathbf{r},\mathbf{R})\rangle \tag{2.12}$$

   or by using the variational principle:

$$E_{\mathrm{el}}(\mathbf{R}) = \min_{\Psi} \langle\Psi|\, H_{el}\,|\Psi\rangle \tag{2.13}$$

2. then the ground state configuration of the nuclei $\mathbf{R}^0$ and the related energy are found as the minimum of the Born-Oppenheimer energy

$$E_{\mathrm{BO}}(\mathbf{R}) \quad = \quad E_{\mathrm{el}}(\mathbf{R}) + E_{\mathrm{core-core}}(\mathbf{R}) \tag{2.14}$$

$$\longrightarrow E_{\mathrm{BO}}(\mathbf{R}^0) \quad = \quad \min_{\mathbf{R}} \left[E_{el}(\mathbf{R}) + E_{\mathrm{core-core}}(\mathbf{R})\right] \tag{2.15}$$

The central problem therefore consists in solving Equation 2.12 to get the eigenvalue $E_{\mathrm{el}}(\mathbf{R})$ and the associated wave function $|\Psi(\mathbf{r},\mathbf{R})\rangle$. This is the so-called electronic many-body problem, which is impossible to solve; this can be easily understood from the following example: the water molecule H_2O contains $N = 10$ electrons. In three-dimensional space, this means that the spatial part of the many-body wave function $|\Psi(\mathbf{r_1},\mathbf{r_2},\ldots,\mathbf{r_N})\rangle$ is defined in a Euclidean space of dimension $3N = 30$. The water molecule is roughly ~ 2 Å large. If we take a cubic box 4 Å wide, with a $M = 20 \times 20 \times 20 = 8000$ mesh to interpolate the wave function, the determination of any matrix elements requires $M^{3N} = 8000^{30} \approx 10^{117}$ operations. However, this should be repeated several times if one desires the ground-state wave function from the variational principle (Eqn. 2.13). If one desires to get just a single matrix element with a computer performing 10^{17} calculations per second, it would requires roughly 10^{100} seconds, or $\sim 3\times10^{92}$ years. For comparison, the observable universe is only 13.8×10^9 years old. If the many-body problem cannot be solved for a molecule as simple as H_2O, one can easily give up to study more complex quantum systems. The main issue is that the complexity of the problem increases exponentially with the number of electrons. If the problem cannot be solved, it remains possible to change the problem to one that is solvable. This is the basis of DFT, which will be presented in the next Section.

2.2.2 Density Functional Theory

In the previous discussion, the impossibility to solve the many-body Schrödinger equation stems from the fact that we explicitly considered the many-body wave function $|\Psi(\mathbf{r},\mathbf{R})\rangle$ as the "variable" of the problem. The basis of density functional theory is to consider that the fundamental variable is no longer the many-body wave function, but the electronic density instead, and that the associated ground state properties, such as the energy, can be derived from the knowledge of the density, instead of the knowledge of the wave function.

If the wave function $|\Psi\rangle$ associated to the ground state of the N-electron system depends on the spatial coordinates $\mathbf{r}_1, \mathbf{r}_2, \mathbf{r}_3, \ldots, \mathbf{r}_N$, the electronic density $n(\mathbf{r})$ is defined as:

$$d(\mathbf{r}) = \sum_i^N \delta(\mathbf{r} - \mathbf{r}_i) \tag{2.16}$$

$$n(\mathbf{r}) = \langle \Psi(\mathbf{r}_1, \mathbf{r}_2, ..., \mathbf{r}_N) | \, d(\mathbf{r}) \, | \Psi(\mathbf{r}_1, \mathbf{r}_2, ..., \mathbf{r}_N) \rangle \tag{2.17}$$

As the density only depends on spatial coordinates, the problem of $3N$ variables is reformulated as a 3 variables problem, expected to be simpler to solve and requiring less computational resources. Hohenberg and Kohn demonstrated that it is indeed possible to reformulate the many-body problem. We will explain in the following Section the Hohenberg-Kohn theorems, as well as how the theory is put in practice through the Kohn-Sham *ansatz*.

2.2.2.1 The first Hohenberg-Kohn theorem

We will now see how the many-body problem can be recast into a problem which only make use of the electronic density.

The first Hohenberg-Kohn theorem [3] stipulates:

"The electronic density of the ground state $n_0(\boldsymbol{r})$ of the many-body electronic system is entirely and uniquely determined by the external potential $U_{ext}(\boldsymbol{r})$ modulo a constant"

Proof[2] : *Ad absurdum.* We consider two external $U_{\text{ext}}^{(1)}(\mathbf{r})$ and $U_{\text{ext}}^{(2)}(\mathbf{r})$ which differs beyond a simple shift through a constant term, and we assume that both are associated to the same ground state electronic density $n_0(\mathbf{r})$. Because these two potentials are different, then there is two Hamiltonians associated with $U_{\text{ext}}^{(1)}(\mathbf{r})$ and $U_{\text{ext}}^{(2)}(\mathbf{r})$, respectively $H^{(1)}$ and $H^{(2)}$, also associated their ground state wave functions $|\Psi^{(1)}\rangle$ and $|\Psi^{(2)}\rangle$ respectively. As $|\Psi^{(2)}\rangle$ is not the ground state of the system associated to the Hamiltonian $H^{(1)}$, we can write successively:

$$\begin{aligned} E^{(1)} &= \langle \Psi^{(1)} | H^{(1)} | \Psi^{(1)} \rangle \\ &< \langle \Psi^{(2)} | H^{(1)} | \Psi^{(2)} \rangle \\ &< \langle \Psi^{(2)} | H^{(2)} | \Psi^{(2)} \rangle + \langle \Psi^{(2)} | H^{(1)} - H^{(2)} | \Psi^{(2)} \rangle \\ &< E^{(2)} + \int d\mathbf{r} \, \left[U_{\text{ext}}^{(1)} - U_{\text{ext}}^{(2)} \right] \, n_0(\mathbf{r}) \end{aligned}$$

$$\implies E^{(1)} < E^{(2)} + \int d\mathbf{r} \, \left[U_{\text{ext}}^{(1)} - U_{\text{ext}}^{(2)} \right] \, n_0(\mathbf{r}) \tag{2.18}$$

[2] The proof reported here is only valid for a non-degenerated system. The extension of this proof to degenerate case can be found in the literature [7].

In the same fashion, as $\left|\Psi^{(1)}\right\rangle$ is not the ground state of the system associated with the Hamiltonian $H^{(2)}$, we can write an analog development:

$$\begin{aligned} E^{(2)} &= \langle\Psi^{(2)}|H^{(2)}|\Psi^{(2)}\rangle \\ &< \langle\Psi^{(1)}|H^{(2)}|\Psi^{(1)}\rangle \\ &< \langle\Psi^{(1)}|H^{(1)}|\Psi^{(1)}\rangle + \langle\Psi^{(1)}|H^{(2)} - H^{(1)}|\Psi^{(2)}\rangle \\ &< E^{(1)} + \int d\mathbf{r}\, \left[U^{(2)}_{\text{ext}} - U^{(1)}_{\text{ext}}\right]\, n_0(\mathbf{r}) \end{aligned}$$

$$\implies E^{(2)} < E^{(1)} + \int d\mathbf{r}^3\, \left[U^{(2)}_{\text{ext}} - U^{(1)}_{\text{ext}}\right]\, n_0(\mathbf{r}) \tag{2.19}$$

Summing 2.18 and 2.19 yields the strict inequality $E^{(1)}+E^{(2)} < E^{(2)}+E^{(1)}$, which is not possible. Therefore, the assumption that the same electron density $n_0(\mathbf{r})$ is associated with both $U^{(1)}_{\text{ext}}(\mathbf{r})$ and $U^{(2)}_{\text{ext}}(\mathbf{r})$ is incorrect.

Hence, the electronic density is only determined by the external potential (*modulo* a constant).

2.2.2.2 The second Hohenberg-Kohn theorem

The second theorem can be summarized as [3]:
"A universal functional $E[n]$, which gives the energy in regards to the electronic density $n(\boldsymbol{r})$, exists for any external potential $U_{ext}(\boldsymbol{r})$. For each $U_{ext}(\boldsymbol{r})$, the ground state energy is the energy which minimizes this functional, and the associated density $n(\boldsymbol{r})$ is the exact ground state density $n_0(\boldsymbol{r})$"

Proof: As any properties of a given system are determined the electronic density $n(\mathbf{r})$, they can be expressed as density functionals. Particularly, the total energy can be written as a functional of the density:

$$E[n] = T[n] + U[n] + \int U_{ext}(\mathbf{r})\, n(\mathbf{r}) d\mathbf{r} \tag{2.20}$$

$$= F[n] + \int U_{ext}(\mathbf{r})\, n(\mathbf{r}) d\mathbf{r} \tag{2.21}$$

In Expression 2.21, $F[n]$ is a partial contribution of the electronic system (kinetic and electrons-electrons energies) to the total energy, and is also a density functional, which does not depend on the external potential, and is the same for any electronic system. Hence, $F[n]$ is a *"universal functional"* of the density.

Now, we consider a system which has a ground state density $n^{(1)}$ associated to the external potential $U^{(1)}_{ext}(\mathbf{r})$. In this case, the Hohenberg-Kohn functional is equal to the expectation value of the Hamiltonian with the ground state $\left|\Psi^{(1)}\right\rangle$:

$$E^{(1)} = \left\langle \Psi^{(1)} \left| H^{(1)} \right| \Psi^{(1)} \right\rangle \tag{2.22}$$

If we consider another density $n^{(2)}$ associated to another wave function $\left|\Psi^{(2)}\right\rangle$ (different from $\left|\Psi^{(1)}\right\rangle$, therefore not associated to the ground state), we can see that the energy $E^{(2)}$ of this other state is superior than the ground state energy $E^{(1)}$:

$$\begin{aligned} E^{(1)} = \left\langle \Psi^{(1)} \middle| H^{(1)} \middle| \Psi^{(1)} \right\rangle &< \left\langle \Psi^{(2)} \middle| H^{(1)} \middle| \Psi^{(2)} \right\rangle \\ &< E^{(2)} \end{aligned} \tag{2.23}$$

The direct consequence is that the aforementioned energy functional $E[n]$, expectation value obtained for the ground state density $n_0(\mathbf{r})$, must necessarily be inferior to the value obtained through any other density n. From the knowledge of the universal functional $F[n]$, minimizing $E[n]$ by tuning the electronic density n (and under particle conservation constraints) leads to both the ground state density and total energy. Unfortunately, the exact analytic form of $F[n]$ is not known.

2.2.3 DFT in practice and the Kohn-Sham ansatz

The theorems enunciated in the previous Section demonstrates the possibility to shift from the many-body wave function as a variable to the electron density. However, there is no practical way to implement it, as the universal functional $F[n]$ is unknown. An alternative approach was proposed by Kohn and Sham, and consists in mapping the unsolvable problem to one that is easily solvable, yielding the same solution in term of electronic density. This is the Kohn-Sham *ansatz*: a fictional system of non-interacting particles is considered, which are moving in an external potential v_s, yet produce the same ground state density $n_0(\mathbf{r})$ as the real, many-body system. Such a system would be characterized by the following one-electron Schrödinger equation:

$$\left(-\frac{\nabla^2}{2} + v_s(\mathbf{r})\right) |\phi_i(\mathbf{r})\rangle = \epsilon_i \, |\phi_i(\mathbf{r})\rangle \tag{2.24}$$

where $|\phi_i(\mathbf{r})\rangle$ are the one-body wave functions and ϵ_i the one-body eigenenergies.

To map the non-interacting Kohn-Sham system to the many-body one, we need to determine $v_s(\mathbf{r})$. The many-body energy as given by Equation (2.21) can be rewritten as follows:

$$E[n] = \int U_{ext}(\mathbf{r}) n(\mathbf{r}) d\mathbf{r} + T_e[n] + \frac{1}{2} \int\int \frac{n(\mathbf{r}) n(\mathbf{r}')}{|\mathbf{r} - \mathbf{r}'|} d\mathbf{r} d\mathbf{r}' + E_{xc}[n] \tag{2.25}$$

Basically, we just rewrote the unknown universal functional $F[n]$ as a sum of three density functionals: $T_e[n]$ is the kinetic energy of the electrons, the third term is the Coulomb interaction between electrons rewritten as a functional of the density (named Hartree energy $E_H[n]$), and the last term is the exchange-correlation energy. The Kohn-Sham *ansatz* consists in rewritting $F[n]$ as follows:

$$F[n] = T_e[n] + E_H[n] + E_{xc}[n] \tag{2.26}$$

$$\Longrightarrow F[n] = T^{\mathrm{KS}}[n] + E_H[n] + E_{xc}^{\mathrm{KS}}[n] \tag{2.27}$$

$$\text{with} \quad E_{xc}^{\mathrm{KS}}[n] = E_{xc} + T_e[n] - T^{\mathrm{KS}}[n] \tag{2.28}$$

Basically, a term of kinetic energy $T^{\mathrm{KS}}[n]$ has been introduced, which corresponds to the kinetic energy of the non-interacting particles. The exchange-correlation energy has been rewritten to include the difference of kinetic energy from the many-body system $T_e[n]$ to the non-interacting one (which are not identical). Hence, technically, $F[n]$ has not changed, and it has been reformulated as the sum of three terms, the first two ($T^{\mathrm{KS}}[n]$ and $E_H[n]$) with known analytical forms.

The ground state density $n_0(\mathbf{r})$ can be found by minimizing $E[n]$ with respect to $n(\mathbf{r})$ in Equation 2.25 by the means of Lagrange multipliers accounting for the conservation of the number of particles N:

$$\frac{\delta}{\delta n}\left[E[n] + \mu \int n(\mathbf{r}) d\mathbf{r}\right] = 0 \tag{2.29}$$

$$\iff \frac{\delta E[n]}{\delta n} = \mu \tag{2.30}$$

where μ is the Lagrange multiplier and has a relevant physical meaning: it is the chemical potential of the electron system, defined as the derivative of the energy with respect to the number of particle ($\partial E/\partial N = \mu$). Hence, we have:

$$\frac{\delta E[n]}{\delta n} = \frac{\delta T^{\mathrm{KS}}[n]}{\delta n} + U_{ext}(\mathbf{r}) + \int \frac{n(\mathbf{r}')}{|\mathbf{r} - \mathbf{r}'|} d\mathbf{r}' + \frac{\delta E_{xc}^{\mathrm{KS}}}{\delta n} = \mu \tag{2.31}$$

If we consider the Kohn-Sham hypothesis, there exists a system of non-interacting particle moving in a potential $v_s(\mathbf{r})$ yielding the same ground state density $n_0(\mathbf{r})$ as the many-body system. The variational principle for this system is written as:

$$\frac{\delta E[n]}{\delta n} = \frac{\delta T^{\mathrm{KS}}[n]}{\delta n} + v_s(\mathbf{r}) = \mu \tag{2.32}$$

Equations (2.31)and (2.32) have the same mathematical form and coincide whenever:

$$v_s(\mathbf{r}) = U_{ext}(\mathbf{r}) + \int \frac{n(\mathbf{r}')}{|\mathbf{r} - \mathbf{r}'|} d\mathbf{r}' + \frac{\delta E_{xc}^{\mathrm{KS}}[n]}{\delta n(\mathbf{r})} \tag{2.33}$$

Therefore, with this reformulation of $F[n]$, then the many-body problem can be recast as a one-body problem yielding the same electronic density, if the external potential $v_s(\mathbf{r})$ takes the form as given in Equation 2.33. Moreover, as we know that the ground state density of a non-interacting particles system can be calculated from the one-body wave functions, solutions of a Schrödinger equation, then one simply need to solve the Kohn-Sham equations:

$$\begin{cases} \left(-\dfrac{\nabla^2}{2} + U_{ext}(\mathbf{r}) + \displaystyle\int \frac{n(\mathbf{r}')}{|\mathbf{r} - \mathbf{r}'|} d\mathbf{r}' + U_{xc}(\mathbf{r}, [n])\right) |\phi_i(\mathbf{r})\rangle = \epsilon_i |\phi_i(\mathbf{r})\rangle \\ n(\mathbf{r}) = \displaystyle\sum_i^N \langle \phi_i(\mathbf{r}) | \phi_i(\mathbf{r}) \rangle \end{cases} \tag{2.34}$$

which is the form taken by Equation (2.24) with the constraint (2.33), the orthonormalization of the wave functions $\langle \phi_i(\mathbf{r}) | \phi_j(\mathbf{r}) \rangle = \delta_{ij}$ and where we wrote $U_{xc}(\mathbf{r}, [n]) = \delta E_{xc}^{\mathrm{KS}}[n]/\delta n(\mathbf{r})$.

Note that the Kohn-Sham equations can be rewritten with variational formulation. Considering Equation (2.37) rewritten as functional of one-body wave functions $|\phi_i(\mathbf{r})\rangle$ and

that $T^{\mathrm{KS}} = \sum_i^N \langle\phi_i(\mathbf{r})| -\frac{1}{2}\nabla^2 |\phi_i(\mathbf{r})\rangle$, then the minimization under orthonormalization constraint of $\phi_i(\mathbf{r})$ is written as:

$$\begin{aligned} 0 &= \frac{\delta}{\delta\langle\phi_i(\mathbf{r})|}\Bigg[T^{\mathrm{KS}}[n] + \int U_{ext}(\mathbf{r})n(\mathbf{r})d\mathbf{r}) \\ &\quad + E_H[n] + E_{xc}[n] - \sum_{ij}\xi_{ij}(\langle\phi_i|\phi_j\rangle - \delta_{ij})\Bigg] \end{aligned} \tag{2.35}$$

Or equivalently:

$$\left(-\frac{1}{2}\nabla^2 + U_{ext} + U_H + U_{xc}\right)|\phi_i\rangle = \sum_j \xi_{ij}\,|\phi_j\rangle \tag{2.36}$$

where $U_H = \delta E_H/\delta n$. Setting the gauge $\xi_{ij} = \delta_{ij}\epsilon_i$ leads Equation 2.36 back to its standard Kohn-Sham formulation.

At this stage, we notice that the third term in Equation (2.33), the Kohn-Sham exchange-correlation potential $U_{xc}(\mathbf{r}, [n])$, remains unknown. In principle, it should encompass different terms accounting for physical effects which are not explicitly considered in the non-interacting picture: the indiscernibility of the electrons (and the related Pauli exclusion principle), the spatial correlations between electrons (quantum fluctuations), and the error (self-interaction) originating from the Hartree formulation of the electron-electron Coulomb interactions. Also, it should contain the difference of kinetic energy between the real system (interacting particles) and the Kohn-Sham system (non-interacting particles), as explicitly written in Equation 2.28. Finally, as $E_{xc}^{\mathrm{KS}}[n]$ does not depend on the external potential but *only* on the electronic density, it is a *universal* density functional, and should have the same form for all systems.

The total energy $E[n]$ of the interacting particle system is not the sum of eigenvalues ϵ_i of the Kohn-Sham system, and is given by:

$$E[n] = \sum_i^N \epsilon_i - \int U_{xc}(\mathbf{r})n(\mathbf{r})d\mathbf{r} - E_H[n] + E_{xc}[n] \tag{2.37}$$

and can therefore be retrieved from the Kohn-Sham eigenvalues and eigenfunctions.

We have shown that it is possible to determine the electronic density of the many-body system from the Kohn-Sham *ansatz*. Even though the equations are simpler, there remains the issue related to the $E_{xc}[n]$ term, as we do not know its exact analytical expression. Fortunately, it is still possible to approximate it, which will be the topic of the next Section.

2.2.4 Approximate exchange-correlation energy functional

In principle, the $E_{xc}[n]$ is a universal functional of the density n and should have the same analytical form independently of the system. Yet, its analytical form is not known. Moreover, the kinetic energy of the real system is not guaranteed to be equal to the kinetic energy of the fictitious Kohn-Sham system. The $E_{xc}[n]$ is therefore expected to

contains the difference between these two kinetic energies. There are many different possibilities to approximate the $E_{xc}[n]$ terms, which will be briefly reviewed in the following sections.

2.2.4.1 LDA - Local Density Approximation

The first approximation of $E_{xc}[n]$ is the local density approximation (LDA), and built from the homogeneous electron gas model. Indeed, for such a simple system, it is straightforward to obtain an analytical expression for the exchange part of $E_{xc}[n]$. All physical properties of the homogeneous electron gas depends on a single parameters, the density $n(\mathbf{r})$, which is by definition the same for any $\mathbf{r}$: $n(\mathbf{r}) = n_0$. Therefore, the exchange-correlation energy of the gas also depends on the density $E_{xc} = E_{xc}[n(\mathbf{r})] = E_{xc}[n_0]$. From the knowledge of the total energy, one can extract the exchange-correlation term. If we assume that the exchange-correlation energy density at a given point $\mathbf{r}$, $\epsilon(\mathbf{r})$, only depends on the density at this point and that it is equal to the exchange-correlation energy per particle of a homogeneous electron gas of density n_0, we can use ϵ_{xc} locally for any system where $n(\mathbf{r})$ is not uniform (as it is the case in most realistic systems), we can write the exchange-correlation energy as a local functional of the density $n(\mathbf{r})$:

$$E_{xc}^{\mathrm{LDA}}[n] = \int n(\mathbf{r})\epsilon_{xc}^{\mathrm{hom}}[n(\mathbf{r})]d\mathbf{r} \tag{2.38}$$

$$\tag{2.39}$$

where $\epsilon_{xc}^{\mathrm{hom}}$ is the exchange-correlation energy density of the homogeneous electron gas at a given uniform density. The exchange-correlation energy of the homogeneous electron gas can be written as the sum of two contributions, the exchange part E_x^{hom} and the correlation part E_c^{hom}:

$$E_{xc}^{\mathrm{hom}}[n] = E_x^{\mathrm{hom}}[n] + E_c^{\mathrm{hom}}[n] \tag{2.40}$$

The exchange term has an analytical form, derived from Hartree-Fock methods [3]:

$$E_x^{\mathrm{hom}}[n] = -\frac{3}{4}\left(\frac{3}{\pi}\right)^{\frac{5}{3}} \int n^{4/3}(\mathbf{r})d\mathbf{r} \tag{2.41}$$

The correlation term $E_c^{\mathrm{hom}}[n]$ is not calculated analytically. Instead, it is approximated by fitting an analytical function on curves obtained using Quantum Monte-Carlo simulations of a homogeneous electron gas, and by subtracting the known exchange and kinetic part of the total energy.

The most popular formulations are those of Vosko, Wilkes and Nussair [8] (VWN) and Perdew and Zunger [9] (PZ).

Being the first $E_{xc}[n]$ approximation, the LDA is widely used even today, and indeed, this simple approximation managed to be quite efficient at predicting properties of crystalline systems, with good accuracy compared to experiments. Nevertheless, the approximation also has shortcomings: indeed, structures relaxed within the LDA tend to have their lattice parameters underestimated. Moreover, strong electronic correlations cannot be treated efficiently within the LDA, and this may strongly impact the accuracy of the

predicted electronic properties (band gaps of semiconductors or insulators tend to be underestimated, for example).

The exchange-correlation energy expressed above is valid for spin-degenerate systems. The generalization of the LDA to magnetic system by accounting for the spin state of the electrons, assuming that the magnetic properties originates solely from the intrinsic magnetic moment of the electrons. The principle is to treat two different electron densities: the spin-up electronic density $n^{\uparrow}(\mathbf{r})$ and the spin-down electronic density $n^{\downarrow}(\mathbf{r})$. This usually means that magnetic systems have twice more equations to solve.

The exchange-correlation energy must be rewritten to be spin-dependant, $E_{xc}[n] = E_{xc}[n^{\uparrow}, n^{\downarrow}]$. In the case of collinear magnetism, this is done by using two exchange-correlation potentials:

$$u_{xc}^{\uparrow} = \frac{\delta E_{xc}[n^{\uparrow}, n^{\downarrow}]}{\delta n^{\uparrow}} \quad \text{and} \quad u_{xc}^{\downarrow} = \frac{\delta E_{xc}[n^{\uparrow}, n^{\downarrow}]}{\delta n^{\downarrow}}$$

The generalized approximation is the *local spin density approximation* (LSDA) and the exchange part is expressed as:

$$E_x^{\mathrm{LSDA}}[n^{\uparrow}, n^{\downarrow}] = -2^{\frac{2}{3}} \frac{3}{4} \left(\frac{3}{\pi}\right)^{1/3} \int \left(n^{\uparrow\frac{4}{3}} + n^{\downarrow\frac{4}{3}}\right) d\mathbf{r} \tag{2.42}$$

2.2.4.2 GGA - Generalized Gradient Approximation

The shortcomings of the LDA motivated the use of more elaborated functionals: indeed, there is no reason that the electronic density $n(\mathbf{r})$ does not depend on the electron density in its vicinity $n(\mathbf{r}+\delta\mathbf{r})$. The generalized gradients approximations (GGA) are semi-local approximations of $E_{xc}[n]$ which locally account for the variations of the electron density by expressing the exchange-correlation energy as a functional of the density and as a functional of its gradients (and higher order derivatives):

$$E_{xc}^{\mathrm{GGA}}[n] \quad = \quad \int n(\mathbf{r}) \epsilon_{xc}[n, \nabla n, \nabla^2 n, ...] d\mathbf{r} \tag{2.43}$$

Amongst the most used formulations reported in the litterature, there are the one of Perdew, Burke and Ernzerhof (PBE) [10] and Perdew and Wang (PW91) [11].

2.2.4.3 Beyond LDA and GGA: DFT+U and hybrid functionals

As local and semi-local approaches, the LDA and GGA are known to illy treat strong exchange-correlation effects (for example, low band gap semiconductors are predicted metallic). A popular solution at minimal computational cost is the DFT+U formalism, which consists in adding a Hubbard correction U in the Hamiltonian to increases Coulombian repulsions in d and f orbitals: as these populations are very localized, Coulombian repulsion is underestimated with semi-local approaches. The introduction of extra-Coulombian repulsion in d or f orbitals usually open the electronic band gap

in illy treated semiconductors, and is written as an additional orbital-dependent term in the Hamiltonian:

$$\frac{1}{2}U\sum_{i\neq j} n_i n_j \tag{2.44}$$

where U is the screened Coulomb parameter and n_i is the occupation number of orbital i. The U parameter can either be chosen so that the calculated gap corresponds to the experimental one, as an empirical parameter. Another possibility is to calculate the value of U from DFT in a self-consistent approach (as proposed in Reference [12] for example).

Another solution to overcome the shortcomings of LDA and GGA are hybrid functionals of E_{xc}. They have been introduced in the early nineties and were mainly used in quantum chemistry calculations for atoms and molecules. Later, their use has been extended to periodic systems. The principle behind hybrid functionals is rather simple, and consists in mixing the typical semi-local functional (LDA and GGA) with a fraction of Hartree-Fock exchange. Non-local effects of the exchange energy are therefore explicitly treated.

The relevance of this approach is justified by the so-called *adiabatic connection formula* [13]. In principle, the exchange-correlation energy of the Kohn-Sham system is not equal to the echange-correlation energy of the many-electron interacting system: this difference arises from the transfer of part of the many-body kinetic energy T_{xc} to the exchange-correlation term of the Kohn-Sham system. However, it has been shown that there exists an *exact* (yet unknown) relation connecting T_{xc} and E_{xc} [13]. Let us consider the following family of Hamiltonians $H_{\mathrm{el}}(\lambda)$ with different electron-electron interaction characterized by a single parameter λ varying from 0 (non-interacting limit) to 1 (fully interacting limit):

$$H_{\mathrm{el}}(\lambda) \;=\; T_{\mathrm{e}} + \lambda\, U_{\mathrm{ee}} + u_\lambda \tag{2.45}$$

This function is decomposed into different terms: T_{e} is the kinetic energy operator, U_{ee} the electron-electron potential energy operator and u_λ is defined in such a way that all $H_{\mathrm{el}}(\lambda)$ produce the same ground-state density n. For $\lambda = 1$, we have the fully interacting many-body system and u_λ corresponds to the external potential ($u_{\lambda=1} = U_{\mathrm{ext}}$). For $\lambda = 0$, then we have the non-interacting Kohn-Sham system ($u_{\lambda=0} = v_s$ which is the Kohn-Sham potential associated to density n). It can be shown that the Kohn-Sham exchange-correlation energy corresponds to the average of the exchange-correlation potential energy for $\lambda \in [0, 1]$; the integration over λ generating the kinetic part of E_{xc}:

$$E_{xc} \;=\; \int_0^1 E_{xc,\lambda}\, d\lambda \tag{2.46}$$

where $E_{xc,\lambda}$ is the potential energy of exchange-correlation at intermediate λ, written as:

$$E_{xc,\lambda} \;=\; \langle \Psi_\lambda | U_{\mathrm{ee}} | \Psi_\lambda \rangle - E_H \tag{2.47}$$

where E_H is the classical Hartree energy and Ψ_λ the ground-state wave functions at given coupling strength λ. Equation (2.46) is the adiabatic connection formula [13, 14], and its behaviour is illustrated in Figure 2.1: for $\lambda = 0$, then $E_{xc,\lambda=0} = E_x$ where $E_x = \langle \Psi_0 | U_{\mathrm{ee}} | \Psi_0 \rangle - E_H$ is the exchange energy of the system as exactly defined within

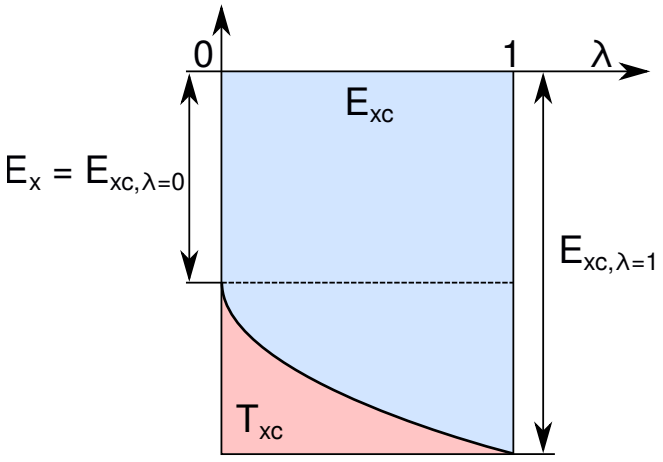

FIGURE 2.1: Schematic representation of the adiabatic connection. The Kohn-Sham exchange-correlation energy E_{xc} (light blue area) is obtained as the potential energy of exchange-correlation of the many-body interacting system $E_{xc,\lambda=1}$ corrected with the transfered kinetic energy T_{xc} (light red area) along the path of integration of coupling constant λ between 0 and 1.

the Hartree-Fock method on the basis of the Kohn-Sham wave functions Ψ_0. For $\lambda = 1$, then $E_{xc,\lambda=1}$ is the potential energy of exchange-correlation of the many-body system. The quantity E_{xc} as defined in Equation (2.46) corresponds to the light blue area of Figure 2.1 and differs from the many-body exchange-correlation energy of the fully interacting system by T_{xc} (light red area), corresponding to the transfer of many-body kinetic energy along the integration path over λ from 0 to 1.

Hence, it should be possible in principle to obtain E_{xc} by mixing the exchange energy as defined in Hartree-Fock methods (E_x) and the many-body exchange-correlation potential energy ($E_{xc,\lambda=1}$). However, the exact value of this mixing is unknown and depends on the shape of the λ dependence of $E_{xc,\lambda}$. If the dependence is strictly linear between $\lambda = 0$ and $\lambda = 1$, then:

$$E_{xc} = \frac{1}{2}(E_x + E_{xc,\lambda=1}) \tag{2.48}$$

An *hybrid functional* based on Equation (2.48) is then built by substituting $E_{xc,\lambda=1}$ by its LDA formulation, as proposed by Becke [15]:

$$E_{xc}^{\text{hyb,Becke}} = \frac{1}{2}(E_x + E_{xc}^{\text{LDA}}) \tag{2.49}$$

In order to better capture the non-linear λ dependence, more sophisticated mixing schemes have been proposed. In their generic analytical formulation, hybrid functionals are expressed as a combination of various LDA and GGA functionals with Hartree-Fock exchange:

$$E_{xc}^{\text{hyb}}[n] = E_{xc}^{\text{LDA}} + a_0(E_x^{\text{HF}} - E_x^{\text{LDA}}) + a_x(E_x^{\text{GGA}} - E_x^{\text{LDA}}) + a_c(E_c^{\text{GGA}} - E_c^{\text{LDA}})$$

The different terms are:

- E_{xc}^{LDA}: exchange-correlation functional as defined in the LDA.

- E_x^{HF} : Hartree-Fock exchange obtained for the non-interacting particles system.
- E_x^{LDA}: LDA exchange functional.
- E_x^{GGA}: GGA exchange functional.
- E_c^{LDA}: LDA correlation functional.
- E_c^{GGA}: GGA correlation functional.

The coefficient a_0, a_x and a_c are optimized with different LDA and GGA exchange-correlation functionals and weight the semi-local approximations in $E_{xc}^{\mathrm{hyb}}[n]$.

A nomenclature has been adopted for hybrid functionals, related to the different terms: the first letter correspond to the GGA functional used for the exchange energy, followed by the number of coefficients a_0, a_x and a_c to be optimized, followed by the letters corresponding to the GGA functional used for the energy: for example the popular B3-LYP functional uses the *Becke* GGA functional for the exchange energy [16], and the *Lee-Yang-Parr* GGA functional for the correlation energy [17]. The three coefficients are :

$$\begin{aligned} a_0 &= 0.20 \\ a_x &= 0.72 \\ a_c &= 0.81 \end{aligned}$$

The B1-WC functional has been optimized by D. I. Bilc *et al* [18] at the Université de Liège and uses the *Perdew-Burke-Ernzerhof* GGA functional for the correlation energy, and the *Wu-Cohen* [19] GGA functional for the exchange energy. Only a_0 is optimized. A value of $a_0 = 0.16$ has been obtained. The other coefficients are fixed at: $a_x = 1 - a_0$ and $a_c = 1$.

The B1-WC was designed to predict properties of oxides with a better agreement to experiments as compared to the semi-local approaches, specifically perovskite $BaTiO_3$ and $PbTiO_3$. The performance of hybrid functionals has been reviewed in References [20, 21], concluding that it is an ideal formalism to get past the typical shortcomings of semi-local functionals. Numerous manuscripts have been published, based on the B1-WC functional in several fields of material physics, such has ferroelectrics [18, 22], ferromagnets [23] or thermoelectrics [24, 25]. Additionally, it has proven to properly characterize the 2-dimensional electron gas at the $SrTiO_3/LaAlO_3$ interface [26–29]

The calculations involved in the present work have been mostly performed using the B1-WC functional.

2.2.5 Solving the Kohn-Sham equations

The Kohn-Sham *ansatz* allows one to calculate the exact density and energy of the ground-state of a many-body electron system by solving independent-particles equations. The approximation of the exchange-correlation energy E_{xc} chosen, there remains to effectively solve the equations. In practice, the external Kohn-Sham potential $v_s(\mathbf{r})$ depends implicitly on the electronic density $n(\mathbf{r})$. Hence, both electronic density and external potential must be determined self-consistently. The routine for finding both is illustrated in Figure 2.2.

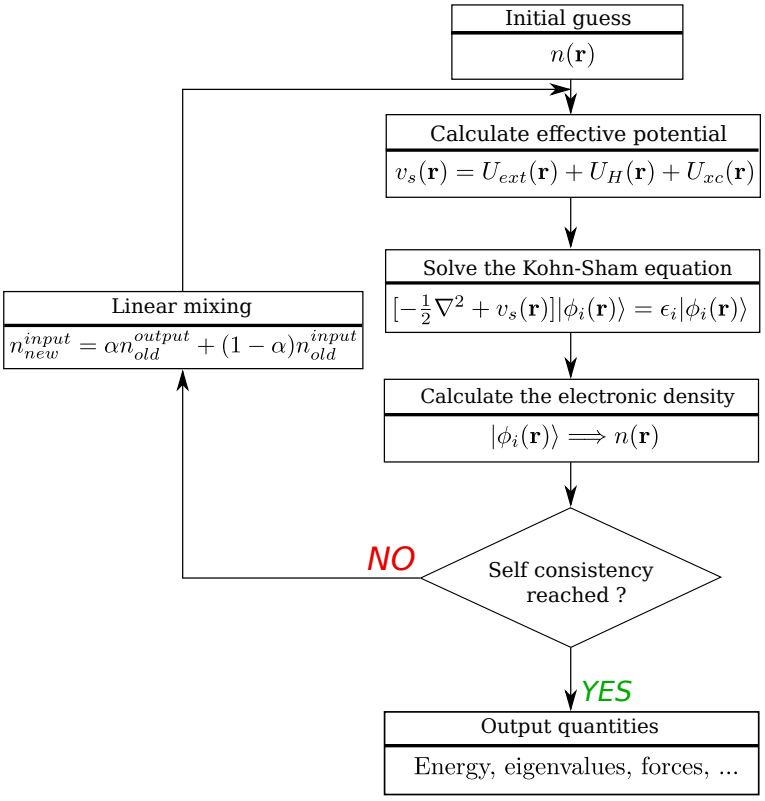

FIGURE 2.2: Schematic representation of the self-consistent loop for solution of Kohn-Sham equations.

First, an initial guess of the density $n(\mathbf{r})$ (which can be, for example, the sum of contributions calculated for the individual atoms) generates a Kohn-Sham potential $v_s(\mathbf{r})$. Then, the Kohn-Sham equations are solved with this external potential: the calculated single particle wave-functions $|\Psi_i(\mathbf{r})\rangle$ determines a new electronic density (different from the initial one), which is then used to generate a new external potential $v_s(\mathbf{r})$. This procedure iteratively generates n and v_s and should converges to a self-consistent Kohn-Sham solution. The convergence criteria are usually based on the difference of energy, density or potential between two successive steps, which should decreases as the procedure goes on.

The procedure can only converges with a judicious choice of the new potential and density calculated at the last iteration. However, converging toward a self-consistent solution is not always straightforward. Often, strong oscillations can lead to large computational times, if not a complete divergence of the solution. A simple solution to reduce oscillations is the approach of *linear mixing*: instead of using the new calculated density $n(\mathbf{r})$ to generate $v_s(\mathbf{r})$, the electronic density input at step $i+1$ is estimated as a fixed linear combination of n_i^{input} and n_i^{output} at step i, as given by:

$$n_{i+1}^{\text{input}} = \alpha n_i^{\text{output}} + (1-\alpha) n_i^{\text{input}} = n_i^{\text{input}} + \alpha(n_i^{\text{output}} - n_i^{\text{input}}) \tag{2.50}$$

where α is the mixing parameter. In the absence of any other information during the calculation, linear mixing forces the procedure to evolve in an approximate *steepest descent* direction for minimizing the energy.

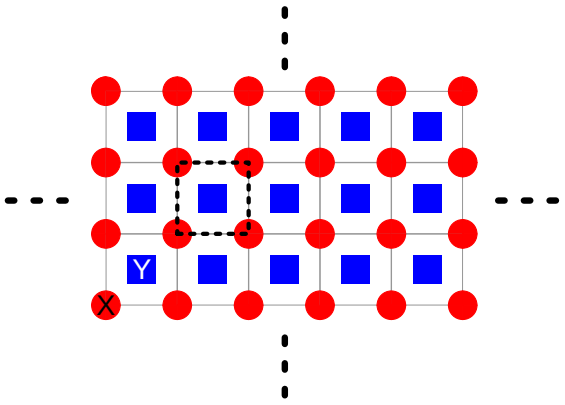

FIGURE 2.3: A 2-dimensional crystal lattice composed of two atoms X and Y, with a periodic pattern all over space. The crystallographic unit cell is defined by the dashed line.

2.2.6 Boundary conditions and summation in reciprocal space

Crystalline materials are characterized by a highly ordered microscopic structure, forming a crystal lattice. The bulk properties of a crystal can be conveniently modelled by accounting for a single unit cell, usually the small unit that can be used to reproduce the pattern of the lattice, repeated infinitely in all directions as illustrated in Figure 2.3. With these considerations, we can use periodic boundary conditions when modelling such systems, to account for the translational invariance.

Moreover, periodic boundary conditions allows one to use the Bloch theorem to model the electronic wave functions within the unit cell. This theorem imply that, within a periodic potential, the electronic wave function $\psi_{n,\mathbf{k}}(\mathbf{r})$ can be written as the product of a plane wave and a function $u_{n,\mathbf{k}}(\mathbf{r})$ that has the same real-space periodicity of the crystal lattice:

$$\psi_{n,\mathbf{k}}(\mathbf{r}) = e^{i\mathbf{k}.\mathbf{r}}\, u_{n,\mathbf{k}}(\mathbf{r}) \tag{2.51}$$

where $\mathbf{k}$ is a reciprocal space vector and n the band index. The function $u_{n,\mathbf{k}}(\mathbf{r})$ has to be expanded on a well defined basis set, usually plane-waves or local functions (atomic orbitals). In the reciprocal space is defined the reciprocal lattice associated to the lattice in real space, and according to the symmetries of the system several vectors $\mathbf{k}$ correspond to the same solution $\psi_{n,\mathbf{k}}(\mathbf{r})$. As these $\mathbf{k}$ vectors are redundant in the description of the physics, the reciprocal space is restricted to a small region containing all the non-equivalent $\mathbf{k}$ vectors. This region is called the irreducible Brillouin Zone (IBZ), and correspond to a Wigner-Seitz cell of the reciprocal lattice.

In the limit of an infinite periodic system, the sum over a fixed amount of k-points in the IBZ can be substituted by an integral over all the k-points within the IBZ. In practice however, the value of the sum converge quickly with a finite number of k-points, in a uniform mesh within the cell. The sampling of the Brillouin zone must be carefully tested to have a satisfying level of precision.

Periodic boundary conditions are very useful to describe bulk materials, but are not appropriate when studying systems where the long-range microscopic order is no longer valid, like at surfaces, for isolated thin films, molecular systems, or systems with defects, which are not expected to be ordered in real solids.

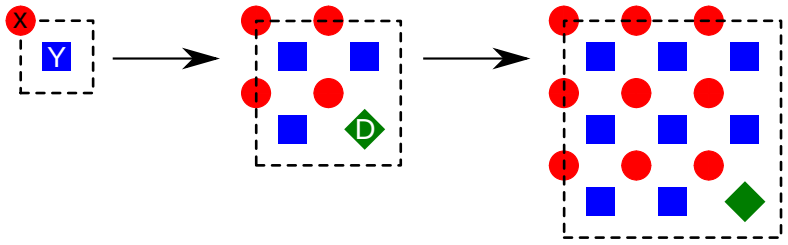

FIGURE 2.4: The unit cell of a 2-dimensional periodic system containing two atoms X and Y is expanded as a 2×2 supercell contains 4 X atoms and 4 Y atoms, which can contains one defect. Here, a Y atom is substituted by a defect D, leading to a defect density of 1/4. A larger 3×3 supercell can be used to model a defective system with a lower density of defects of 1/9.

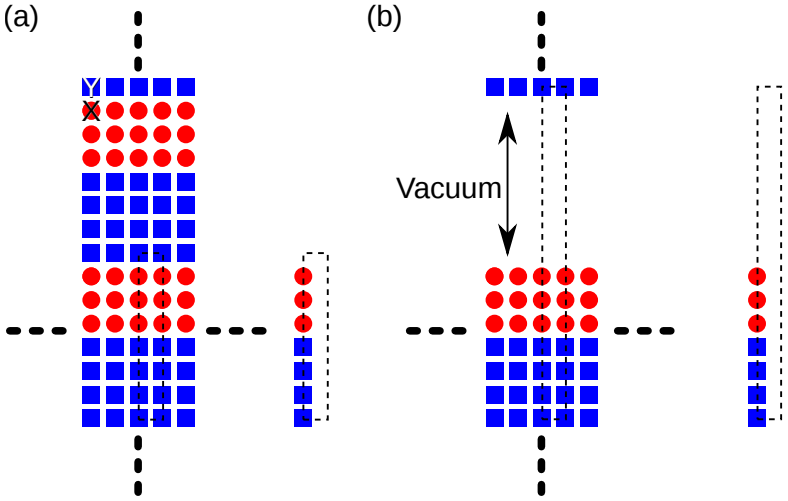

FIGURE 2.5: (a) An heterostructure of two stacked materials, alternating between four monolayers of atomic planes X and three monolayers of atomic planes Y. (b) Surfaces can be modelled by including a vacuum inside the unit cell. In this simple schematic representation, there is two types of surface, of both X and Y terminations.

In the particular case of point defects (vacancies, antisite defects, substituted atoms,...), a convenient way to model them is the supercell approach. In this approach, the periodic conditions remain in application, and so does the Bloch theorem, but the crystallographic cell no longer corresponds to the unit cell of the pristine lattice: it is larger, and it is possible to include the point defects in such a cell (as illustrated in Figure 2.4). Of course, given the periodic conditions, the distribution of defects also follows the new periodicity. If one is interested into the properties of the isolated defect, one must consider using a rather large supercell, and check if the interactions between the defect and its periodic images are negligible.

The supercell approach can also be used to study heterostructures made of different materials stacked on top of each other (where the "building blocks" are the unit cells of the parent compounds), as seen in Figure 2.5.(a) and thin films with a vacuum. When modelling a surface, a vacuum area is explicitly included in the cell, as shown in Figure 2.5.(b). If this vacuum area is large enough, the interactions between the surface and the periodic image become negligible, and we can consider the surface as isolated.

2.2.7 Pseudopotentials

In quite a lot of situations, the interesting properties of a material is due to the outer shells electrons of the different atomic species constituting the material, as they are the electrons involved in the bonding between neighbouring atoms. The principle of pseudopotentials is to replace the strong Coulombian potential of the atomic nucleus and the effect of the inner shell electrons (tightly bound to the nucleus) by an effective potential acting on the outer shell electrons, accounting for both Coulombian interactions from nucleus and inner shell electrons. The pseudopotentials can be calculated from the individual atoms, and be transferred to study more complex systems. Finally, using pseudopotentials have the advantage of reducing the complexity of a given problem and to be less computationally intensive, as only the outer shell electrons a treated explicitly in the Kohn-Sham calculations. This is necessary when using a plane-wave basis set, yet less important when using a local basis set. An introduction to pseudopotentials can be found in Reference [3].

2.2.8 Simulation programs implementing DFT

There exists a large variety of computer programs that implement DFT. Some of them are open-source, such as ABINIT or SIESTA, whereas some are proprietary, such as VASP or CRYSTAL. The different DFT codes differ by how they implement DFT, as well as by different optimization algorithms, the functionals for exchange-correlation (semi-local functionals, hybrid functionals), the boundary conditions (periodic or finite), and so on.

The choice of a given DFT package can also be motivated by the basis set used to expand the electronic wave functions: in many cases, wave functions are usually built either from plane-wave basis sets (ABINIT, VASP,...) or with localized basis sets (SIESTA, CRYSTAL,...). The later offers the advantage to be less computationally demanding and more appropriate when modelling finite systems (films, molecules). Indeed, at the surface of a film, or outside of a molecule, the charge density decreases drastically, and it is more straightforward to reproduce this behaviour from localized function than with spatially extended plane waves.

Almost all the calculations involved in the present work has been performed using the CRYSTAL package (unless specified otherwise) which is briefly presented in the following section.

2.2.8.1 The CRYSTAL package, general features

The CRYSTAL [30, 31] package can perform *ab initio* calculations of the ground state energy, energy gradients, electronic wave function, density and various properties of solid state systems.

With CRYSTAL, the single particle wave functions $\psi_i(\mathbf{r};\mathbf{k})$, solutions of the Kohn-Sham equations, are expanded as a linear combination of Bloch functions, defined in term of functions $u_{n,\mathbf{k}}(\mathbf{r})$ (Equation (2.51)), which are built as linear combinations of local functions (atomic orbitals). These local functions are linear combinations of Gaussian type functions $\chi(\mathbf{r})$, whose exponents and coefficients are defined beforehand and shall

be optimized depending on the desired accuracy. Different functions of symmetry *s*, *p*, *d*, *f* and even *sp* can be used to build the basis functions.

As mentioned previously, localized basis sets are more appropriate to study finite systems, motivating their use in the present work. They also present other advantages:

- the exchange energies are easier to calculate, however this is not the case for kinetic energies;
- the interactions between electrons localized in $3d$ orbitals around the Fermi level are better reproduced with local functions than plane waves, as these orbitals are much more localized in real space.

Each atomic orbital is a combination of Gaussian functions χ:

$$\chi(r,\theta,\phi) = \left(\sum_j C_j e^{-\alpha_j r^2}\right)\left[r^l Y_{lm}(\theta,\phi)\right] \tag{2.52}$$

with α_j being the exponents and C_j the coefficients of the radial parts of the atomic orbitals whereas $Y_{lm}(\theta,\phi)$ are spherical harmonics. The choice of the basis set is a fundamental and crucial step in defining the level of calculation and its accuracy, especially when dealing with periodic systems where many chemical bonds can be found.

With CRYSTAL and its post-processing tool *properties*, we are able to compute the following properties (amongst several others):

- the electronic structure of periodic and non-periodic systems: wave functions, electronic density, eigenenergies and related band structure and density of states, the total energy;
- forces and stresses to relax the atomic structure and find the configuration of minimal energy;
- magnetic properties within the collinear-spin approximation.
- ...

2.3 Boltzmann transport theory

Part of this work focuses on the thermoelectric properties of novel materials exploiting low-dimensional electron systems to increase their performance. These materials are often characterized by a dimensionless factor ZT, related to their efficiency in converting an applied electric voltage to heat and *vice-versa*. :

$$ZT = \frac{S^2\sigma}{\kappa_e + \kappa_l}T \tag{2.53}$$

In the above relation, S is the Seebeck coefficient, σ the electrical conductivity, T the temperature and κ_e and κ_l the electronic and lattice contributions to the thermal conductivity. This factor is known as the thermoelectric Figure of Merit, and more informations and discussions on the involved quantities are given in Chapter 6. In order to

study thermoelectric compounds from first-principles, one should be able to compute these properties for any given compound, and we will describe in this Section how to proceed to do so from the Boltzmann transport equation. In the following discussion, we will mostly focus in the electronic properties, hence we will avoid further discussion on κ_l. All the others coefficients S, σ and κ_e are properties that can be derived from the electronic structure.

The Boltzmann transport equation can be written[3] as:

$$\frac{df(\mathbf{r},\mathbf{k},t)}{dt} = \nabla_{\mathbf{r}} f(\mathbf{r},\mathbf{k},t)\mathbf{v_k} + \nabla_{\mathbf{k}} f(\mathbf{r},\mathbf{k},t)\frac{\mathbf{F}}{\hbar} + \frac{\partial f(\mathbf{r},\mathbf{k},t)}{\partial t} = \left.\frac{\partial f(\mathbf{r},\mathbf{k},t)}{\partial t}\right|_{scatt} \tag{2.54}$$

This equation describes the statistical behaviour of a fluid not being in the thermodynamic equilibrium. In the present case, we only consider a fluid of electrons[4]. The different quantities involved in this equation are:

- $f(\mathbf{r},\mathbf{k},t)$, which is the statistical distribution of the electrons (Fermi-Dirac) and can be both space and time dependent (the $\mathbf{r}$ and $\mathbf{k}$ values are altered by external fields and collisions);
- $\epsilon_{\mathbf{k}}$ is the energy of the electrons with a momentum $\mathbf{k}$;
- $\mathbf{F}$ is the force driving the group motion of the electrons and is related to the applied fields;
- $\left.\frac{\partial f(\mathbf{r},\mathbf{k},t)}{\partial t}\right|_{scatt}$ is the variation in distribution due to scattering;
- $\mathbf{v_k}$ is the group velocity of electrons with a momentum $\mathbf{k}$.

The group velocity of electrons $\mathbf{v_k}$ is calculated from the derivatives of the eigenenergies in the reciprocal space:

$$\mathbf{v_k} = \frac{1}{\hbar}\nabla_{\mathbf{k}}\epsilon_{\mathbf{k}} \tag{2.55}$$

Let us consider that the electrons are submitted to a temperature gradient and an electric field. Under such constraints, their statistical distribution changes and reach a steady state. For the steady state case with small temperature gradient and/or electric field, we can assume that the time variation of the distribution is much smaller than the spatial variation of the distribution; hence, we can neglect the term $\partial f/\partial t$, and we can rewrite Equation (2.54):

$$\mathbf{v_k}\frac{\partial f_{\mathbf{k}}}{\partial T}\nabla T + \mathbf{v_k}\,(-e)\frac{\partial f_{\mathbf{k}}}{\partial \epsilon_{\mathbf{k}}}\mathbf{E} \;=\; \left.\frac{\partial f_{\mathbf{k}}}{\partial t}\right|_{scatt} \tag{2.56}$$

where $(-e)$ is the charge of electron, T is the temperature and $\mathbf{E}$ is the electric field. An additional approximation can be made to further simplify the equation, known as the relaxation time approximation. It consists in considering a linear evolution from the equilibrium distribution $f^0_{\mathbf{k}}$ to the steady state distribution $f_{\mathbf{k}}$ under the temperature

[3] For clarity, these equations will be written in SI units in this Section.

[4] The Boltzmann transport equation is more general and can be used in different context, like phonon transport.

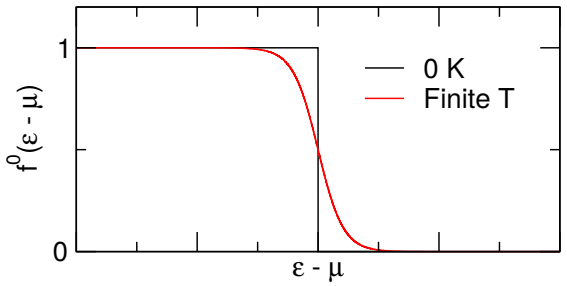

FIGURE 2.6: The Fermi-Dirac distribution, at 0 K and at finite temperature.

gradient and/or applied electric fields, as follows:

$$\mathbf{v_k}.\frac{\partial f_\mathbf{k}}{\partial T}\nabla T + \mathbf{v_k}.(-e)\frac{\partial f_\mathbf{k}}{\partial \epsilon_\mathbf{k}}\mathbf{E} = \frac{f^0_\mathbf{k} - f_\mathbf{k}}{\tau_\mathbf{k}} \tag{2.57}$$

where $\tau_\mathbf{k}$ is the relaxation time.

In the case of fermions like electrons, the equilibrium distribution follows the Fermi-Dirac statistic:

$$f^0_\mathbf{k} = \frac{1}{e^{(\epsilon_\mathbf{k}-\mu)/k_BT}+1} \tag{2.58}$$

where $f^0_\mathbf{k}$ is the electronic distribution at the equilibrium and μ is the chemical potential. This distribution has a step-like shape at 0 K, and gets smoother as temperature increases (as shown in Figure 2.6). Let us now take a look to the different transport quantities, the electric current $\mathbf{J}$ and the thermal current $\mathbf{Q}$. These currents originates from the applied electric field and thermal gradients, and the relation between the causes and the effects can be written with the following expressions:

$$\mathbf{J} = L_{EE}\mathbf{E} + L_{ET}\nabla T \tag{2.59}$$
$$\mathbf{Q} = L_{TE}\mathbf{E} + L_{TT}\nabla T \tag{2.60}$$

The electrical conductivity is defined under an electric field only ($\nabla T = 0$):

$$\mathbf{J} = \sigma\mathbf{E} \implies \sigma = L_{EE} \tag{2.61}$$

The thermal conductivity is defined when there is no current ($\mathbf{J} = 0$):

$$\mathbf{Q} = -\kappa_e\nabla T \Longrightarrow \kappa_e = -\left(L_{TT} - \frac{L_{TE}\cdot L_{ET}}{L_{EE}}\right) \tag{2.62}$$

The Seebeck coefficient S is also defined when $\mathbf{J} = 0$, and using Equations (2.59) and (2.60) it follows that:

$$\mathbf{E} = S\nabla T \Longrightarrow S = -\frac{L_{ET}}{L_{EE}} \tag{2.63}$$

Now that these quantities and coefficients are well defined, we can go back to the simplified Boltzmann equation (2.57). We have:

$$f_\mathbf{k} = f^0_\mathbf{k} - \tau_\mathbf{k}\mathbf{v_k}\frac{\partial f_\mathbf{k}}{\partial T}\nabla T - \tau_\mathbf{k}\mathbf{v_k}\,(-e)\frac{f_\mathbf{k}}{\partial \epsilon_\mathbf{k}}\mathbf{E} \tag{2.64}$$

If we make the reasonable hypothesis that the steady state distribution $f_{\mathbf{k}}$ is a small deviation from the equilibrium distribution $f^0_{\mathbf{k}}$, hence we have $f^0_{\mathbf{k}} \approx f_{\mathbf{k}}$ and, based on the knowledge of the analytical formulation of $f^0_{\mathbf{k}}$ given in Equation (2.58), the following derivatives can be expressed:

$$\mathbf{v_k}.\frac{\partial f_{\mathbf{k}}}{\partial T}\nabla T \approx \mathbf{v_k}\frac{\partial f^0_{\mathbf{k}}}{\partial T}\nabla T = \mathbf{v_k}\left(-\frac{\epsilon_{\mathbf{k}}-\mu}{T}\right)\frac{\partial f^0_{\mathbf{k}}}{\partial \epsilon_k}\nabla T \tag{2.65}$$

$$\mathbf{v_k}\,(-e)\frac{f_{\mathbf{k}}}{\partial \epsilon_{\mathbf{k}}}\mathbf{E} \approx \mathbf{v_k}\,(-e)\frac{f^0_{\mathbf{k}}}{\partial \epsilon_{\mathbf{k}}}\mathbf{E} \tag{2.66}$$

We now have the linearized Boltzmann equation:

$$f_{\mathbf{k}} = f^0_{\mathbf{k}} - \tau_{\mathbf{k}}\mathbf{v_k}.\frac{\partial f^0_{\mathbf{k}}}{\partial T}\nabla T - \tau_{\mathbf{k}}\mathbf{v_k}.(-e)\frac{f^0_{\mathbf{k}}}{\partial \epsilon_{\mathbf{k}}}\mathbf{E} \tag{2.67}$$

The thermal current $\mathbf{Q}$ and the electric current $\mathbf{J}$ can now be expressed in term of the steady state electronic distribution $f_{\mathbf{k}}$, only accounting electronic transport:

$$\mathbf{J} = \frac{1}{\Omega}(-e)\sum_{\mathbf{k}}\mathbf{v_k}f_{\mathbf{k}} = \frac{1}{\Omega}(-e)\sum_{\mathbf{k}}\mathbf{v_k}\mathbf{v_k}\tau_{\mathbf{k}}\left[e\frac{\partial f^0_{\mathbf{k}}}{\partial \epsilon_{\mathbf{k}}}\mathbf{E} - \frac{\partial f^0_{\mathbf{k}}}{\partial T}\nabla T\right] \tag{2.68}$$

$$\mathbf{Q} = \frac{1}{\Omega}\sum_{\mathbf{k}}\epsilon_{\mathbf{k}}\mathbf{v_k}f_{\mathbf{k}} = \frac{1}{\Omega}\sum_{\mathbf{k}}\epsilon_{\mathbf{k}}\mathbf{v_k}\mathbf{v_k}\tau_{\mathbf{k}}\left[\frac{\partial f^0_{\mathbf{k}}}{\partial T}\nabla T - e\frac{\partial f^0_{\mathbf{k}}}{\partial \epsilon_{\mathbf{k}}}\mathbf{E}\right] \tag{2.69}$$

where Ω is the volume of the unit cell the crystal. Expressions (2.68) and (2.69) show that the coefficients L_{EE}, L_{ET}, L_{TE} and L_{TT} in Equations (2.59) and (2.60) can be calculated from the derivatives of the energies $\epsilon_{\mathbf{k}}$ and the derivatives of the equilibrium distribution. As the function $\partial f^0_{\mathbf{k}}/\partial \epsilon_{\mathbf{k}}$ only takes significant values around the chemical potential μ, the electrons who contributes to the conductivity are those with energies around μ, in agreement with band theory.

While the Seebeck coefficient S, the electrical conductivity σ and the thermal conductivity κ are usually referred to as as *coefficients*, they may actually be anisotropic and shall actually be referred to as second-order *tensors*. Similarly to the density of state, the conductivity distribution tensor is a distribution over the energies and accounts for all the contributions to the conduction from electrons with a given energy ϵ:

$$\sigma_{\alpha\beta}(\epsilon) = e^2\sum_{\mathbf{k}}\tau_{\mathbf{k}}v_\alpha(\mathbf{k})v_\beta(\mathbf{k})\delta(\epsilon-\epsilon_{\mathbf{k}}) \tag{2.70}$$

In Equation (2.70), the group velocities are summed and expressed with respect to their individual components.

If we assume that, for any $\mathbf{k}$, the relaxation time is constant and equal to $\tau_{\mathbf{k}} = \tau$, then the conductivity distribution becomes:

$$\sigma_{\alpha\beta}(\epsilon) = e^2\tau\sum_{\mathbf{k}}v_\alpha(\mathbf{k})v_\beta(\mathbf{k})\delta(\epsilon-\epsilon_{\mathbf{k}}) \tag{2.71}$$

Once the conductivity distribution is calculated, the different transport properties can be calculated by integrating over the energies [32]:

$$\sigma_{\alpha\beta}(T,\mu) = \frac{1}{\Omega}\int_{-\infty}^{+\infty}\sigma_{\alpha\beta}(\epsilon)\left[-\frac{\partial f_\mu(T;\epsilon)}{\partial\epsilon}\right]d\epsilon \tag{2.72}$$

$$\kappa^e_{\alpha\beta}(T,\mu) = \frac{1}{e^2T\Omega}\int_{-\infty}^{+\infty}\sigma_{\alpha\beta}(\epsilon)(\epsilon-\mu)^2\left[-\frac{\partial f_\mu(T;\epsilon)}{\partial\epsilon}\right]d\epsilon \tag{2.73}$$

$$S_{\alpha\beta}(T,\mu) = \frac{1}{eT}\frac{\int_{-\infty}^{+\infty}\sigma_{\alpha\beta}(\epsilon)(\epsilon-\mu)\left[-\frac{\partial f_\mu(T;\epsilon)}{\partial\epsilon}\right]d\epsilon}{\int_{-\infty}^{+\infty}\sigma_{\alpha\beta}(\epsilon)\left[-\frac{\partial f_\mu(T;\epsilon)}{\partial\epsilon}\right]d\epsilon} \tag{2.74}$$

Again, the factor $-\partial f/\partial\epsilon$ appears in the integrands in Equation (2.73), (2.74) and (2.74), hence only the electronic states of energy close to μ will be involved in these different properties.

2.3.1 Computing the thermoelectric tensors with the BoltzTraP software

BoltzTraP [32] is a computational tool which can be used to compute S, σ and κ_e, amongst other electronic structure related properties, and is based on the Boltzmann transport theory within the constant relaxation time approximation (CRTA). The different eigenenergies $\epsilon_{\mathbf{k}}$, Fermi level, symmetries in real and reciprocal space and additional structural information (volume) are typically output from DFT calculations, and can be used as input for BoltzTraP to compute the aforementioned properties. As Boltzmann transport theory involves derivatives of the energies, the electronic band structure must be well-resolved to be properly interpolated by analytical functions. The BoltzTraP code includes a routine for the expansion of the band structure, based on smooth Fourier interpolation. As the fitted functions are analytical, it is straightforward to compute the group velocities and the tensors $S_{\alpha\beta}$, $\sigma_{\alpha\beta}$ and $\kappa^e_{\alpha\beta}$, from the formula (2.71), (2.73), (2.74) and (2.74).

The Boltzmann transport equation in the constant relaxation time approximation does not provide a value of the relaxation time τ. This is not a problem for the Seebeck tensor, as a constant τ disappears in the expression (2.74) of S. However, it does not disappears from κ_e and σ. Therefore, BoltzTraP can only provide the values of σ/τ and κ_e/τ, and τ has to be determined by other means. A simple solution is to fit the relaxation time to conductivity measurements at known carriers densities.

In general, the Fermi level μ and the temperature T are parameters which control the behaviour of the properties in a given energy landscape. The Fermi level is well defined for a metal (with a defined Fermi surface), and falls within the electronic band gap in case of a semiconductor. In the semi-classical picture, the position of μ with respect to the band edges also depends on the majority carrier density (holes or electrons), which can be controlled *via* doping (chemical substitution...). These considerations highlight another implicit hypothesis when calculating the transport coefficients: the rigid band approximation. In a lot of cases, we can purposely consider the band structure of the host material as rigid and ignore the effect of impurities and carrier concentration. This hypothesis greatly reduces the complexity of the problem, as it is computationally intensive to compute the properties of defective system, and usually requires large supercells

to probe realistic densities of dopant. In the later part of the manuscript, we will come back on theses approximations and their shortcomings in specific cases.

2.4 In summary

In this Chapter, we presented the general framework behind DFT, the practical implementation of the theory through the Kohn-Sham *ansatz* to solve complex electronic problems, the different aspects of the approximate exchange-correlation functionals, the principle and advantages brought by pseudopotentials and a brief presentation of the CRYSTAL package and its main features. As a general theory, DFT can be used to study a large amount of solid state electronic systems. In this work, we will present different systems: bulk crystallines phases, superlattices, heterostructures with surfaces and defectives systems. The technicalities for each study will be detailed in their specific Chapter. Of course, we purposefully ignored to detail every intricacies of DFT, deemed irrelevant for the present work, and we encourage the curious reader who desire a deeper understanding of the theory to read the work of Richard Martin [3] or Sholl and Steckel [33].

In addition to the general aspect of *ab initio* calculations, we introduced Boltzmann's transport theory, how to calculate the transport tensors involved in thermoelectricity, and the BoltzTraP code implementing this theory based on the *ab initio* band structure.

Chapter 3

Reviewing the origin of the 2D electron system at the $SrTiO_3/LaAlO_3$ interface

In this Chapter, we review the origin of the two-dimensional electron system (2DES) at the interface of polar/non-polar oxides. Specifically, we will focus on the seminal interface between $SrTiO_3$ (STO) and $LaAlO_3$ (LAO), which hosts a two-dimensional electron gas without relying on chemical doping. We will review the different propositions, available in the literature, aiming to explain the origin of the 2DES, and we will present in detail the specificities of an electric field driven mechanism, commonly referred to as "polar catastrophe".

3.1 Interfaces and two-dimensional electron systems

A 2DES consists in an electron gas where the electrons are free to move in a two dimensional plane, but are tightly confined in the transversal direction to that plane. This confinement ensures quantized energy levels for motion in this transversal direction. The realization of such a 2DES can be realized within quantum wells, which can be engineered at interfaces between different insulating materials. Such materials with a well defined interface are called heterostructures.

In a perfect and infinite crystal, the atoms are perfectly arranged in a Bravais lattice. However, this picture is not exact in reality, as crystals present defects and interfaces with other materials/phases, and the properties of the electrons and atoms near the interface are not the same as those of the bulk phase. These new emerging effects can be exploited for specific applications.

The most common 2DES are found within metal-oxide-semiconductor field-effect transistors (MOSFETs). MOSFETs are made of different compounds, namely a metal, an insulating oxide, and a doped semiconductor (usually, silicon): with a good combination of band alignment, band bending at the interface, and with the application of a gate voltage, a thin sheet of electrons can be formed in the semiconductor close to its interface with the oxide, highly mobile in the plane of the interface. These MOSFETs are the

most common transistors in digital circuits and provide the basic switching functions (between an insulating and a conducting phase) required for the implementation of logic gates.

In the precedent example, the 2DES is not a steady state of the interface, and must be activated by gating. It is however possible to achieve a 2DES at the interface between polar and non-polar oxides, where the interface is at the origin of a quantum well, while the polar oxide provides the electron carriers, bringing them within the quantum well. While the density of carrier within the well can still be controlled by a gate voltage, the 2DES already exists without the application of a gate voltage.

The realization of such an interface is performed through the deposition of a film on the surface of a substrate material. When the deposited film bonds with the substrate, the growth is called epitaxy, and the nature of the substrate surface determines the orientation of the deposited film. For an efficient bonding, the atomic structure of the deposited film and the substrate must be similar, but the two materials do not necessarily need to have the same crystal class or symmetry. If the film is thin, then its crystal structure will adapt to the substrate to fit its geometry. Hence, the in-plane lattice parameters are either increased or decreased depending on the substrate lattice parameters compared to their bulk values, and the relative difference in in-plane lattice parameters defines the epitaxial strain. In addition to the in-plane strain, an out-of-plane strain also occurs through the Poisson effect: if the film is expanded in-plane, then the it is contracted in the out-of-plane direction, and *vice-versa*. Hence, for the same overlayer termination, the choice of a specific substrate can be used to tune the properties near the interface, such as the ferroelectric, magnetic, orbitals ordering, orbital degeneracy and splitting.

The technique of growth of oxides heterostructures with satisfying quality is rather recent compared to the growth of semiconductor-based heterostructures, for different reasons: on one hand, the apparent lack of direct applications did not motivate their development, and experimental limitations made these systems less studied despite the large array of physical properties. Nowadays, the techniques have improved, and it is possible to synthesize good substrates with a well defined surface (for example, for STO, the novel chemical treatments make it possible to obtain a perfect SrO or TiO_2 layer for a (001) surface [34–36]).

Once the substrate obtained, the deposition of the film on top of the substrate can be done by several methods, the most popular ones being pulsed laser deposition (PLD) and molecular beam epitaxy (MBE). PLD is based on the principle of vapour deposition: in a chamber, high power laser pulses strikes a target material which will constitute the film to be deposited on the substrate. The target is vaporized from the impact and transformed as a plasma, the ions in the plasma have high velocities and are redirected toward a heated substrate, where they condense and form the film. The process can be done either in an ultra high vacuum or in the presence of a background gas: this is the case for oxide heterostructures, which are grown in presence of gaseous oxygen to properly oxygenate the deposited film. The growth conditions (in terms of laser fluence, temperature and oxygen partial pressure) are important parameters which control the quality of the heterostructures and their overall properties (for example, low oxygen partial pressure leads to large concentration of oxygen vacancies). MBE is processed in an ultra high vacuum chamber, where the target material to be deposited is heated until sublimation, then migrated toward the substrate where it is adsorbed at the surface

to form the film. The main advantage of MBE is that the species have lower kinetic energy as they approach the substrate, limiting the formation of defects during growth. The growth process can be monitored with reflection high-energy electron diffraction (RHEED). The pattern of the electron diffracted at the surface yields information on the roughness of the surface, and can be used to control with precision the number of deposited layers.

3.2 General technicalities

Before going further, we specify the general technicalities of our first-principles calculations, for which the results are presented and discussed in this Chapter, as well as Chapter 4 and 5. We use the CRYSTAL code [37] to compute from DFT the structural and electronic of bulk $LaAlO_3$ and $SrTiO_3$ systems, as well as heterostructures based on these compounds.

3.2.1 Structural models

As our methodology limits the size of the systems we aim to study, we need to use appropriate structural models in the same spirit as described in Section 2.2.6. The key quantity to model is the interface between LAO and STO, as shown in Figure 3.1.(a). Such a system has to be reduced in a thin film geometry, usually a few nanometres thick. Examples of possible STO/LAO heterostructures along the (001) direction are shown in Figures 3.1.(b-g): (b) displays the unit cell (black dashed line) of a vacuum/$(STO)_4$/$(LAO)_2$/vacuum slab with a TiO_2/LaO interface where periodic boundary conditions are applied in all directions. The large vacuum region[1] ensures that the LAO surface does not interact with the STO surface. The STO sublattice has to be thick enough to mimic a STO substrate. This type of heterostructures has the disadvantage to present a STO surface which pollutes the computed results (with the presence of surface electronic states, surface distortions, ...); to circumvent this, a symmetry plane (or center) can be imposed to the system, resulting in a symmetric slab with two identical surfaces as shown in (c) and ensures that the two surfaces are treated equivalently in the calculations while suppressing the STO surface (in the illustration, the system consists in vacuum/$(LAO)_2$/$(STO)_{7.5}$/$(LAO)_2$/vacuum).

Beyond the heterostructures with surfaces explicitly included in the unit cell, it is possible to build periodic superlattices with no vacuum region. An example is shown in (d) as a stoichiometric $(STO)_5$/$(LAO)_5$ superlattice. If the superlattice is stoichiometric, then the cell must include necessarily a TiO_2/LaO interface and a AlO_2/SrO interface. As discussed in the next Section, the LAO sublattice is polar with a built-in electric field, and therefore, the closed circuit electrical boundary conditions imposed by the periodic boundary conditions lead to an (opposite) electric field in the STO sublattice so that the average electrostatic potential over the whole cell is zero. Another possibility are symmetric off-stoichiometric superlattices, shown in (e) and (f) with respectively two TiO_2/LaO and two AlO_2/SrO interface. The off-stoichiometry of the LAO sublattice leads to a doped system, with no electric-field in the LAO layer. These superlattices are

[1] The thickness of the vacuum region depends on the system: in the slab geometry, CRYSTAL fixes the size of the simulation box to 500 Å, ensuring that the vacuum region has a similar thickness, usually between 450 and 500 Å.

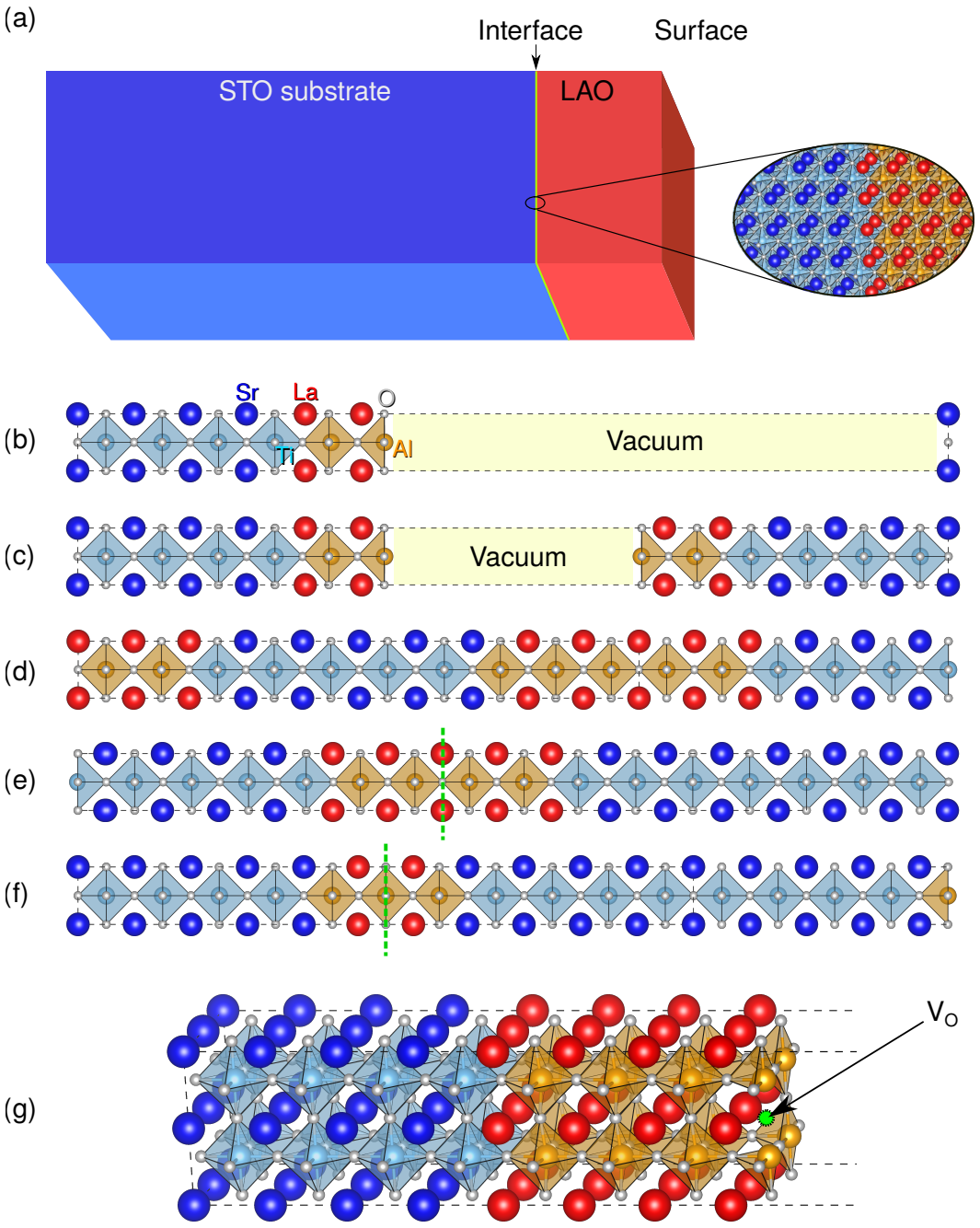

FIGURE 3.1: (a) Schematic representation of a STO(001)/LAO heterostructure with a visible surface. The key system to model at the atomic scale is the interface shown in the zoom on the right. Several structural models can be used while keeping the periodic boundary conditions: (b) a $(STO)_4/(LAO)_2$/vacuum heterostructure; (c) a symmetric vacuum/$(LAO)_2/(STO)_{7.5}/(LAO)_2$/vacuum heterostructure; (d) a stoichiometric $(STO)_5/(LAO)_5$ superlattice, without any vacuum region; (e) an off-stoichiometric and symmetric $(STO)_{8.5}/(LAO)_{4.5}$ superlattice with two *n*-type (TiO_2/LaO) interfaces; (f) an off-stoichiometric and symmetric $(STO)_{8.5}/(LAO)_{2.5}$ superlattice with two *p*-type (AlO_2/SrO) interfaces; (g) the film featured in (c) expanded as a 2×2 supercell including one oxygen vacancy (V_O) at the surface. The unit cell is displayed as dashed black lines. The green vertical dashed lines show the symmetry planes in the symmetric superlattices.

particularly useful to study the doped interfaces, as it fixes the carrier density to 0.5 electrons (e^-) (0.5 holes (h^+)) per unit cell (□).

To mimic the strain induced by the STO substrate to the LAO layer, the in-plane cell parameter is fixed to the relaxed value of bulk cubic STO.

Finally, it is possible to incorporate defects by the means of supercells. An example is given in (g), where a symmetric slab with a surface region in expanded as a 2×2 supercell incorporating one oxygen vacancy at the AlO_2 surface in LAO. The periodic boundary conditions leads to an area density of oxygen vacancies of 1/4□.

In the present Chapter as well as Chapters 4 and 5, calculations are performed either on the bulk compounds, off-stoichiometric superlattices (Figure 3.1.(e-f)), pristine symmetric films including a vacuum region (Figure 3.1.(c)) and defective symmetric films including a vacuum region (Figure 3.1.(g)). The thicknesses of the films will be specified for each type of calculations.

The symmetric heterostructures in the slabs geometry shall be referred to as STO(001)/LAO$_m$ for different LAO thicknesses m, independently of the thickness of the STO layer acting as the STO substrate.

3.2.2 Methodological details for the DFT calculations

Regarding the Gaussian basis set, all the electrons have been included for Ti [38], O [39] and Al [40], while we use a Hartree-Fock pseudopotential [39] for Sr and the Stuttgart energy-consistent pseudopotential [41] for La. The basis sets of Sr and O have been optimized for STO. In the basis set of La, the Gaussian exponents smaller than 0.1 were disregarded and the remaining outermost polarization exponents for the $10s$, $11s$ shells (0.5672, 0.2488), $9p$, $10p$ shells (0.5279, 0.1967), and $5d$, $6d$, $7d$ shells (2.0107, 0.9641, 0.3223), together with Al $4sp$ (0.1752) exponent from the 8-31G Al basis set, were optimized for LAO.

The exchange-correlation energy is modelled with the B1-WC hybrid functional [42]. A Monkhorst-Pack mesh [43] of $6 \times 6 \times 6$ special k-points is used for cubic bulk LAO and STO, ensuring a proper convergence of the total energy and forces below 1 meV. The sampling is then refined into a $12 \times 12 \times 12$ mesh of special k-points for the computation of properties such as the electronic density of state or the vibration modes at the Γ point in the IBZ.

For the heterostructures, the Brillouin Zone sampling is adapted to a $6 \times 6 \times 1$ mesh. It is then refined to $12 \times 12 \times 2$ to compute the electronic band structure and related density of state. A smearing of the Fermi surface has been set to $k_BT = 0.001$ Ha. The self-consistent DFT cycles are considered to be converged when the energy change between cycles are smaller than 10^{-8} Ha. The optimization of the atomic positions are performed with convergence criteria of 1.5×10^{-4} Ha/Bohr in the root-mean square values of the energy gradients, and 1.2×10^{-3} Bohr in the root-mean square values of the atomic displacements. The evaluation of the Coulomb and exchange series is determined by five parameters, fixed to their default [44] values: 7, 7, 7, 7 and 14.

The technical details for the calculations of the systems with oxygen vacancies are similar to the ones used for the pristine slabs in term of basis sets, convergence threshold and

investigated geometrical configurations for the heterostructures. Oxygen vacancies (V_O) have been modelled by removing explicitly an oxygen atom from its site (core and electrons), while leaving "ghost" oxygen basis functions on the site to properly model the electron density within the vacancy. Different sizes of supercell have been used in the study (mainly 2×2 and 2×3 supercells), with adapted Brillouin zone sampling with respect to supercell size. formation energies $E^0_{f,\mu=0}$ are calculated in the O-rich limit from the relation:

$$E^0_{f,\mu=0} = \frac{1}{n_v}\left[E_V - [E_0 - n_v\frac{1}{2}E_{O_2}]\right] \tag{3.1}$$

where E_V and E_0 are the calculated total energy of the systems with and without V_O, n_v the number of V_O in the supercell, and E_{O_2} the calculated total energy of the single O_2 molecule in the triplet state.

Equation 3.1 only consider the enthalpic contribution at 0 K to the formation energies, within a vacuum environment. To account for the atmosphere during growth, considering the environment as a reservoir, one has to consider the chemical potential of oxygen $\mu_O(p,T)$ relative to the gaseous phase at finite oxygen partial pressure p and temperature T, so that:

$$E^0_{f,\mu} = \frac{1}{n_v}\left[E_V - [E_0 - n_v\frac{1}{2}(E_{O_2} + \mu_{O_2})]\right] \tag{3.2}$$

$$E^0_{f,\mu} = E^0_{f,\mu=0} + \mu_O(p,T) \tag{3.3}$$

In the relation above, $\mu_O(p,T)$ is calculated from the thermodynamic model [45, 46]: the details of the calculation can be found in Appendix A. $\mu_O(p,T)$ is usually considered as a parameter depending on the environment; for the purpose of this study, we set $\mu_O = -2$ eV according to the growth conditions of standard STO(001)/LAO heterostructures and is identical to the value used in Reference [47].

3.3 $SrTiO_3$ and $LaAlO_3$ in their bulk form

LAO and STO are two compounds of the ABO_3 perovskite family, which forms a class of oxide compounds that attracted a significant amount of interest in the field of material science. This is due to the large panel of properties they offer and the many potential applications related to these properties. The first perovskite compound discovered was $CaTiO_3$ in 1839 by Gustav Rose, who simply named the crystal perovskite in honour of Russian mineralogist Lev Perovski (1792-1856). The name nowadays refers to the ABX_3 structure, where A and B are cations and X is an anion, oxygen in the case of oxides, or fluorine for fluoride, or chlorine for chlorides. F, O and Cl are elements with large electronegativity, hence these perovskites are known for their strong ionic character.

Within the 5-atoms unit cell of oxide perovskites, the B cation is located at the center of an octahedron formed by the 6 neighbouring O atoms, while the A atoms are positioned at the corner of the cubic cell, as shown in Figure 3.2.(a). The B cation is usually a transition metal bonding with the neighbouring oxygens forming the octahedron, thanks to O $2p$ – B d bonding.

The formal valence of oxygen in ABO_3 perovskites is most of the time O^{2-}, which constraints the valence configurations for the cations: either $A^{1+}B^{3+}$, $A^{2+}B^{4+}$ and

$A^{3+}B^{3+}$ generally ($A^{4+}B^{2+}$ has been witnessed in $PbTiO_3$). The valence of the cations has a great importance when considering perovskites deposited as films on a substrate, as the individual layers may hold different charges per unit cell. For example, in the (001) direction, we can have respectively (AO^0, AB_2^0) neutral planes for $A^{1+}B^{3+}$; or charged planes (AO^+, AB_2^-) or (AO^-, AB_2^+) for $A^{2+}B^{4+}$ and $A^{3+}B^{3+}$ respectively. As a consequence, even though a perovskite is centrosymmetric in bulk form, it can display a polarity in film form depending on the deposition process. We will come back to this point when addressing the STO(001)/LAO interface.

The perovskite family is generally not strictly cubic: most of the time, the crystal structure stabilizes in a symmetry subgroup involving rotations and distortions of the BO^6 octahedra. The different structures of oxide perovskites have been described by Goldschmidt [48], who proposed a tolerance factor α to classify the possible distortions from the ideal cubic structure:

$$\alpha = \frac{r_A + r_O}{\sqrt{2}(r_B + r_O)} \tag{3.4}$$

where r_A, r_B and r_O are respectively the ionic radii of the A, B and O species. Equation (3.4) may be rewritten as $\alpha = d_{AO}/\sqrt{2}d_{BO}$ where d_{AO} and d_{BO} are the bond lengths between A and O and B and O respectively. Depending on the value of α, the structure will adapt:

- For $\alpha = 1$, the adopted structure is the cubic one, as represented in Figure 3.2.(a). This is the case, for instance, for $BaZrO_3$. If this criterion is not satisfied, then distortions occur and the symmetry is reduced. For $\alpha \approx 1$, some distortions may appear, like in $SrTiO_3$ ($\alpha = 1.001$).
- For $\alpha < 1$, in this case the radius of A is too small and does not fill the available space in the cube. To maximize the AO bond properties, the BO_6 octahedra rotates. The motions associated with this instability, with respect to the cubic structure, are named antiferrodistortive motions: the O atoms no longer occupy the center of the faces of the cube, as shown in Figure 3.2.(b); in addition to this motion, the A cation can also moves through polar or anti-polar distortions. Anti-polar motions appear in the *Pnma* phase due to the coupling with oxygen rotation modes [49], which is stable for many perovskites with $0.8 < \alpha < 1.0$ (this is the case for $CaTiO_3$).
- For $\alpha > 1$, the radius of B is too small compared to A, and the cubic structure is unstable. The motion associated with this instability is the off-centering of the B cations (shown in Figure 3.2.(c)), where B move away from its centrosymmetric position. Such a distortion leads to the appearance of a polarization if all the B cations moves in the same direction. Other distortions may also appears, but this will not be a topic of discussion.

The variety of possible distortions for perovskites, in addition to other properties such as magnetism (with spin ordering), charge ordering, orbital ordering, and superconductivity, makes this family an ideal system to study and for engineering possible applications.

In the present Section, we will review the basic properties of the bulk phases of LAO and STO perovskites, in terms of experimental data and computational results, to highlight the performance of the hybrid functional formalism (with the B1-WC functional) which will be used in the rest of this manuscript to study the STO(001)/LAO interface.

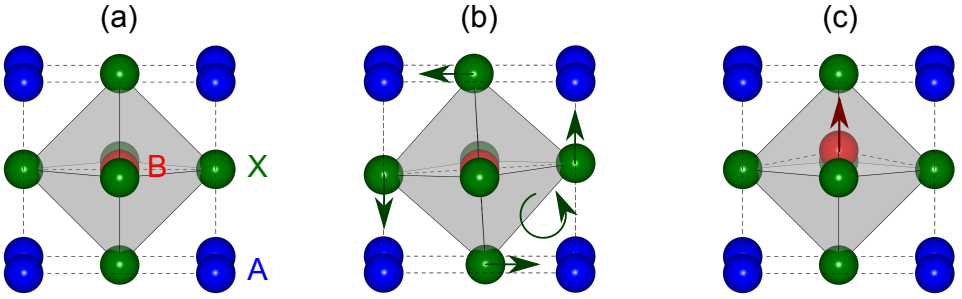

FIGURE 3.2: (a) 5-atoms cubic cell of the ideal, symmetric perovskite structure ABO_3; (b) the same cell with a rotated BO_6 octahedron. Note that the translational symmetry associated with the cubic primitive cell is lost; (c) the same cell, with an off-centring motion of the B cation. The arrows highlight the displacements of the atoms. The structures are drawn with the VESTA code [50].

We will also address the electronic properties of reduced $SrTiO_{3-\delta}$ from first-principles.

3.3.1 Structural properties

In terms of structure, both STO and LAO are members of the oxide perovskite family. At room temperature, STO exists in its cubic form with a lattice parameter of $a = 3.905$ Å. However, at 110 K, STO undergoes a structural phase transition to a tetragonal phase ($I4/mcm$), involving antiferrodistortive motions of the octahedra according to a $a^0a^0c^-$ pattern the Glazer notation [51], with a subsequent increase of the c/a ratio. The optimized lattice parameters of cubic STO ($Pm\bar{3}m$) and tetragonal STO ($I4/mcm$) are given in Table 3.1, as calculated with the B1-WC and the GGA-PBE functionals. Notably the a value of the cubic phase as calculated with the B1-WC functional ($a = 3.880$ Å) shows a good agreement with the experimental value.

LAO adopts a rhombohedral structure ($R\bar{3}c$), which can be approximated by a pseudo-cubic structure with a lattice parameter $a = 3.811$ Å. The octahedral tilting in LAO is characterized by $a^-a^-a^-$ distortions with respect to the cubic phase[2]. Upon growth on a STO substrate, the in-plane lattice parameter of LAO will be strained to adopt the value of the lattice parameter of STO. Such a distortion will reduce to out-of-plane lattice parameter of LAO through the Poisson effect. To estimate this distortion, we also relaxed a tetragonal phase of LAO ($P4/mmm$) where a is set to the value of the relaxed STO value, while c is allowed to relax. The values of the lattice parameters are given in Table 3.1, we also show the results obtained from GGA-PBE and values measured from experiments. There is an overall improvement in accuracy of the predicted parameters using the B1-WC, the relative error is about -0.52%, compared to 1.02% for the GGA-PBE value.

3.3.2 Electronic properties

Both LAO and STO are band insulators, with electronic band gap of 5.60 eV and 3.25 eV respectively [54, 55]. Both have a strong ionic characters, with nominal valence

[2]In the following Sections, when addressing the STO(001)/LAO interface, we neglect the role of the rotations in most cases.

	$SrTiO_3$			$LaAlO_3$					
	Cubic $Pm\bar{3}m$	Tetragonal $I4/mcm$		Cubic $Pm\bar{3}m$	Rhombohedral $R\bar{3}c$		Tetragonal $P4/mmm$		
	a	a	c	a	a	c	a	c	c/a
B1-WC	3.880	5.482	7.772	3.791	5.382	13.115	3.880	3.739	0.96
PBE	3.940	5.565	7.894	3.850	5.470	13.305	3.940	3.750	0.95
Expt.	3.905[a]			3.811[b]			3.905	3.750	0.96

TABLE 3.1: Relaxed lattice parameters of LAO and STO, for different E_{xc} functionals, in the cubic phase, the ground state phase ($I4/mcm$ for STO, $R\bar{3}c$ for LAO) and in a constrained, tetragonal phase ($P4/mmm$) where $a = b$ is fixed to the value for relaxed cubic STO. The parameters corresponds to the crystallographic cell for the $I4/mcm$ and $R\bar{3}c$ phases. The experimental values are taken from: [a] [52],[b] [53]

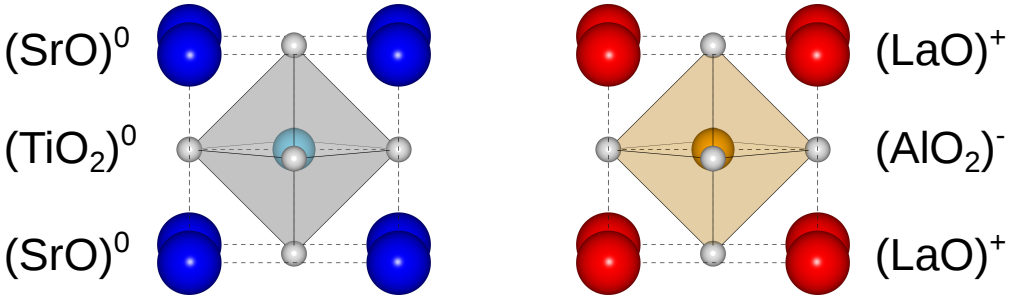

FIGURE 3.3: The unit cells of STO and LAO in the cubic phase, with excess charge in (001) planes as calculated from the oxidation numbers of the species: $(Sr^{2+}O^{2-})^0$ and $(Ti^{4+}O_2^{2-})^0$ for STO, $(La^{3+}O^{2-})^+$ and $(Al^{3+}O_2^{2-})^-$ for LAO.

$Sr^{2+}Ti^{4+}O_3^{2-}$ and $La^{3+}Al^{3+}O_3^{2-}$. In the (001) direction, the alternating AO and BO_2 planes are neutral, in the case of STO, and charged in the case of LAO, as shown in Figure 3.3.

The electronic band structure, calculated within B1-WC, for cubic STO, LAO and rhombohedral LAO is displayed in Figure 3.4, with the associated indirect and direct (measured at the Γ point) band gaps given in Table 3.4, calculated in the GGA (PBE flavor), variational pseudo-self interaction correction functional [56] (VPSIC) and B1-WC, and compared to the experimental values. Note that as the room temperature phase of LAO is the rhombohedral one, the experimental value of the band-gap can be directly compared to the calculated ones. The gaps for cubic STO and rhombohedral LAO calculated from PBE are underestimated by about ∼1 eV compared to the experimental values. This relates to the well known band gap issue of standard (semi-) local DFT. The large magnitude of the error on the electronic band gaps motivates the use of beyond standard DFT exchange-correlation functionals, such as VPSIC or the B1-WC, which both reduces the absolute errors to $0.2 - 0.3$ eV.

In addition to the gaps calculated for the room-temperature phases of LAO and STO, we calculated those of constrained cubic LAO (in the $Pm\bar{3}m$ space group) and tetragonal LAO (in the $P4/mmm$ space group). For these phases, the direct and indirect gaps are slightly altered compared to that of the $R\bar{3}c$ phase. The gaps calculated from B1-WC remains above 5 eV in all cases. The correct description of the bands gaps of LAO and

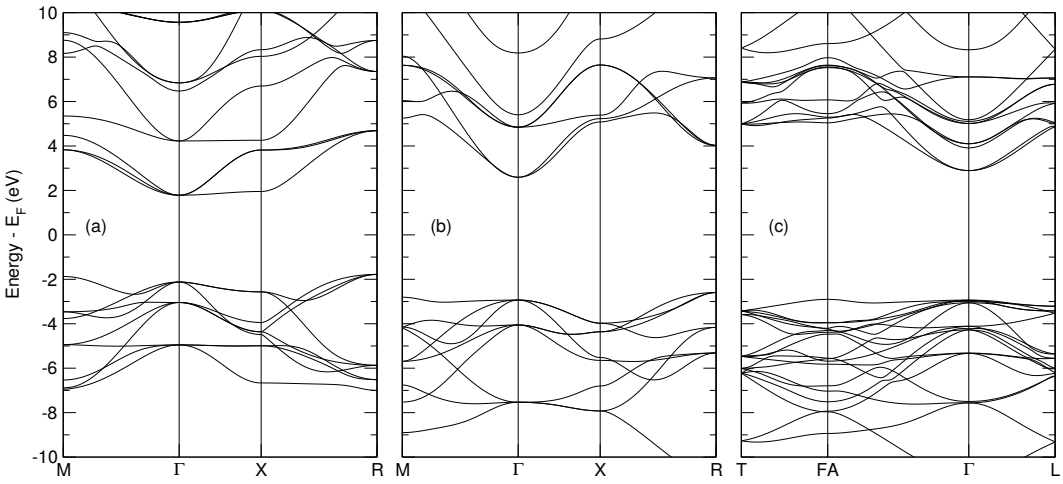

FIGURE 3.4: Electronic band structures of (a) cubic STO, (b) cubic LAO, (c) rhombohedral LAO, calculated with the B1-WC functional.

	Symmetry	Gap	PBE	VPSIC	B1-WC	Expt.
$SrTiO_3$	$Pm\bar{3}m$	$E_{g,i}$	2.24	2.94	3.56	3.25[a]
		$E_{g,d}$	2.60	3.30	3.91	3.75[a]
$LaAlO_3^C$	$Pm\bar{3}m$	$E_{g,i}$	3.86	5.23	5.19	
		$E_{g,d}$	4.22	5.51	5.53	
$LaAlO_3^T$	$P4/mmm$	$E_{g,i}$	4.81	4.84	5.23	
		$E_{g,d}$	5.23	5.21	5.62	
$LaAlO_3^R$	$R\bar{3}c$	$E_{g,i}$	4.59		5.78	5.60[b]
		$E_{g,d}$	4.68		5.82	5.60[b]

TABLE 3.2: Indirect ($E_{g,i}$) and direct band gap ($E_{g,d}$, at the Γ point) of cubic STO, cubic LAO (^{C}), tetragonal LAO (^{T}) and rhombohedral LAO (^{R}). The VPSIC values are taken from Reference [57]. The experimental values are taken from: [a] [54],[b] [55]

STO at the bulk level is important in order to validate the methodology and address the properties of heterostructures based on these compounds.

3.3.3 Dielectric properties of $SrTiO_3$ and $LaAlO_3$

The dielectric properties of LAO and STO constitute key physical parameters determining the behaviour of the 2DES at the STO/LAO interface, as well as its origin in terms of the polarity induced mechanisms. It is therefore important that the *ab initio* calculations reproduce the experimental values of bulk LAO and STO, to ensure its predictive power when treating explicitly the interface. The relative dielectric constants of STO and LAO, calculated with the B1-WC functional, are listed in Table 3.3. For LAO, we calculated the value of the component of the relative dielectric tensor for the cubic phase, the tetragonal phase (where the lattice parameter $a = b$ is constrained to match the STO lattice parameter), and the rhombohedral phase, to compare with the experimental value. The calculated dielectric properties are in satisfying agreement with the experimental data. The *ab initio* approach allows to probe the effect of the strain on the out-of-plane dielectric component of strained LAO, which is decreased by

	Symmetry	ε_{xx}	ε_{zz}	Expt.
$SrTiO_3$	$Pm\bar{3}m$	250	250	300[a]
$LaAlO_3^C$	$Pm\bar{3}m$	27	27	
$LaAlO_3^T$	$P4/mmm$	36	23	
$LaAlO_3^R$	$R\bar{3}c$	21	21	21-24[b]

TABLE 3.3: Components of the relative static dielectric tensor of cubic STO, cubic LAO (^{C}), tetragonal LAO (^{T}) and rhombohedral LAO (^{R}), calculated with the B1-WC functional. The experimental values are taken from: [a] [58],[b] [59]

about ∼15% of its bulk value. Moreover, the AlO_6 octrahedra tilting also decreases the dielectric constant, which is related to the competition between the oxygen rotations and the polar modes in perovskites. This result highlights the sensitivity of the LAO dielectric constant to structural distortions. At this stage, we note that, although these DFT calculations do not take into account the temperature as a parameter, the B1-WC results (*i.e.* at 0 K) are in agreement with the room-temperature properties of LAO and STO, as calculated for their room-temperature phases.

3.3.4 Electronic structure of reduced $SrTiO_{3-\delta}$

An hypothesis for the origin of the 2DES at the STO/LAO interface is that the carrier originates from oxygen vacancies (V_O) in the STO substrate. Indeed, it is known that reduced $SrTiO_{3-\delta}$ behave like a metal in a large temperature range [60], despite STO having a large band gap (and therefore is not usually referred to as a semiconductor). The effect of vacancies is even visible to the eye, as the clear insulating STO turns into a metallic dull crystal upon reduction, as shown in Figure 3.5. It is also superconducting at low temperature, and the density of mobile carrier remains weakly dependent on temperature from 1.3 to 50 K [61], as expected of a doped semiconductor in the saturation regime. However, these observations are inconsistent with reports of deep donor states for the V_O in STO as calculated from state-of-the-art first-principles methods[3], either based on hybrid functionals [62, 64, 65] or DFT+U [66], which predicts a single state with a double occupancy about ∼0.7 eV below the conduction band of STO. This defect state arises from the two dangling electrons of the V_O, which remain tightly bound in the vacancy and at the Ti sites in its direct vicinity, with a a strong Ti $d_{3z^2-r^2}$ character. In this situation, the thermal excitation of carriers from the defect state to the conduction band is in contradiction with the increase of resistivity observed with increasing temperature [67]. Moreover, the carrier density of $SrTiO_{3-\delta}$ is also lower in magnitude than the density of V_O, suggesting that not all the electrons provided by vacancies actually contribute to transport.

It has been shown since then from GGA+U calculations [69] ($U = 4.36$ eV) that a single V_O with two dangling electrons prefers the ionized state V_O^{1+} than the neutral V_O^0, with a single bound electron and a defect state 0.4 eV below the conduction band, whereas the other electron is promoted to the conduction band and is completely delocalized. In order to verify if the B1-WC functional can reproduce this result, we performed a calculation

[3] As for the LDA/GGA functionals, the systematic underestimation of the band gap results in the donor state lying in the conduction band, providing two electrons fully delocalized in the Ti t_{2g} state [62, 63].

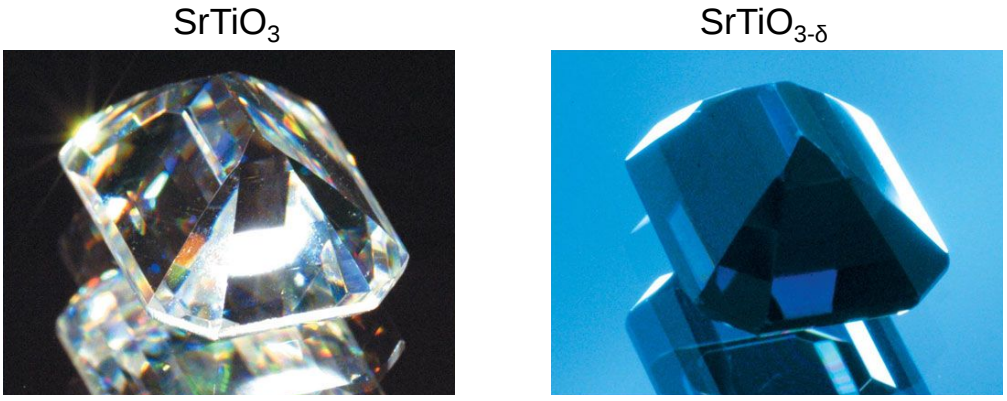

FIGURE 3.5: Micrographs of a STO crystal showing the effect of removing oxygen atoms through a thermal treatment, leaving oxygen vacancies in the lattice: the clear oxidized insulator turns into a dull blue conductive crystal. Adapted from Reference [68].

on a $4 \times 4 \times 4$ supercell of cubic STO containing 1 neutral V_O (with two dangling electrons), corresponding to a density of vacancy of $\sim 2.7 \times 10^{20}$ cm^{-3} ($\delta \approx 0.016$), and accounting for the spin-polarization of the defect state. The corresponding density of state (DOS) is displayed in Figure 3.6.(a): in this DOS, a defect state with a single electron (and therefore fully spin-polarized) is located $\sim$1 eV below the minimum of the conduction band (CBM), and is well localized within the vacancy and in the Ti nearest-neighbours with a Ti $d_{3z^2-r^2}$ character, as shown in Figure 3.6.(b). The other electron is transferred to the conduction band and is fully delocalized, as shown in Figure 3.6.(c).

These results explains the properties of reduced $SrTiO_{3-\delta}$: a V_O act as a single-donor, with the apparition of occupied and localized in-gap states $\sim$1 eV below the conduction band, which have been observed in angle-resolved photo-emission spectroscopy (ARPES) experiments $\sim 1 - 1.3$ eV below the conduction band minimum [70, 71] and which are occupied by a single electron per state, whereas the other electron provided by the vacancy is promoted to the conduction band and is fully delocalized. In that regard, the B1-WC result is quantitatively closer to the experiments than the GGA+U calculations from Reference [69]. These results challenge the conventional picture of V_O in STO, which predicts the neutral V_O (with a double occupancy) to be the most stable if the Fermi level lies close the CBM [65]. The origin of this discrepancy lies in the Coulombian repulsion between electrons in the localized level: inclusion of on-site Coulombian interactions prevents the stabilization of neutral vacancies [72], and favours the charged V_O^{1+} state[4]. This also implies that V_O acts as magnetic impurities. It should also be noted that the strong Coulombian repulsion is related to the highly spatially localized nature of the defect state, which is different than what is witness in doped semiconductors where the effective Bohr radius is usually one order of magnitude larger than the lattice parameter, leading to highly delocalized carriers with weaker Coulomb interactions.

These results show that the B1-WC functional can properly reproduce the effect of screened Coulombian interactions, often modelled through mean-field static correlation with the U term. In the following Section, we will address the properties of the STO/LAO interface, and the different possible mechanisms at the origin of the 2DES; as V_O provide free carriers which may be confined at the interface, and the in-gap states

[4] the energy difference between the two phases is -274 meV as calculated for the whole $4 \times 4 \times 4$ supercell.

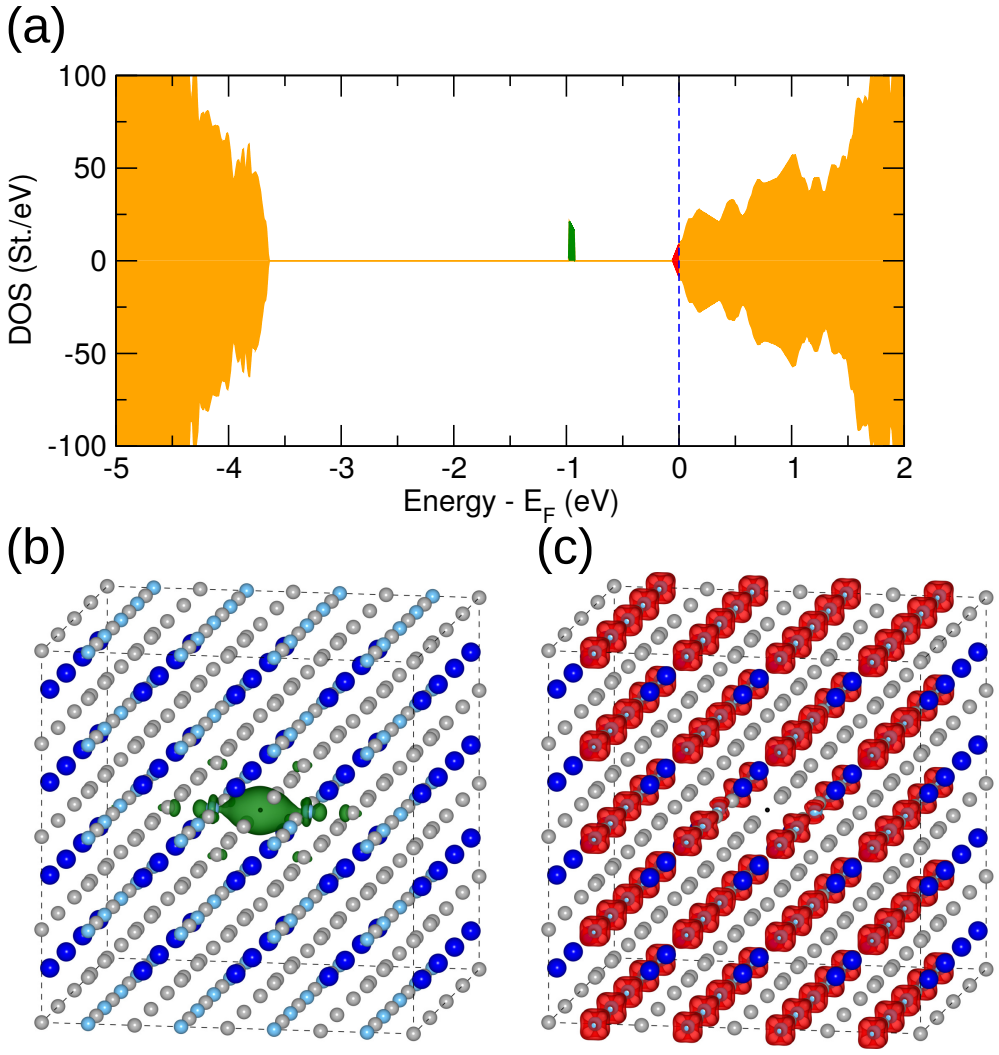

FIGURE 3.6: (a) Electronic DOS of the $4 \times 4 \times 4$ supercell of cubic STO, containing 1 V_O. In green, the donor state occupied with a single electron, fully-spin polarized. In red, the delocalized remaining electron occupying the bottom of the conduction band. The vertical dashed line is the Fermi level; the positive (negative) values account for majority (minority) spin states. (b) Isosurfaces of electron density for the localized defect state (5×10^{-4} Bohr^{-3}); (c) Isosurfaces of electron density for the delocalized electron in the conduction band (5×10^{-3} Bohr^{-3}). In (b) and (c), the oxygen vacancy is located at the center of the supercell.

associated with V_O appears in ARPES experiments on the STO/LAO interface [71], it is a reasonable hypothesis and we will consider this scenario, which shall be addressed in the present Chapter. We will also stress how theoretical methods with a quantitative predictive power is important to avoid a spurious description of the system.

3.4 The band alignment between $SrTiO_3$ and $LaAlO_3$

For a LAO thin film deposited on top a STO substrate with a (001) surface, two possible interfaces are identified: if the STO substrate is terminated by a TiO_2 plane, then the first LAO atomic layer will be a LaO plane. This is usually referred to as the *n*-type

interface in the literature, which is the interface which has been observed to host a 2DES. If the STO substrate is terminated by a SrO plane, then the first atomic layer of LAO will be a AlO_2 plane. This one is referred to as the *p*-type interface, and has mostly been reported as insulating, contrasting with the *n*-type interface, and attracting less attention from the research community.

A crucial aspect of interfaces that need to be addressed is the relative alignment of the valence and conduction bands of the two compounds across the interface. An issue occurs when dealing with interfaces between insulating phases such as LAO and STO. A single DFT calculation on a bulk structure provides the electronic band structure of the compound where the occupancy of the bands is based on the number of electrons in the system: hence, it is easy to identify the valence band and the conduction band in an insulator from DFT with a well defined band gap. However, the corresponding energies are given with respect to a reference which is defined by the code (the average electrostatic potential for example) and which is system dependent. Therefore, the references as calculated for bulk LAO and bulk STO are different, and it is not trivial to determine how the valence and conduction bands of both systems align. In order to obtain a single reference energy, it is usual to perform a DFT calculation on an heterostructure, usually a superlattice as shown in Figure 3.1.(d), with an interface explicitly present in the cell and to project the density of states along the different layers to identify the band offset.

Regarding this superlattice method, another problem appears in the case of heterostructures including a polar layer: depending on the modelled interfaces, a built-in field appears in the polar layer, and the band profile evolves with the electrostatic potential along the heterostructure. For a STO/LAO (001) superlattice, this occurs in the case of a stoichiometric superlattice, as shown in Figure 3.1.(d): there is two different interfaces in the supercell, one *n*-type and one *p*-type. As discussed in the next Sections, this leads to a built-in electric field in the LAO layer, and an opposite electric field in the STO layer so that the average electrostatic potential remains zero (due to the periodic boundary conditions as discussed in Section 3.2.1). It is not trivial to calculate the band offset in this situation. A flat potential can be achieved in the LAO overlayer with a charge transfer from the *p*-type interface to the *n*-type interface: full compensation is reached if 0.5 $e^-/\square$ are transferred to the *n*-type interface.

Following this, stoichiometric superlattices are not appropriate to study the band offsets. To cancel the field in the STO and LAO subsystems, it is possible to build a cell containing additional layers, leading to off-stoichiometry and two identical interfaces. For example, adding one $(LaO)^+$ layer and one $(TiO_2)^0$ layer results in two *n*-type interfaces, as shown in Figure 3.1.(e). The additional LaO layer provides an extra charge, in this case a single electron, which will be shared by the two *n*-type interfaces, 0.5 $e^-/\square$, corresponding exactly to the amount required to fully cancel the field in LAO. This method is similar to semiconductor heterostructures with flat energy levels and an local dipole across an interface, where the relative alignment of the bands are independent of the thickness of the subsystems. For two *p*-type interfaces, additional $(SrO)^0$ and $(AlO_2)^-$ layers will results in an extra hole ejected to the STO subsystems, shared by the two *p*-type interfaces. We expect the band alignment far from the interface to be unaffected by the metallic character of this heterostructure (this is not guaranteed, as doping induces band bending). With this method, based on a symmetric and off-stoichiometric $(STO)_{12.5}/(LAO)_{12.5}$ superlattices, we calculated the band offsets for the two types of interface, by plotting the layer-resolved electronic density of state (projected onto each

STO and LAO sublayer, as well as the additional atomic planes). The results are displayed in Figure 3.7.(a) for the n-type interface and (b) for the p-type interface. To evaluate the band offsets, we proceed as follow: the valence band offset is calculated from the misalignment of the O $2p$ states near the top of the valence band. With the same approach, the conduction band offset is calculated from the misalignment of the Ti $3d$ and La $4d$ states. For the n-type interface, the LAO valence band lies slightly lower than the STO valence band, with a valence band offset of -0.36 eV, close to the experimental value of -0.35 eV [73] and a conduction band offset of 1.47 eV. For the p-type interface, we evaluate a valence band offset of -0.13 eV and a conduction band offset of 1.34 eV. Hence, we obtain an average value of -0.25 eV for the valence band offset and 1.41 eV for the conduction band offset. The sum of the offsets (1.66 eV) is in satisfying agreement with the difference of band gaps between both subsystems (1.63 eV), validating this approach. The valence band of both subsystems are almost completely aligned, which is why we will ignore the valence band offset in some of the following schematic representations of the band structure of the STO/LAO interface.

3.5 The polar discontinuity at the $SrTiO_3(001)/LaAlO_3$ interface

We have described the bulk properties of LAO and STO as well as addressed their band profile if no electric field is present in either subsystems. We can therefore focus on the mechanisms at the origin of the 2DES at the STO/LAO interface. Both STO and LAO are centrosymmetric in their bulk form, but display a formal polarization depending on the direction. When a surface or an interface is formed, the formal polarization leads to the appearance of a built-in field. A way to determine whether or not an interface is polar has been proposed by Tasker [74] and consists in using the formal ionic charge of each atoms as a point charge, without any geometric or electronic relaxation. The surface is then polar if the bulk unit cell contains a dipole moment; a few examples are given in Figure 3.8. The underlying hypotheses behind this naive approach appears to be satisfied in the case of centrosymmetric structures as discussed by Bristowe *et al.* [75] and Stengel *et al.* [76], who applied the concepts of the modern theory of polarization in the case of polar surfaces. Their main conclusion is as follows: a surface is polar if the bulk polarization perpendicular to the interface of two materials are not equal as described by the interface theorem in Reference [77]: if the system appears to be polar by Tasker's criterion, then it is equivalent to consider the net surface charge $\sigma = \mathbf{P} \cdot \hat{\mathbf{n}}$ at each side of the interface. In the case of an interface between two-semi-infinite systems, such charges at the interface and the surface produce a diverging electrostatic potential, which makes the system highly unstable. This issue is known as a "polar catastrophe". Generally, the existence of a built-in field is accompanied by some charge screening, and reconstruction (atomic and/or electronic) is expected for unstable surfaces. In the case of a thin film however, the evolution of the electrostatic potential is finite and may be stabilized without any reconstruction, depending on the energy costs of the reconstruction mechanisms. Amongst the possible compensation mechanisms, there is a distinction between extrinsic and intrinsic mechanisms. The first kind involves external sources, for example, molecular adsorption can help the compensation of some polar surfaces if the process involves doping of the surface, where the carriers can screen the built-in field. Of course, this implies the presence of the dopant species in the

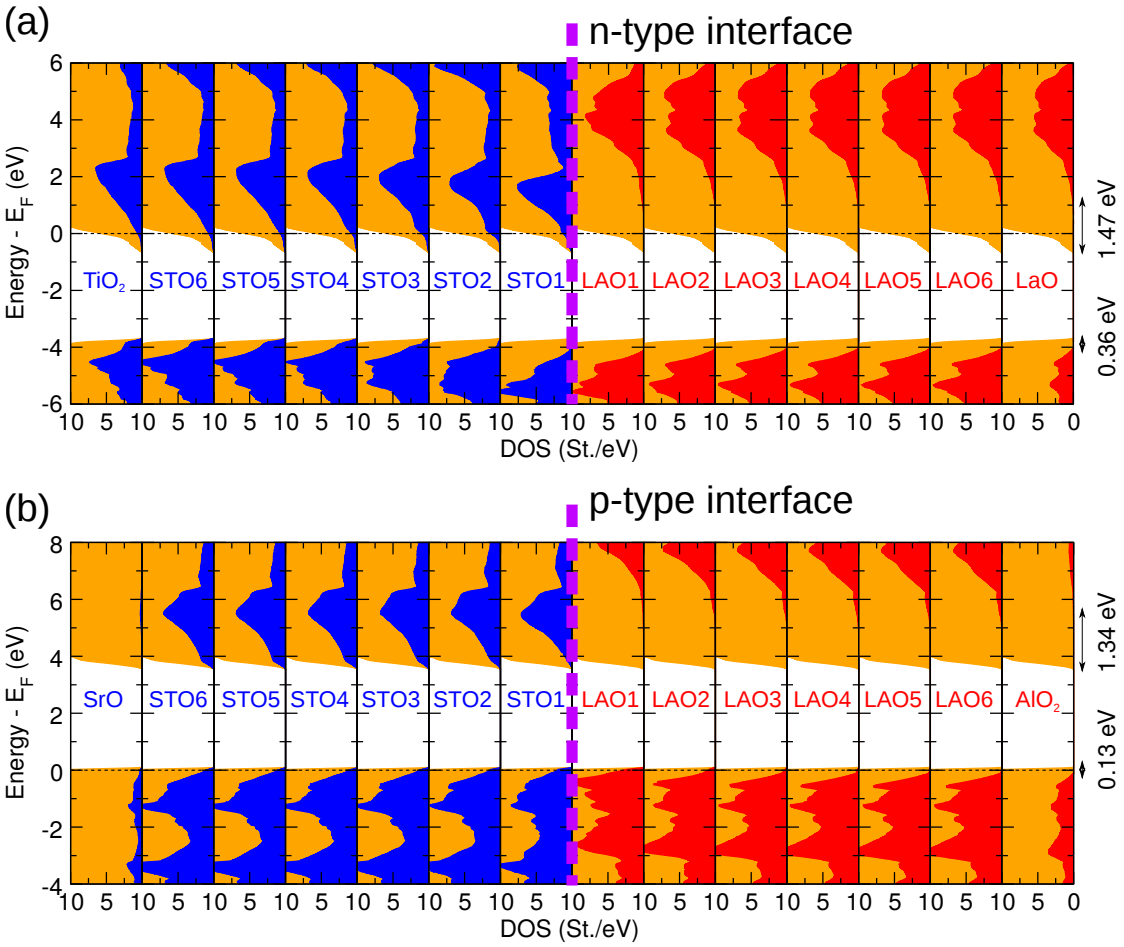

FIGURE 3.7: Electronic DOS projected on the different sublayer of off-stoichiometric $STO_{12.5}/LAO_{12.5}$ symmetric superlattices, with (a) two n-type interfaces and (b) two p-type interfaces, calculated with the B1-WC functional. As the superlattices are symmetric, only half of the superlattice data is displayed. The band offsets are written on the right, calculated from the central layers in each superlattice, the farthest from the interface. Blue (red) corresponds to the STO (LAO) contribution. The orange background is the total DOS. The horizontal dashed line is the Fermi level: note that for the n-type superlattice, the electron remains confined within the STO. For the p-type superlattice, the hole spreads over the whole heterostructure.

atmosphere. On the other hand, intrinsic mechanisms do not involve external sources of dopant, but a redistribution of the charges in the system.

The STO(001)/LAO interface is the most representative example of non-polar/polar oxide interface and has been first studied by Ohtomo and Hwang [78]. They synthesized this interface by epitaxial growth of LAO on the (001) surface of STO, alternating charged planes of LaO^{1+} and $AlO_2{}^{1-}$. This is in line with the description of a charged surface by Tasker, for the example given in Figure 3.8.(c). A built-in potential is thus raised as LAO is grown on STO(001), as shown in Figure 3.9. This Figures summarizes the polar discontinuity at the LAO/STO interface: a built-in field in the LAO overlayer diverges as its thickness increases, and may be compensated if a charge is transferred from the surface to the interface: in the case of the n-type interface, 1/2 electron per unit cell area (0.5 $e^-/\square$) is transferred to the TiO_2 layer at the interface; in the case of the p-type interface, 1/2 hole per unit cell area (0.5 $h^+/\square$) is transferred to the SrO

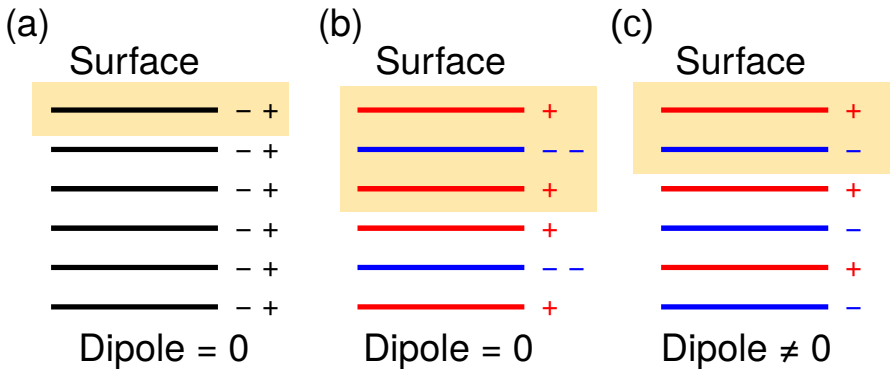

FIGURE 3.8: Examples of surface classification by Tasker [74] based on the planar formal ionic charges: (a) for the same charge between cations and anions in the same plane, leading to a neutral plane; (b) for uneven charged planes, but with no dipole; (c) alternating charged planes, with a net dipole moment.

layer at the interface. In the case of the n-type interface, such a transfer is favoured by the possibility of transition metal Ti to acquire a mixed valence state: hence, the Ti^{4+} at the interface can become $Ti^{3.5+}$ by hosting the 1/2 electron in its Ti t_{2g} conductions states.

3.5.1 A critical thickness of $LaAlO_3$ as a threshold for conductivity

With such considerations, it has been postulated that the 2DES appearing at the n-type interface is related to the polar discontinuity, the strongest argument in favour of this hypothesis being that a critical thickness d_c of about ~4 monolayers of LAO is required to observe an insulator-to-metal phase transition (MIT) at the interface: the sheet resistivity decreases by several orders of magnitude above this thickness, even for samples grown at high oxygen partial pressure ($p_{O_2} \approx 10^{-4}$ mbar), where the oxygen vacancies are expected to be reduced and not contribute to conductivity. The origin of this transition has been attributed to the presence of a thin sheet of electrons in the STO subsystem, confined near the interface [79]. The reader may notice that at this stage, we still not have addressed the *exact* origin of the carriers. The existence of a critical thickness however suggests that the electrostatic potential raised in the film is involved and must reach a critical value to trigger a compensation mechanism. Consequently, the existence of a threshold thickness is a strong argument in favour a *polar catastrophe* scenario.

A few important aspects of the critical thickness must be addressed. While Hall experiments suggests that no mobile carriers are present below d_c, there has been several reports of signature of $Ti^{3.5+}$ below the onset for conductivity [80–84], even as early as 2 u.c. thick LAO [85, 86], based either on hard x-ray photoelectron spectroscopy (HAXPES) or resonant inelastic x-ray scattering (RIXS), at odds with the Hall experiments. A few of these results are given in Figure 3.10. Notably, a strong evolution of the signal is witnessed with growing LAO thickness below 6 monolayers. The common hypothesis for these results is the presence of immobile carriers at the interface, which cannot be measured from Hall experiments. These results suggest that different critical thicknesses (for different physical properties) may be at the origin of this discrepancy, or that the onset for conductivity requires a large density of carriers, beyond a given threshold.

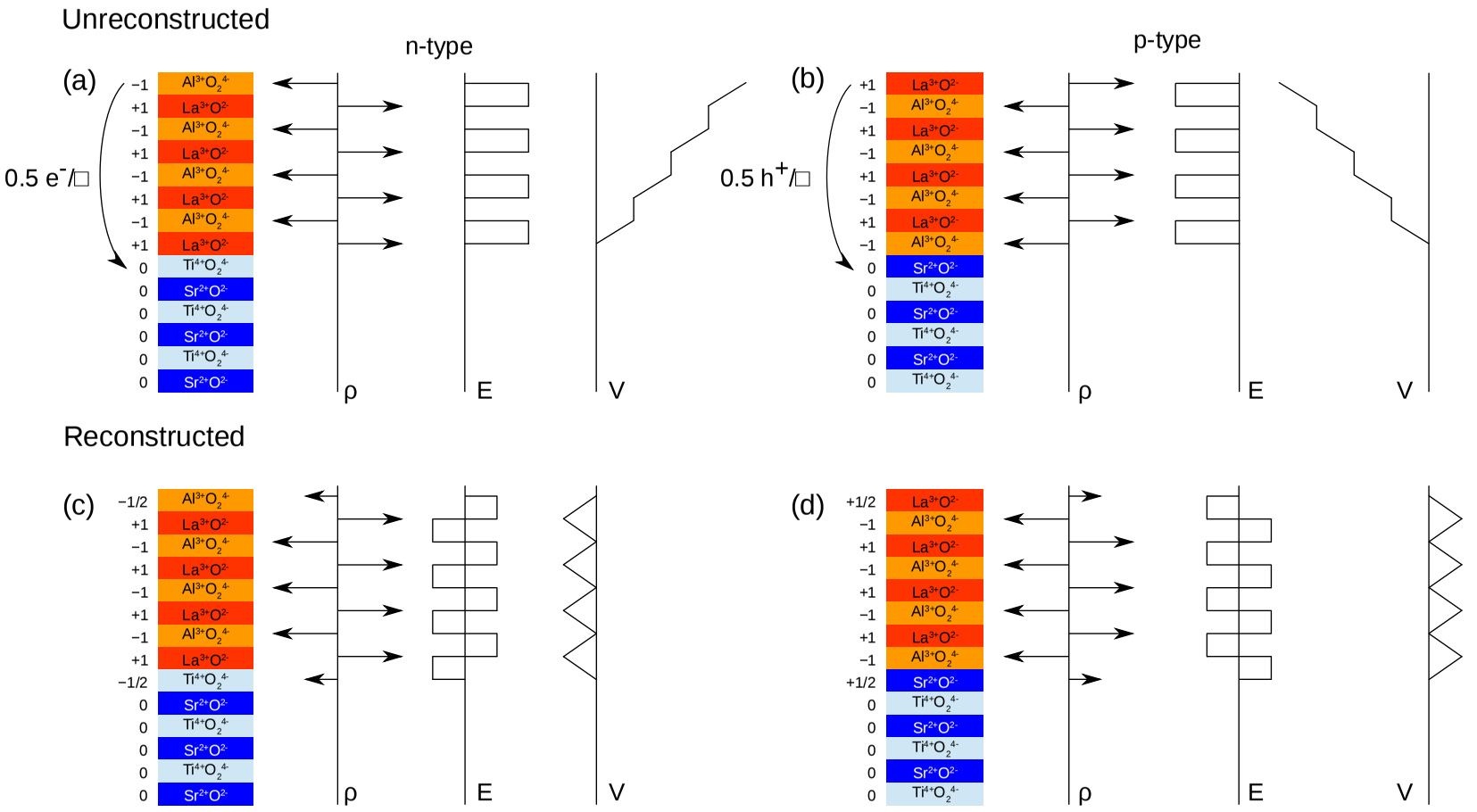

FIGURE 3.9: The polar discontinuity at the STO(001)/LAO interface, with a schematic representation of the formal planar charge ρ, the electric field E and the potential V is represented for the n-type interface (a, c) and p-type interface (b, d). On top, the unreconstructed case as expected from a pristine structure (no defects, perfect stoichiometry). Below, the reconstructed case for the fully compensated case, implying a charge transfer of $1/2$ $e^-/\square$ (for the n-type case) and $1/2$ $h^+/\square$ (for the p-type case) from the top layer of the LAO film to the STO substrate.

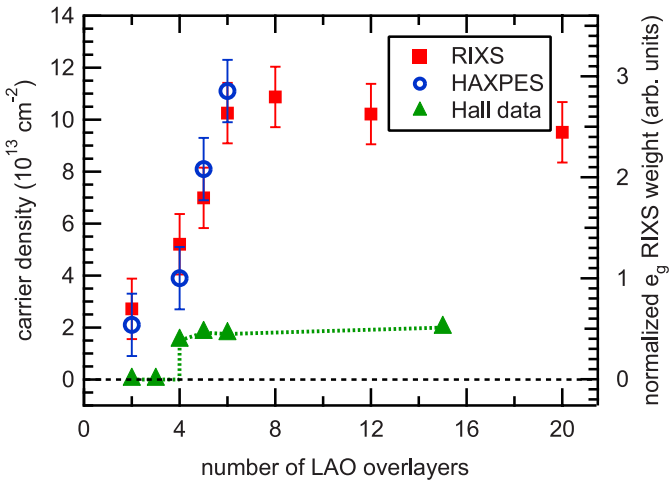

FIGURE 3.10: Sheet carrier densities at the n-type LAO/STO interface measured *via* Hall experiments [87], HAXPES experiments [85] and RIXS experiments [86]. Figure adapted from Reference [86].

Another property of the threshold thickness for conductivity is its tunability, by replacing the LAO layer with an alloy made of LAO and STO, as observed by Reinle-Schmitt *et al.* [26], referred to as LASTO:x (x being the *ratio* between the two compounds), as shown in Figure 3.11. The authors rationalize these observations by proposing that alloying tunes the polarity of the overlayer without significantly changing the dielectric properties of the film in comparison to LAO, thus only tuning the polar discontinuity at the interface. The behaviour of the threshold thickness for the alloy-based heterostructures follows the following law with respect to the composition x:

$$d_c^{\text{LASTO:}x} = d_c^{\text{LAO}}/x \tag{3.5}$$

For a composition $x = 0.5$, the threshold thickness becomes twice the value expected for the bare LAO case.

Finally, it has been shown from experiments [88, 89] that the threshold thickness can be reduced by adding a STO capping layer on top of the LAO film: a finite sheet carrier density measured by Hall effect experiments have been observed in samples with a LAO interlayer thickness of 1 or 2 u.c., much below what is observed for the uncapped heterostructures.

The last two paragraphs highlight specific aspects of the link between the critical thickness and the polar catastrophe: on one hand, this property can be tuned by tuning the polarity of the overlayer film, which is a strong argument in favour of the polar catastrophe scenario. On the other hand, the addition of a simple, insulating and non-polar STO capping layer has been shown to decrease d_c, at odds with the polar catastrophe.

Clarifying these experimental observations are amongst the primary objectives of this work.

3.5.2 A two-dimensional electron gas at the n-type interface

We will now briefly describe the properties of the 2DES at the STO(001)/LAO interface. This Section does not aim to cover all the specificities of this system; for the

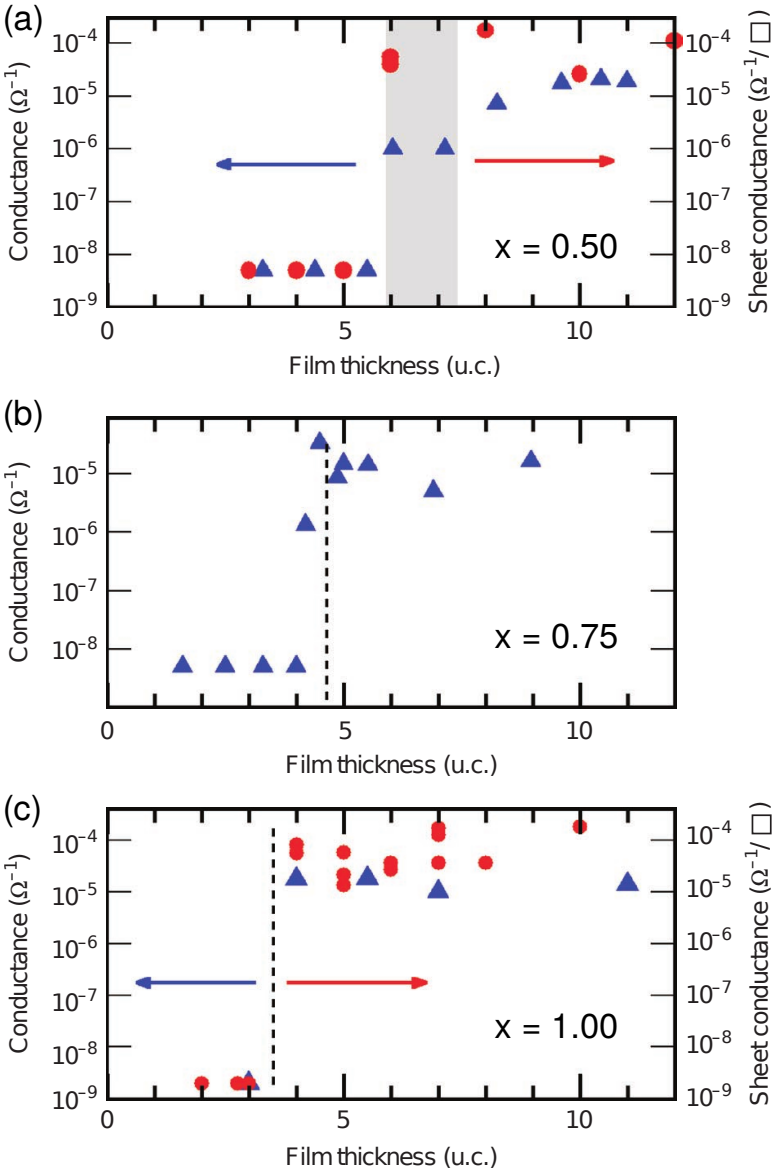

FIGURE 3.11: Conductance of LASTO:x films measured at room temperature for compositions (a) $x = 0.50$, (b) $x = 0.75$, and (c) $x = 1$. The dashed vertical lines for $x = 1.0$ and 0.75 indicate the determined threshold thicknesses d_c. For $x = 0.5$, is represented by a grey band for the more gradual transition. The blue triangles and red points belong to different sets of samples. Figure adapted from Reference [26].

interested reader, a review of the most important aspects of 2DES at polar/non-polar oxide interface can be found in Reference [90].

One of the key properties of the 2DES at the STO(001)/LAO interface is that the spatial extension of the electron is quite limited in the transverse direction of the interface. Depending on the oxygen partial pressure and the annealing process after the synthesis of the samples, the extension of the gas vary drastically: for samples grown at low p_{O_2} ($\sim 10^{-6}$ mbar) and without annealing process, the gas spreads from 10 to 100 μm. In this case, the electrons are not localized near the interface and has a 3-dimensional character [91, 92]. It has been postulated that in such a case, the electrons may originate from oxygen vacancies present in the STO substrate [91], and which are not a characteristic

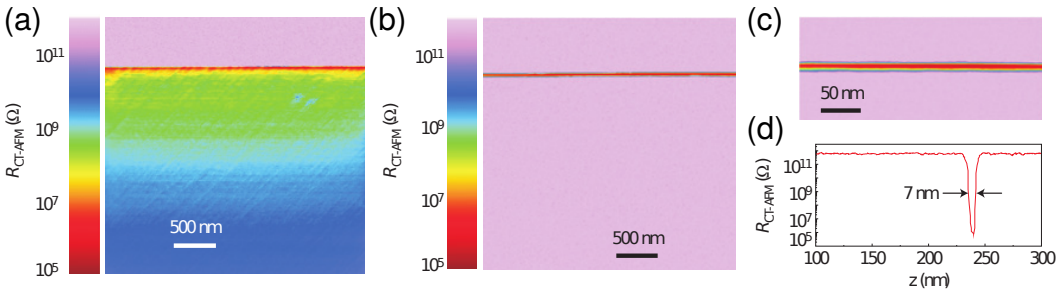

FIGURE 3.12: Spatial mapping of resistance near the STO(001)/LAO interface for (a) a non-annealed sample; (b) an annealed sample, (c) zoom on the data shown in (c); (d) resistance profile across the interface in the annealed case, highlighting the localization of the 2DES within a few nanometers of the interface. Figure adapted from Reference [93].

of the STO/LAO interface. The effect of annealing for samples grown at low p_{O_2} reduces the extension of the electrons to only a few nanometers from the interface [93], similarly to samples grown at high p_{O_2} ($\sim 10^{-4}$ mbar). In the later case, the electron system has a 2-dimensional character, and can be considered as a 2DES which appears from intrinsic mechanisms: Figure 3.12 shows the effect of annealing on the sheet resistance profile across the interface. The extension of the 2DES has been estimated to be between 4 and 10 nm, the majority of the carriers lying in the first unit cell of STO [85, 94, 95].

The intrinsic 2DES has been shown to be composed of two types of carriers, one confined close to the interface ($\sim$2 nm), and one which spreads away from the interface, deeper in the substrate ($\sim$11 nm) [96]. This relates to the nature of the first available empty states of STO hosting the carriers. In the bulk cubic phase of STO, the first (empty) conduction states are of Ti t_{2g} character, which arises from the splitting of the $3d$ states of Ti under the octahedral crystal field into t_{2g} (d_{xy}, d_{xz} and d_{yz}) and e_g ($d_{3z^2-r^2}$ and $d_{x^2-y^2}$), the later being further away from the conduction band bottom and remaining empty. When a (001) surface is created on STO, the t_{2g} energy levels are splitted, as an effect of the surface symmetry breaking [97]. For the STO/LAO interface, as soon as the interface is doped, the injected carriers will partially fill the t_{2g} states, split between the d_{xy} and d_{xz}/d_{yz} (degenerate) states, corresponding to delocalized and localized states near the interfaces.

First-principles calculation based on DFT [98–101] have been performed for the STO/LAO interface, showing that the occupied orbital with the lowest energy is mainly of d_{xy} character. The d_{xy} population has a strong 2-dimensional character, which is related to their high band velocity in the xy plane, parallel to the interface; on the other hand, the d_{xz}/d_{yz} spreads further in the substrate, with a more pronounced 3-dimensional character and lower mobility in the xy plane [101]. The DFT calculations in References [99, 101] and [28] shows that the carrier density at the interface change the overall splitting between the filled bands, in agreement with spectroscopy experiments [28], as shown in Figure 3.13. Note that there is a strong discrepancy between the density extracted from Hall experiments and spectroscopy experiments, which can already be seen from Figure 3.10: the carrier densities extracted from Hall measurement is around one order of magnitude lower than the densities extracted from HAXPES and RIXS. Popovic *et al.* [101] argued that due to their 2-dimensional character, the electrons are likely to be subject of Anderson localization [102]. In addition to this discrepancy, the

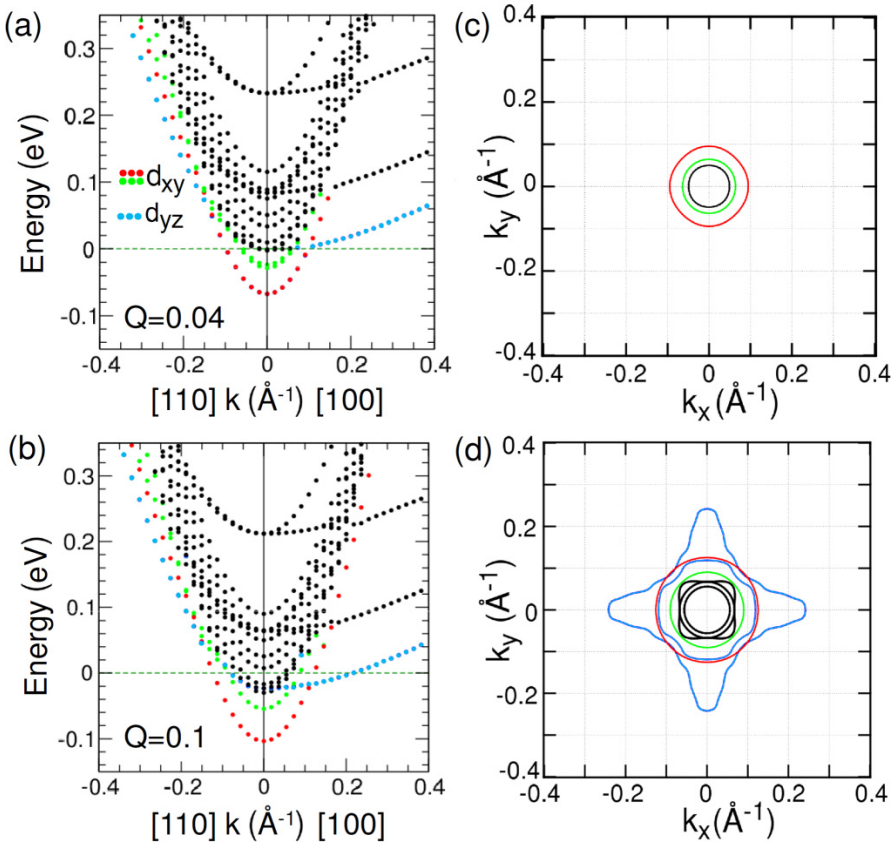

FIGURE 3.13: Band energies of the STO/LAO interface calculated from DFT-VPSIC calculations, for different amount of electrons transferred at the interface (a) $Q = 0.04\ e^-/\square$ and (b) $Q = 0.1\ e^-/\square$. The corresponding Fermi surfaces are shown in (c) and (d). Figure adapted from Reference [28].

experimental carrier densities of annealed samples are always lower than the limit of $0.5\ e^-/\square$ (3.3×10^{14} cm^{-2}) expected from the polar catastrophe.

The mechanism behind the localization of the carriers near the interface is not trivial. Typically, confinement occurring at junctions in metal-oxide-semiconductor interface is attributed to the band bending near the interface. However, it has been argued that the band bending at the STO(001)/LAO interface is not sufficient to explain the low thickness of the 2DES [103]. Chen *et al.* [98] proposed that the orbital coupling between the Ti and La atoms lower the Ti t_{2g} states close to the interface, which favours their occupancy with respect to the deeper Ti sites. Stengel [104], by the mean of model Hamiltonians based on first-principles calculations, also stresses that moving electrons away from the interface has an energy cost which is inversely proportional to the dielectric constant of STO $\varepsilon^{\mathrm{STO}}$, and that the dielectric properties of STO are important to determine the spread of the 2DES. The importance of the dielectric properties of the STO substrate will be discussed in Chapter 4, specifically in regards to its impressive temperature dependence. Finally, it has been shown from first-principles calculations [27] that the localization process is spontaneous at low density, only populating the d_{xy} bands below a threshold density $n_c \sim 10^{14}$ cm^{-3}. Above this value, the electrons "spill" to the d_{xz}/d_{yz} states extending farther from the interface. The authors provide a link between the carrier density and the binding energy (and therefore the spatial spread of the 2DES). This aspect will also be a topic of discussion in Chapter 4.

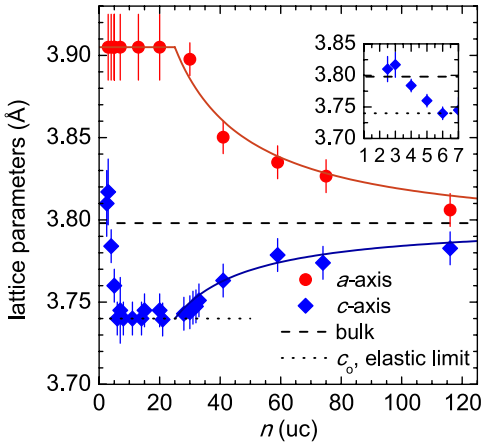

FIGURE 3.14: *a*- and *c*- axis lattice parameters of the LAO overlayer grown of top of STO(001), as a function of film thickness. The solid lines are a guide to the eyes, the dashed horizontal lines indicates the pseudo-cubic LAO lattice parameter. The inset shows the detail of the expansion of *c* for the lower thicknesses. Figure adapted from Reference [29].

Along with these basic features, the 2DES at the STO(001)/LAO interface also present a large array of interesting properties, which do not exist in the parent compounds or present unexpected behaviour. Amongst these properties, we should mention superconductivity [105, 106], which can be tuned by an electric field effect [107]. In addition, there has been signatures of ferromagnetism [108], with the presence of a hysteresis loop and transport properties associated with a large magnetoresistance [109–111]. Ferromagnetism and superconductivity are usually exclusive properties, but for the case of the STO(001)/LAO interface, they have been shown to either coexist [112, 113] or being phase separated [114].

The STO(001)/LAO interface also displays some interesting structural properties. As discussed earlier in this Chapter, there is a constraint on the in-plane LAO lattice parameter a (= 3.81 Å) expected from an epitaxial strain, to fit the STO lattice parameter (= 3.91 Å), and in principle should be accompanied with a contraction of the out-of-plane c parameter according to Poisson's law. However, experimentally, what is observed is that the out-of-plane lattice parameter c is expanded of about ∼2% [115]. This expansion has been rationalized as an electrostrictive effect [29], and disappears for a LAO thickness between 6 and 20 u.c., recovering the expected Poisson's contraction, and a signature of complete screening of the built-in field in LAO (shown in Figure 3.14). In addition, x-ray diffraction experiments [116] have provided evidence of atomic displacements in $LaAlO_3$, in agreement with the presence of an electric field in the film, since off-centring of the cations is measured with respect to the perovskite cubic structure. These structural properties, evidence of a built-in field in LAO, are a strong argument in favour of the polar catastrophe scenario.

3.6 A controversy for the origin of the carriers

The STO(001)/LAO *n*-type interface is characterized by a metal-insulator phase transition (MIT) depending on the thickness of the LAO overlayer as-grown on the STO

substrate. Above a LAO thickness of $3-4$ u.c., the interface is metallic, and this behaviour is attributed to the presence of a 2DES confined near the interface. The critical thickness is a feature that is well reproduced in experiments. Moreover, the properties discussed in the previous Sections have been observed by different groups with different methods. This suggests a universal mechanism behind the appearance of the 2DES. Despite the reproducibility of these experiments and a consensus on the existence of the 2DES, there remains a controversy on its *exact* origin. The debate stems from the many possibilities available to explain the origin of the carriers, and the difficulty to discriminate amongst them based on the observed properties. Amongst the proposed mechanisms, it is usual to differentiate those which are intrinsic or extrinsic, depending on the *exact* origin of carriers. For example, the presence of dopant species may be considered as extrinsic. Similarly, defects acting as donors such as oxygen vacancies may appear by the growth process. On the other hand, intrinsic mechanisms do not rely on external factors. However, the distinction between intrinsic or extrinsic mechanisms may be a source of confusion. For example, oxygen vacancies at the surface of the LAO layer have been argued to be stabilized by the existence of an electrostatic field in the LAO layer, as evidenced from first-principles calculations [47, 117]. In a sense, this "atomic reconstruction" can also be called a polar catastrophe, similarly to the Zener breakdown scenario, since the oxygen vacancies at the LAO surface prevent the divergence of the electrostatic potential in the LAO film and provide carriers. The semantics are confusing and therefore not appropriate. Instead, it has been proposed [57] that it would be more appropriate to differentiate the mechanisms between those which are electric-field driven and those which are not.

3.7 Electric-field driven mechanisms from first-principles

We will now provide a description of the two most popular known hypotheses at the origin of the 2DES at STO(001)/LAO interface, the Zener breakdown and the surface oxygen vacancies. The mechanisms can be explained in the framework of a polar catastrophe, where the diverging electrostatic potential in the LAO film is the driving force behind the instability leading to the appearance of the 2DES. The main argument in favour of these mechanisms is the existence of threshold LAO thicknesses to witness different phenomena, such as signatures of $Ti^{+3.5}$ valence at the interface from spectroscopy, or the change in sheet resistance. Indeed, as will be argued in the following discussion, the intricacies of the different mechanisms result in differences in properties.

3.7.1 Electric-field driven Zener breakdown

Oxide typically includes transition metal atoms, such as Ti, which are much more inclined to change their bulk valence state than non-transition metals. Hence, for the STO(001)/LAO interface, it is possible for the electrons to rearrange themselves to avoid a polar catastrophe, as the electrostatic potential diverges with increasing LAO thickness. This is the so-called Zener breakdown scenario, and does not involve any atomic reconstruction, since only the electronic population changes. In this Section, we will focus on the Zener breakdown hypothesis and its description from first-principles calculations based on the hybrid functional formalism.

The Zener breakdown stems from the electrostatic behavior of the STO(001)/LAO interface and can be formulated in terms of the conservation of the normal component of the displacement field **D** across the interface [76]. In the (001) direction, the LAO layers can be considered as a serie of capacitors with $(LaO)^{1+}$ and $(AlO_2)^{1-}$, corresponding to surface charge $\sigma_0^{LAO} = 0.5\ e/\square$, where e is the electron charge and $\square$ is the in-plane unit cell area ($= a^2$). Hence, considering the polarity of each LAO monolayer, the LAO film has a formal polarization of $P_0^{LAO} = -e/2\square$. As the STO atomic planes are neutral, there is no formal polarization in the STO substrate. The formal polarizations of STO and LAO are therefore:

$$P_0^{STO} = 0 \tag{3.6}$$
$$P_0^{LAO} = -e/2\square \tag{3.7}$$

The transverse component of the displacement field, in each environment (STO, LAO, vacuum) is then:

$$D^{STO} = \varepsilon_0 E_0^{STO} + P_0^{STO} \tag{3.8}$$
$$D^{LAO} = \varepsilon_0 E_0^{LAO} + P_0^{LAO} \tag{3.9}$$
$$D^{vac} = 0 \tag{3.10}$$

In the absence of free charges, which is the case for band insulators, the normal component of the displacement field has to be preserved [77]. Hence, the vacuum fixes $D = 0$ across the whole heterostructure, and an electric field appears in the LAO overlayer, such that:

$$E_0^{STO} = -\frac{P_0^{STO}}{\varepsilon_0} = 0 \tag{3.11}$$
$$E_0^{LAO} = -\frac{P_0^{LAO}}{\varepsilon_0} = \frac{1}{\varepsilon_0}\frac{e}{2\square} \tag{3.12}$$

Since $LaAlO_3$ is an insulator, the material will polarize under the effect of an electric field, leading to a depolarizing field and surface induced charges σ_{ind}^{LAO}. The polarization induced in LAO P_0^{LAO} is therefore screened by the depolarizing field E_{ind}^{LAO} and its value depends on the dielectric constant ($\varepsilon_r^{LAO} \sim 24$, see Table 3.3). The resulting electric field E^{LAO} and surface charge are given by:

$$E^{LAO} = E_0^{LAO} - E_{ind}^{LAO} = \frac{1}{\varepsilon_0 \varepsilon_r^{LAO}}\frac{e}{2\square} = 0.25\ \text{V/Å} \tag{3.13}$$
$$\sigma^{LAO} = E^{LAO}\varepsilon_0 = 0.02\ e/\square \tag{3.14}$$
$$\sigma_{ind}^{LAO} = \sigma_0^{LAO} - \sigma^{LAO} = 0.48\ e/\square \tag{3.15}$$

Within this model, the built-in electric field is estimated to be equal to 0.25 V/Å. Consequently, the electrostatic potential increases linearly with LAO thickness, about $c \times E^{LAO} \approx 0.9$ eV per monolayer (c being the out-of-plane lattice parameter of LAO). This effect can also be viewed in a band diagram, where the valence states of LAO are raised at higher energy with the electrostatic potential, as shown in Figure 3.15.(a) for the n-type interface. For a LAO thickness d above a threshold value d_c, the valence O $2p$ states at the surface of LAO are raised above the STO conduction band minimum, and a charge transfer occurs from the O $2p$ to the Ti t_{2g} states of STO: a 2DES appears at the interface, as shown in Figure 3.15.(b); as a by-product of the charge transfer, a

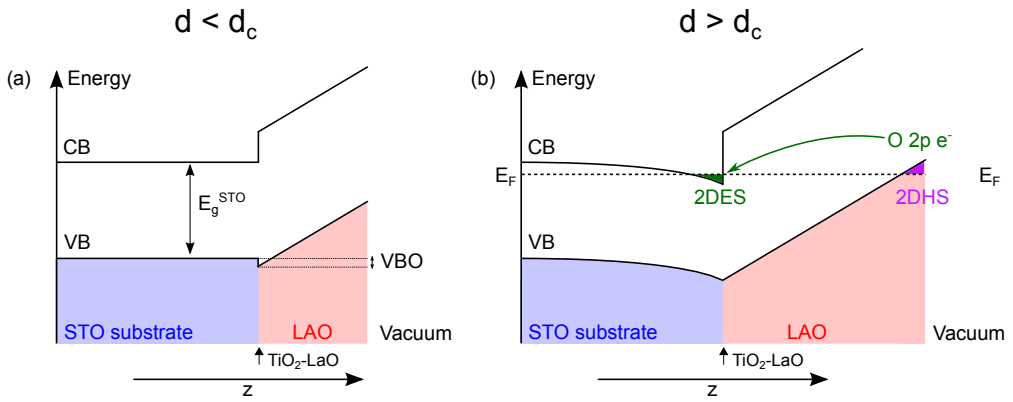

FIGURE 3.15: Band diagram representation of the Zener breakdown scenario (a) for a LAO thickness d below the critical thickness d_c, (b) for a LAO thickness d above the critical thickness d_c.

2-dimensional hole system (2DHS) is expected to exist at the surface of LAO according to the Zener breakdown picture.

First-principles calculations performed on STO(001)/LAO$_m$ heterostructures[5] agrees with this picture. Figure 3.16.(a) shows the evolution of the heterostructure electronic band gap with respect to the number of LAO monolayers, and in Figure 3.16.(b) the profile of the macroscopic average of the electrostatic potential across the heterostructures. From these results, we make the following observations: i) the electrostatic potential in the STO is flat, as expected from our earlier considerations; ii) the electrostatic potential varies linearly with increasing LAO thickness, the slope is estimated to be -0.25 V/Å for $1 \leq m \leq 4$, and this translates in the linear decrease of the band gap with increasing LAO thickness, with a slope of -0.9 eV/u.c., in agreement with the precedent estimation for $\varepsilon_r^{\mathrm{LAO}} = 24$; iii) the field in LAO is expected to raise the valence states in the LAO system, which is shown in the layer-resolved density of state for the different heterostructures (Figure 3.17); and iv) for $m \geq 5$ u.c., the system is metallic, and for the metallic phases, the slope of the electrostatic potential decreases. The MIT is expected to occur at $m = 4.2$ u.c. based on the linear projection of the evolution of the band gap below the onset for charge transfer. This is the critical thickness of LAO at which an electronic reconstruction, also referred to as a Zener breakdown, occurs. It is also the onset above which the LAO O $2p$ valence state overlap the Ti t_{2g} conduction states of the STO substrate in the density of state:

$$d_c^{\mathrm{ZB}} = 4.2 \text{ u.c.} \tag{3.16}$$

The Zener breakdown occurs when the drop of electrostatic potential Δ across the LAO film is equal to the sum of the band gap of STO E_g^{STO} and the valence band offset VBO, as shown in Figure 3.15.(a). Hence, it is possible to calculate d_c^{ZB} from the Zener breakdown model, by estimating the thickness needed to reach a potential drop equal to Δ if the slope of the potential is a constant field E^{LAO}:

$$d_c^{\mathrm{ZB}} = \frac{\Delta}{E^{\mathrm{LAO}}} = \varepsilon_0 \varepsilon_r^{\mathrm{LAO}} \frac{\Delta}{P_0^{\mathrm{LAO}}} \tag{3.17}$$

[5]The system actually consists in vacuum/LAO$_m$/STO$_{13.5}$/LAO$_m$/vacuum symmetric films, with two equivalent n-type interfaces, similar to the structure shown in Figure 3.1.(c). The vacuum area is roughly 450 Å thick.

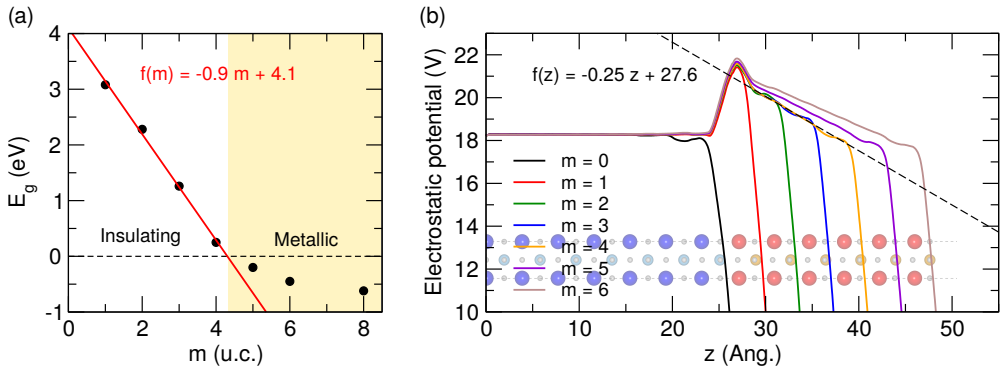

FIGURE 3.16: (a) Electronic band gap for STO(001)/LAO$_m$/vacuum heterostructures, for different LAO thicknesses m (u.c.), calculated as the difference between the bottom Ti t_{2g} band and the top of the LAO O $2p$ band, the negative values corresponds to metallic phases; (b) Macroscopic average of electrostatic potential in a STO(001)/LAO$_m$ for varying LAO overlayer thicknesses m. The slope of electrostatic potential in the LAO layer is estimated to be -0.25 V/Å below the onset for Zener breakdown. Above this threshold ($m > 4$ u.c.), the slope decreases with increasing LAO thickness, at as the interface progressively get doped.

which predicts the same value as in Equation 3.16 by taking the following values $c = 3.79$ Å, $E_g^{\text{STO}} = 3.57$ eV and $\varepsilon_r^{\text{LAO}} = 24$. The critical thickness d_c^{ZB} depends on different physical parameters: the electronic band gap of STO, the valence band offset, the dielectric constant of LAO and the LAO formal charges, which are all intrinsic parameters to the system. Our first-principles calculations predicts d_c^{ZB} between 4 and 5 monolayers of LAO. This is an overestimation if we compare to the experiments, for which the onset for conductivity is between 3 and 4 u.c. (Figure 3.10).

This overestimation may be attributed to the overestimation of the band gap: all things being equal, correcting the value of the band gap by the experimental one (3.25 eV [54]), the critical thickness becomes $d_c^{\text{ZB}} = 3.8$ u.c., in better agreement with the experiments[6].

Above the critical thickness, each additional LAO layer have their valence electrons at higher energies than the bottom of the conduction band of STO. These electrons are therefore transferred from the surface to the interface. The density profile extends over the whole STO film in our simulation, as shown in Figure 3.18: close to the interface, the electrons have a dominant Ti d_{xy} character, whereas away from the interface, the electrons have a dominant mixed Ti d_{xz}/d_{yz} character. This transfer pins the valence band edge of the LAO system to the conduction band minimum of STO, which implies that the field in LAO is modified by the charge transfer, according to the following law:

$$E^{\text{LAO}} = \frac{\Delta}{d^{\text{LAO}}} \tag{3.18}$$

Assuming that Δ is constant, the field in LAO decreases as $1/d^{\text{LAO}}$ as the LAO thickness increases. Additionally, the electron transfer leads to the appearance of a 2DES system in the STO subsystem as shown in Figure 3.15, with a sheet charge density σ_s [99] as

[6] We must stress that the predicted critical thickness is actually quite sensitive to the exchange-correlation energy functional E_{xc}, and may change from 3 u.c. to 6 u.c. depending on the method [47, 118, 119]. This relates to the sensitivity of Kohn-Sham band gaps to E_{xc}, but as well on the other parameters determining the Zener breakdown, such as $\varepsilon_r^{\text{LAO}}$. Hence, the improved accuracy of the B1-WC functional in determining these parameters leads to a better agreement with experiments.

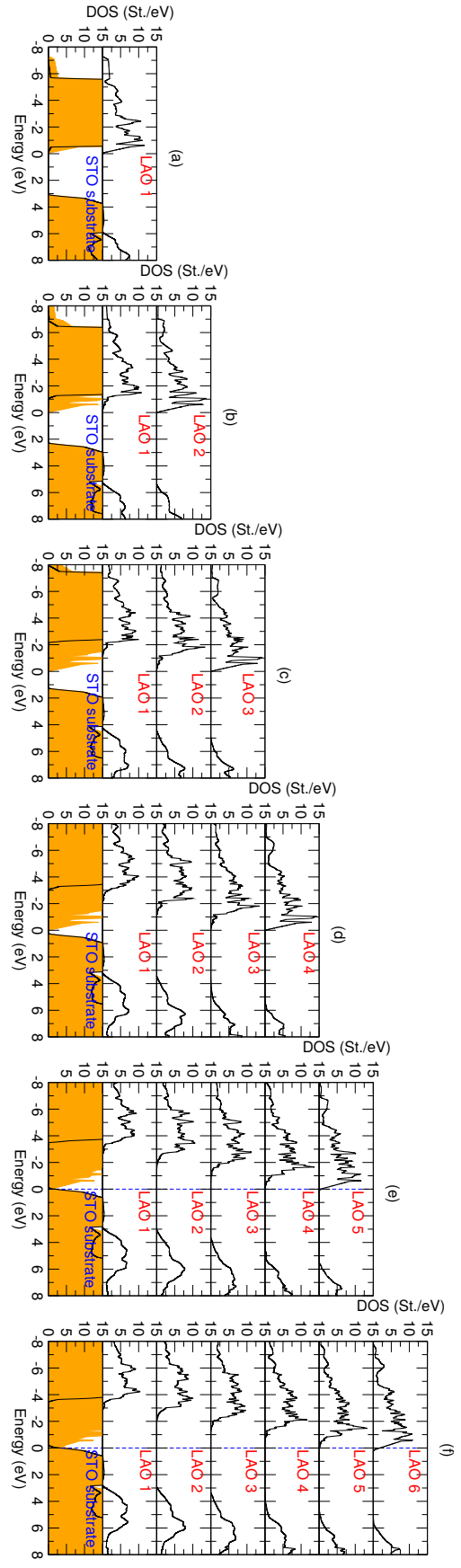

FIGURE 3.17: Layer-resolved density of state of STO(001)/LAO$_m$ heterostructures, for varying LAO overlayer thicknesses m. The orange area is the total density of state. The vertical dashed line is the Fermi level for the metallic films.

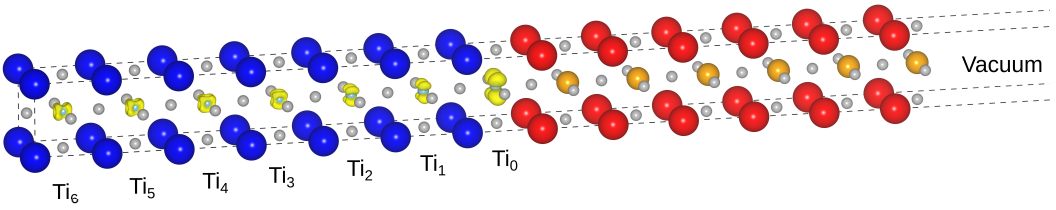

FIGURE 3.18: Isosurfaces of electron charge density calculated for a STO(001)/LAO_6/vacuum heterostructure (10^{-3} $Bohr^{-3}$) with a n-type interface. Close to the interface, the population have a dominant d_{xy} character. Far from the interface, the Ti occupancy has a a dominant mixed character d_{xz}/d_{yz}.

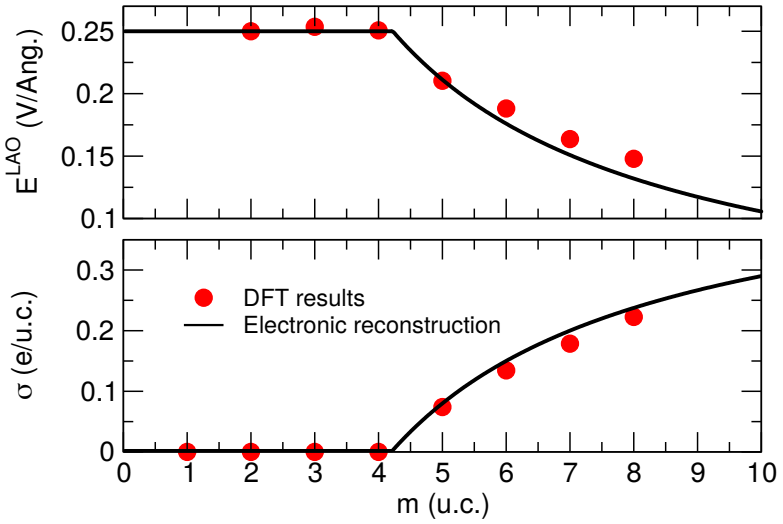

FIGURE 3.19: Comparison between the Zener breakdown model (the parameters set as in the main text) and the DFT results, for the electric field in the LAO overlayer and the charge density within the STO substrate.

calculated from Equations (3.18), (3.17) and (3.14).

$$\begin{aligned} \sigma_s &= \sigma_0^{\mathrm{LAO}} + \varepsilon_0 \varepsilon_r^{\mathrm{LAO}} E^{\mathrm{LAO}} \\ \Leftrightarrow \sigma_s &= \sigma_0^{\mathrm{LAO}} + P_0^{\mathrm{LAO}} \frac{d_c^{\mathrm{LAO}}}{d^{\mathrm{LAO}}} \\ \Leftrightarrow \sigma_s &= \frac{1}{2}\frac{e}{\square}\left(1 - \frac{d_c^{\mathrm{LAO}}}{d^{\mathrm{LAO}}}\right) \end{aligned} \tag{3.19}$$

The sheet carrier density depends on the dielectric constant of LAO, the thickness of the LAO overlayer and the band gap of STO. In the limit of an infinitely thick LAO overlayer, σ converges to $\sigma_0^{\mathrm{LAO}} = 0.5\ e/\square$. The evolution of the built-in field E^{LAO} and the sheet carrier density σ with respect to LAO thickness are given in Figure 3.19, as computed from first-principles and with the model based on the parameters c, E_g^{STO} and $\varepsilon_r^{\mathrm{LAO}}$. The overall agreement between the model and the DFT results is satisfying.

The main features of the Zener breakdown model can be summarized as follows:

- Below a LAO critical thickness d_c^{ZB}, the interface is insulating, with the presence of a built-in field in LAO. The electrostatic potential drop across the LAO layer linearly evolves with the thickness of LAO.

- At a critical thickness d_c^{ZB}, the surface O $2p$ valence states reach the energy of the unoccupied Ti t_{2g} states of the STO substrate, raised by the electrostatic potential: a Zener breakdown occurs, and the charges are transferred from the surface to the interface.
- Above the critical thickness d_c^{ZB}, the valence band edge of LAO is pinned to the bottom of the conduction band of STO by the charge transfer, and the band gap remains closed. This leads to the presence of a 2DES in the STO, confined close to the interface, and the presence of holes at the -AlO_2 surface of LAO.

The predictions of the model are in good agreement with first-principles results. Moreover, there is a large array of experimental results supporting the Zener breakdown hypothesis. Notably, the critical thickness has been consistently determined to be 4 u.c. by several groups and methods, for films grown either from PLD [87] or MBE [73] at high p_{O_2}, with the contribution of V_O to the conductivity removed by annealing. Additionally, the sheet carrier density ($n_s \sim 4-9\times10^{13}$ cm^{-2} measured at low LAO thicknesses $<$ 8 u.c.) is in good agreement with the densities estimated from HAXPES [85] and RIXS [86] experiments at the same thicknesses (Figure 3.10). However, at higher LAO thicknesses, the measured carrier densities do not increase, in contrast with the predictions of the Zener breakdown model. There are other experimental evidences against this scenario. There has been mention of sizeable density of Ti $3d$-like states measured below the critical thickness (as early as 2 u.c. of LAO), with core-level spectroscopic measurements suggesting that the breakdown occurs almost immediately [82, 85, 86]; however, as these charges remains trapped and do not contribute to interface conductivity, they may not originate from a polar catastrophe, and it is possible that they originate from oxygen vacancies buried in the STO substrate. In addition to the presence of sub-critical Ti $3d$ carriers, no mobile holes have been found at the LAO surface, and no hole states have been detected near the Fermi level [120, 121]. There has however been reports of the existence of a hole-sheet if the LAO is capped with STO, even at sub-critical LAO thicknesses [89, 122, 123]. In References [89] and [122] however, the holes are attributed to the O $2p$ states of the surface TiO_2 layer, whereas in Reference [123], the LAO interlayer thickness is larger than the threshold thickness value and the authors attribute the 2DHS to stem from the O $2p$ states of the AlO_2 layer at the p-type interface with the capping layer. Finally, there has been reports of suppressed conductivity at any LAO thicknesses for samples grown at very high $p_{O_2}(\sim 10^{-3}-10^{-2}$ mbar) [91, 124].

From a theoretical point of view, a polar catastrophe should also occur for the p-type interface, with transfer of hole-like carriers to the p-type interface, in the O $2p$ states of the AlO_2 layer (shown in Figure 3.20). The polar catastrophe scenario for the p-type interface is also supported by first-principles calculations, which predict a charge transfer above a critical thickness of LAO around 6.2 u.c. [57], related to the larger gap in LAO. A striking difference between the electron doping and the hole doping is that the holes do not remain confined near the interface, but spreads over the whole heterostructure. This may be related to the nature of the host sites O, which are not keen to change from their octet state. In contrast to the n-type interface, no MIT has been witnessed for the p-type interface, suggesting that other compensation mechanisms are at play here, and do not involve any charge transfer.

The Zener breakdown scenario, and its simulation from first-principles is a consequence of considering pristine systems, without any defects which may alter the electric field

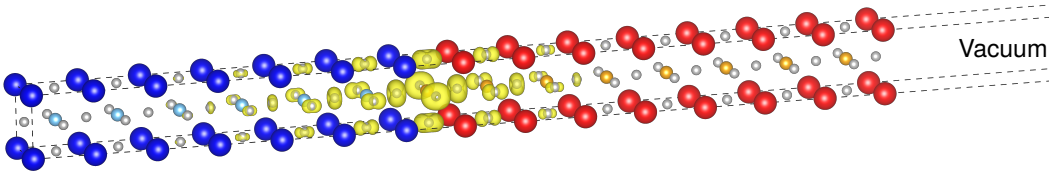

FIGURE 3.20: Isosurfaces of hole charge density calculated for a STO(001)/LAO_8/vacuum heterostructure (10^{-3} $Bohr^{-3}$) with a *p*-type interface. For this interface, the holes are localized in the BO_2 and AO planes in the STO and LAO layer.

in the LAO overlayer, its dielectric properties, *etc.* However, other compensation mechanisms may occur earlier than the Zener breakdown, which might explain some of the discrepancies between this simple, naive picture and the experiments.

3.7.2 Electric-field driven surface redox mechanism

Until now, we have discussed how the STO(001)/LAO heterostructure behave if no atomic reconstruction/defects occurs during growth, assuming a pristine heterostructure. Similarly to semiconductors, STO is sensitive to doping, and donor impurities have been suspected to be at the origin of the 2DES at its interface. In fact, it is well known that La impurities [125] and oxygen vacancies [67] act as *n*-type donors. The present Section focuses on the role of oxygen vacancies in such heterostructures.

Even if the STO substrate is insulating before the growth of the LAO epitaxy, it can be expected that the growth process induces oxygen vacancies. In the original paper [78], it was already reported that the 2DES properties are affected by the growth conditions, in terms of mobility, sheet resistance, electron densities. Since then, there has been several studies focusing on the role of the oxygen partial pressure p_{O_2} during growth, as well as the effect of annealing on the 2DES properties [91, 93, 126, 127]. Three regimes have been identified: low p_{O_2} ($\sim 10^{-6}$ mbar), high p_{O_2} ($\sim 10^{-4}$ mbar) and very high p_{O_2} ($\sim 10^{-2}$ mbar). For samples grown at low p_{O_2} as in Reference [78], the sheet carrier densities are estimated within the range $10^{14} - 10^{17}$ cm^2, with Hall mobilies around 10^4 $cm^2\,V^{-1}\,s^{-1}$ and sheet resistance around 10^{-2} Ω. For high p_{O_2}, the carrier density is reduced significantly to values around $10^{13} - 10^{14}$ cm^{-2}, in better agreement with the expectations of the polar catastrophe (at least, for low LAO thicknesses), and with the resistance increasing by a few orders of magnitude. Samples grown at low p_{O_2} have carrier densities around $10^{13} - 10^{14}$ cm^{-2} if annealed after growth, suggesting that the carriers found in the unannealed low p_{O_2} samples originates from vacancies. Finally, samples grown or annealed at high p_{O_2} remains insulating. The different regimes and the associated transport properties are shown in Figure 3.21, for samples with LAO thickness $\sim$20 nm.

These results question the validity of the Zener breakdown scenario, which cannot explain by itself the p_{O_2} dependence of the transport properties. Theoretical studies based on DFT [47, 117, 128] have considered the possibility of intrinsic doping from polarity induced oxygen vacancies at the LAO surface. However, the first studies [117, 128] were performed in the GGA, which is known to underestimate band gaps and to predict spuriously the properties of defects [129]. The last study [47] are based on a partial

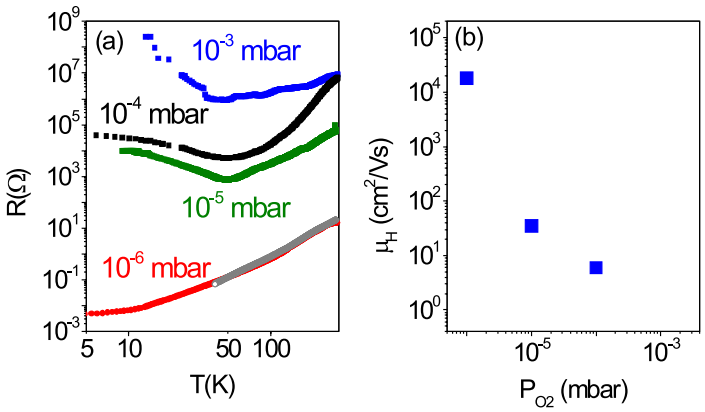

FIGURE 3.21: (a) Temperature dependence of the resistance of STO/LAO samples (with LAO thicknesses ∼20 nm) grown at different p_{O_2}; (b) carrier mobilities at 4 K for samples grown at different deposition p_{O_2}. Adapted from Reference [91]. The grey data in (a) is the resistance of the STO substrate after removing the LAO overlayer by mechanical polishing.

implementation of Hartree-Fock exchange (at fixed geometry, after relaxation using semi-local functionals), and goes beyond oxygen vacancies, considering other intrinsic defects. However, the study is limited to a single defects planar density. This warranted to study the STO(001)/LAO heterostructures including oxygen vacancies using the hybrid functional B1-WC, motivated by its performance to model the properties of the parent bulk compounds (notably, of reduced $SrTiO_{3-\delta}$) and its performance to predict the results expected of the Zener breakdown scenario.

We first investigated the effect of oxygen vacancies considering a uniform distribution of oxygen vacancies at different positions in an otherwise pristine STO(001)/LAO_m/vacuum heterostructure with a n-type interface, modelled through a symmetric slab as shown in Figure 3.1.(c) and (g)[7]. For a 2×2 supercell containing one V_O, the area density η is equal to 1/4□. We first analyze the electronic structure of the defective system STO(001)/LAO_4/vacuum with oxygen vacancies (η = 1/4□). Without any vacancies, this heterostructure is still predicted insulating within our formalism, just below the onset for Zener breakdown. It is therefore the ideal system to study different cases, based on the position of the vacancies. The layer-resolved density of state of such defective systems are given in Figures 3.22.(a-d), for vacancies located (a) in the TiO_2 layer at the interface; (b) in the middle of the LAO overlayer; (c) in the AlO_2 layer at the surface; (d) in the TiO_2 layer at the interface and in the AlO_2 layer at the surface.

It follows, based on these results:

- Oxygen vacancies in the TiO_2 layer at the interface are characterized by in-gap states slightly below the conduction band (up to ∼1 eV), with a main Ti $3d_{3z^2-r^2}$ character, which does not compensate the field in LAO as the donor electrons remain within the STO system.
- If the oxygen vacancies are within the LAO layer, the defect in-gap states (shown with black arrows in Figure 3.22) are always empty: they are always above the STO conduction band (∼1 eV), hence the electrons will always be transferred to the interface.

[7] The heterostructures consist in a vacuum/LAO_m/$STO_{7.5}$/LAO_m/vacuum symmetric film, expanded as 2×2 and 2×3 supercells

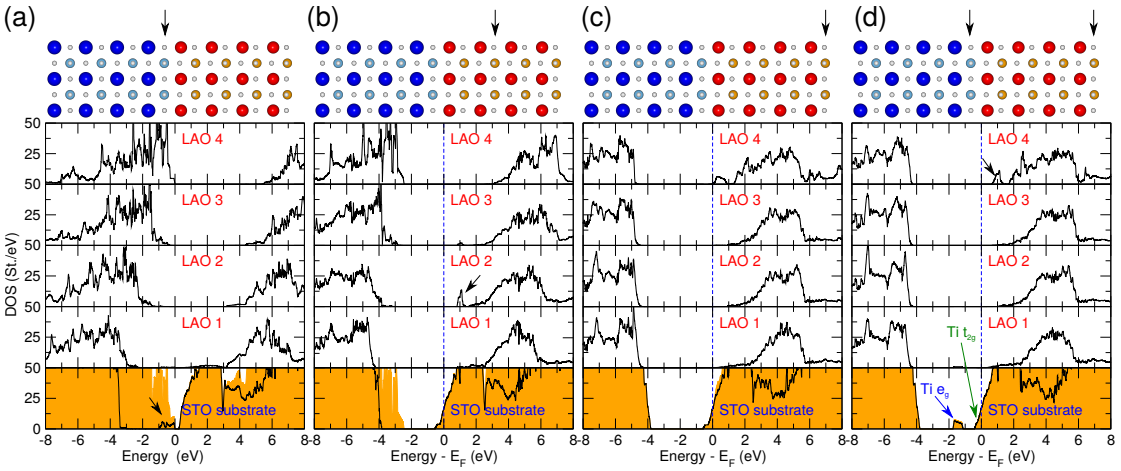

FIGURE 3.22: Layer-resolved density of state of STO(001)/LAO_4/vacuum heterostructures with V_O ($\eta = 1/4\square$) at different positions: (a) in the TiO_2 layer at the interface; (b) in the middle of the LAO overlayer; (c) in the AlO_2 layer at the surface; (d) in the TiO_2 layer at the interface and in the AlO_2 layer at the surface. The arrows indicate the positions of the V_O in the schematic representation of the heterostructures (top), and show the localized in-gap defect states in the densities of state.

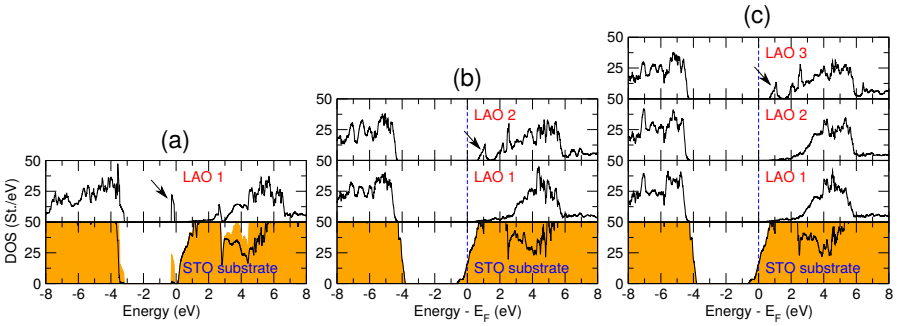

FIGURE 3.23: Layer-resolved density of state of STO(001)/LAO_m/vacuum heterostructures with V_O ($\eta = 1/4\square$) located in the AlO_2 layer at the surface.

- If the vacancies are at the LAO surface, the field is compensated over the whole LAO film. For vacancies buried within the LAO, the field will only be compensated between the interface the LAO plane containing the vacancy.
- The defect states being always empty if the vacancies are in the LAO layer, the V_O act as double donor. For $\eta = 1/4\square$, the vacancies at the LAO surface completely compensate the field in LAO, the electrostatic potential is completely flat.

The case where the vacancies are at the LAO surface is the most interesting case, since the carriers are transferred to the interface and they contribute the most to the screening of the built-in field. Figures 3.23.(a-c) show the layer-resolved density of state for STO(001)/LAO_m heterostructures with oxygen vacancies at the surface. For $m = 1$, the donor state is occupied, and below the conduction band of STO (hence, no charge transfer occur), for $m \geq 1$, the donor state are always above the conduction band, and charge transfer occurs. Hence, even in the absence of built-in field, it is always more favourable for the donor electrons to transfer to the interface rather then staying at the surface. More importantly, in contrast to the Zener breakdown scenario, oxygen vacancies at the LAO surface leaves no mobile holes.

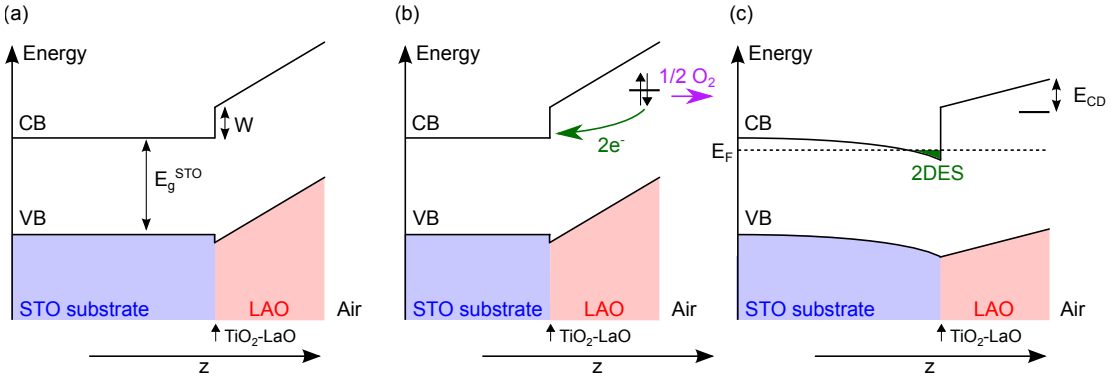

FIGURE 3.24: Schematic band diagram of the STO(001)/LAO interface along the transverse direction z: (a) the system below the critical thickness; (b) the creation of a double donor state through the formation of V_O at the surface. The donor electrons are transferred to the interface; (c) the charge transfer compensates the built-in field in LAO, depending on the charge density at the interface.

If we consider that each V_O at the LAO surface provide 2 electrons to the n-type interface, it is then interesting to know if the formation of these defects can be stabilized by the built-in electric field, and for which LAO thickness this stabilization occurs (it could occurs either before or after the threshold thickness for the Zener breakdown). The question has been addressed by Bristowe *et al.* [117, 130], who build a generic model to understand the role of surface V_O and how they may explain the experimental data where the Zener breakdown hypothesis fails. We therefore aim to exploit this model, where the parameters are set by our predictions from first-principles, and to compare the results with the polar catastrophe expectations. The model is shown as a schematic representation in Figure 3.24, and is valid as long as the defect state is above the conduction band of STO (for $m > 1$).

The model is set as follow: we consider the formation energy of a single V_O at the surface of the film, $E_f(\eta)$, in the presence of an area density η of surface V_O:

$$E_f(\eta) \quad = \quad C + E_\varepsilon(\eta) + \alpha\eta \tag{3.20}$$

where C is the energy cost of creating 1 V_O at the surface of LAO (in the absence of electric field), $E_\varepsilon(\eta)$ is the energy associated with the electric field in the polar layer, and the last term is a mean-field V_O-V_O interaction (beyond electrostatics). From Equation (3.20), we consider the surface excess energy Ω, accounting for the built-in electric field and the presence of an area density of η oxygen vacancies at the surface:

$$\begin{aligned} \Omega(\eta) \quad &= \quad \int_0^\eta E_f(\eta')\, d\eta' \\ \iff \Omega(\eta) \quad &= \quad C\eta + \Omega_{\varepsilon,\mathrm{LAO}}(\eta) + \frac{1}{2}\alpha\eta^2 \end{aligned} \tag{3.21}$$

where the term $\Omega_{\varepsilon,\mathrm{LAO}}(\eta)$ accounts for the gain of electrostatic energy subsequent to the charge transfer. The C term is a chemistry related term and depends on the energy cost of breaking bonds and on the overall chemical process, we also include within that term the electronic energy gain of the electron transfer from the defect state to the Ti t_{2g} states of STO, and depends on the defect state binding energy E_{CD} and the conduction

band offset W:

$$C = E^0_{f,\mu} - Z(W - E_{CD}) \tag{3.22}$$

where $E^0_{f,\mu}$ is the formation energy of one single V_O at the AlO_2 surface of LAO and the rest of the term are defined in Figure 3.24. The term $\Omega_{\varepsilon,\mathrm{LAO}}(\eta)$ takes the following analytical form:

$$\Omega_{\varepsilon,\mathrm{LAO}}(\eta) = \frac{d^{\mathrm{LAO}}}{2\varepsilon^{\mathrm{LAO}}}\left[(\sigma_c - \eta Ze)^2 - \sigma_c^2\right] \tag{3.23}$$

This term is basically the energy gain of discharging a capacitor, and depends explicitly on the amount of transferred donor electrons Z per V_O. The electron charge is designated by e. σ_c is the nominal charge, and corresponds to the charge density at the interface required to cancel the built-in field: $\sigma_c = 1/2\ e/\square$. The equilibrium density of V_O η_{eq} is the one minimizing $\Omega(\eta)$:

$$\begin{aligned} \left[\frac{\partial\Omega}{\partial\eta}\right]_{\eta=\eta_{eq}} &= 0 \\ \Longleftrightarrow \eta_{eq} &= \frac{d^{\mathrm{LAO}}\ Z\ e\ \sigma_c - C\ \varepsilon^{\mathrm{LAO}}}{\left[\frac{d^{\mathrm{LAO}}}{\varepsilon^{\mathrm{LAO}}}\right](Ze)^2\ \varepsilon^{\mathrm{LAO}} + \alpha\ \varepsilon^{\mathrm{LAO}}} \end{aligned} \tag{3.24}$$

The stabilization of V_O ($\eta_{eq} > 0$) occurs at a critical thickness d_c^{SR}:

$$d_c^{\mathrm{SR}} = \frac{C\ \varepsilon^{\mathrm{LAO}}}{Z\ e\ \sigma_c} \tag{3.25}$$

Above this critical thickness d_c^{SR}, and for large values of d^{LAO}, η_{eq} converges toward σ_c/Ze, toward a complete screening of the LAO electric field. In contrast to the Zener breakdown scenario, the critical thickness does not depend explicitly on the value of the band gap (Equation (3.16)). The model can be compared to first-principles results by comparing the DFT formation energies $E^0_{f,\mathrm{DFT}}$ and the model $\bar{E}_f$:

$$\begin{aligned} \bar{E}_f &= \frac{1}{\eta}\Omega(\eta) = \frac{1}{\eta}\int_0^\eta E_f\ d\eta' \\ &= C + \frac{1}{\eta}\Omega_{\varepsilon,\mathrm{LAO}}(\eta) + \frac{1}{2}\alpha\eta \end{aligned} \tag{3.26}$$

which is the energy difference between the system with a given density η of surface V_O and the pristine system ($\eta = 0$), per surface V_O, and is basically the quantity calculated from Equation (3.1). The parameters of the model are set in the following way: the chemical potential μ_O is set to -2 eV (see Appendix A for details), similar to the value used in Reference [47, 117]; for the V_O-V_O mean-field interaction, we do not find a significant difference in formation energy between oxygen vacancies at the surface of STO(001)/LAO_1 heterostructures at different densities η, hence we set $\alpha = 0$ eV Å^2. Given that the donor state is always above the conduction band minimum, we have $Z = 2$. Once these parameters set, the C and $\varepsilon_r^{\mathrm{LAO}}$ are calculated through a fitting procedure of the model on DFT formation energies, yielding $C = 5.3$ eV and $\varepsilon_r^{\mathrm{LAO}} = 22$ (slightly inferior to the value estimated from the Zener breakdown model). The comparison between the model and the DFT formation energies estimated from Equation 3.2 are given in Figure 3.25.(a), showing that the model is in satisfying agreement with our

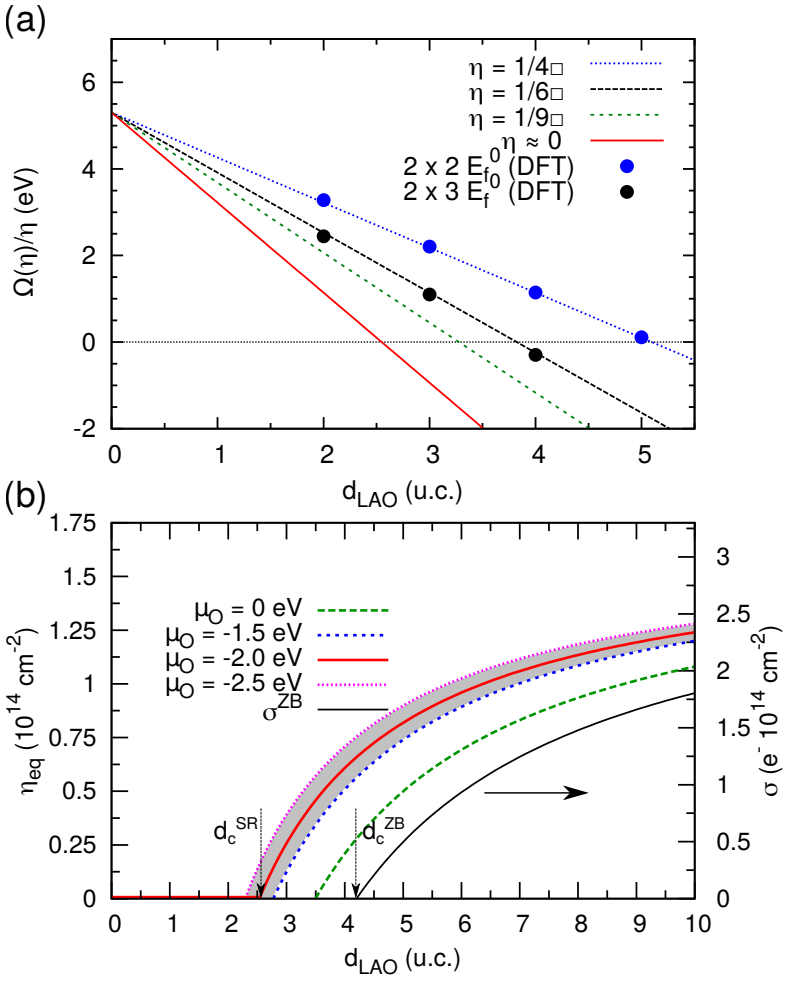

FIGURE 3.25: (a) Formation energies of V_O at the LAO surface versus LAO thickness d^{LAO} for different vacancy densities $\eta = 1/4\square$, $1/6\square$, $1/9\square$ and the limit toward $\eta = 0$, with parameters $\mu_O = -2$ eV (see Appendix A for the details), $\varepsilon_r^{LAO} = 22$, $C = 5.3$ eV and $\alpha = 0$ eV Å^2, the dots are the values calculated from DFT using a 2×2 (blue) and 2×3 (black) supercells in the slab geometry with two identical surfaces and one V_O per cell on each surface (Figure 3.1.(g)); (b) equilibrium density of V_O with respect to LAO thicknesses for different values of the chemical potential. On the right axis, the corresponding carrier density at the interface if all the transferred charges contribute to transport ($\sigma = Z\eta$), and the predicted carrier density calculated within the Zener breakdown model. The arrows show the threshold thicknesses predicted by the surface redox (d_c^{SR}) or the Zener breakdown (d_c^{ZB}) models.

calculations, despite the high density of V_O in the simulation cell, as the defective heterostructures are modelled through 2×2 and 2×3 supercells ($\eta^{DFT} = 1/4\square$ and $1/6\square$).

In the limit of low density, we predict that $\bar{E}_f = \Omega(\eta)/\eta$ becomes negative as early as $d^{LAO} = 2.5$ u.c., which corresponds to the onset for stabilization of surface V_O as shown in Figure 3.25.(b). The equilibrium density of surface V_O, η_{eq}, with respect to LAO thickness is given in Figure 3.25.(b): we also consider a range of 1 eV across μ_O to account for variations between the different growth conditions available in the literature, but this does not significantly alter the predicted threshold thickness. The effect of post-growth annealing is to shift μ_O toward 0 eV, hence we also consider this

case in Figure 3.25.(b): in this case, we only consider the enthalpic contribution to C at 0 K; the threshold thickness is shifted to 3.5 u.c.. In all cases, the model predicts the stabilization of surface V_O below the critical thickness for Zener breakdown:

$$d_c^{\mathrm{SR}} < d_c^{\mathrm{ZB}} \tag{3.27}$$

This means that the redox process is energetically more favourable than the creation of an electron-hole pairs across the LAO films in absence of a field: this occurs when $C < Ze\,\Delta$. Similarly to the Zener breakdown model, and for $\alpha \approx 0$, the surface redox model predicts a $1/d^{\mathrm{LAO}}$ thickness dependence for the carrier density at the interface above the threshold thickness, if all the transferred charges released by surface V_O contribute to transport.

3.7.3 Discussion

In the thick layer limit ($d^{\mathrm{LAO}} \to \infty$), the Zener breakdown and the surface redox model predicts the same properties in term of charge density at the n-type interface. In the surface redox model, the potential drop is given by:

$$V \;=\; (\sigma_c - \eta\, Z\, e)\frac{d^{\mathrm{LAO}}}{\varepsilon^{\mathrm{LAO}}} \tag{3.28}$$

As we have $\alpha \approx 0$, and substituting η_{eq} to η above the threshold thickness, the potential drop across the LAO film is roughly equal to C/Ze, essentially independent of LAO thickness, similarly to the Zener breakdown scenario. The potential drop is pinned as early as the V_O are stabilized at the surface. The reduction in rumpling (cation-anion displacements) as measured by surface x-ray diffraction [116] and the sudden drop of the c-axis expansion above the threshold thickness [29] (reaching the elastic limit as early as $m = 6$ u.c., as shown in Figure 3.14), is achieved quicker than predicted by the Zener breakdown alone, suggesting an earlier onset for charge transfer, in agreement with the surface redox scenario. Additionally, no holes have ever been found at the LAO surface. The surface redox model is in better agreement with this observation, given that the donor state are ∼1 eV away from the Fermi level (pinned near the bottom of the STO conduction band) in absence of field, as in the fully compensated regime shown in Figures 3.23(b-c). The p_{O_2} dependence of the sheet resistance also find an explanation.

There remains open questions about the 2DES at the interface: if the origin of the carrier are V_O, which arises for LAO thickness < 4 u.c., why are the samples with smaller LAO thickness insulating ? It has been suggested that charge localization occurs through the Anderson mechanism [102]. In-gap states with a Ti $3d$ character have also been observed, at higher binding energies [83, 120, 131, 132], around −1 eV below the Fermi level. This description also fit the binding energy of the electron stuck in a V_O inside the STO substrate. Another possibility is that the growth process induces acceptor defects, such as in cation intermixing, already observed in experiments [79, 116, 133–138] and predicted to induces acceptor-like in-gap states [47]. It has also been suggested [117] that such trapping states may be induced by the same donor V_O at the LAO surface: for low LAO thickness, surface V_O generate trapping potential with a deep character, which become more shallow and numerous with increasing LAO thickness, releasing the carriers which may contribute to transport. In all case, these hypotheses imply that the onset for conductivity is different then the onset for surface V_O stabilization and subsequent charge transfer, and occurs at larger LAO thickness then d_c^{SR}. It is worth mentioning that our

calculations involving V_O are still very close to pristine STO(001)/LAO_m heterostructures, with a perfect interface, and no defects within the STO and LAO subsystems. Accounting for possible intrinsic defects change the results expected from a pristine interface, as studied in the present chapter. The interfacial defects may be characterized as either deviations respecting the stoichiometry (inter-diffusion of atoms across the interface, such as Sr $\leftrightarrow$ La or Ti $\leftrightarrow$ Al), and off-stoichiometric defects. The former is known to alter slightly quantitatively the expectations of the electric-field driven mechanisms, by inducing a potential shift at the interface, but do not dope the interface [57], nor change the overall dielectric properties of the subsystems. The later however may impact significantly the properties of the interface. A more detailed discussion can be found in Reference [130]. Finally, for heterostructures grown with a metallic capping layer characterized by a high work function ϕ_M, x-ray photo-emission spectroscopy spectra [139] display signatures of metal oxidation, implying a chemical reaction between the LAO layer and the metallic capping layer. The degree of oxidation is also found to be correlated to the sheet carrier density. These results cannot be explained by the Zener breakdown alone, and are consistent with a redox process of the LAO surface: in this case, the oxygen atoms originating from the LAO remain trapped by the metallic layer, and the chemistry process and energetics will be different than that of the bare LAO surface process.

3.7.4 Tuning the polar discontinuity at oxide interfaces

As discussed earlier, it has been shown that the threshold thickness can be tuned by replacing the LAO overlayer by an alloy made of STO and LAO, $Sr_{1-x}La_xTi_{1-x}Al_xO_3$, referred to as LASTO:$x$ in Reference [26] where x is the compositional *ratio*. This observation can be rationalized within the electric field driven mechanisms. The rationale is that the formal polarization of the LASTO:x overlayer $P_{0\,\mathrm{LASTO}:x}^{0}$ can be changed continuously as:

$$P_0^{\mathrm{LASTO}:x} \;=\; x\, P_0^{\mathrm{LAO}} \tag{3.29}$$

if we assume a perfectively random alloying of both the A (Sr and La) and the B (Ti and Al) cations through the film so that x $(1-x)$ is the probability to find the La/Al (Sr/Ti) cations at a given A/B site, in a virtual crystal approximation approach. Hence, for a composition $x = 0.5$, then the formal polarization of the alloy is half the formal polarization of the pristine LAO overlayer.

If the band gap of the alloy remains larger than the band gap of STO, the band alignment remains similar to that of the STO(001)/LAO interface, and the dielectric properties of the polar layer close to that of LAO, the predicted threshold thickness for a Zener breakdown model becomes:

$$d_c^{\mathrm{ZB,LASTO}:x} \;=\; \frac{1}{x}\, d_c^{\mathrm{ZB,LAO}} \tag{3.30}$$

Therefore, for a composition $x = 0.5$, the threshold thickness is expected to be twice the threshold thickness expected for the STO(001)/LAO heterostructure. A schematic illustration of this situation is given in Figure 3.26, showing the electrostatic potential build-up with respect to composition.

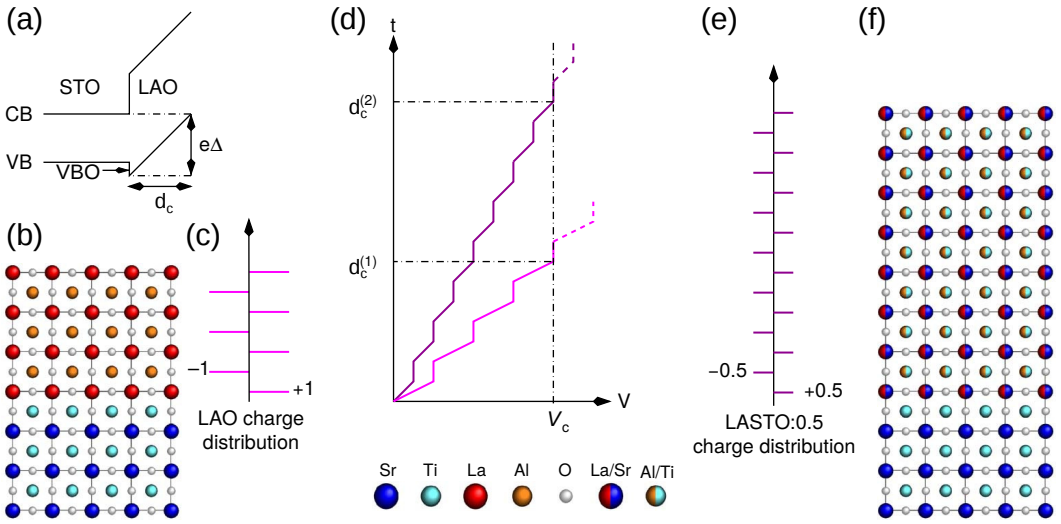

FIGURE 3.26: Electrical potential built-up at the interface between STO and LASTO:0.5: (a) the schematic band diagram of the standard STO(001)/LAO interface showing the band bending in the LAO layer, showing the potential build-up required for a Zener breakdown, (b) schematic STO(001)/LAO structure with (c) the LAO planar charge distribution. The schematic potential build-up as a function of the thickness is shown in (d) for LAO and the alloy LASTO:0.5, assuming the LAO and alloy have the same ε_r but different formal polarization. The threshold thickness for Zener breakdown $d_c^{(1)}$ and $d_c^{(2)}$ are given for LAO and LASTO:0.5 respectively. (e) the planar charge distribution for the LASTO:0.5 overlayer and (f) the schematic STO/LASTO:0.5 atomic structure. Figure adapted from [26].

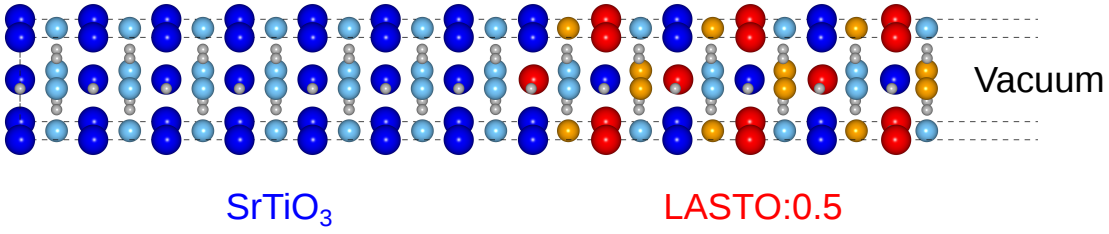

FIGURE 3.27: Geometry of the investigated system: the STO(001)/LASTO:0.5/vacuum system is modelled in a symmetric slab geometry, with a central off-stoichiometric STO layer and two LASTO:0.5 overlayers at each side of the slab, treated equivalently from the symmetry. The overlayer solid solution is modelled in a "checkerboard" configuration, alternating the cations along the transverse direction. Here the polar overlayer thickness is 6 u.c.

To investigate the specific case of LASTO:0.5, we performed calculations on heterostructures where the LAO overlayer is replaced by LASTO:0.5, with thicknesses $m = 1$ to 7 u.c.; the alloy is modelled as a homogeneous solid solution in a "chequerboard" configuration, as shown in Figure 3.27.

The layer-resolved density of state for overlayer thicknesses up to 7 u.c. is given in Figure 3.28.(a-g): in all cases, the interface remains insulating, and we observe a linear decrease of the band gap, in agreement within the Zener breakdown scenario.

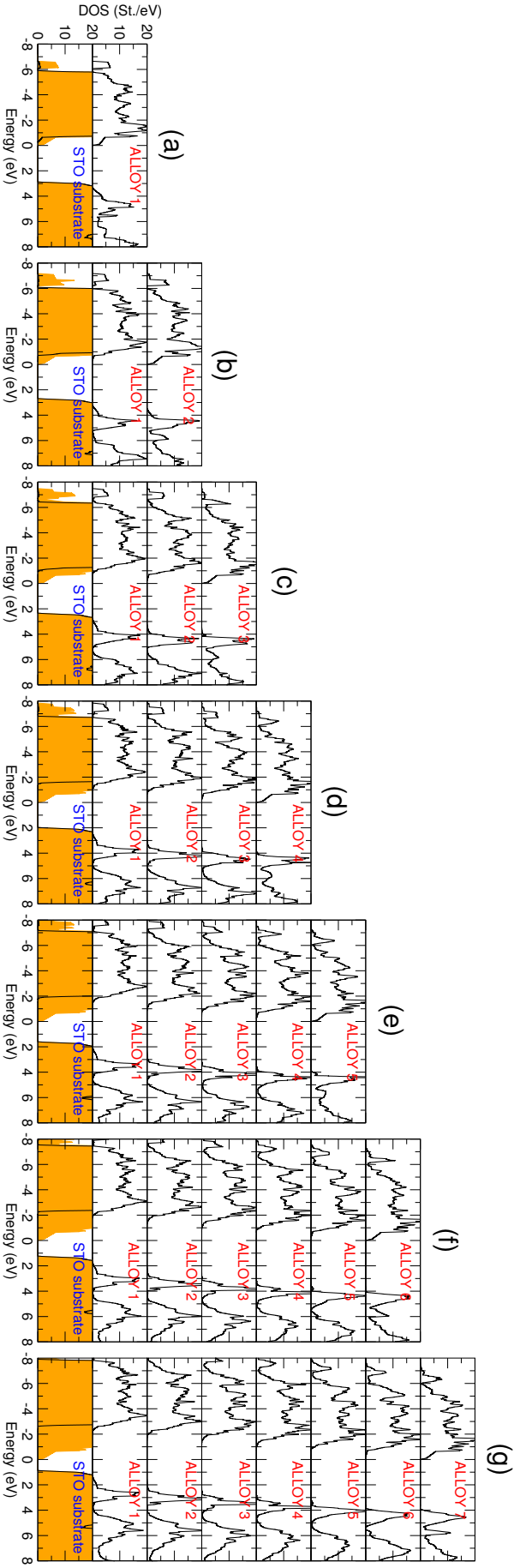

FIGURE 3.28: Layer-resolved density of state of STO(001)//(LASTO:x)$_m$/vacuum heterostructures, for varying overlayer thicknesses m (from $m = 0$ to $m = 7$ u.c.). The orange area is the total density of state.

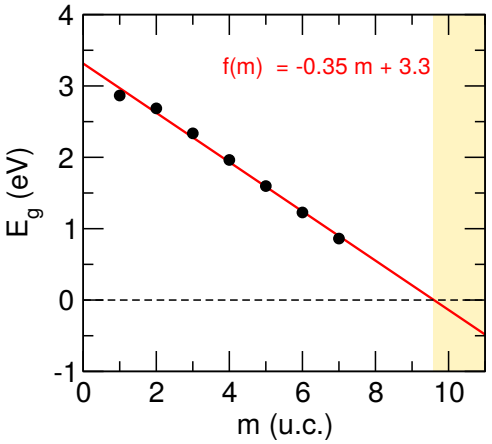

FIGURE 3.29: Electronic band gap for STO(001)/(LASTO:0.5)$_m$/vacuum heterostructures, for different thicknesses m (u.c.), calculated as the difference between the bottom Ti t_{2g} band and the top of the LAO O $2p$ band. The yellow area designate the thickness above which the interface is expected to be metallic as a result of a Zener breakdown.

Without performing an in-depth analysis as we did for the LAO case, by extrapolating the linear decrease of E_g (Figure 3.29), we estimate a critical thickness

$$d_c^{\mathrm{ZB,LASTO:}x} = 9.3 \text{ u.c.} \tag{3.31}$$

which is in agreement with the Zener breakdown model for $\varepsilon_r^{\mathrm{LASTO:0.5}} = 27$ (this value is confirmed by our hybrid functional *ab initio* calculation of the bulk solid solution dielectric constant in the same atomic configuration). This corresponds to a built-in field of 0.11 V/Å before the breakdown.

The tunability of the critical thickness rationalized with the Zener breakdown scenario is in good agreement with the DFT calculations. Nevertheless, looking at the actual experimental [26, 140] threshold thickness for $x = 0.5$ (Figure 3.11.(a)), the MIT occurs between $5-6$ u.c., thus the Zener breakdown model overestimates the critical thickness (in our DFT calculations, the structure with $m = 7$ u.c. is insulating, with a band gap of 0.86 eV), even when adjusting the potential drop to correct the overestimation of the STO band gap within the hybrid functional approach ($d_c^{\mathrm{ZB}} = 8.5$ u.c.) as we did for the $x = 1.00$ case. It is therefore warranted to see to which extent the surface redox model predicts a threshold thickness in better agreement with the experimental value.

Let us first consider the $x = 0.50$ composition case. If we *assume* that the chemical term C remains close to the value calculated for the LAO surface, the equilibrium density of surface V_O η_{eq} can be estimated for the alloy case by setting $\varepsilon_r^{\mathrm{LASTO:0.5}} = 27$ and $\sigma_c = xe/2\square = 0.25\ e/\square$. For simplicity, we keep $\alpha = 0$ as for the $x = 1.00$ composition. The results are displayed in Figure 3.30: we predict a threshold thickness between 6 and 7 u.c. of LASTO:0.5, closer to the experimental result. In addition, we can see that the predicted surface density of V_O is lower than for the bare LAO case: only a transfer of 0.25 $e^-/\square$ is required to completely screen the built-in field in the polar layer in this case. This value is however only reached in the infinitely thick limit.

For $x = 0.75$, we predict a threshold thickness between 4 and 5 u.c., also in better agreement with the experimental value compared to the Zener breakdown scenario (6.1 u.c.). The threshold thicknesses for each composition are shown in Figure 3.31, with respect to μ_O. Of course, all of these predictions are based on the hypothesis that C is the same

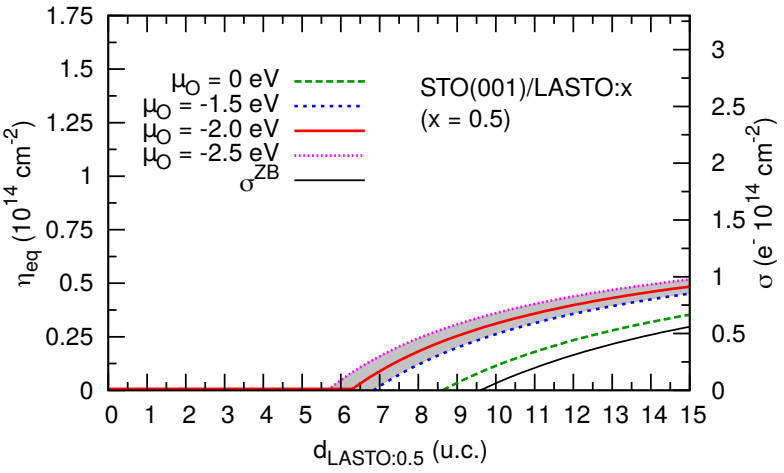

FIGURE 3.30: Equilibrium density of V_O at the surface of the LASTO:0.5 overlayer η_{eq} calculated within the surface redox model with parameters $C = 7.3$ eV $+ \mu_O$, $\varepsilon_r^{\text{LASTO:0.5}} = 27$, $\sigma_c = 0.25$ $e/\square$, $\alpha = 0$. On the right axis, the corresponding electron density at the interface, with the prediction from the Zener breakdown model σ^{ZB}.

in all cases, which remains to be proven; as the term is related to the chemistry of the surface, it is reasonable to expect some change.

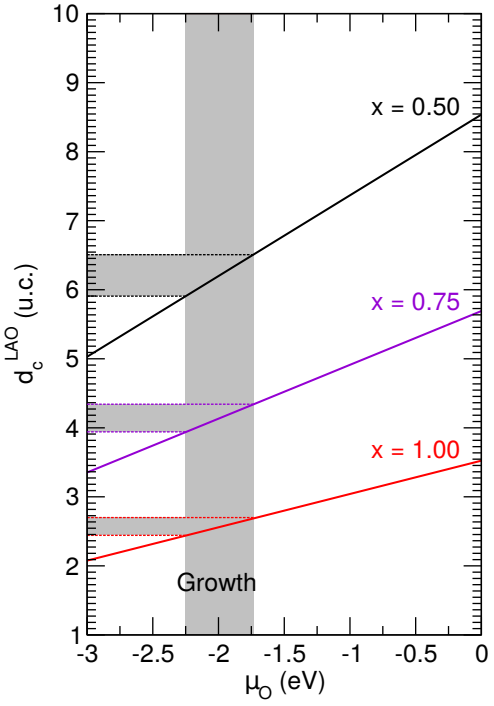

FIGURE 3.31: Polar layer threshold thickness of STO(001)/LASTO:x heterostructures as a function of oxygen chemical potential μ_O as predicted by the surface redox model $d_c^{\text{SR}} = C\varepsilon^{\text{LASTO:}x}/Ze\sigma_c$, estimated by fixing C to its value calculated for the $x = 1.00$ composition (pure LAO overlayer). The grey band indicates how μ_O scatter based on experimental setup for standard STO(001)/LAO growth (see Figure A.1, Appendix A).

3.8 Conclusions

In this Chapter, we have reviewed the properties of bulk $LaAlO_3$ and $SrTiO_3$ from hybrid functional based DFT, showing how the introduction of Hartree-Fock exchange through the B1-WC functional significantly improves the quantitative accuracy of DFT with respect to experimental results. We also introduced briefly the properties of the interface between these two oxides, as well the features of the emerging 2-dimensional electron system localized near the interface.

We have presented the two most popular hypotheses for the origin of the carriers at the interface, namely the Zener breakdown and the polarity-induced surface redox mechanisms. The key physical parameters of these two models are notably well described with the B1-WC, which motivates the review of these models from first-principles with this novel approach. We show and discuss how the predictions of these models and *ab initio* calculations compare with the experimental results. Our results point toward surface redox as the origin of the carriers near the interface: indeed, oxygen vacancies at the LAO surface are stabilized at a lower LAO film thickness than the onset for Zener breakdown; this is related to the lower energy cost to form oxygen vacancies at the LAO surface compared to the creation of an electron-hole pairs across the LAO film. This justifies how some properties expected from the electron reconstruction, such as a metallic LAO surface, are not witnessed in experiments. Of course, the models and the first-principles calculations only involve a pristine interface. This may explain the failed predictions of the models with respect to some features of the 2DES witnessed in experiments, such as the sheet carrier density, typically overestimated within the models (for large LAO film thickness). The introduction of acceptor trapping states in these models is therefore worth investigating.

Furthermore, we also discussed how the electric-field driven mechanisms may explain the experiments performed on STO(001)/LASTO:x heterostructures, and highlight how the surface redox model may be more appropriate to explain the measured threshold thicknesses with respect to the composition of the polar layer.

The relevance of the electric-field driven mechanisms is put to test by different experiments. Notably, on one hand, for the STO(001)/LASTO:x heterostructures, if all the carriers are provided by these mechanisms, then the doping of the interface is also determined by the composition x, and difference in properties may be expected. Chapter 4 will present the interplay between the carrier density at the interface and the confinement effect, by probing the superconducting phase of the 2DES. On the other hand, experiments performed on STO(001)/LAO_m/STO_n heterostructures, where the LAO film is covered by a STO capping layer, also present some interesting features, such as a decreased threshold thickness for conductivity, which is not expected from the electric-field driven mechanisms. This issue will be addressed in Chapter 5.

Chapter 4

Confinement and Electronic Structure at Polar Oxide Interfaces

In this Chapter, we explore the effect of confinement of the 2DES at polar oxide interfaces at the high carrier density limit. We will discuss how the carrier density at the interface may be tuned by changing the polarity of the polar overlayer, and how the associated effects on carrier confinement and superconducting phase properties evolves with respect to carrier density. The results presented have been published in Reference [141]. The author of this thesis provided the DFT results, whereas the co-authors of Reference [141] provided the experimental results and the Poisson-Schrödinger model.

We then study the effect of structural confinement on the 2DES system, by reducing the thickness of the STO substrate holding the carriers. This study is another collaboration with experimentalists [142], who performed spectroscopy measurements on bi-layered STO(001)/LAO_{12}/STO_m/LAO_4 heterostructures, for different STO interlayer thicknesses m. We rationalize the experimental results with first-principles calculations, assessing the effect of confinement on the properties of the 2DES in the STO interlayer in terms of orbital occupancy.

4.1 Probing Confinement and Electronic Structure at Polar Oxide Interfaces

One of the most elusive aspect of the 2DES at the STO(001)/LAO interface is that, in spite of numerous evidences toward an electric-field driven mechanism at the origin of the interfacial carriers, the probed sheet carrier density is always below the upper bound of sheet carrier density predicted from either the electronic reconstruction or the surface redox process ($n_s = 3.3 \times 10^{14}$ cm^{-2}). We have seen in the last part of the precedent Chapter that it is possible to tune the polarity of the overlayer by alloying the LAO film with STO: this is also expected to change the charge density at the interface. In this Section, combining state-of-the-art experimental and theoretical methods (namely, DFT and Poisson-Schrödinger modelling), we show how this change in interfacial density change the confinement effects at the STO/LAO interface. By probing

the superconducting phase thickness at low temperature of the 2DES at the STO/LAO and STO/LASTO:0.5 interfaces, we observe a change in confinement which can only be rationalized if the total charge expected from the electric-field driven mechanisms is transferred. In addition, we explore how to tune the carriers profile by reducing the thickness of the STO film hosting the 2DES.

4.1.1 Experiments

The investigated samples have been prepared as follows: before the deposition of the polar layer, Hall-bar patterns with crystalline TiO_2-terminated surface of (001) single-crystal STO substrate were defined using photo-lithography, followed by a subsequent amorphous STO deposition used as hard mask and lift-off process. The polar layers were then grown by PLD using standard growth conditions [143]: a KrF laser (248 nm) with a pulse energy of 40 mJ ($\approx$ 0.8 J cm^{-2}), repetition rate of 1 Hz; growth temperature of 800 °C, at oxygen partial pressure $p_{O_2} = 10^{-4}$ mbar. The samples were cooled after growth to 540 °C at $p_{O_2} = 200$ mbar and maintained at this temperature and pressure for one hour before being cooled down to room temperature at the same atmosphere. The growth rate was ∼55 laser pulses per monolayer. The deposition was fully monitored by RHEED and specular spot intensity oscillations indicated a layer-by-layer growth. Rutherford backscattering spectroscopy (RBS) analysis revealed a film stoichiometry in agreement, within experimental uncertainties (1.5%) with the nominal concentration of $x = 0.5$ for a 40 nm thick film.

The experiments on the samples were performed in the following way: aluminium wires were ultrasonically bonded to the sample. Gold pad was deposited by sputtering on the backside of the sample as back-gate electrode. A direct current bias was applied across the STO substrate between back gate and the conducting interface. Superconductivity measurements were performed in a ^{3}He/^{4}He dilution refrigerator (Leiden Cryogenics) with a base temperature of 50 mK and a superconducting magnet allowing field up to 15 T to be reached. Samples were attached to a rotator head for anisotropic magnetic field measurements. Precise parallel and perpendicular orientations with respect to the magnetic field were determined using both longitudinal resistance R_{xx} and Hall resistance R_{xy}. In the parallel direction, an off-axis angle is estimated to be smaller than 0.02° from the R_{xy} signal. Current was applied to the conducting channel from a Keithley 6220 high precision current source. Voltages were recorded using Keithley 2182 nanovolt meters.

Figure 4.1.(a) shows a schematic of the atomic structure of the interface between STO and LASTO:0.5: in the thick LASTO:0.5 limit, a charge density of 0.25 $e^-\square$ ($\approx$1.7 $\times 10^{14}$ cm^2) is expected to be present at the interface to avoid a polar catastrophe (see Chapter 3). The oscillations of the RHEED intensity provide a measure of the thickness of the layer during the PLD growth, as shown in Figure 4.1.(c) for a 10 u.c. thick overlayer. Topographic scan using atomic forces microscopy (AFM) shows a sharp step-and-terrace structure on the film surface with a single unit-step heigh in the inset of Figure 4.1.(c). Both the RHEED and AFM data indicate a high growth quality of the overlayer. In order to analyse the quality of the interface, by probing the intermixing strength and the sharpness of the STO/LASTO:0.5 interface, a detailed scanning transmission electron microscopy (STEM) study is required. Hall bars were defined using a pre-patterning technique for transport measurements [144] (Figure 4.1.(b)); a gate

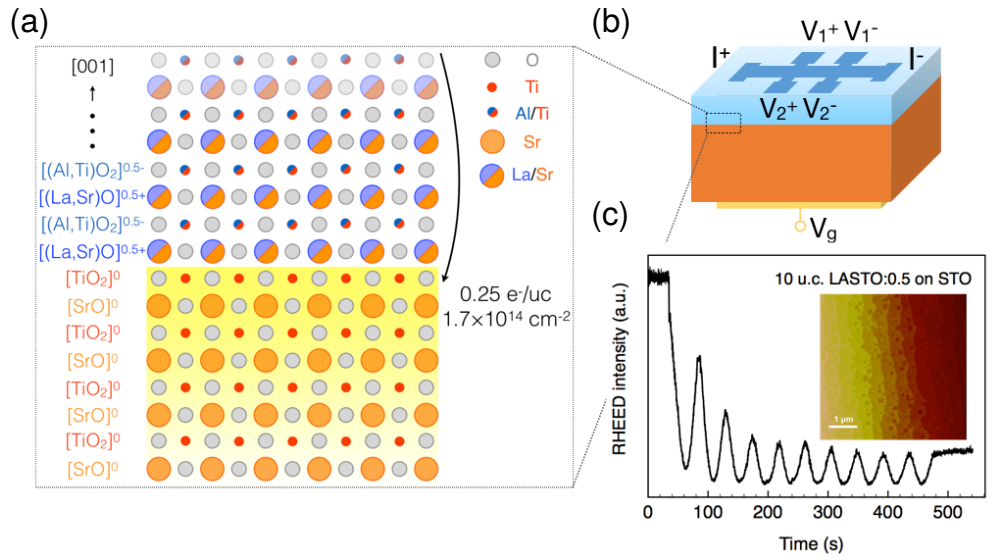

FIGURE 4.1: (a) Illustration of the interfacial structure with atomic arrangement and charges per atomic plane. Electrons with a surface density of 0.25 $e^-/\square$ are expected to be transferred to the interface according to polarity-driven mechanisms. (b) A sketch of the STO/LASTO:0.5 field-effect device (5×5 mm^2) with the back-gate electrode used to apply the gate bias (V_g) facing the 500 μm wide Hall bar. (c) Oscillation of *in situ* RHEED intensity during the growth of a 10 u.c. thick LASTO:0.5 overlayer and (inset) its surface topography acquired by atomic force microscopy (AFM), revealing the step-and-terrace morphology.

electrode deposited at the backside of the substrate is used to tune the properties of the 2DES.

4.1.2 Theoretical study

The technical details for the DFT calculations have been given in Chapter 3. The geometry of the investigated systems consists in off-stoichiometric $(\mathrm{STO})_m/(\mathrm{LAO})_{2.5}$ and $(\mathrm{STO})_m/(\mathrm{LASTO{:}0.5})_{2.5}$ superlattices. Two examples are given in Figure 4.2 for $m = 12.5$: the off-stoichiometry ensures a charge transfer of 0.5 $e^-/\square$ and 0.25 $e^-/\square$ respectively to the n-type interface. The inversion symmetry forces an equal treatment of the two interfaces at the DFT level, hence in the present Chapter, we will only show the results for half a superlattice. Moreover, to simplify the notations, we will neglect the additional layers in the name of the superlattice, so that $m = 12.5 \rightarrow 12$ u.c., for example[1]. To better investigate the confinement effect of the 2DES in STO, we set $m = 30$ u.c., corresponding to a large unit cell with 330 atoms. The thickness of the STO sublattice is about 12 nm thick, with the superlattice approach, we therefore probe about 6 nm. As we will show in the following, the 2DES in term of 3-dimensional electron density actually extends up to tens nanometres. The DFT approach present a significant limitation in terms of size. The effective masses associated to the different Ti t_{2g} bands have been calculated from the band structure. Each t_{2g} band has two light effective masses associated to light carriers and one heavy effective mass associated to the heavy carriers: for Ti d_{xy}, $m^*_{xx} = m^*_{yy} = m^*_L$ and $m^*_{zz} = m^*_H$. The rest can be deduced from

[1]This convention is the same as the one used in the original manuscripts [141, 142].

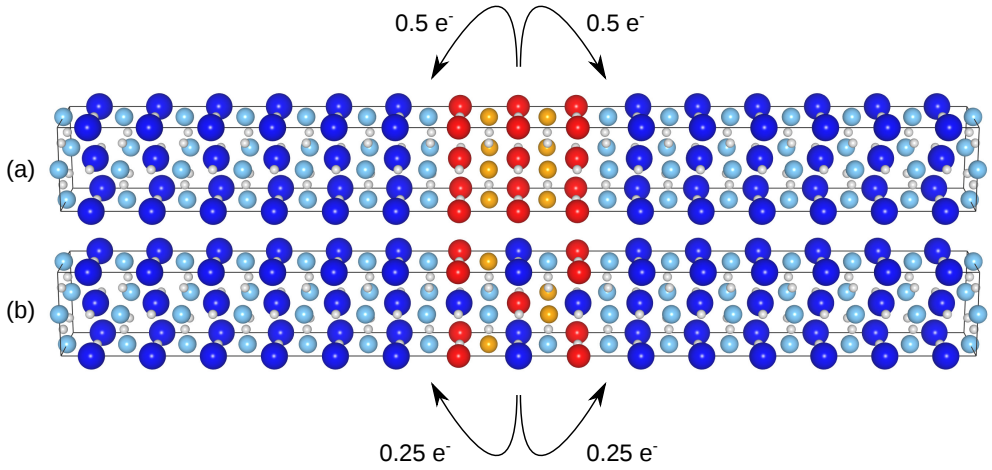

FIGURE 4.2: Structure of (a) a $(STO)_{12}/(LAO)_2$ and (b)$(STO)_{12}/(LASTO{:}0.5)_2$ off-stoichiometric superlattices, with the additional TiO_2 and LaO planes. The symmetry plane is shown by the green dashed line. The off-stoichiometry of the LAO (LASTO:0.5) interlayer ensures that 0.5 (0.25) electrons is transferred to each adjacent TiO_2 plane, mimicking a fully-compensated n-type interface.

the symmetry. For both superlattices, we have $m_L^* = 0.4\ m_e$ and $m_H^* = 5.9\ m_e$ (very close to the calculated value for cubic STO: $m_L^* = 0.4\ m_e$ and $m_H^* = 6.1\ m_e$).

The limit in size in the DFT approach warrants a theoretical modelling without the aforementioned restriction. Poisson-Schrödinger modelling is a popular approach in the field of semiconductor heterostructures, and consists in solving self-consistently the Poisson equation and the Schrödinger equation for free-like carrier in specific dielectric environment [145]. Using parameters calculated from DFT, the Poisson-Schrödinger calculations provides the confinement, energy levels and charges distribution for both kind of interfaces. The model [143] is built in the following way: the band mass and envelope function approximations are used. A triangular potential well $V(z)$, corresponding to a constant electric field in the STO system, is taken as a starting point. The energy levels E_α^n for each band α in the well can be calculated using the following Equations:

$$-\frac{\hbar^2}{2m_z^{*,\alpha}}\frac{\partial^2\xi_n^\alpha(z)}{\partial z^2} + eV(z)\xi_n^\alpha(z) + E_0^\alpha\xi_n^\alpha(z) = \epsilon_n^\alpha\xi_n^\alpha(z) \tag{4.1}$$

$$E_n^\alpha(\mathbf{k}_{||}) = \frac{\hbar^2k_x^2}{2m_x^{*,\alpha}} + \frac{\hbar^2k_y^2}{2m_y^{*,\alpha}} + \epsilon_n^\alpha \tag{4.2}$$

Equation (4.1) is the Schrödinger equation. In the above Equations, $m_i^{*,\alpha}$ are the band mass for the band α along the i direction, ξ_n^α are the amplitude of the envelope function, ϵ_n^α are the solution of the Schrödinger equation (4.1), E_0^α is the energy minimum of the band α, and E_n^α are the energy level of different sub-bands. The Fermi energy E_F can be determined by the following Equation, setting the total sheet carrier density equal to n_{2D} for the different cases[2]:

$$n_{2D} = \sum_{n,\alpha}\Theta(E_F - \epsilon_n^\alpha)\frac{1}{\pi\hbar^2}\sqrt{m_x^{*,\alpha}m_y^{*,\alpha}}\,(E_F - \epsilon_n^\alpha) \tag{4.3}$$

[2] $n_{2D} = 0.5\ e^-/\square$ for STO/LAO and $n_{2D} = 0.25\ e^-/\square$ for LASTO:0.5, assuming a complete screening of the built-in field in the polar layer in the thick limit

where Θ is the Heaviside function. The 3-dimensional density is calculated as:

$$\rho_{3D}(z) = e\sum_{n,\alpha}\Theta(E_F-\epsilon_n^\alpha)\frac{1}{\pi\hbar^2}\sqrt{m_x^{*,\alpha}m_y^{*,\alpha}}\,(E_F-\epsilon_n^\alpha)\,\xi_n^\alpha(z)^2 \tag{4.4}$$

and is then used in the Poisson equation to compute a new potential well corresponding to the charge distribution profile:

$$-\frac{\partial}{\partial z}\left(\varepsilon_0\varepsilon_r(E)\frac{\partial V(z)}{\partial z}\right)=\rho_{3D}(z) \tag{4.5}$$

The resulting potential well $V(z)$ is then re-injected in Equation (4.1). These operations are iterated multiple times until a defined convergence criterion δ_V^c is satisfied, based on the relative change in potential between two iterations (more details can be found in Reference [146]). Note that in Equation (4.5), the relative dielectric constant $\varepsilon_r(E)$ is electric-field dependent, based on its observed behaviour with respect of an electric field. The electric-field dependence of the dielectric constant of STO is also temperature dependent: we therefore identify two regimes, a high temperature regime and a low temperature regime, which are both displayed in Figure 4.3. The general form $\varepsilon_r^{\mathrm{STO}}(E)$ in both regimes is:

$$\varepsilon_r^{\mathrm{STO}}(E) = 1+\frac{B}{\left[1+\left(\frac{E}{E_0}\right)^2\right]^{1/3}} \tag{4.6}$$

where $B=250$, $E_0=10^7$ V m^{-1} for the room temperature regime, and $B=25\,462$, $E_0=82\,213$ V m^{-1} for the low temperature regime respectively. The room temperature regime is set so that at low field, $\varepsilon_r^{\mathrm{STO}}(E)$ takes the value calculated in DFT. This will allow us to compare the two methods, and to see if the simple Poisson-Schrödinger model can reproduce the DFT results. On the other hand, the dielectric constant being a parameter in the Poisson-Schrödinger model, we can probe the effect of its divergence at low field and low temperature on the confinement of the 2DES, which should be representative of the superconducting phase (and impossible to do in DFT).

4.1.3 Results

We shall first present the experimental results. Transport measurement performed at low temperature shows the appearance of a superconducting ground state below a critical temperature $T_c\approx 200$ mK, generally lower than that of the standard STO/LAO interface [107]. In Figure 4.4.(b), the critical magnetic field $H^*(T)$ for perpendicular and parallel orientation of a STO/LASTO:0.5 interface in its virgin state are shown with respect to temperature. The critical temperature for each magnetic field was defined as the temperature at which the sheet resistance R_s reaches half the normal state value ($\sim$500 mK). The in-plane coherence length $\xi_\parallel(T)$ is calculated from the Ginzburg-Landau formula using the perpendicular field $H_\perp^*(T)$ (Equation (4.7)):

$$\xi_\parallel(T) = \sqrt{\frac{\Phi_0}{2\pi\mu_0 H_\perp^*(T)}} \tag{4.7}$$

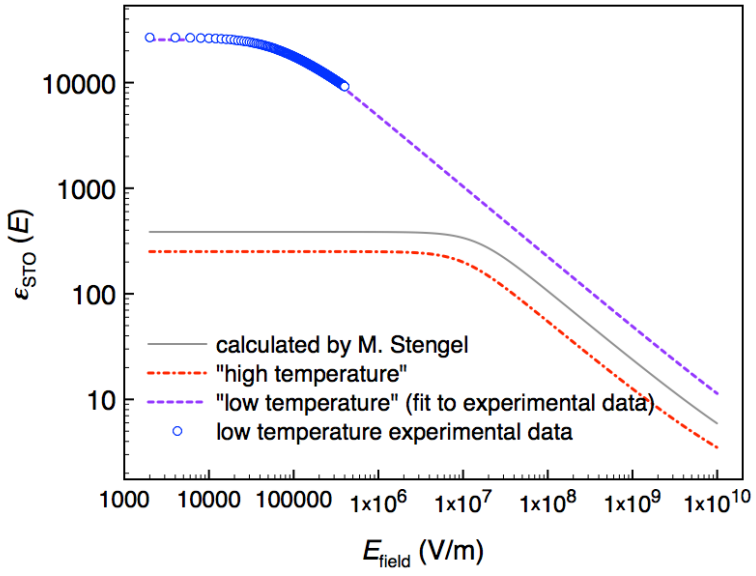

FIGURE 4.3: Field dependence of the relative dielectric constant of STO, $\varepsilon_r^{\mathrm{STO}}(E)$, which is used in the Poisson-Schrödinger calculation. Grey line: the calculation by Stengel [104]; red dot-dashed line: calculated data following the behaviour calculated in Reference [104], but with a fixed low field $\varepsilon_r^{\mathrm{STO}}(E = 0) = 250$, which is obtained by the DFT calculation with the B1-WC functional; blue open circles: experimental data measured at 4 K; purple dashed line: fitting to low temperature experimental data using Equation (4.6).

Using the measured perpendicular field $H_{\perp}^{*}(T)$ and extrapolating for $T = 0$ K, a value of ∼55 nm is estimated, similar to the one observed for standard STO/LAO interface [147]. For the parallel critical field $H_{\parallel}^{*}(T)$, its temperature dependence follows the 2-dimensional behaviour of a superconducting thin film [148]:

$$H_{\parallel}^{*}(T) \quad \propto \quad \sqrt{1 - \frac{T}{T_c(H = 0}} \tag{4.8}$$

Then, it is possible to calculate the thickness of a 2-dimensional superconductor from the following Equation:

$$d_{SC} \quad = \quad \frac{\sqrt{3}\Phi_0}{\pi\xi_{\parallel}(T)\mu_0 H_{\parallel}^{*}(T)} \tag{4.9}$$

For the STO/LASTO:0.5 interface, we obtain $d_{\mathrm{SC}} \approx 24$ nm, independent of the temperature, and a value which is about twice larger than the one obtained for the standard STO/LAO interface [94, 96, 147]. It should be said that the thickness obtained from this analysis is a characteristic thickness which agrees well with the out-of-plane spread of the 2DES in the standard STO/LAO interface, determined from other methods [94, 96].

Exploiting the field effect, the carrier density at the interface can be tuned with the gate voltage, changing the superconducting properties of the interface. Figure 4.4.(a) shows the modulation of the superconducting transitions with respect to the applied gate voltage V_g (from −400 V to +325 V). T_c is found to be effectively tuned; however for the largest negative voltage (with the strongest depletion regime), the system remain metallic and superconducting, in contrast to what is observed for the standard

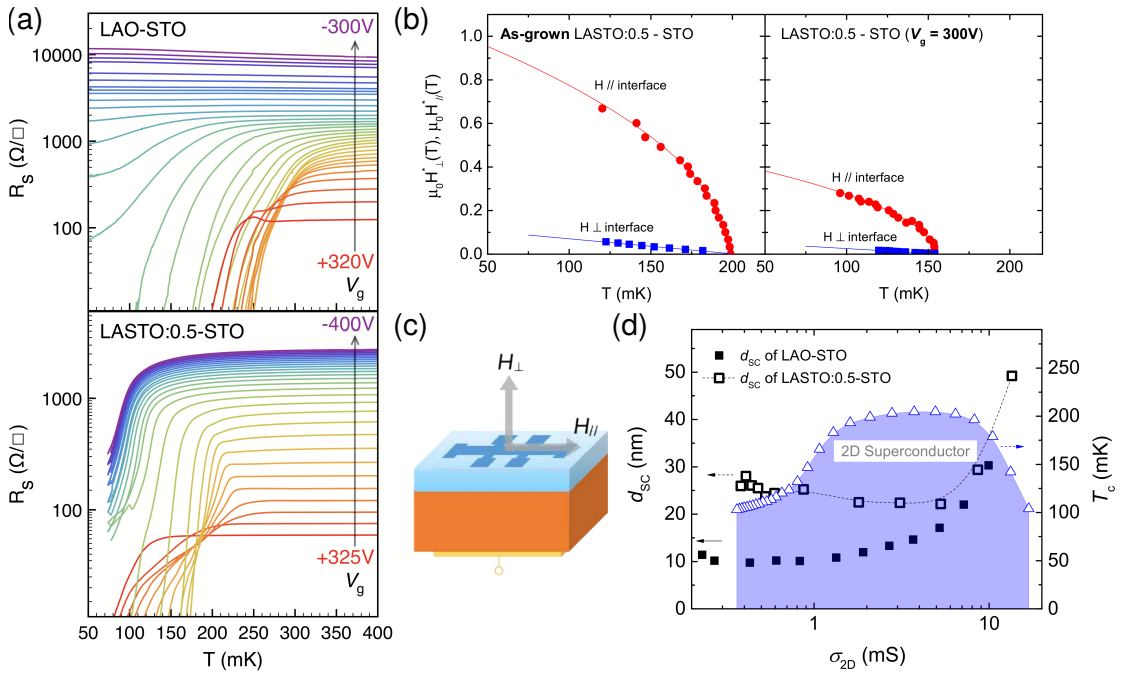

FIGURE 4.4: (a) Field-effect modulation of sheet resistance R_s as a function of temperature on a semi-logarithmic scale of the STO/LAO interface (top) and STO/LASTO:0.5 interface (bottom). For STO/LASTO:0.5, the gate voltage varies from -400 to +325 V in steps of 25 V. (b) Perpendicular (dots) and parallel (squares) critical fields ($H^*_\perp$,$H^*_\parallel$) as a function of temperature T for the as-grown state (left panel) ans for a state with $V_g = 300$ V (right panel) for STO/LASTO:0.5. The solid line for $H^*_\parallel$ is a fit to the data using the Ginzburg-Landau formula for a 2-dimensional film (Equation (4.7)), the line for $H^*_\perp$ is a guide to the eye. (c) Configurations for the measurements of superconducting critical fields applied perpendicular and parallel to the interface plane. (d) Phase diagram of the STO/LASTO:0.5 interface, showing in blue the superconducting state, plotted as a function of the normal-state sheet conductance. The superconducting layer thickness d_{SC} (left axis, black open square) is compared to that of the standard STO/LAO interface [149] (left axis, black solid squares). The black dotted line is a guide to the eye.

STO/LAO interface (top panel of Figure 4.4.(a)). As we will see in the following, the presence of superconductivity and high conduction at the highest depletion regime can be attributed to the occupancy of the $d_{xz/yz}$-symmetry states at the STO/LASTO:0.5 interface. The evolution of T_c *versus* σ_{2D} (sheet-conductance in the normal state) is shown in Figure 4.4.(d), and displays a dome-like shape, reaching a maximum of 206 mK. For different values of V_g, the parallel and perpendicular critical magnetic fields were measured; data for $V_g = 300$ V is shown in the right panel of Figure 4.4.(b), and with these measurements, it is possible to estimate the superconducting layer thickness d_{SC} across the phase diagram. The results are displayed in Figure 4.4.(d), where we compare the d_{SC} values for the STO/LASTO:0.5 and STO/LAO samples. We observe that the superconducting thicknesses for the STO/LASTO:0.5 samples are larger than the ones measured for the STO/LAO samples over the whole phase diagram: for the alloyed samples, d_{SC} falls in the range of 20-30 nm for a wide interval of σ_{2D}, while it remains in the range of 10-15 nm for the STO/LAO interface. Assuming that this superconducting thickness mirrors an effective width of the confining potential, we attribute this enhancement to the difference in transferred charge through a modified polar discontinuity.

To support this idea, we model the quantum confinement at these oxide interfaces using first-principles calculations and Poisson-Schrödinger model. Previous DFT studies on STO/LAO interfaces [27, 28, 118, 150–153] have investigated the fully-compensated interface through symmetric superlattices, with two n-type interfaces ($n_{2D} = 3.3 \times 10^{14}$ cm^{-3}). Lower carrier densities have been reached by artificially removing some charges at the interface and compensating with a positive charged background [27, 28]. In our study, the interfacial charge is directly modified by explicitly tuning the polar discontinuity, by switching LAO to LASTO:0.5 solid solution. The results of our theoretical calculations are given in Figure 4.5. The STO/LASTO:0.5 interface system is sketched in Figure 4.5.(a). The 3-dimensional charge profile n_{3D} as computed from DFT are shown in Figure 4.5.(b). The vertical dashed-dotted line indicates the extension of the supercell. Performing calculations for lower STO thicknesses, we have noticed that the charge profile extends further into the substrate as the supercell width is increased, but this occurs on a logarithmic charge density scale. Looking at the plot, we see that most carriers are located in the first unit cells in both cases; but moving away from the interface, a crossing between the two profile occurs (at $z \approx 3.5$ nm). For the lower carrier density regime, the charge is more spread into the STO substrate away from the interface, whereas for the higher density case, it is more localized close to the interface. Note that in the case of DFT calculations, the charge profile are determined from the self-consistent DFT dielectric constant, calculated as $\varepsilon_r^{STO} = 250$ in zero field, which reflects the room-temperature value.

To access the low temperature case which is experimentally measured, we need to overcome the limitations of the DFT approach: i) the STO size limit and ii) the low temperature diverging value of the dielectric constant ε_r^{STO}, not captured in the DFT simulations. To bypass these limitations, a self-consistent Poisson-Schrödinger model is employed, where the main parameters are obtained from DFT. The field-dependence of the dielectric constant is adjusted according to measurement in two temperature regimes, as discussed in Section 4.1.2. The resulting profiles for the room-temperature configuration ($\varepsilon_r^{STO}(E = 0) = 250$) is first compared with the DFT data in Figure 4.5.(b): the two approaches provide similar charge density profile, specifically close to the interface, therefore validating Poisson-Schrödinger approach with respect to the DFT calculations; it further highlights that while the supercell in the DFT calculation is rather large, it remains too small to properly describe the tail of the carrier density profile, better accessible from the Poisson-Schrödinger approach. From the latter approach, we determine that for both surface carrier densities, the spatial extension at the 3-dimensional density threshold for the occurrence of superconductivity ($n_{3D,th} \approx 4 \times 10^{18}$ cm^{-3} [154], shown as a horizontal dotted line in Figures 4.5.(a) and (b)) is roughly 10 nm. In the literature, the thicknesses of the 2DES estimated by different techniques differ a lot, from a few unit cells to 10 nm [85, 93, 94, 140]; it may be due to the large decaying nature of the carrier density, decreasing by a factor of 10 in 5 nm. Particularly, the tail of this distribution may fall below the sensitivity of some of the techniques used to probe the 2DES thickness.

At low temperature, STO behave as a quantum paraelectric and its dielectric constant increases by several orders of magnitude at zero-field. The field-dependent dielectric constant in the low-temperature regime is modelled through Equation 4.6. Using this low-temperature $\varepsilon_r^{STO}(E)$, we compute the charge density profiles from the Poisson-Schrödinger approach for the two interfaces, shown in Figure 4.5.(c). The main effect of the large ε_r^{STO} is to open the confining potential for the STO/LASTO:0.5 interface,

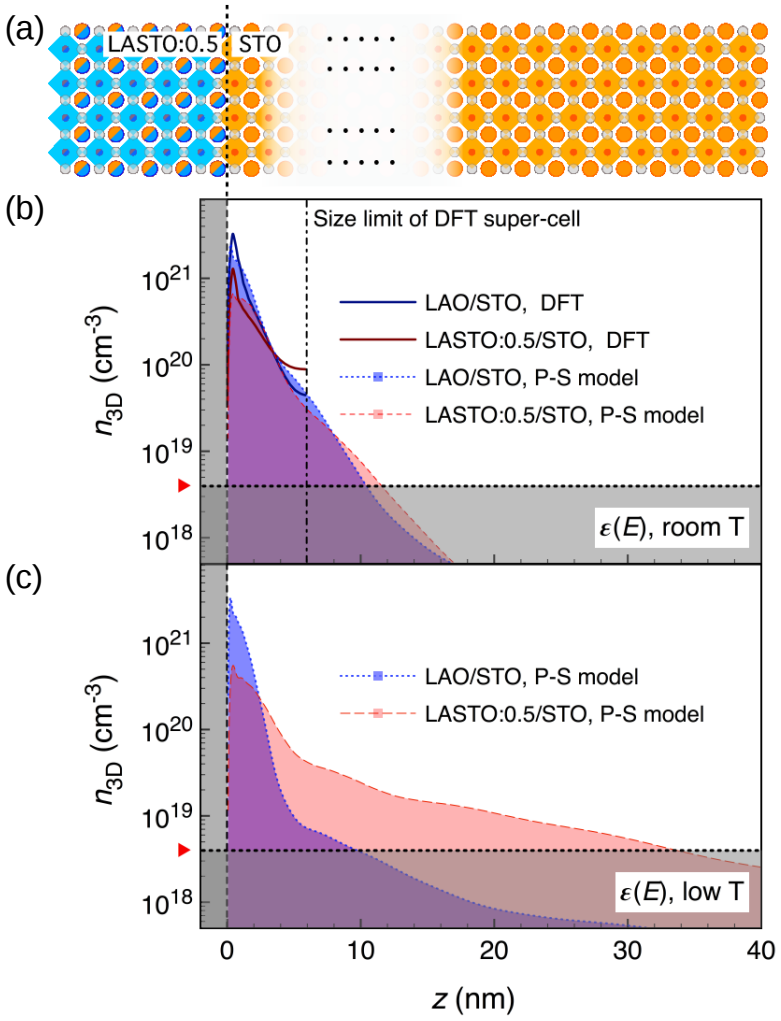

FIGURE 4.5: (a) Schematic of atomic structure of the LASTO:0.5/STO interface. (b) Results from the DFT calculations (solid lines) and the Poisson-Schrödinger model (dotted/dashed lines) for a room-temperature field dependent STO dielectric constant. (c) Charge profile estimated with the Poisson-Schrödinger model using the low-temperature STO dielectric constant. The black dashed line indicates the interface. The dash-dotted line corresponds to the size limit of the DFT supercell. Dotted lines and the red triangles indicate the 3-dimensional density threshold ($n_{3D,th} \approx 4 \times 10^{18}$ cm^{-3}) for the occurrence of superconductivity in STO.

leading to a spread of the charge density in the STO substrate, further from the interface. At the $n_{3D,th}$ (shown as the vertical dotted line in Figure 4.5.(c), the extension of the 2DES is roughly 10 nm for the standard STO/LAO interface, in agreement with the estimation of the superconducting thickness extracted from the critical field measurements discussed previously. The extension of the 2DES for the STO/LASTO:0.5 interface extends up to 32 nm, in agreement with the increase in superconducting thickness measured for this case. We argue that this change in superconducting thickness and confinement scale actually stems from a modified polar discontinuity. The modelling also highlights the effect of the dielectric of the substrate and the total 2-dimensional carrier density on the confinement of the charge, in agreement with a recent tight-binding study [155], and consistent with the argument of Stengel who argue that the energetic cost of moving the electrons away from the interface scale inversely with the dielectric

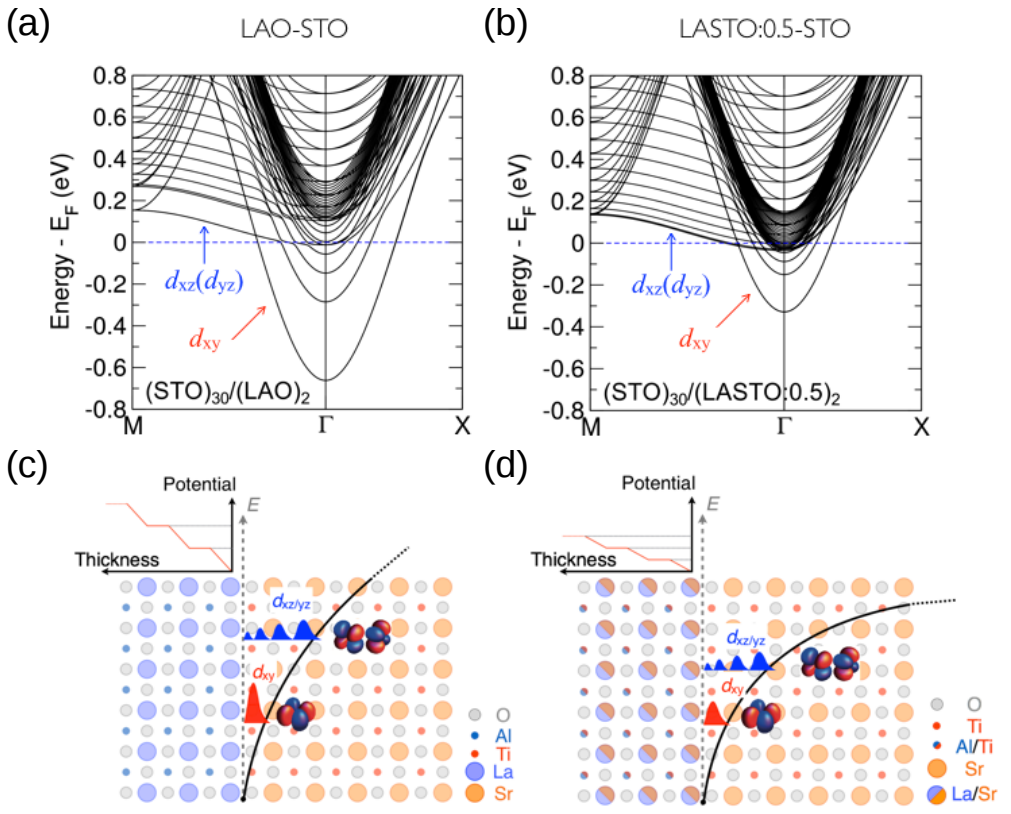

FIGURE 4.6: On the top, band structures of (a) the $(STO)_{30}/(LAO)_2$ and (b) $(STO)_{30}/(LASTO{:}0.5)_2$ superlattices, calculated from DFT. The Ti t_{2g} bands are labelled according to their symmetry (d_{xy}, $d_{xz,yz}$). On the bottom, schematics of the atomic arrangements, built-in electric potential (red lines), quantum confinement potential (black lines) and d_{xy}-$d_{xz,yz}$ band splittings of (c) the STO/LAO and (d) STO/LASTO:0.5 interfaces. For a larger extension of the 2DES, the band splitting is reduced.

constant of the STO substrate [104]. In addition, we can see that, in the low temperature regime, the Poisson-Schrödinger modelling gives a lower integrated charge density for $n_{3D}(z) > n_{3D,th}$ (blue area in Figure 4.5.(c) as compared to the one in Figure 4.5.(b)): this is also related to the remarkable behaviour of ε_r^{STO} with respect to temperature and electric field: a sizeable portion of the charge spreads further into the substrate, away from the interface, but with a density below $n_{3D,th}$.

The effect of the surface carrier density and the quantum confinement on the electronic band structures calculated from DFT for the two superlattices $(STO)_{30}/(LAO)_2$ and $(STO)_{30}/(LASTO{:}0.5)_2$ is displayed in Figure 4.6. The Fermi level lies at 0 eV and the symmetries of the bands are shown by the red and blue arrows. The effect of the total charge density is witnessed through the changes in the splittings between sub-bands as well as bands with different symmetry: for a larger extension of the 2DES, as shown in panel (b), and which occurs for the STO/LASTO:0.5 interface, the sub-band spacing is reduced and the $d_{xz/yz}$ bands are occupied at lower densities. The occupancy of the $d_{xz/yz}$ bands is dependent on the supercell size, and this effect may actually be witnessed in experiments. We shall discuss this aspect in Section 4.2.

4.1.4 Discussion

The agreement between the experimental estimation of the superconducting layer thicknesses of the 2DES at the STO/LAO and STO/LASTO:0.5 interface and the Poisson-Schrödinger modelling provides a strong argument in favour of an electric-field driven mechanism as the origin of the 2DES. Despite the similar mobile carrier densities extracted from Hall experiments [26] for the two interfaces, the calculations and the superconducting critical field measurements show that the change of the superconducting thickness is a direct result of the reduced total transferred charge (from 0.5 to 0.25 $e^-/\square$), as a modification of the polar discontinuity. Although a large fraction of these charges do not contribute to electric transport, the total transferred charge still defines the strength of the electric field in the STO and consequently its effective dielectric constant in the vicinity of the interface, which sets the spatial spread of the 2DES in the out-of-plane direction. If we set the total charge density corresponding to the density expected from the Hall effect measurements ($\sim$0.05 $e^-/\square$), then the strength of the electric field is depleted, resulting in a deconfinement of the 2DES, with a spatial extension over $\sim$60 nm at the critical density $n_{3D,th}$. This shows that all charges with nominal charge density predicted by the polar catastrophe are transferred to the interface. These results contrasts with the work of Ueno *et al.* [156], who reports no significant change in the superconducting thickness with charge density (tuned through a gate voltage) and at odds with their theoretical calculations based on a triangular quantum well model which predicts a reduction of the thickness with increasing gate voltage (and carrier density).

As a consequence of the larger charge profile at the STO/LASTO:0.5 interface, the band structure shows a larger occupancy of the d_{xz}/d_{yz} bands to the density of state, as shown in Figure 4.6.(a) and (b). This electronic configuration is at the origin of the modified phase diagram shown in Figure 4.4: indeed, the overall reduced T_c observed for the STO/LASTO:0.5 system, as compared to the standard interface, can be attributed to a more shallow confining potential, yielding a reduced n_{3D} as the extension increases [143, 157]. In addition, the field effect is not efficient enough to deplete the 2DES in order to suppress the superconductivity, nor to reach a highly resistive state (Figure 4.4.(a), bottom panel). This is clearly different from the standard STO/LAO case. Hence, from the presence of superconductivity and the low resistance state in the depletion regime, we argue that the $d_{xz/yz}$-symmetry states are occupied even at low doping due to the reduced energy splittings between bands, further emphasizing the relevance of theses orbitals on superconductivity and the high-electron mobility of the 2DES.

4.2 Finite size effects

Controlling the properties of the 2DES at oxide interfaces through finite size effects offers new perspectives yet to be explored. The idea has been scrutinized experimentally by collaborators [142] by synthesizing STO/LAO heterostructures where the STO film thickness can be tuned below the natural extension of the 2DES in standard interfaces. This is done by growing a serie of LAO/STO/LAO thin film heterostructures on STO substrates to control the extension of the quantum well through the thickness of the STO interlayer.

These heterostructures are sketched in Figure 4.7.(a): on a (001)-oriented TiO_2-terminated STO substrate, a first LAO layer with a thickness of 12 u.c. is grown by PLD. On top of

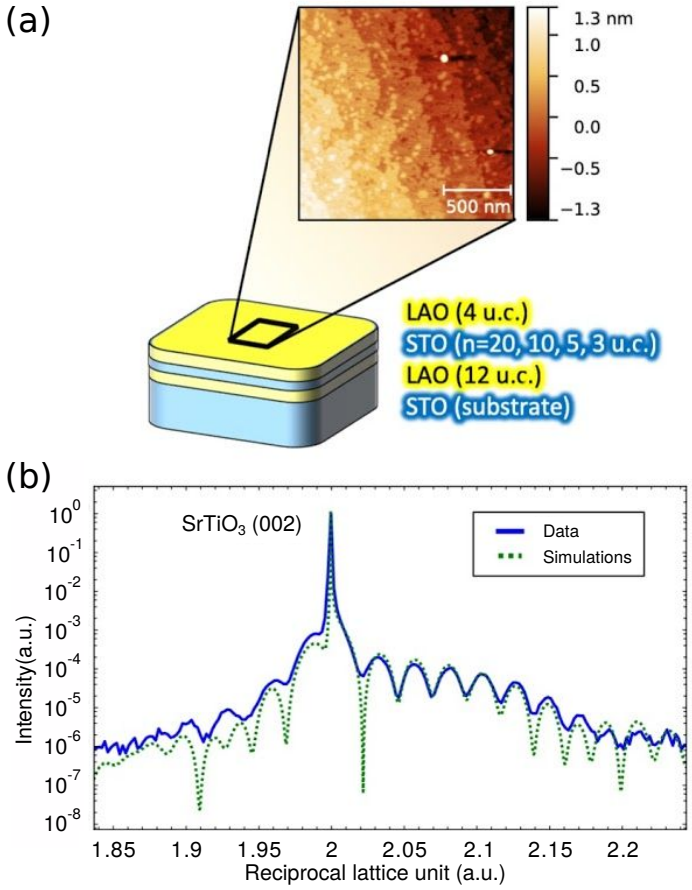

FIGURE 4.7: (a) Schematic representation of the samples, and AFM image showing the topography of the topmost layer; (b) XRD data of an example $STO(001)/LAO_{10}/STO_{35}/LAO_5$ sample, showing the (002) reflection of the substrate together with the fringes originated from the ultra-thin films. The data are compared to a simulated pattern using the following out-of-plane axis values: $c^{LAO}(5 \text{ u.c.}) = 3.773$ Å, $c^{LAO}(35 \text{ u.c.}) = 3.91$ Å, $c^{LAO}(10 \text{ u.c.}) = 3.766$ Å.

this LAO layer, a STO layer is then deposited, and hosts the 2DES of interest induced by grown another 4 u.c. thick LAO overlayer. In the nomenclature used in this work, we describe such systems such as $STO(001)/LAO_{12}/STO_n/LAO_4$. These heterostructures contain two 2DES localized in two regions, one at the top interface between the LAO overlayer and STO interlayer, and one at the interface between the substrate and the 12 u.c. thick LAO interlayer (acting as a spacing layer). As will be detailed below, ARPES mostly probes the top 2DES whose out-of-plane extension is limited by the STO interlayer thickness. The thickness of the STO layer is varied from $n = 20$ u.c. corresponding to the self-confinement of the electron system that is observed in standard STO/LAO interfaces (∼8 nm), down to $n = 5$ u.c. (∼2 nm). The layers thicknesses are determined by XRD, an example is shown in Figure 4.7.(b).

4.2.1 ARPES experiments

The electronic structure of the topmost 2DES is investigated using (resonant) Soft X-ray Angle-Resolved Photoemission Spectroscopy (SX-ARPES) at the ADRESS beamline at the Swiss Light Source (Paul Scherrer Institute) in Switzerland [158]. The advantage

of soft x-rays compared to the commonly used Vacuum Ultraviolet (VUV) ones is that they overcome the extreme surface sensitivity of the ARPES technique. Moreover, this technique has a probing depth ∼4 times higher than VUV-ARPES [159].

The probing depth of SX-ARPES in these experiments accentuates the signal from the topmost STO/LAO interface, with the signal coming from the deeper second interface being less than 10% of the total for the ultimate limit of the $n = 5$ u.c. samples. All the data presented here (unless stated otherwise) has been acquired using a photon energy of 466 eV corresponding to the L_2 absorption edge of Ti, providing a clearer photoemission yield for the d_{yz} band compared to the d_{xy} one [71]. Additionnally, using s-polarized x-rays silence the signal coming from the d_{xz} band due to the symmetry of the experimental setup [158].

The experimental SX-ARPES intensity images representing the evolution of the electronic structure of the 2DES in the STO interlayer of samples with different thicknesses n are shown in Figure 4.8.(b-d). The data was acquired in the same conditions along the ΓX direction of the Brillouin zone at a temperature of 13 K. Figure 4.8.(b) ($n = 20$ u.c.) reveals an electronic structure similar to the one of a standard n-type STO(001)/LAO interface [28, 160] (schematically represented in Figure 4.8.(a)). At the Fermi level, the band structure is dominated by a weakly-dispersing band originating from the Ti d_{yz} orbitals, as predicted by our DFT calculations.

Superimposed to this heavy band, two bright spots appears at $k_{\|} = \pm 0.09$ Å^{-1}: these corresponds to the points where the band originating from the Ti $d_{yz/xz}$ orbitals hybridizes with the Ti d_{xy} orbitals. Large out-of-plane localization of these bands makes its SX-ARPES yield (and visibility) lower with respect to the deeper penetrating d_{yz}-derived bands [161]. Due to matrix element effects, the intensity is different across between the two Brillouin zones (Γ_{00} and Γ_{01}) and not symmetric around the Γ_{00} point.

Comparing these data with the measurements performed for the lower STO thicknesses ($n = 10$ and 5 u.c.), a clear enhancement of the ARPES yield of the d_{yz} band can be witnessed, along an energy broadening of the spectral structures, particularly for the $n = 5$ u.c. samples. We will focus on this sample in the following discussion.

The detail of the spectral broadening for the $n = 5$ u.c. sample is enlarged in Figure 4.9 (left panel), along with an energy distribution curve (EDC) taken at $k_{\|} = -0.2$ Å^{-1} (right panel). This distribution (blue dots) clearly shows a double-peak structure in the range from 0 to −0.2 eV of binding energy. The double peak structure indicates the presence of a replica band. The origin of this band may be possibly attributed to two phenomena: the formation of a polaronic sideband due to enhanced electron-phonon coupling, or the quantization effect on the d_{yz} band generating sub-band levels.

STO and STO-based interfaces are known to host polaronic charge carriers recognizable by a hump in the spectral function located at around 90-120 meV higher binding energies with respect to the quasiparticle (QP) peak [160, 162, 163], originating from electron coupling with the LO3 vibrational mode of the O cage [160]. Hence, the double peak of the EDC could fit this picture, with two peaks identifying the QP and its polaronic hump. Using a single peak-dip-hump spectral function, it is not possible to fit the double peak structure. In contrast, using two peak-dip-hump functions yields a remarkable fit with the experimental data as shown in the right panel of Figure 4.9 (blue line). The best fit is obtained for an energy separation of 95 ± 4 meV between the two peaks. Performing the fitting procedure for several EDC across the ARPES data yields an

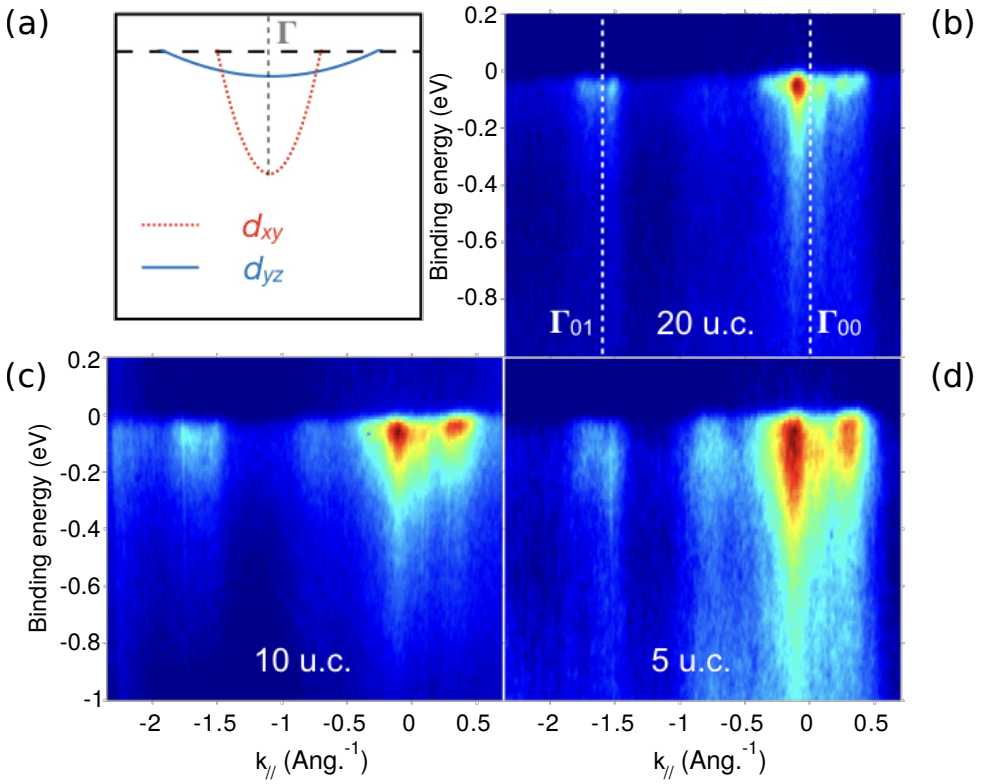

FIGURE 4.8: (a) Schematic representation of the electronic structure along the ΓX direction of the 2DES of a "standard" bulk STO/LAO interface; b-d) show the experimental electronic structures for the $n = 20$, 10 and 5 u.c. samples.

average energy separation of 99 ± 4 meV between the two bands. Hence this analysis suggests the presence of another d_{yz} sub-band at the origin of the second peak. We attribute the appearance of this band due to a modification of the quantum well hosting the 2DES.

4.2.2 Theoretical results

Can theoretical calculations support these calculations ? By performing DFT calculations on a vacuum/LAO_4/$STO_{9.5}$/LAO_4/vacuum symmetric slab using the variational pseudo self-interaction correction (VPSIC) [56] and the B1-WC hybrid functional, we calculate an energy separation of the first two d_{yz} bands of 116 meV (VPSIC) and 131 meV (B1-WC). These results are in satisfying agreement with the experimental data shown in Figure 4.9. Note that with both functionals, the STO subsystem remains insulating (below the onset for Zener breakdown, as discussed in Chapter 3). Assigning the Fermi level position by comparing the calculations to the SX-ARPES bandwidth, the first quantum well state resides completely below the Fermi level in both calculations, while the second is cut by the Fermi level. This occurrence has already been observed by Wang *et al.* in anatase TiO_2 [164], making this scenario a possibility.

Another possible option to assess the effect of finite size effect on the 2DES is to perform DFT calculations on symmetric and off-stoichiometric $(STO)_m/(LAO)_2$ superlattices as done in the preceding Section, albeit with smaller STO thicknesses. As these structures

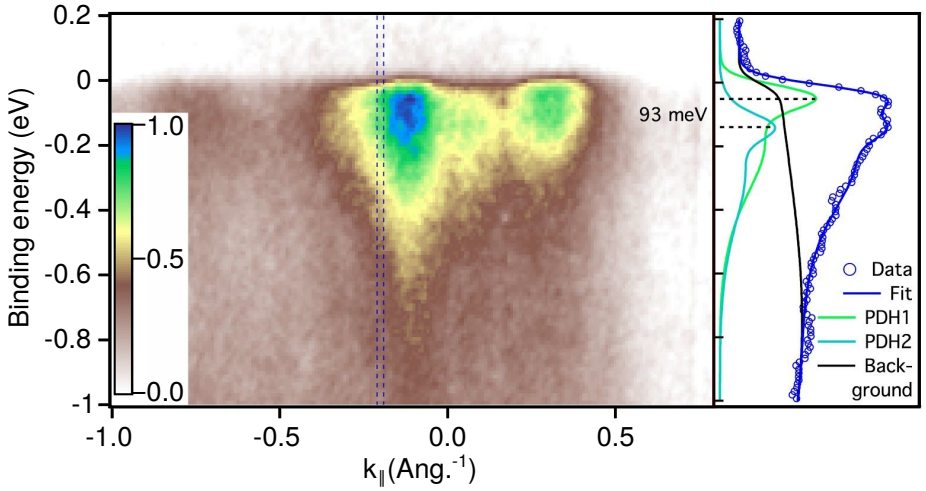

FIGURE 4.9: Detail of the electronic structure (left panel) of the $n = 5$ u.c. sample along the ΓX direction. The blue dashed lines represent the integration window of the energy distribution curve (right panel) plotted together with the fitting results. The horizontal dashed lines highlight the double-peak structure discussed in the main text.

are metallic, the band filling (0.5 $e^-/\square$) sets the Fermi level self-consistently. The B1-WC calculations confirm the shift of the d_{yz} band to lower binding energy for ultra-thin STO layers. Figure 4.10 shows the Mulliken charges on each TiO_2 layer for STO subsystems of different thicknesses, comparing the behaviour of the d_{xy} (left panel, a) and the $d_{yz/xz}$ (right panel, b) orbital states. When the STO thickness is reduced, one can see in all case a progressive shift of the charge toward the interface. More interestingly, one can notice a charge transfer from the d_{xy} to the $d_{yz/xz}$ states along with the decrease of the STO thickness, and in the ultra-thin limit, the amount of charge accumulated in the two bands becomes nearly equal. This finding supports the idea that in the narrow limit a consistent amount of charge can populate the second quantum well state with the $d_{yz/xz}$ orbital character. We attribute this behaviour to two concomitant effects: i) reducing the STO thickness (and thus the quantum well width) increases the splitting between sub-bands of same symmetry, and ii) as the charge accumulates closer to the interface, the occupancy of the $d_{yz/xz}$ states localized farther away from the interface, is favoured because their energies are lowered due to static correlation effects [165, 166]. These effects, usually modelled through a Hubbard-like repulsion term (U), are reproduced in a similar fashion in our DFT calculation by the inclusion of Hartree-Fock exchange in the exchange-correlation term. These results suggest that a combination of quantum confinement and electron correlations, controlled by the thickness of the embedded STO interlayer can shift the quantum well states across the Fermi level of the 2DES and thus give control of the charge carriers density.

The increase of energy band splitting as a consequence of reduced quantum well width can be observed in the electronic band structure of the superlattices shown in Figure 4.11. The observation of such trends in experiments[3] is difficult, as the energy resolution is low for the thicker STO layer where the quantum well states are close in energy, whereas

[3]SX-ARPES has also been performed on a $n = 3$ u.c. samples, with an even larger yield and bandwidth for the d_{yz} band, in agreement with the trend observed in DFT. However, the spectroscopy data is too blurry to perform any quantitative analysis. More information can be found in the Supplementary Information of Reference [142].

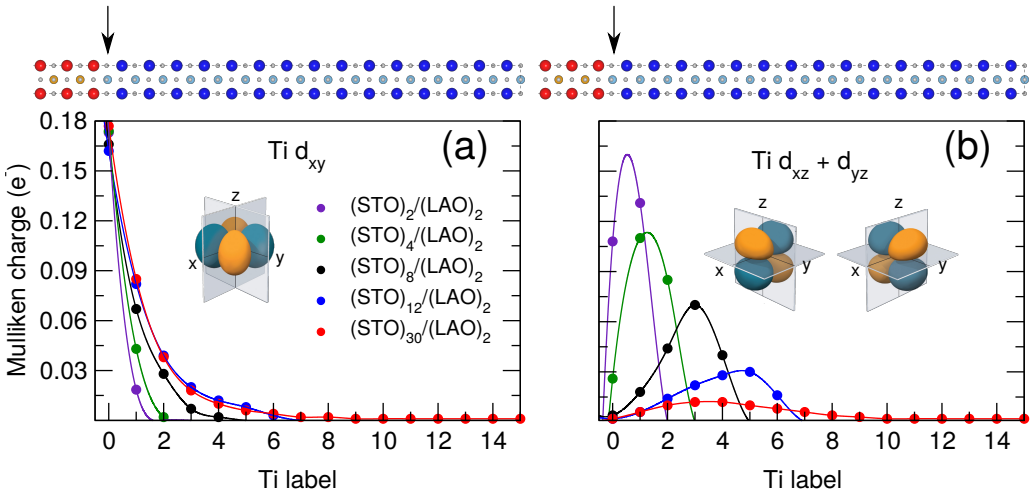

FIGURE 4.10: Mulliken decomposition of the 2DES in $(STO)_m/(LAO)_2$ superlattices, projected onto (a) the Ti d_{xy} orbitals and (b) the Ti $d_{xz/yz}$ orbitals. On top, schematic view of the $(STO)_{30}/(LAO)_2$ superlattice, with the first TiO_2 plane from the interface shown by arrows. The data is interpolated by the means of cubic splines, as a guide to the eyes. The label of the Ti site at the interface is set to 0. The 3-dimensional representation of the t_{2g} orbitals are adapted from Reference [2].

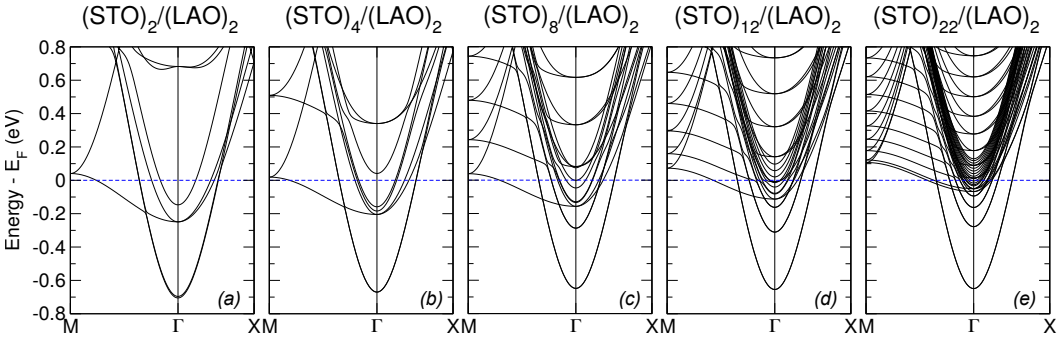

FIGURE 4.11: Computed electronic band structure of $(STO)_m/(LAO)_2$ superlattices ($m = 2$, 4, 8, 12 and 22 u.c.).

growing disorder and interfacial intermixing smears the spectral structures for samples with ultra-thin STO interlayer.

4.3 Conclusions

In this Chapter, we have shown that by alloying the LAO overlayer with STO to form a solid solution with a 50% composition, we are able to tune the polar discontinuity at the interface with STO, leading to a change of 2-dimensional electron density by a factor of 2. The total transferred charge density modulates the interfacial confining potential, leading to a change in confinement of the 3-dimensional charge density. This change in confining potential explains the change of the characteristic superconducting thickness, from 10-15 nm (LAO) to 20-30 nm (LASTO:0.5) as estimated from the out-of-plane critical field measurements. The evolution of the confinement with the change in polarization is captured by large-scale DFT calculations and self-consistent Poisson-Schrödinger modelling, which reproduces the experimental results by assuming that

a full transfer of charges take place at the polar/non-polar interface, with a density predicted by electric-field driven mechanisms. The results shows that the deconfinement of the charge leads to a stronger $d_{xz/yz}$ occupancy far from the interface (with a stronger contribution to the density of states) and explains the persistence of the superconducting state in the depletion regime.

In addition, we show from first-principles the effect of structural confinement on the 2DES system: by reducing the thickness of the STO layer holding the 2DES, the occupancy of the Ti $d_{xz/dyz}$ bands increases and may become comparable to the occupancy of the Ti d_{xy} state in the ultra-thin limit. These calculations also support spectroscopy experiments performed on STO(001)/LAO_{12}/STO_n/LAO_4 heterostructures, as they shows increased occupancy of the $d_{yz/xz}$ states upon decreases of the STO interlayer thickness. This study support the possibility to tune the energy and population of different quantum well states through finite size effects. In a wider perspective, this work sets forth further manipulation of low-dimensional electron systems at oxides interfaces.

Chapter 5

First-principles study of capped $SrTiO_3(001)/(LaAlO_3)_m/(SrTiO_3)_n$ structures

It has been shown that the properties of the 2DES at the STO/LAO interface can be altered through modification of the LAO surface. For example, adsorbed molecules can either increase or decrease the sheet resistivity of the interface [167–169]. Moreover, it is possible to passivate the LAO surface by growing metallic capping layer (such as Al or Co), reducing the critical thickness to only 1 u.c. [139, 170]. More puzzlingly, there has been reports claiming that capping the LAO overlayer with insulators, such as STO, also alters considerably the properties of the interface. In the present Chapter, we aim to exploit the improved accuracy of hybrid functional DFT to properly describe these layered systems and to bring further insights on the specificities of these heterostructures, compared to the standard STO(001)/LAO system.

5.1 Introduction

While the number of study of STO(001)/LAO_m heterostructures are countless, much less focus has been given to capped STO(001)/LAO_m/STO_n systems, despite interesting features which are important in the overall understanding of the interfaces. The most important of all is the possibility to suppress the threshold thickness of LAO up to 1 u.c. by capping the LAO layer with a thick STO overlayer, as reported by Huijben *et al.* [88]. The room temperature sheet resistance of such systems, with a TiO_2/LaO (n-type) interface between the STO substrate and LAO interlayer, and a AlO_2/SrO (p-type) interface between the LAO interlayer and the STO capping layer, is given in Figure 5.1.(a), for STO(001)/LAO_m/STO_{10} systems. The samples have been prepared by PLD, at oxygen partial pressure $p_{O_2} = 3 \times 10^{-5}$ mbar, and temperature $T = 850$ °C. The room temperature carriers density estimated from the Hall resistance are given in Figure 5.1.(b). The sheet resistance is of the order of 10^4 $\Omega/\square$, the same order of magnitude as for the conducting standard STO/LAO interface, at any LAO thickness above 1 u.c.: the threshold thickness is therefore suppressed. The sheet carrier density start at $\sim 5 \times 10^{13}$ cm^{-2} at $d^{\mathrm{LAO}} = 1$ u.c., and saturates to $\sim 1.5 \times 10^{14}$ cm^{-2}. This contrasts with the sheet carrier density for the standard STO/LAO interface, where the

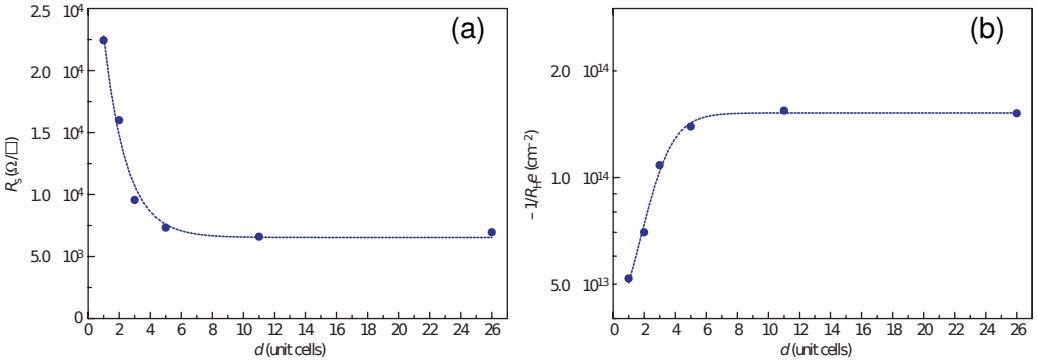

FIGURE 5.1: Electronic properties of STO/LAO heterotructures at 300 K for different separation distances between the n-type and p-type interfaces for STO(001)/LAO$_m$/STO$_{10}$: (a) dependence of the sheet resistance R_s on the separation distance d^{LAO}; (b) dependence of $-1/R_H e$ on the separation distance d^{LAO} (R_H is the Hall coefficient, and e the electron charge).

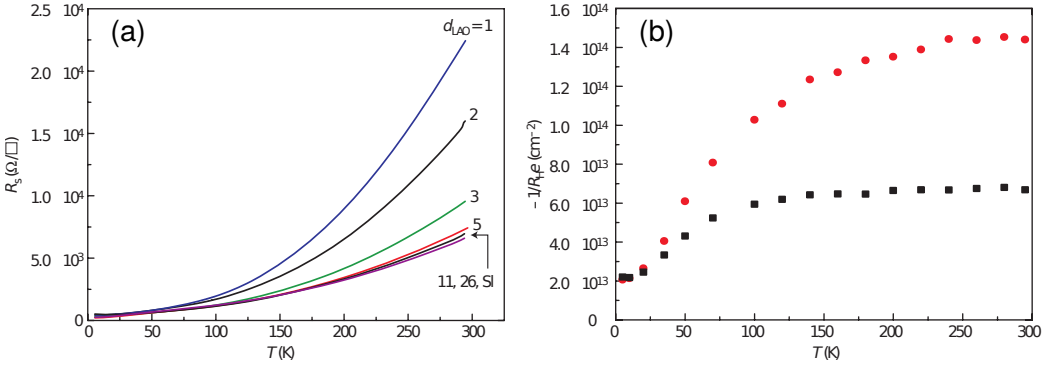

FIGURE 5.2: (a) Temperature dependence of the sheet resistance $R_s(T)$ for different thicknesses of the LAO interlayer in STO(001)/LAO$_m$/STO$_{10}$ heterostructures. A measurement of a single TiO$_2$/LaO interface (SI) is also shown. (b) Temperature dependence of $-1/R_H e$ of STO(001)/LAO$_m$/STO$_{10}$ heterostructures with LAO thicknesses of 2 u.c. (squares) and 5 u.c. (circles). Adapted from Reference [88].

carrier density derived from Hall measurement effects saturates around $\sim 2 \times 10^{13}$ cm^{-2} (Figure 3.10). It is however in better agreement with the charge density derived from RIXS measurements. For the standard STO/LAO system, the discrepancy between the Hall measurements and RIXS may stem from the mobility of the carrier at the interface: in this case, it is possible that capping layer have an effect on the mobility of the carriers. Above all, the most striking feature in these systems is the suppression of the critical thickness d_c^{LAO}. Indeed, as discussed in Chapter 3, the threshold thickness arises from the competition between the electric field in the LAO overlayer and the cost of interface doping and charge transfer. This question the validity of the electric-field driven mechanisms. Another difference with the standard STO/LAO system is the temperature dependence of the resistivity: for all samples, the resistivity increases with temperature over a large temperature range, even below 50 K as shown in Figures 5.2.(a). The associated mobile carrier sheet density as derived by Hall measurements decreases up to 2×10^{13} cm^{-2}.

Another study about such STO(001)/LAO$_m$/STO$_n$ heterostructures focused on the properties of these systems in the low thickness limit ($m = 1, 2$ u.c. and $n = 1, 2, 10$ u.c.)

by Pentcheva *et al.* [89, 122]. Complementing the experimental results, DFT-GGA calculations have been performed. The main results are shown in Figure 5.3 in term of temperature dependence of the sheet resistance (a), as well dependence of the sheet resistance with d^{LAO} (at different p_{O_2} during growth). The temperature dependence of R_S at fixed $d^{\mathrm{LAO}} = 2$ u.c. is similar to that of Figure 5.2.(a) for varying LAO thicknesses. The room temperature sheet resistance is reduced by a factor of ∼2 when changing the thickness of the capping layer from 1 u.c. to 2 u.c., but then no longer evolves much for thicker capping layer. Interestingly, the dependence of the room temperature sheet resistance on the oxygen partial pressure during growth (p_{O_2}) is large for $d^{\mathrm{LAO}} < 4$ u.c. in STO(001)/LAO$_m$/STO$_{10}$ samples, but is relatively small for thicker LAO interlayer. Reference [89] also reports an insulating phase for STO(001)/LAO$_1$/STO$_m$ samples with capping layer thickness inferior to $m = 10$ u.c.: there is not a single threshold thickness for the occurrence of conductivity, suggesting that the conductivity may originates from extrinsic sources. However, the DFT calculations of Reference [89] shows the possibility of electronic reconstruction as early as $d^{\mathrm{LAO}} = 2$ u.c. (if capped with a 2 u.c. thick STO), which is due to the surface dipole states of the STO capping layer, triggering a Zener breakdown at a lower d^{LAO} than required for the uncapped STO/LAO system. As these calculations were performed using the GGA, they also present the well-known band gap underestimation problem of local/semi-local DFT: in their case, the STO band gap is roughly equal to ∼2 eV, based on the layer-resolved density of state, close to the computed PBE value reported in Table 3.2. We can therefore question the possibility of electronic reconstruction in the STO(001)/LAO$_2$/STO$_m$ samples. Nevertheless, the electronic reconstruction scenario implies the presence of a 2-dimensional hole system (2DHS) in the STO capping layer, and led the authors to propose a two-bands model interpretation for their Hall effect measurements, with opposed effective masses m_e^* for the electrons and m_h^* for the holes (and $|m_h^*| \approx 0.1|m_e^*|$ based from the extracted mobilities), and argue that the two-bands model could not be fit without this constraint.

The possibility of existence of a 2DHS in STO triggered further studies focusing in these capped heterostructure [123], this time with a rather large LAO interlayer thickness $d^{\mathrm{LAO}} = 40$ u.c. to probe the properties of the individual n-type and p-type interfaces. Figure 5.4 shows data extracted from Reference [123]: (a) the Hall resistance, (b) the carrier mobility, (c) the sheet resistance and (d) the sheet carrier density, for the bottom (n-type) and top (p-type) interface. The most striking differences with the reports of Pentcheva *et al.* [89] is that hole carriers at the p-type interface and the electron at the n-type interface are strikingly similar in features, in mobilities and in carrier density as well. If all the charges originate from a Zener breakdown as claimed by the authors, then it is expected that there is as much holes as electrons for the two interfaces. However, the mobilities for both carrier are expected to be different: notably, the holes are expected to have a larger effective mass. However, the authors claim that the electrons actually have a larger effective mass than their band mass due to polaronic effects [160]. An interesting reported property is that the p-type interface of an oxygen deficient heterostructures (with no post-growth annealing process) is insulating, suggesting compensation between the 2DHS and the electrons released from oxygen vacancies.

The authors of References [123] and [171] argue that the 2DHS lies close to the p-type *interface* in the STO capping layer due to the charge transfer from the last AlO_2 layer before the capping layer, whereas Pentcheva *et al.* [89] claim that the holes are localized at the TiO_2 *surface* of the capping layer. It should be mentioned that these two pictures are not necessarily in contradiction with each other, as the main results of Pentcheva *et al.* [89] concerns heterostructures with $d^{\mathrm{LAO}} = 2$ u.c., below the onset for charge transfer

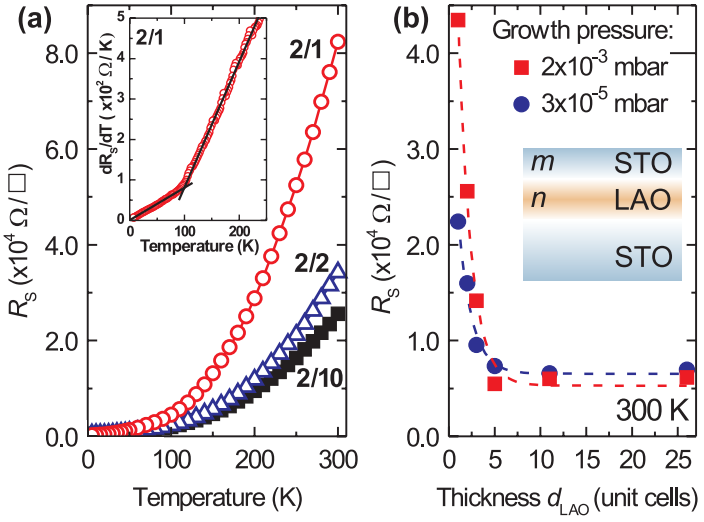

FIGURE 5.3: (a) Temperature dependence of the sheet resistance $R_s(T)$ for STO(001)/LAO$_2$/STO$_1$ (red circles, 2/1), STO(001)/LAO$_2$/STO$_2$ (blue triangles, 2/2) and STO(001)/LAO$_2$/STO$_{10}$ (black squares, 2/10). All the samples are grown at $p_{O_2} = 2 \times 10^{-3}$ mbar. Inset: dR/dT as a function of temperature with different linear fits below and above 100 K. (b) Evolution of the sheet resistance of STO(001)/LAO$_m$/STO$_{10}$ samples for varying LAO thickness and a fixed number of 10 u.c. of STO capping. The red squares/blue circles correspond respectively to $p_{O_2} = 2 \times 10^{-3}$ mbar and $p_{O_2} = 3 \times 10^{-5}$ mbar during growth. Adapted from Reference [89].

from the O $2p$ states of the last AlO$_2$ layer to the n-type interface. These experiments highlight the difficulty to characterize properly these STO(001)/LAO$_m$/STO$_n$ systems.

Aside from the data available in the literature, collaborators from the Triscone research group of the University of Geneva provided us with additional experimental data on such STO(001)/LAO$_m$/STO$_n$ structures. The sheet conductance measured on their samples is shown in Figure 5.5. Depending on the thicknesses of the LAO and STO overlayers, the samples are either insulating ($m+n<4$) or metallic ($m+n \geq 4$). These results are also different than that of Reference [89]. The apparent contradictions, either between these experiments or with the most popular hypotheses about the origin of the 2DES (polar catastrophe), kickstarted our theoretical study. Our objective is to study these systems from first-principles to identify the possible origin(s) of the charge carriers for low LAO thicknesses and to clarify the properties observed in experiments.

5.2 Technical details

The technical details for the calculations involved in the present Chapter are the same as given in Section 3.2. In this Chapter, we will only discuss a specific type of capped STO(001)/LAO$_m$/STO$_n$ heterostructures, with an n-type interface (TiO$_2$/LaO) between the substrate and the LAO interlayer, and a p-type (AlO$_2$/SrO) interface between the LAO interlayer and the STO capping layer. The surface of the STO capping layer has therefore a TiO$_2$ termination. The structural models used in the DFT calculations consists in symmetric slabs including a vacuum region as described in Section 3.2.1. The geometry of two vacuum/(STO)$_n$/(LAO)$_m$/(STO)$_{13.5}$/(LAO)$_m$/(STO)$_n$/vacuum slabs

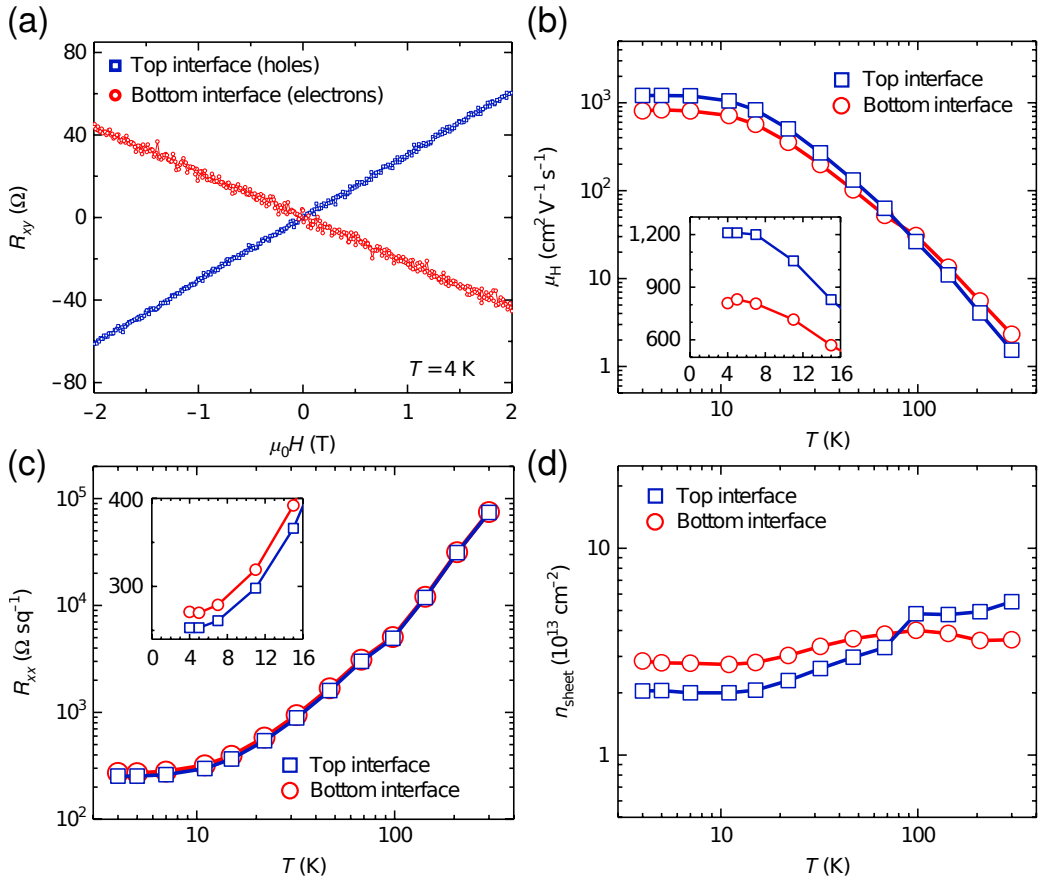

FIGURE 5.4: Transport properties of a STO(001)/LAO$_{40}$/STO$_{10}$ sample: (a) Hall resistance R_{xy} versus magnetic field $\mu_0 H(T)$ at $T = 4$ K for the top and bottom interfaces. The signs of the slopes for the top is an indication of opposite charges of the carrier for the two interface. (b) Temperature dependence of the mobility $\mu_H(T)$ for the two interfaces, with an inset with a linear scale. (c) Temperature dependence of the sheet resistance $R_{xx}(T)$ for the top and the bottom interfaces, with an inset with a linear scale. (d) Temperature dependence of the sheet carrier density $n_{\text{sheet}}(T)$ for the two interfaces. Adapted from Reference [123].

is shown in Figure 5.6. We also perform calculations for geometries with oxygen vacancies. The calculations for the defective systems involve a slab with a thinner central STO layer as the substrate (7.5 u.c. instead of 13.5 u.c.), as done for the calculations presented in Section 3.7.2. For the rest of this Chapter, we shall refers to STO(001)/LAO$_m$/STO$_n$ heterostructures with respect to the overlayer thicknesses (m,n): for example, the heterostructures in Figure 5.6 are referred to as (5,0) and (4,1).

5.3 Pristine heterostructures

We are mainly interested in the electronic properties of STO(001)/LAO$_m$/STO$_n$ heterostructures. For this purpose, we first take a look at the value of the band gaps of these systems for different (m,n). The associated values are given in Figure 5.7, where the gap is calculated as the energy difference between the minimum of the conduction band (CBM) and the maximum of the valence band (VBM). In the colour scale, blue means a positive band gap, and therefore an insulating phase, whereas red corresponds

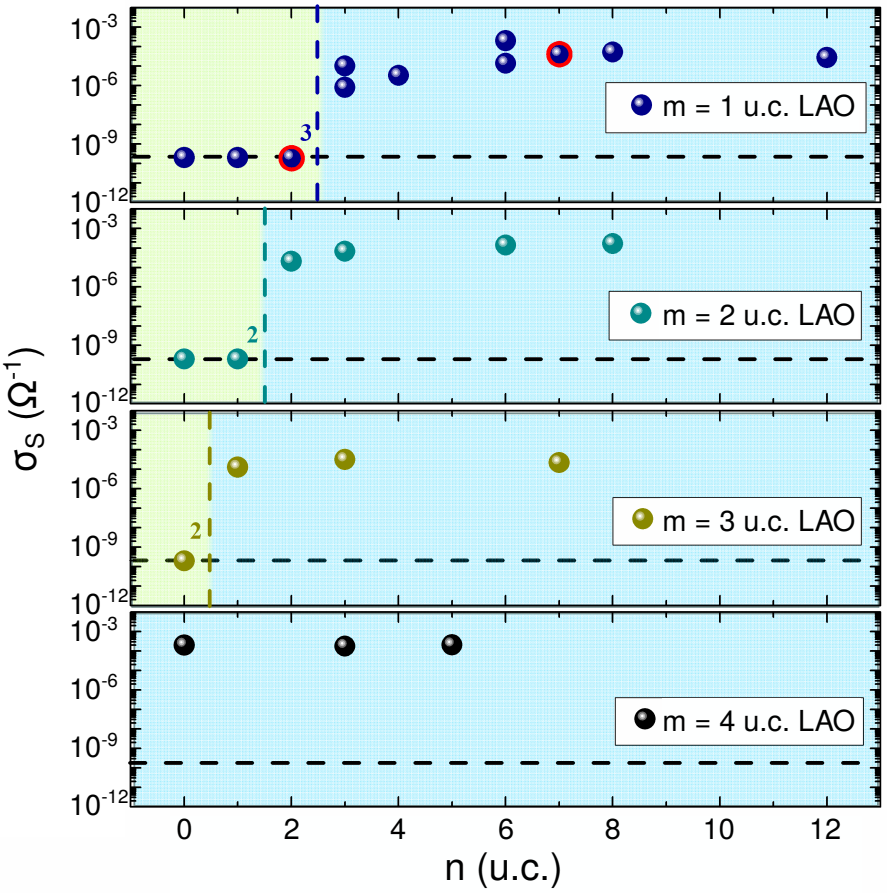

FIGURE 5.5: Sheet conductance σ_S measured on STO(001)/LAO$_m$/STO$_n$ samples for $m = 1$, 2, 3 and 4 u.c. for varying thicknesses of the capping layer. A transition to a metallic phase is witnessed for the samples as long as $m+n = 4$ u.c., and σ_S increases by several orders of magnitude. Data provided by the Triscone Group (DQMP, University of Geneva).

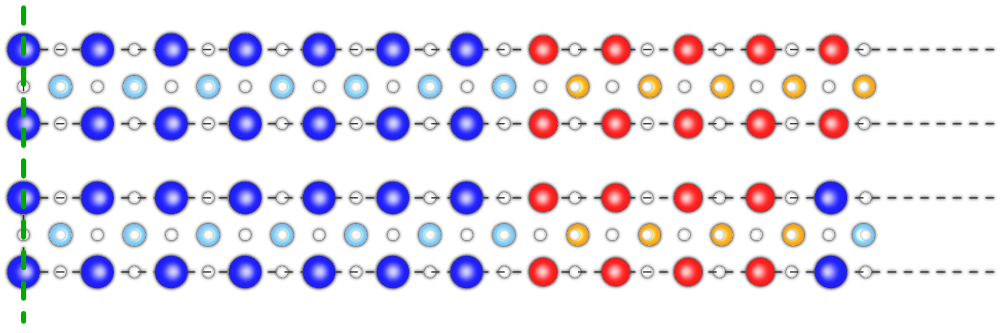

FIGURE 5.6: Structures in the slab geometry used in the DFT calculations: they are symmetric (symmetry plane shown as a green dashed line), with a central STO layer mimicking the substrate, and a bare LAO overlayer (top) or a LAO interlayer, capped with STO (bottom). The capped structures display the two possible interfaces along the (001) direction, and is always BO_2-terminated. On top, a STO(001)/LAO$_5$ heterostructure; on bottom, a STO(001)/LAO$_4$/STO$_1$ heterostructure.

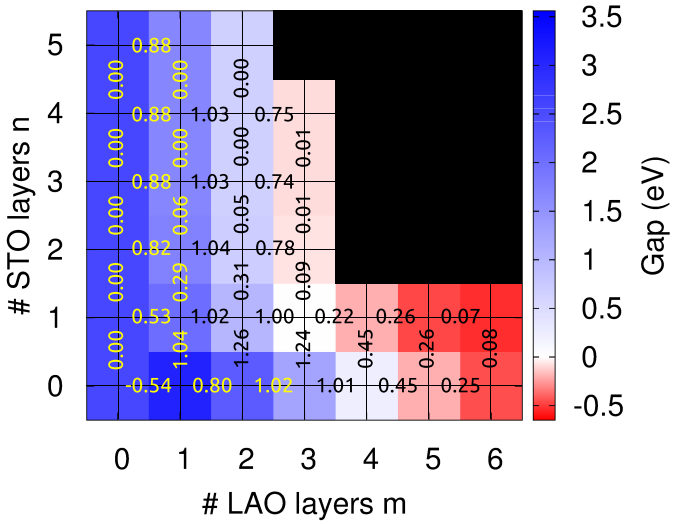

FIGURE 5.7: Coloured map of the band gap with respect to LAO and STO thickness in term of number of monolayers. In the coloured scale, the maximum value (blue) is the electronic band gap of cubic STO calculated within the B1-WC functional, the minimum value (red) is the energy difference between the Fermi level and the bottom Ti d_{xy} band in the fully-compensated STO/LAO system. Additionnally, the variation of the band gap is given (in eV) between the different tiles of the map. The black part of the map has not been calculated.

to an overlap between the CBM and the VBM: Zener breakdown occurs, and the interface becomes metallic. Figure 5.7 also contains the data for uncapped structures (m,0), to be compared with the capped system.

For a bare STO film with a TiO_2 surface ($m = 0$), the band gap is 2.6 eV, about 1 eV smaller than the bulk value 3.6 eV. This is attributed to a O $2p$ valence band, extending 1 eV above the bulk valence band, as shown in Figure 5.9.(a) (blue line). The surface state originates from a distortion at the TiO_2 surface of STO, where a small dipole appears at the surface, as the O and Ti ions move away from each other due to the surface relaxation (shown in Figure 5.8.(a), for slab (0,0): the rumpling is the most prominent in layer 6, at the surface). These are well known features of the STO TiO_2 surface, and are better known as Tamm states [172, 173]. The band gap at the surface is reduced by a factor of about $\sim \sqrt{2}$ compared to that of the bulk, which is well supported by experiments [174], and we shall discuss its role in the following discussion.

Looking at (m, 0) structures (bare LAO surface, no capping layer), the surface states disappears with $m = 1$, but are partially compensated by LAO states raised by the built-in field (and accounting the band offset). The gap slightly increases for ($m = 1$,0), as m increases, the band gap decreases linearly until $m = 5$. Above this value, a Zener breakdown occurs, and electrons are transferred from the O $2p$ states at the AlO_2 surface to the Ti t_{2g} states at the n-type interface. As a signature of the built-in electric field in LAO, a sizeable rumpling appears in the LAO layer as shown in Figure 5.8.(a-f). The amplitude of the rumpling depends on the amount of charge transferred to the interface.

If we look at the capped heterostructures for slabs (1, $n > 0$), we can see that the gap decreases as soon as $n = 1$ is deposited on top of the LAO monolayer: this is related to the presence of in-gap states near the valence band, identified as the O $2p$ states from the capping layer TiO_2 surface (as in the bare STO film), closing the gap of $\sim$1 eV, as shown in Figure 5.9.(a); it should be mentioned that no in-gap states appears for the

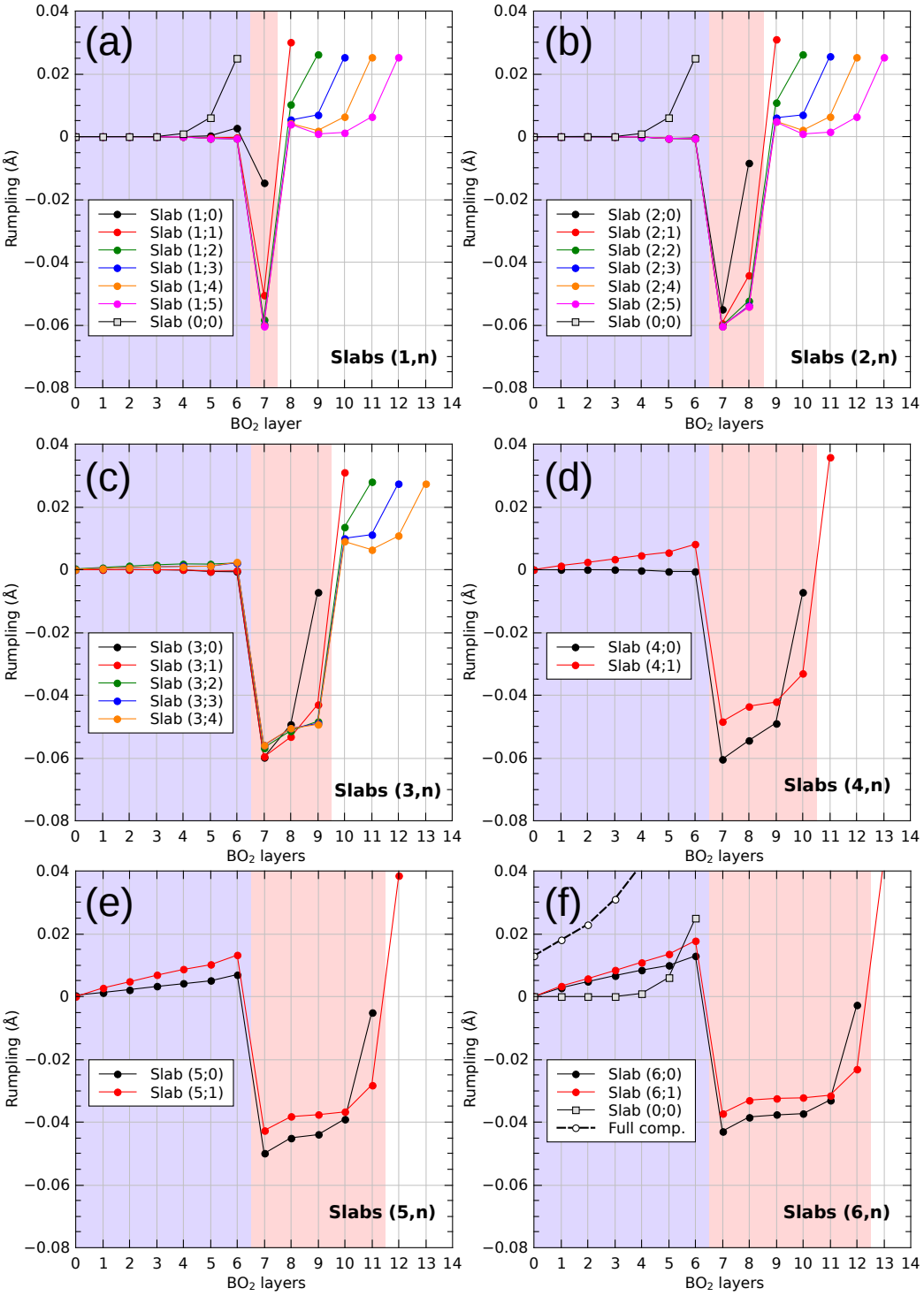

FIGURE 5.8: Rumpling in STO(001)/LAO$_m$/STO$_n$ heterostructures, defined as the relative distance of the B cations and the O anions to the median plane of the BO_2 layers. For the different plots, the rumpling for slab (m,n) is shown with $m = 1$ (a), 2 (b), 3 (c), 4 (d), 5 (e) and 6 (f). The light blue overlay shows the STO substrate, the light red overlayer shows the LAO layer, and the white background concerns the capping layer. The TiO_2 plane at n-type interface is labelled 6. Rumpling appears in the STO films i) at the surface if there is no overlayer as for slab (0,0) or ii) at the interface if metallic. For a fully compensated interface ($n_{2D} = 0.5\ e^-/\square$), the rumpling in STO is a larger and extends further away from the interface, shown in (f).

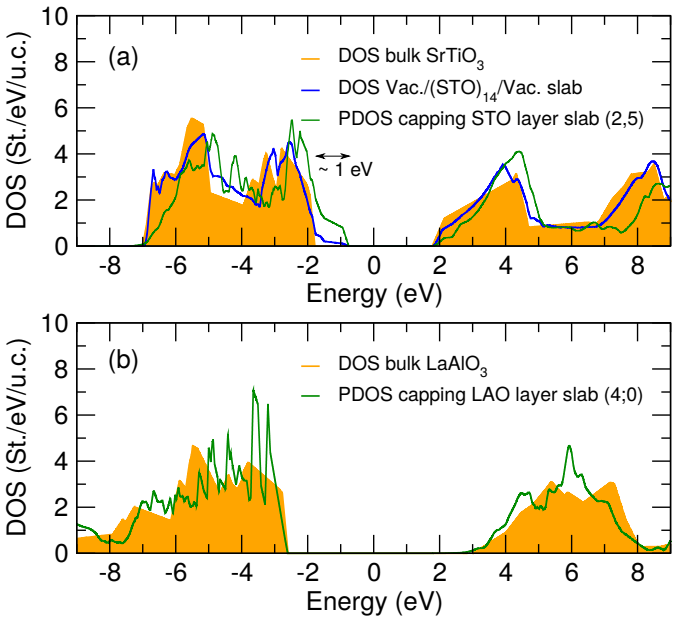

FIGURE 5.9: Density of state of STO and LAO systems, (a) for bulk cubic STO, as well as a 14 u.c. thick STO film, and the DOS projected on the last STO layer of slab (2,5). The in-gap states near the STO valence band are clearly identified; (b) for bulk cubic LAO, and the DOS projected onto the last LAO layer of slab (4,0): no in-gap states are identified in this case.

bare LAO film, as shown in Figure 5.9.(b). The rumpling in the capping layer near the surface is similar to that of the bare STO films, as shown in Figures 5.8.(a) and (b).

The evolution of the band gap quickly saturates with increasing n: an insulator-to-metal transition (MIT) occurs as early as $m = 3$ u.c. of LAO, but cannot occurs below this threshold ($n = 0$, 1, 2) as the band gap remains too large for any charge transfer to occur: for slab (2,1), the calculated band gap is 1.02 eV, as shown in Figure 5.11.(a), remarkably close to the value estimated from scanning tunneling spectroscopy at room temperature (∼1 eV) [122].

The stabilization of the band gap with n is related to the absence of electric field in the STO capping layer as illustrated in Figure 5.10 (aside from the small dipole at the surface), as would be expected from an electrostatic point of view. In this picture, the low sheet resistance measurements from Reference [89] for samples with only 2 monolayers of LAO, cannot be explained through a Zener breakdown as argued by the authors, with a coexistence of spatially separated n-type and p-type carriers sheets. The STO band gap as calculated from GGA is severely underestimated, which is the reason behind the apparent small band overlap for the (2,2) capped structures in Figure 1 of Reference [89].

In our case, the STO band gap is slightly overestimated of ∼0.4 eV. Even after applying a scissor-like correction term to the calculated band gap, no metallic phase occurs for (2,n) as the DFT bang gap remains above 0.6 eV. However, for slabs with $m = 3$, the band gap is nearly closed as early as $n = 1$. For $n > 1$, the gap is completely closed, and a charge transfer occurs between the O $2p$ states at the TiO_2 surface of the capping layer and the Ti t_{2g} states at the TiO_2 interface, below the onset for Zener breakdown for the bare LAO surface. For a clearer look, we show the layer-resolved density of state of slabs (2,n) and (3,n) in Figures 5.11.(a-g): the origin of the charge transfer can be attributed to three electronic effects: 1) the upward shift of the capping layer states due

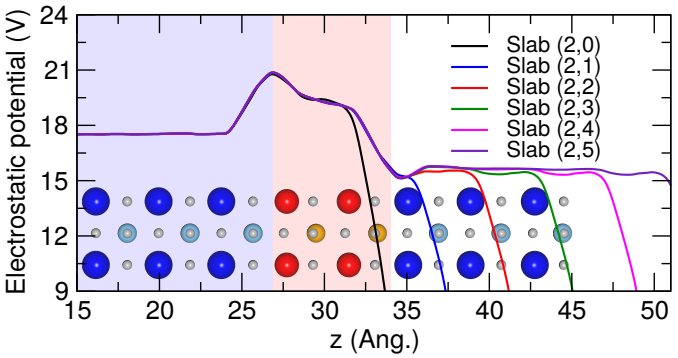

FIGURE 5.10: Macroscopic electrostatic potential in capped heterostructures, calculated on slabs (2,n) with n = 0, 1, 2, 3, 4 and 5. Aside from the small dipole at the surface, the macroscopic potential is flat in the capping layer.

to the built-in potential of LAO, 2) the band offset at the interface between the LAO and the capping layer, and finally 3) the dipole surface state originating from the O $2p$ surfaces states extending ∼1 eV above the bulk STO valence band maximum. For a sufficiently thick LAO interlayer, the surface states may overlap the STO conduction band.

The theoretical results demonstrate the possibility of electronic reconstruction below the onset of Zener breakdown for the standard STO(001)/LAO system, with the existence of a 2-dimensional hole gas at the surface of the capping layer. However, they also shows that electronic reconstruction cannot occurs for the lowest thicknesses (m < 3 u.c.), questioning the interpretation given in Reference [89]. Another concern is that the sheet conductivity in Reference [89] depends on the oxygen partial pressure during growth for $d^{\mathrm{LAO}} < 4$ u.c., which cannot be explained from a Zener breakdown alone. Finally, there is no report of post-growth annealing treatment for the samples of References [88, 89, 122], suggesting the possibility of oxygen vacancies as possible dopants. We have shown in Chapter 3 that surface redox processes occurring at the LAO surface is a more plausible origin for the occurrence of conductivity at the interface based on energy argument. However, in the heterostructures discussed in this Chapter, the LAO surface no longer exists. Hence we need to reconsider the role of oxygen vacancies in the case of the capped heterostructures. For this purpose, we perform DFT calculations on capped heterostructures explicitly including oxygen vacancies.

5.4 Revisiting the surface redox model for capped structures

The surface redox model of Bristowe *et al.* [117, 130] presented in Section 3.7.2 Chapter 3 can be adjusted to include the capping layer of STO. The model is built in the following way: from the evolution of the macroscopic electrostatic potential as shown in Figure 5.10 for pristine system, we deduce that the capping layer do not change the overall evolution of electrostatic potential in the LAO layer. Moreover, the electrostatic potential in the STO capping layer is almost completely flat, even with the surface dipole identified earlier (as it is mainly localized in the last TiO_2 layer). Therefore, as confirmed by first-principles calculations, we consider that there is no electric field in the capping layer, and that the potential is flat and at a level raised by the LAO built-in field. This

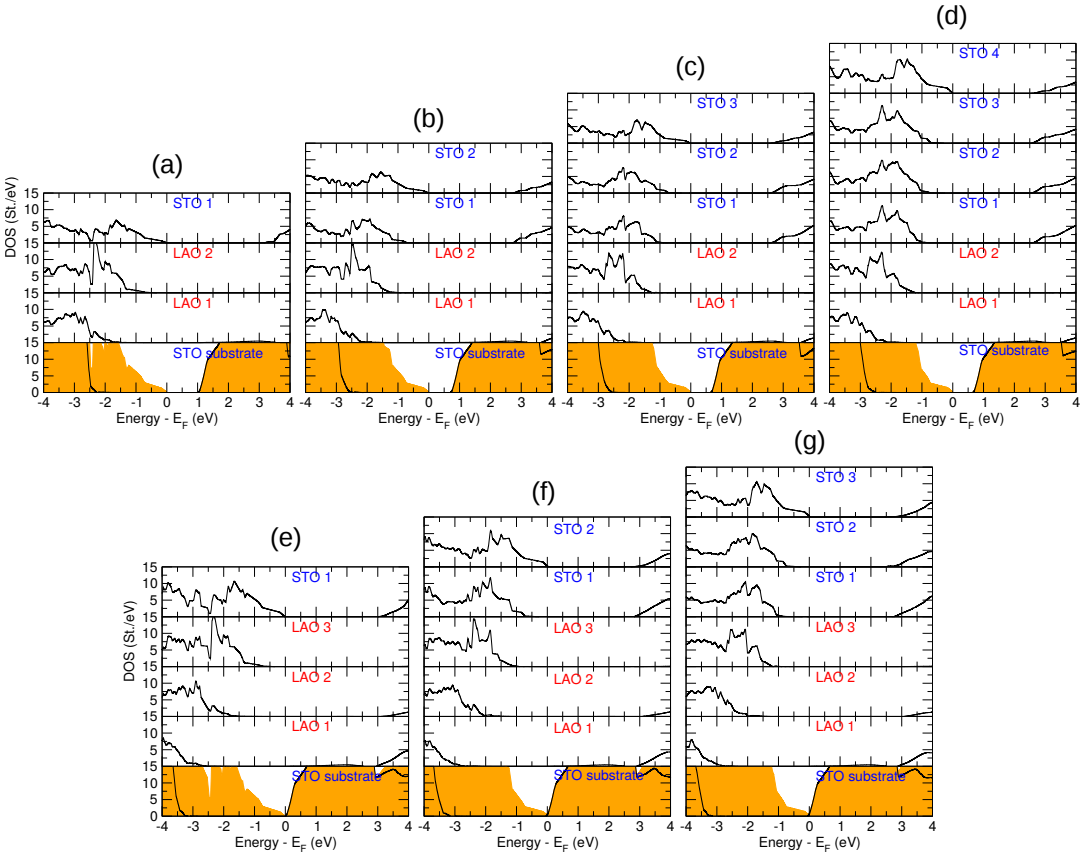

FIGURE 5.11: Layer-resolved density of state of STO(001)/LAOm/STO$_n$ heterostructures, for $m = 2$ and 3 u.c.. The yellow area is the total density of state. The surface of the last STO layer contributes the most to the density of states in the vicinity of the band gap. For $m = 3$ u.c., a small overlap occurs between the surface states and the substrate STO conduction states.

situation is sketched in Figure 5.12.(a), omitting the valence band offset. If an oxygen vacancy (V_O) is created at the surface of the capping layer, two electrons are released and transferred to the lowest conduction states in the system, *i.e.* the Ti t_{2g} states of the STO substrate near the interface, as shown in Figure 5.12.(b). As a consequence of the charge transfer, a 2DES appears at the n-type interface, screening the built-in field in LAO, yet at the origin of an electric field in the STO capping layer, expected to be small from the large STO dielectric constant.

With these considerations, the surface redox model can be rewritten for the capped heterostructures as the surface excess energy Ω accounting for the built-in electric field in the LAO layer, the presence of an area density η of V_O at the STO surface, and the appearance of a field in the STO capping layer:

$$\Omega(\eta) \quad = \quad C\eta + \frac{1}{2}\alpha\eta^2 + \Omega_{\varepsilon,\mathrm{LAO}}(\eta) + \Omega_{\varepsilon,\mathrm{STO}}(\eta) \tag{5.1}$$

where the first term is the chemical cost of creating an array of V_O with an area density η at the surface of the capping layer, the second term is a defect-defect interaction term, $\Omega_{\varepsilon,\mathrm{LAO}}(\eta)$ is the energy gain, released by the electric field in the LAO layer, whereas $\Omega_{\varepsilon,\mathrm{STO}}(\eta)$ is a penalty related to the field raised in the capping layer by the charge

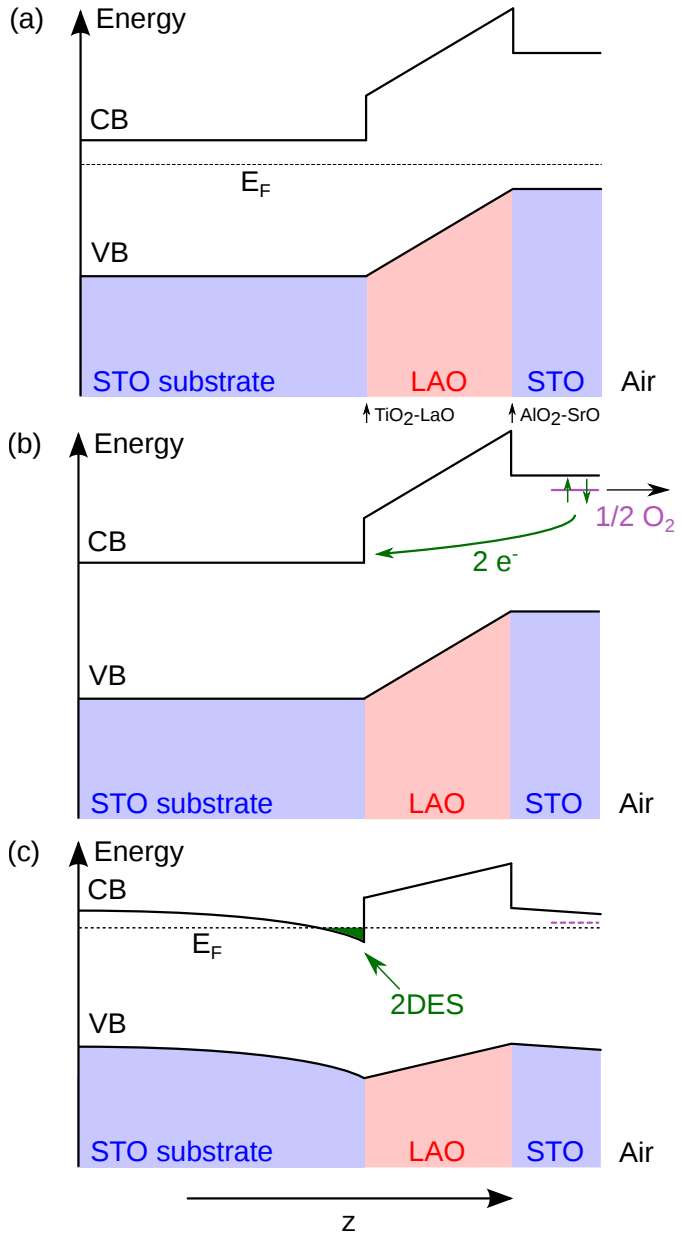

FIGURE 5.12: Schematic band diagram of the STO(001)/(LAO)$_m$/(STO)$_n$ system along the transverse direction z: (a) the pristine system, without oxygen vacancies; (b) the creation of a double donor state through the formation of V_O at the surface. The donor electrons are transferred to the interface, as they are raised above the STO conduction band by the LAO built-in field; (c) the charge transfer compensates the built-in field in LAO, depending on the charge density at the interface. For clarity, we omitted the valence band offsets (known to be small).

transfer. In details, the chemical term is formulated as:

$$C = E^0_{f,\mu} + ZE_{CD} \tag{5.2}$$

where $E^0_{f,\mu}$ is the formation energy of one single V_O at the TiO_2 surface of the capping layer and ZE_{CD} the energy cost of transferring Z electrons at the n-type interface in absence of electric field in the LAO layer. The last two terms of Equation (5.1) are explicitly written as:

$$\Omega_{\varepsilon,\mathrm{LAO}}(\eta) = \frac{d^{\mathrm{LAO}}}{2\varepsilon^{\mathrm{LAO}}}\left[(\sigma_c - \eta Ze)^2 - \sigma_c^2\right] \tag{5.3}$$

$$\Omega_{\varepsilon,\mathrm{STO}}(\eta) = \frac{d^{\mathrm{STO}}}{2\varepsilon^{\mathrm{STO}}}\left[\eta\, Ze\right]^2 \tag{5.4}$$

$\Omega_{\varepsilon,\mathrm{LAO}}(\eta)$ takes the same form as for the bare LAO case, where $\sigma_c = 0.5\ e/\square$ is the nominal charge, d^{LAO} and d^{STO} the LAO and capping layer thicknesses, $\varepsilon^{\mathrm{LAO}}$ and $\varepsilon^{\mathrm{STO}}$ the dielectric constant of the LAO and capping layer dielectric constant. Both terms depends on the density of V_O, η, as well as the amount of electrons transferred ($Z = 2$ in the case of double donors, as expected from defect states raised above the substrate STO CBM). The equilibrium density of V_O η_{eq} at any STO and LAO thicknesses is given by minimizing Ω with respect to η:

$$\left[\frac{\partial\Omega}{\partial\eta}\right]_{\eta=\eta_{eq}} = 0 \tag{5.5}$$

$$\Longleftrightarrow \eta_{eq} = \frac{d^{\mathrm{LAO}} Z\, e\, \sigma_c - C\varepsilon^{\mathrm{LAO}}}{\left[\dfrac{d^{\mathrm{LAO}}}{\varepsilon^{\mathrm{LAO}}} + \dfrac{d^{\mathrm{STO}}}{\varepsilon^{\mathrm{STO}}}\right](Ze)^2\varepsilon^{\mathrm{LAO}} + \alpha\varepsilon^{\mathrm{LAO}}} \tag{5.6}$$

The threshold thickness for the spontaneous appearance of V_O at the surface of the film is given by:

$$d_c^{\mathrm{LAO}} = \frac{C\varepsilon^{\mathrm{LAO}}}{\sigma_c Ze} \tag{5.7}$$

and does not depend on the capping layer thickness.

We aim to fit the model to the *ab initio* formation energies of V_O at the surface, in the same fashion as we did for the bare LAO case in Chapter 3. For this purpose, we perform DFT calculations on STO(001)/LAO$_m$/STO$_n$ including V_O at the TiO_2 surface of the capping layer, with an area density $\eta = 1/4\square$. Before detailing the fitting process, we show in Figures 5.13.(a-j) the layer-resolved densities of state of these defectives structures. We identify a first difference compared to the bare LAO case (shown in Figure 3.23): electrons are indeed transferred to the substrate, but a sizeable amount remains trapped within the STO capping layer. We attribute this as an effect of the LAO depolarization: as the built-in field is compensated, the conduction states of the capping layer are lowered at the same level as those of the STO substrate. This incomplete transfer hinders a simple fit of the model to the first-principles formation energies as performed in Section 3.7.2 for the bare LAO case, and we need to calculate the amount of charge transferred in STO to fix specific values of Z in the model (with $Z < 2$). Another difference is that in this case, it is not possible to identify the defect state, likely lying in the conducting band of the capping layer. Finally, as can be identified in Figures 5.13.(a-j), the in-gap valence states identified at the -TiO_2 surface

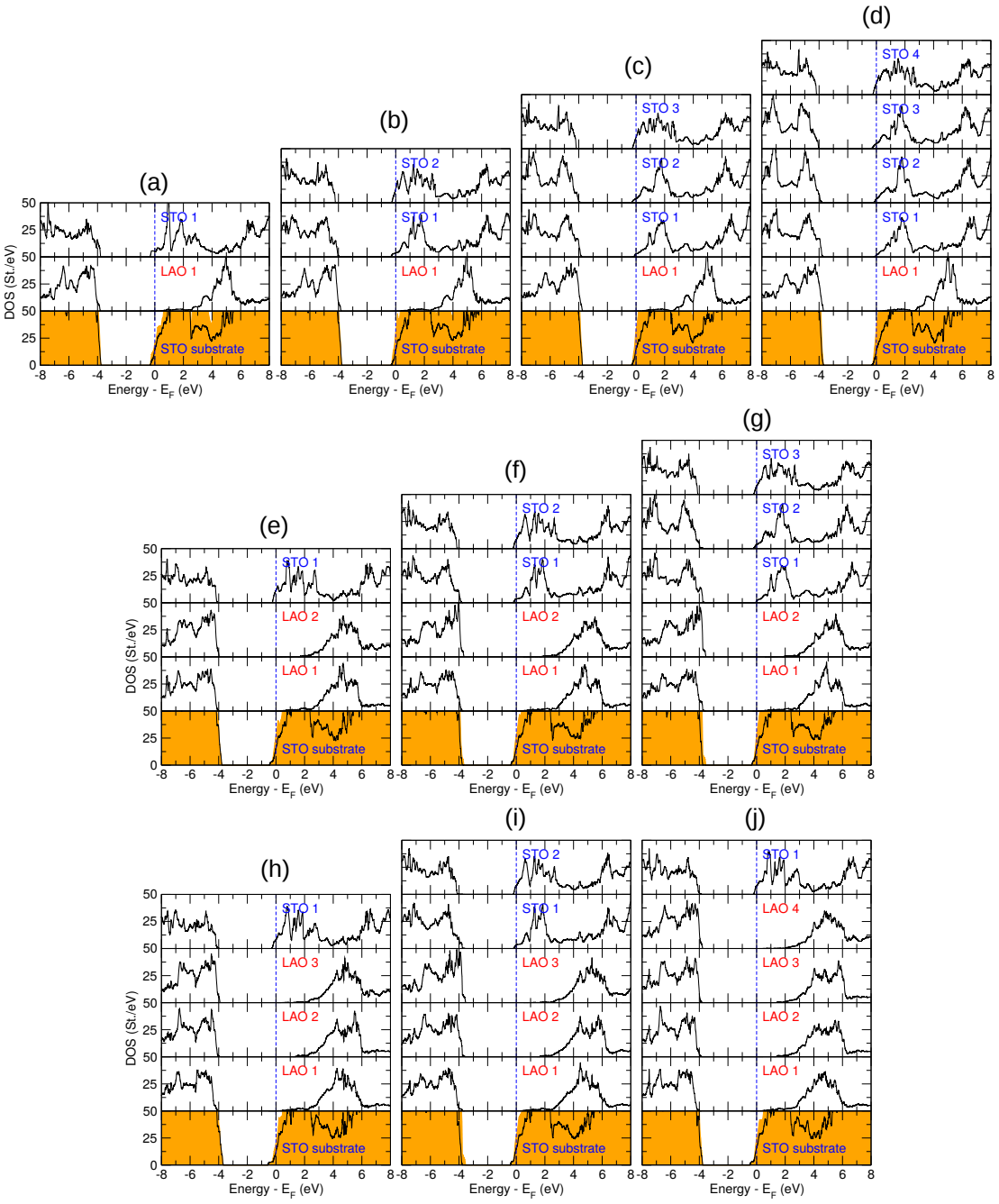

FIGURE 5.13: Layer-resolved density of state of STO(001)/LAO$_m$/STO$_n$/vacuum heterostructures with oxygen vacancies at the TiO_2 surface of the capping layer, with area density $\eta = 1/4\square$, for (a) slab (1,1), (b) slab (1,2), (c) slab (1,3), (d) slab (1,4), (e) slab (2,1), (f) slab (2,2), (g) slab (2,3), (h) slab (3,1), (i) slab (3,2) and (j) slab (4,1). The yellow region shown in the substrate part is the total density of state of the whole structure.

in the pristine slabs are no longer present in the defective structures, and we retrieve the band gap of bulk STO in the outermost STO layer (∼3.6 eV).

For the calculation of the parameters for the model, we proceed as follows: the Z term accounting for the amount of electron transferred is calculated by the Mulliken scheme [175]. The dielectric constants are set as $\varepsilon_r^{\mathrm{LAO}} = 22$ and $\varepsilon_r^{\mathrm{STO}} = 250$: the former

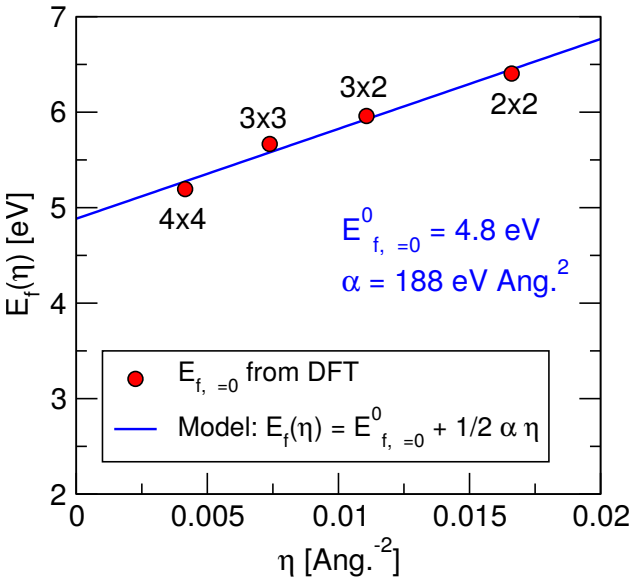

FIGURE 5.14: Formation energies of oxygen vacancies ($\mu_O = 0$ eV) at the TiO_2 surface of a bare STO film calculated from DFT within supercells of different size to probe different area densities η. The evolution of the formation energies with η is fitted through a linear model, the projection to $\eta = 0$ yields $E^0_{f,\mu=0} = 4.8$ eV.

is a result of the fit performed in the study for the bare LAO case as done in Chapter 3, whereas the other is simply the bulk value[1]. Then, we need to calculate the first two terms of Equation 5.1. For this purpose, we calculate $E_{f,\mu=0}$ for V_O at the surface of a bare STO film[2] at different area density η: the results are shown in Figure 5.14. We witness a strong dependence of the calculated formation energy with respect to the supercell size: to account for this dependence, we fit a linear model to account for this apparent V_O-V_O interaction, in a mean-field fashion. The projection to $\eta = 0$ yields $E^0_{f,\mu=0} \approx 4.8$ eV, with an effective interaction term $\alpha = 188$ eV Å^2. A previous similar study in the literature also reported such a strong dependence on the density [176]. The chemical potential of oxygen μ_O takes the same value as in Chapter 3: $\mu_O = -2$ eV, as the growth conditions of the capped samples are similar to that of standard STO/LAO samples (details in Appendix A), leading to $E^0_{f,\mu} \approx 2.8$ eV. From the analysis of the density of state, we estimate $E_{CD} = 0.36$ eV. Finally, based on the analysis of the formation energies calculated from DFT on the STO(001)/LAO$_m$/STO$_n$ structures, we modify $E^0_{f,\mu}$ as a capping layer thickness dependent quantity with a slight saturating decay:

$$E^0_{f,\mu}(d^{\mathrm{STO}}) \quad = \quad 2.7 + 2.2\ \exp\left(-d^{\mathrm{STO}}/0.37a^{\mathrm{STO}}\right) \tag{5.8}$$

expressed in eV, yielding a slight decay from 2.9 eV to 2.7 eV with increasing STO thickness. This will be justified in the following section.

[1] It may be surprising that the dielectric constant of the thin STO film $\varepsilon_r^{\mathrm{STO}}$ would remain as large as it is in its bulk. This is justified by the low dependence on STO thickness of the formation energies of V_O as calculated from DFT compared to the dependence on the LAO thickness, implying that the charge transfer does not raise a large field in the STO capping layer. Hence, even if $\varepsilon_r^{\mathrm{STO}}$ depends on the STO thickness, it remains much larger than that of LAO and this approximation is justified.

[2] A vacuum/STO$_{7.5}$/vacuum symmetric slab with two V_O at both surfaces, within a 2×2, 3×2, 3×3 and 4×4 supercells.

m (u.c.)	n (u.c.)	Z	$\Omega_{\varepsilon,\mathrm{LAO}}(\eta)/\eta$	$\Omega_{\varepsilon,\mathrm{STO}}(\eta)/\eta$	$\Omega(\eta)/\eta$	$E_{f,\mu}^{\mathrm{DFT}}$
4	1	1.61	-3.98	0.06	1.07	1.12
3	2	1.39	-2.82	0.09	2.04	2.00
3	1	1.40	-2.82	0.05	2.13	2.04
2	3	1.28	-1.80	0.11	3.03	3.06
2	2	1.32	-1.83	0.08	3.00	2.98
2	1	1.46	-1.92	0.05	3.06	3.11
1	4	0.80	-0.66	0.06	3.95	3.94
1	3	0.97	-0.76	0.07	3.92	3.91
1	2	0.97	-0.76	0.04	3.90	3.90
1	1	1.08	-0.81	0.03	4.01	4.02

TABLE 5.1: Comparison between the surface redox model and the DFT formation energies calculated from capped STO(001)/LAO$_m$/STO$_n$ heterostructures with surface oxygen vacancies at area density $\eta = 1/4\square$. For all defective systems, we specify the thickness of the LAO and STO capping layer m and n, the amount of transferred electrons Z, as well as the two terms $\Omega_{\varepsilon,\mathrm{LAO}}(\eta)/\eta$ and $\Omega_{\varepsilon,\mathrm{STO}}(\eta)/\eta$. The last two columns on the right are the prediction of the model $\Omega(\eta)/\eta$, with the parameters set as described in the main text, and the DFT formation energies $E_{f,\mu}^{\mathrm{DFT}}$ as calculated from Equation (3.2).

5.5 Results and discussion

The results of the model is given in Table 5.1, compared directly to the DFT formation energies calculated at density $\eta = 1/4\square$. Again, the right quantity to compare with the DFT results is $\bar{E}_f = \Omega(\eta)/\eta$, corresponding to the energy difference between the system with a given density η of surface V_O and the pristine system ($\eta = 0$), per surface V_O:

$$\begin{aligned} \bar{E}_f &= \frac{1}{\eta}\Omega(\eta) \\ &= C(d^{\mathrm{STO}}) + \frac{1}{\eta}\Omega_{\varepsilon,\mathrm{LAO}}(\eta) + \frac{1}{\eta}\Omega_{\varepsilon,\mathrm{STO}}(\eta) + \frac{1}{2}\alpha\eta \end{aligned} \tag{5.9}$$

The model $\Omega(\eta)/\eta$ is in satisfying agreement with the DFT formation energies $E_{f,\mu}^{\mathrm{DFT}}$ as shown in the two columns on the right side of Table 5.1, with absolute errors below 0.1 eV. The slight decay of $E_{f,\mu}^{\mathrm{DFT}}$ calculated for slabs (1,n = 1, 2, 3 u.c.) with $Z \approx 1$ motivated to model a formation energy with a slight dependence on the capping layer thickness d^{STO}. We attribute this evolution with the change in rumpling at the TiO_2 surface (and associated bond length) of the capping layer, as shown in Figure 5.8.(a), which also saturates quickly with d^{STO}. Looking at the DFT formation energies, they are mainly dependent on the $\Omega_{\varepsilon,\mathrm{LAO}}(\eta)/\eta$ term. The $\Omega_{\varepsilon,\mathrm{STO}}(\eta)/\eta$ term is one order of magnitude smaller, as the dielectric constant STO is one order of magnitude larger than that of LAO.

As the model and the DFT formation are in satisfying agreement, we can estimate the equilibrium density of oxygen vacancy η_{eq} as calculated from Equation 5.6. For this purpose, we consider that, at low η, the built-in field in LAO is sufficiently large to avoid any trapping from the STO capping layer, so that the conduction states of the capping layer remains above the Fermi level, and we fix $Z = 2$. The equilibrium density

η_{eq} is shown in Figure 5.15 with respect to the number of LAO and STO layers. The predicted critical thickness of LAO for the capped structures is $d_c^{\mathrm{SR,LAO}} = 1.6$ u.c.. This threshold thickness is below the onset for conductivity calculated for pristine structures ($\sim$2.5 u.c.): the energy cost of creating V_O at the TiO_2 surface of the capping layer is smaller than the energy cost associated with creating such vacancy at the LAO surface, resulting in a smaller critical thickness compared to that of standard STO/LAO.

This result is in good agreement with observed conductivity for STO(001)/LAO$_2$/STO$_n$ samples of Reference [89]. The predicted sheet carrier density at this LAO thickness is $\sim 5 \times 10^{13}$ cm^{-2}; this value is in agreement with the carrier density extracted from Hall measurements of Reference [88].(b) for a (2,10) sample as shown in Figure 5.2 from 50 K to 300 K, roughly $4 - 6 \times 10^{13}$ cm^{-2}. The insulating phase observed for the STO(001)/LAO$_1$/STO$_n$ samples with $n < 10$ u.c. can also be understood within this model: for $n \geq 10$ u.c., we can only speculate that the STO film is thick enough to contain enough oxygen vacancies to significantly dope the interface. For thicker LAO interlayer, η_{eq} converges toward the saturating value $\eta = 1/4\square$ in the infinitely thick limit.

For thick enough LAO, we expect a situation similar to the one computed from DFT, as shown in Figure 5.13, with a fraction of the electrons trapped within the capping layer. This situation corresponds to two spatially separated 2DES sheets, one confined near the n-type interface within the substrate, the other kept within the STO capping layer and decaying from the TiO_2 surface, as shown in Figure 5.16. Such a situation would explain why the properties of the two probed interfaces in the study of Lee *et al.* [123] are so eerily similar in term of mobilities and sheet carrier density, even though the slope of the Hall resistance is reportedly negative for the interface with the capping layer. We also notice that if 50% of the charge is trapped in the capping layer, then the expected carrier density at the n-type interface is expected to saturate to 0.25 $e^-/\square$ or 1.65×10^{14} cm^{-2}, remarkably close to the saturating values reported by Huijben *et al.* [88] for thick LAO interlayer as shown in Figure 5.1.(b). It is also reported in Reference [88] that the sheet resistance of the p-type interface is roughly $\sim 10^7$ $\Omega/\square$, *versus* $\sim 10^4$ $\Omega/\square$ for the n-type interface and $\sim 10^9$ $\Omega/\square$ for the insulating interface. Hence, even though the p-type interface is about 1000 times less conducting than the n-type interface, it is 100 times more conducting than the insulating interface. This is another argument in favour of a doped STO capping layer, likely from surface V_O as predicted by our model and DFT calculations.

At this stage, we also remark several reports of bare STO films with conducting interface when annealed in ultra-high vacuum [177–179], with similar downward band bending as for the n-type interface of STO/LAO, the origin of the carriers attributed to the presence of V_O near the surface. In the case of the capped STO(001)/LAO$_m$/STO$_n$ heterostructures, the formation of V_O at the surface of the capping layer remains driven by the electric field in the LAO interlayer and is stabilized at higher oxygen partial pressure.

Bristowe *et al.* [117] proposed that the empty donors at the surface of the film and the associated potential generated from their effective charge may trap carriers at the interface between the STO substrate and LAO. In the case of oxygen vacancies, such a

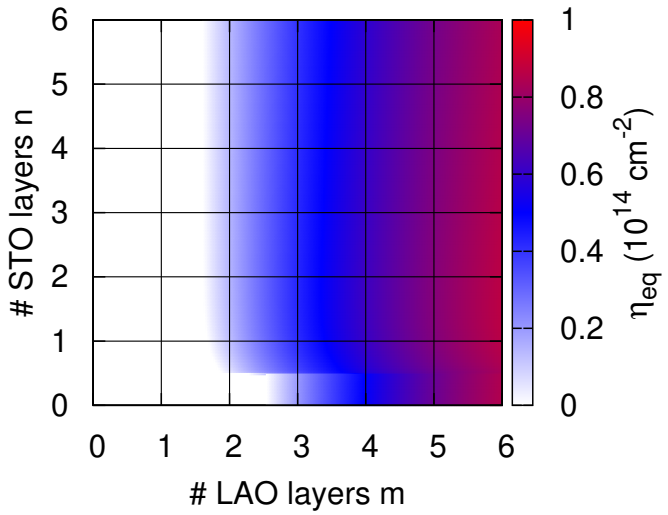

FIGURE 5.15: Equilibrium density of surface oxygen vacancies η_{eq} for STO(001)/LAO$_m$/STO$_n$ as determined by the surface redox model, calculated from Equation (5.6). For $n = 0$, the parameters of the model are set as calculated in Chapter 3, to highlight the change with respect to the uncapped case.

trapping potential would take the form:

$$V_{\text{trap}} = \frac{Ze^2}{\varepsilon^{\text{LAO}}\sqrt{\rho^2 + d_{\text{LAO}}^2}} \tag{5.10}$$

where $\rho = \sqrt{x^2 + y^2}$ is the radial variable in the plan of the interface. Such a potential generates trapping states in the band gap (up to ~ -200 meV below the Fermi level, estimated as the ground state energy of a quadratic fit of the well for $m = 1$). The density of trap increases with LAO thickness, but as the film thickness increases, the trapping potentials also get shallower, releasing the carriers. In the case of STO(001)/LAO$_m$/STO$_n$, the trapping potential of one V_O becomes:

$$V_{\text{trap}} = \frac{Ze^2}{\varepsilon^{\text{x}}\sqrt{\rho^2 + (d_{\text{STO}} + d_{\text{LAO}})^2}} \tag{5.11}$$

where $\varepsilon^{\text{x}} = \varepsilon^{\text{LAO}}(\varepsilon^{\text{LAO}} + \varepsilon^{\text{STO}})/2\varepsilon^{\text{LAO}} \approx 136$. In this picture, the potential wells are roughly 6 times shallower in contrast to the uncapped heterostructures for the same LAO thickness. Hence, the additional role of the capping layer is to screen the trapping well potentials, allowing 2D conduction as early as the donor electrons are transferred to the substrate, in agreement with the conductivity observed on STO(001)/LAO$_2$/STO$_1$ samples [89]. This simple picture assumes that films as thin as 1 u.c. retains dielectric properties close to their thick/bulk phases. The dielectric constant of the STO capping layer could also be influenced by intermixing.

5.6 Conclusions

In this Chapter, we discussed the electronic properties of STO(001)/LAO$_m$/STO$_n$ heterostructures, which present the peculiar property of being metallic at smaller LAO

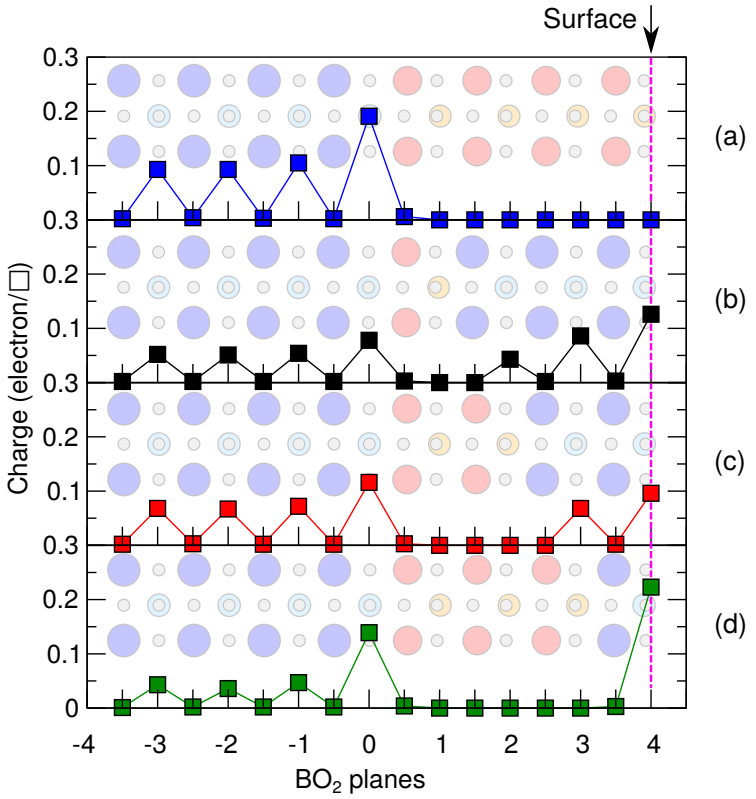

FIGURE 5.16: Charge distribution of STO(001)/LAO$_m$/STO$_n$ heterostructures with V_O at the surface layer at density $\eta = 1/4\square$, for structures (a) (4,0), (b) (1,3), (c) (2,2) and (d) (3,1). The BO_2 planes are labelled with integers, 0 corresponds to the TiO_2 plane at the n-type interface. The profile of charge density in the substrate and in the STO capping layer are similar, despite the small thicknesses in the simulation cell.

thicknesses than that of standard STO(001)/LAO$_m$ interface ($m \geq 4$ u.c.). The observed conductivity cannot be explained within the Zener breakdown scenario: both experiments [122] and our theoretical results predicts a sizeable electronic band gap for LAO thickness at $d^{\mathrm{LAO}} = 2$ u.c. between the O $2p$ valence states of the capping layer and the Ti t_{2g} conduction states of the STO substrate. On the other hand, the surface redox model of Bristowe *et al.* [117, 130] adapted to the case of capped heterostructures predicts a threshold thickness in good agreement with the observed conductivity in the samples of Pentcheva *et al.* [89]. Nevertheless, some discrepancies with experiments remain. Most of the groups [89, 122, 123, 171] who studied these capped heterostructures argue that the STO capping layer hosts a 2-dimensional hole gas. However, we predict that the surface redox processes are energetically more stable than the creation of electron-hole pair across the LAO film, and that at large LAO thickness, both the substrate and the capping layer may hold a 2DES. In addition, we were unable to find an explanation for the trend observed in the data of our collaborators from the University of Geneva (Figure 5.5). Clearly, these capped structures propose interesting features not present in standard STO/LAO, and a better understanding of their observed transport properties would secure the prospects of exploiting these heterostructures for technological applications.

Chapter 6

A modest introduction to thermoelectrics

In this chapter, we present the basics of thermoelectricity, starting from the phenomenology. We then briefly review some of the proposed strategies to improve the TE efficiency.

6.1 Introduction

Energy harvesting and energy conversion are the most fundamental aspects of any kind of technological application: using the motrice force of the wind (or water) to run the mills, using the power of combustion of coal or oil to drive a train or a car, *etc.* The involved processes obey the laws of thermodynamics: energy is furnished (Q) to a system, which transforms it into useful work ($\mathcal{W}$). In a lot of situations, the conversion process can be quite efficient. For example, in Li-ion batteries, the energy is stocked in chemical form, and is then transformed into electrical energy with an efficiency $\eta = \mathcal{W}/Q$ of nearly 100% [180]. Similarly, an electric engine can transform up to 98% of its input load into mechanical work [181].

Since energy is a conserved quantity, the eventual losses designate the part of the energy which is not transformed as useful work. In the last two examples, they are negligible, but this should not be taken as a general statement. In particular, it is impossible to fully convert energy in the form of heat into useful work. An upper limit of efficiency is set by the Carnot heat engine, which involves a theoretical thermodynamic cycle only involving reversible processes. This is related to the second law of thermodynamic, which stipulates that the entropy of an isolated system can never decrease over time: indeed, in a material under a temperature gradient, heat flows irreversibly from the hot side to the cold side, unless external work is provided. Without any external work, this irreversibility is formulated as an increase of entropy in the system. Consequently, the efficiency η of a real engine with a cold source at temperature T_c and a hot source at temperature T_h will always be inferior to the efficiency of a Carnot engine η_{Carnot}:

$$\eta \quad < \quad \eta_{\text{Carnot}} = 1 - \frac{T_c}{T_h} \tag{6.1}$$

so that ultimately, only a fraction of the provided energy is turned into useful work $\mathcal{W}$. A common example is internal combustion engines based on gasoline, as used in automobiles: their thermal efficiency is usually between 25% and 50%, which means that between 50% and 75% of the total heat released by the combustion of the fuel is lost [182] and is evacuated in the environment.

The issue of energy losses has always accompanied the conversion process. The growing environmental concerns stress sizeable efforts to optimize the current energy conversion processes to limit the waste, and consequently stimulate the motivation to find alternative, cleaner energy sources. In the current days, most of the energy resources are consumed in the form of heat provided by the combustion of fossil fuels (mainly oil, coal and natural gas, as shown in Figure 6.1). Broadly speaking, up to 70 % of the heat produced by their combustion is wasted, and mainly rejected in the environment. These wastes are usually completely lost, and serve no purpose despite humanity's ever-growing energy consumption (Figure 6.1). Moreover, concerning waste recycling, there are technical issues related to the traditional conversions processes as the wastes are usually in temperature ranges below 700 K, and present strong variations of power density. Finally, they are stocked in various environment, which hardens the task of harvesting such wastes.

These are the reasons why there is a growing interest in developing efficient thermoelectric (TE) modules, which have the peculiar property to convert heat into electrical power, and *vice-versa*. These TE devices are quite interesting, as electric energy can be stored and be used for later purposes. TE conversion also has numerous advantages: no dependence on the heat source, the easy setup, the longevity of the technology as there are no moving parts involved in the conversion process. TE generators are composed of several submodules, which are thermocouples composed of n-type and p-type semiconductors, as displayed in Figure 6.2. The heat gradient is accompanied concomitantly by the diffusion of majority carriers in both n-type and p-type elements, in the same direction, producing an overall voltage which can be used for electrical power generation.

The lack of exploitation of current TE generators for generic purposes is due to their weak efficiency. As a consequence, as of today, they have been used in rather niche applications. For example, TE modules are used to provide a constant source of energy for the elements of space probes (such as the Voyager probes, displayed in Figure 6.3) requiring to be active over a large period of time. Indeed, photovoltaic power sources become quickly useless when moving far away from the Sun, as the received solar power decreases with a $1/r^2$ law. Hence, the use of TEs is a better option, as long as one can provide a durable heat source. Radioisotope TE generators were designed in this spirit, using the heat generated by decaying radioisotopes. The Voyager probes, more than 40 years after launch, are in the current days roughly 21 billion kilometres away from the Sun, still recording data. The curious reader can check the status of the mission on the NASA website[1].

TE generators are also used inside exhaust pipes of automobiles to convert the wasted heat into electricity. Following this spirit, there is good hope to use them in power plants or industries to convert waste heat, recovering a fraction of the lost energy, bringing additional electrical power.

In addition to power generation, TEs can also be used for cooling applications. These TE devices are known as Peltier coolers, and are mainly used to cool down electronic

[1] `https://voyager.jpl.nasa.gov/mission/status/`.

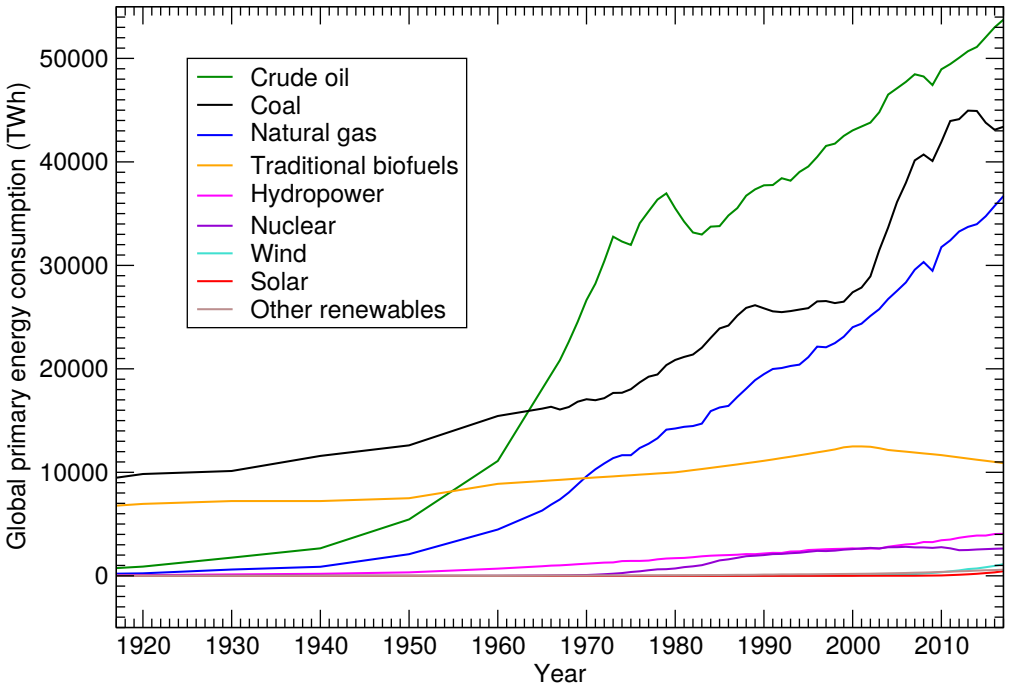

FIGURE 6.1: Global primary energy consumption per year, from 1917 to 2017. "Other renewables" are renewable sources not including solar, wind, hydropower and traditional biofuels. Adapted from [183, 184].

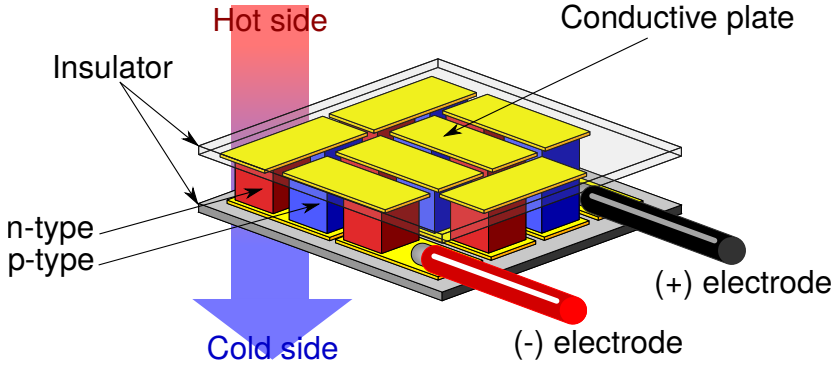

FIGURE 6.2: Schematic representation of a Seebeck power module which generates electrical power from a temperature gradient. Such a module is made of several thermocouples (composed of a n-type and p-type semiconductors).

component subject of the Joule effect. They are also used for more generic purpose, as camping/car coolers or temperatures regulators. Finally, as TE modules can serve as both cooler/electrical power generators, they have been proposed to be used in combination with photovoltaic modules. Indeed, the efficiency of photovoltaic devices decreases as they are heated up. Combined with a photovoltaic module, the TE modules can simultaneously reduce the decrease of performance of the photovoltaic part, while providing additional electrical power output [185].

Even without ever reaching the efficiency of other traditional methods for converting heat into electricity, the use of TEs to harvest waste energy is a sufficient motivation: no matter the amount, any gain is good. Moreover, as the traditional energy sources may become scarcer in the future, TEs use may become mainstream.

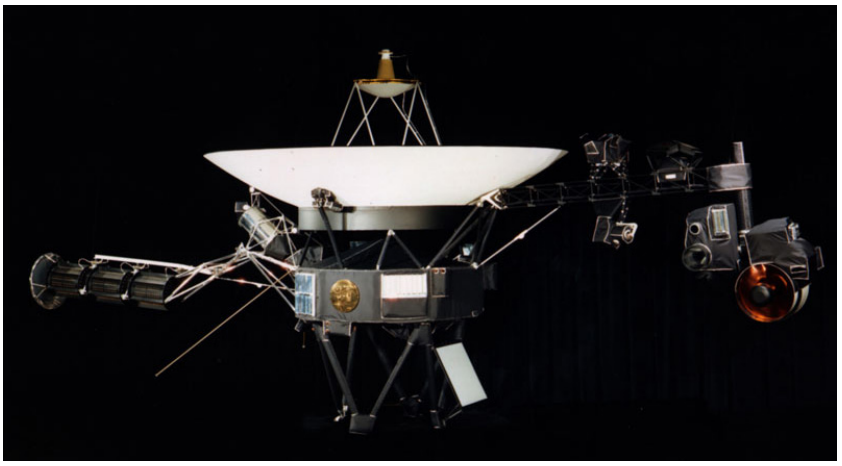

FIGURE 6.3: One of the two Voyager probes. They both use a radioisotope thermoelectric generator (the tube on the left side) to provide an electrical output to their machinery. Adapted from Reference [186].

However, there are several issues which need to be resolved. Nowadays, the best TEs devices are made of compounds composed of Si, Te, Pb or Se, such as Bi_2Te_3 or SnSe, and are not adapted for large scale applications for several reasons:

1. the production costs are high, as some of the aforementioned elements are rare and/or requires to be refined for applications;
2. some of these compounds are also toxic;
3. the stability at high temperature is not guaranteed.

In addition to improving the performance of known good TEs, current research also focus on alternative materials which do not present the aforementioned inconveniences, even if their TE properties are not as good as Bi_2Te_3- or SnSe-based compounds. The search for novel, cheap, non-toxic and robust TE materials for a broader number of applications may yield a profitable market for industries.

6.2 Phenomenological approach to thermoelectrics

In this section, we present a small historical introduction to thermoelectricity, from the discovery of TE effects to the characterization of the performance of TE compounds. The developments in the current Section are inspired from Reference [187].

6.2.1 The Seebeck effect

Thomas Johann Seebeck (1770 - 1831) discovered the first TE effect in 1821. His experimental setup was made of two different conductors a and b, connected together with junctions at their extremities, and a metallic compass in between the two conductors. He observed that the needle of the compass would be deflected by applying a temperature gradient across the setup, as illustrated in Figure 6.4. His first assumption was that the needle was deflected by a magnetic field. However, it was discovered later that

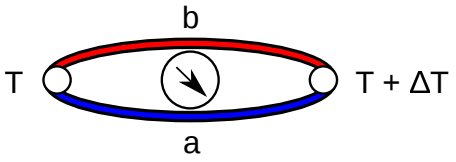

FIGURE 6.4: The experimental setup used by Seebeck to discover the first thermoelectric effect. When a temperature gradient is applied across the setup (here, with a finite difference ΔT between the left and right side), a difference of electrical potential appears at the junction. The needle of the compass can be deflected from this effect.

a difference of electrical potential appeared at the junction of the two materials if they are subject to a temperature gradient. This is the so-called *Seebeck effect*.

The Seebeck coefficient of a material, or thermopower, is the measure of the magnitude of an induced difference of electric potential ΔV in response to the temperature gradient ΔT across that material. In the case of the setup of Seebeck, with conductors a and b, it is expressed as:

$$\Delta V = S_{ab}\ \Delta T \tag{6.2}$$

The Seebeck effect can be exploited for different applications. On one hand, providing a load with a voltage can induce an electric current, which can be used to power electronic devices. On the other hand, the linear response of the Seebeck effect can be used to measure temperatures: this is the operational principle of a thermocouple. The higher the Seebeck coefficient, the higher the electric field.

6.2.2 Peltier and Thomson Effects

Jean-Charles Peltier (1785 - 1845) observed a second TE effect in 1834: if a voltage is applied to two different materials a and b connected in a junction, a temperature gradient appears at this junction. This means that when a current is flowing across the junction, one material generates heat whereas the other absorbs heat. This is the so-called *Peltier effect*.

The linear response with respect to a current can be written in the following way: the produced/absorbed heat Q is proportional to the current I through the Peltier coefficient Π_{ab}, which is a characteristic of the couple a and b:

$$Q = \Pi_{ab} I \tag{6.3}$$

Following the discovery of Peltier, Lord Kelvin predicted and observed that both the Seebeck and Peltiers effects are related: a particular material under a temperature gradient, and traversed by an electric current, exchanges heat with its environment. The reverse is also true: an electric current is generated when the material experiences a temperature gradient, with heat flowing through it. This phenomenon is called *Thomson effect*; the main difference between the Peltier and Seebeck effects is that it does not involve junctions, only a single material.

The Seebeck, Peltier and Thomson effects offer many perspectives for TE applications. On one hand, materials with large TE response could be used for refrigeration or for

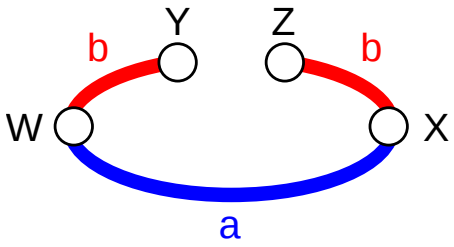

FIGURE 6.5: A basic thermoelectric circuit, made of two materials a and b. For the purpose of describing the relations involved in thermoelectricity, the junctions and extremities are explicitly named.

precise temperature regulation. On the other hand, transforming heat into electricity represent a clean energy source, as there is no by-product in the conversion process, which is of particular interest given the current environmental concerns.

6.3 Basic principles and thermoelectric coefficients

In the phenomenological description of TE, we considered coefficients adapted to a given thermocouple. We need to address their relations to the individual TE coefficients of each materials composing a thermocouple. We consider a basic circuit, composed of two materials a and b, linked together by two junctions X and W, as illustrated in Figure 6.5. In the case of the Seebeck effect, a difference of temperature dT is applied between the junctions X and W, which results in a voltage dV between extremities Y and Z.

In an open circuit, we define the Seebeck coefficient S_{ab} of the thermocouple a and b:

$$S_{ab} = \frac{dV}{dT} \tag{6.4}$$

The sign of S_{ab} is such that if the temperature at junction W is higher than the temperature at junction X, and if the resulting voltage is such as $V_Y > V_Z$, then $S_{ab} > 0$.

For the Peltier effect, a current I flowing through the circuit induces an absorption of heat at one junction, and a production of heat in the other, with a heat pump rate Q. Similarly to the Seebeck coefficient, the Peltier coefficient is defined for the couple a and b:

$$\Pi_{ab} = \frac{Q}{I} \tag{6.5}$$

Finally, let us consider the Thomson effect, where both an electric current and a temperature gradient are applied. Heat is generated or absorbed in each part of the thermocouple, a and b individually. The gradient of the heat flux in each branch is given by:

$$\frac{dQ}{dz} = \tau I \frac{dT}{dz} \tag{6.6}$$

where z is a spatial coordinate along the temperature gradient and τ is the Thomson coefficient of the material (either a or b, with respective τ_a and τ_b). The interdependence

of their related coefficients are given by the Kelvin relations:

$$\Pi_{ab} = S_{ab}T \tag{6.7}$$

$$\tau_a - \tau_b = T\frac{dS_{ab}}{dT} \tag{6.8}$$

In practice, TE applications require at least two materials in association to form junctions. The Seebeck and Peltier coefficient have been defined for a given couple a and b. Yet, for the sake of optimization of each part individually, it is important to know the absolute coefficients related to each material (S_a, S_b, Π_a and Π_b), which are given by the following relations:

$$S_{ab} = S_a - S_b \tag{6.9}$$

$$\Pi_{ab} = \Pi_a - \Pi_b \tag{6.10}$$

In practice, the thermopower of a thermocouple contains the contributions coming from both parts a and b. It is possible to measure the response of a single material by using superconductors, as their electrons do not carry entropy. Therefore, since superconductors have zero thermopower, and they can be exploited to measure the absolute coefficients of a given material. Finally, these coefficients also follow the relations of Kelvin:

$$\Pi_a = S_a\, T \tag{6.11}$$

$$\tau_a = T\frac{dS_a}{dT} \tag{6.12}$$

Now that the phenomenology between current and heat pump rate has been described, we can focus more precisely on how TE efficiency is determined, which is the topic of the next Section.

6.4 Transport equations and Figure of Merit

Let us consider a thermocouple made of two doped semiconductors: one is p-type doped, with $S_p > 0$ and the other is n-type doped with $S_n < 0$. These semiconductors are connected by a conductor and we assumes that its thermopower is equal to zero (in general, metals have low thermopower).

In the following description, we also assume that thermal conduction through convection and/or irradiation is negligible, and that the electrical and thermal conductivities do not depend on temperature. These considerations simplify the following developments. The key aspect of a TE module is that all the thermocouples are connected together in serie for electrical transport, and in parallel for heat transport.

To further simplify the description without loss of generality, we only consider a single thermocouple, with one n-type and p-type material and the same section. This thermocouple is connected to a difference of potential ΔV, and works as a TE cooler, as illustrated in Figure 6.6. The n-type branch has a negative S, whereas the p-type branch has a positive S. They are both connected by a metallic interconnect. The objective is to determine the efficiency of such a thermocouple from thermodynamics. The current in the thermocouple is such that the majority carriers in both semiconductors goes from the cold side to the hot side. Therefore, both electrons and holes carry entropy from the

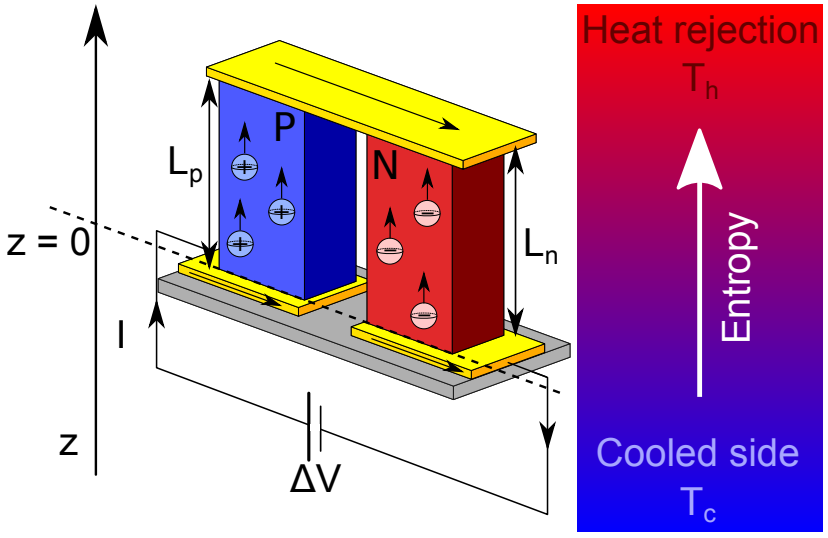

FIGURE 6.6: A diagram of a single-couple refrigerator. Both holes and electrons goes from the cold side to the hot side.

cold side to the hot side, and the thermal flux induced by the current is opposed to the thermal conduction (from hot side to the cold side).

The total heat pump rate can be written, for each branch, as:

$$Q_p = S_p I T - \kappa_p A_p \frac{dT}{dz} \tag{6.13}$$

$$Q_n = -S_n I T - \kappa_n A_n \frac{dT}{dz} \tag{6.14}$$

κ_p and κ_n are the thermal conductivities of the p-type and n-type branches, A_p and A_n are their respective sections. Heat is removed from the cooled side with a total rate Q_c:

$$Q_c = (Q_n + Q_p)|_{z=0} \tag{6.15}$$

Simultaneously, a Joule effect occurs in the circuit due to the electric current I. The generated heat by this effect is equal to $\frac{I^2\rho}{A}$, where ρ is the resistivity. The energy conservation can be written for both branches of the couple by considering that the Joule heat supply is balanced by a non constant thermal gradient:

$$\kappa_p A_p \frac{d^2T}{dz^2} = \frac{I^2\rho_p}{A_p} \tag{6.16}$$

$$\kappa_n A_n \frac{d^2T}{dz^2} = \frac{I^2\rho_n}{A_n} \tag{6.17}$$

Since S is assumed temperature independent, the Thomson coefficient is zero (from Equation (6.12)) and the TE current does not supply or extract heat within the branches.

We need to consider the following boundary conditions. If L_n and L_p are the lengthes of each n-type and p-type branch: at the cold source ($z = 0$), the temperature is equal to the temperature of the cold source. At the hot source ($z = L_p$ or $z = L_n$), the temperature is equal to the temperature of the hot source. The boundary conditions

are then expressed as:

$$T = T_c \quad \text{at} \quad z = 0 \tag{6.18}$$
$$T = T_h \quad \text{at} \quad z = L_n \text{ or } z = L_p \tag{6.19}$$

so that Equations (6.16) and (6.17) yield:

$$\kappa_p A_p \frac{dT}{dz} = -\frac{I^2 \rho_p \left(z - \frac{1}{2}L_p\right)}{A_p} + \frac{\kappa_p A_p (T_h - T_c)}{L_p} \tag{6.20}$$
$$\kappa_n A_n \frac{dT}{dz} = -\frac{I^2 \rho_n \left(z - \frac{1}{2}L_n\right)}{A_n} + \frac{\kappa_n A_n (T_h - T_c)}{L_n} \tag{6.21}$$

Substituting these results in Equations (6.13) and (6.14) and using (6.15), the net heat pumping rate Q_c becomes:

$$Q_c = (S_p - S_n) I T_c - K\Delta T - \frac{1}{2} I^2 R \tag{6.22}$$

where $\Delta T = T_h - T_c$, K is the thermal conductance and R is the electrical resistance of the circuit, both defined as:

$$K = \frac{\kappa_p A_p}{L_p} + \frac{\kappa_n A_n}{L_n} \tag{6.23}$$
$$R = \frac{L_p \rho_p}{A_p} + \frac{L_n \rho_n}{A_n} \tag{6.24}$$

Both Joule and Seebeck effects contribute to the dissipated power $\mathcal{W}$:

$$\mathcal{W} = I\left[(S_p - S_n)\,\Delta T + IR\right] \tag{6.25}$$

The coefficient of performance COP of the TE cooler is the ratio between the extracted heat Q_c and the dissipated electric power $\mathcal{W}$. From Equations (6.22) and (6.25), it follows:

$$\text{COP} = \frac{Q_c}{\mathcal{W}} = \frac{(S_p - S_n)\, I T_c - K\Delta T - \frac{1}{2} I^2 R}{I\left[(S_p - S_n)\,\Delta T + IR\right]} \tag{6.26}$$

It can be observed that, at a given fixed temperature difference ΔT, the efficiency depends on the applied current I. It is then possible to determine which current maximize the efficiency.

An analogous development can be made to determine the efficiency η_e of a thermocouple designed for electricity production. The efficiency is defined as the ratio between the useful electric work delivered to a load resistance r_L and the heat pump rate across the device Q_c:

$$\eta_e = \frac{\mathcal{W}_{useful}}{Q_c} = \frac{I\left[(S_p - S_n)\,\Delta T + IR\right]}{(S_p - S_n) I T_c - K\Delta T - \frac{1}{2} I^2 (R + r_L)} \tag{6.27}$$

This expression can be used to find the current maximizing the efficiency. If the COP and η_e are optimized, it can be shown that the associated extremal values only depend on the temperatures T_c and T_h, as well as the so-called Figure of Merit $Z_{pn}T_A$ of the thermocouple with $T_A = (T_c + T_h)/2$, the average temperature.

Z_{pn} is expressed as a function of the intrinsic absolute coefficients related to the p-type and n-type parts of the thermocouple:

$$Z_{pn} = \frac{(S_n - S_p)^2}{RK} \tag{6.28}$$

This quantity is not fixed and depends on the relative dimensions of the thermocouple. For a specific setup, it is maximal when the product RK is minimal, which occurs when:

$$\frac{L_n A_n}{L_p A_p} = \sqrt{\frac{\rho_p \kappa_n}{\rho_n \kappa_p}} \tag{6.29}$$

When this condition is satisfied, then Z_{pn} becomes:

$$Z_{pn} = \frac{(S_n - S_p)^2}{(\sqrt{\kappa_p \rho_p} + \sqrt{\kappa_n \rho_n})^2} \tag{6.30}$$

Similarly, the individual n-type and p-type components can also be characterized by their own intrinsic Figure of Merit Z, expressed as:

$$Z = \frac{S^2}{\rho\kappa} = \frac{S^2\sigma}{\kappa} = \frac{S^2\sigma}{\kappa_l + \kappa_e} \tag{6.31}$$

Here, $\sigma = \rho^{-1}$ is the electrical conductivity. The thermal conductivity κ have been decomposed into two contributions, the lattice κ_l and the electronic κ_e parts.

The maximum efficiency of cooling of a thermocouple can be written as a function of ZT_A:

$$\eta_{c,\max} = \frac{\gamma T_c - T_h}{(T_c - T_h)(1+\gamma)} \tag{6.32}$$

with $\gamma = \sqrt{1 + Z_{pn} T_A}$.

In a similar fashion, the maximum efficiency for a thermocouple generating electricity is given by:

$$\eta_{e,\max} = \frac{(T_h - T_c)(\gamma - 1)}{T_c + \gamma T_h} \tag{6.33}$$

$$= \eta_{\text{Carnot}} \frac{\gamma - 1}{\gamma + T_c/T_h} \tag{6.34}$$

where $\eta_{\text{Carnot}} = 1 - T_c/T_h$ is the Carnot efficiency, which binds the efficiency as $Z_{pn}T_A$ goes to infinity. The maximum efficiency for a thermoelectric generator working at room temperature is given in Figure 6.7 for different values of ZT.

For a given compound, one usually aim to maximize its own Figure of Merit ZT. This can be done, for example, by controlling the carriers density *via* doping, as we will see in the following Chapters. In principle, it is not guaranteed that the optimization of a thermocouple can be performed by simply optimizing the ZT factor of the individual branches. Generally, however, at the high temperatures usually used to generate electricity, Z_{np} is not far from the average of the individual factors Z_n and Z_p, and therefore optimizing the materials individually is not unreasonable [187]. This is why, in general,

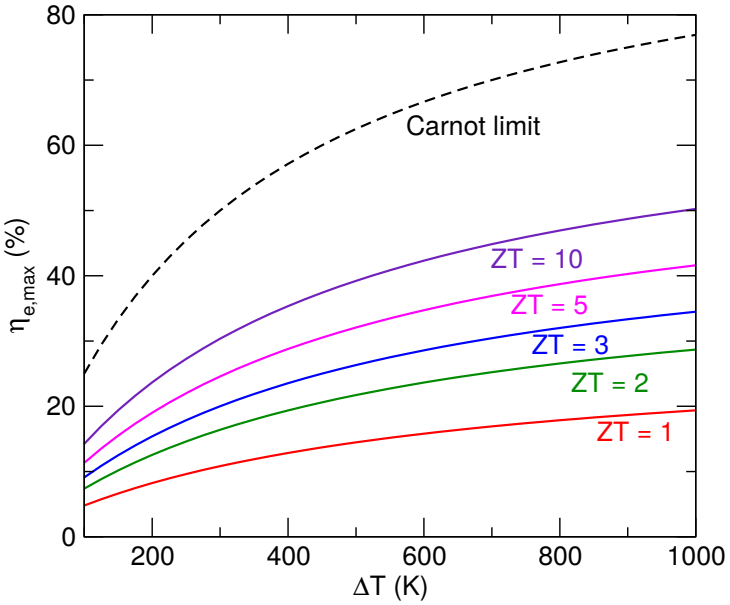

FIGURE 6.7: Maximum efficiency of a thermoelectric generator under a temperature gradient ΔT, as derived from Equation (6.34), for $T_c = 300$ K, and different ZT values.

when looking at the literature, a large number of reports focuses on the transport properties of a given compound of interest (or family of compounds), such as the Seebeck coefficient S, the resistivity ρ or conductivity σ, as well as the thermal conductivity κ, in order to maximize the factor $S^2\sigma/\kappa$.

From Equation (6.31), one can see that, in order to maximize Z, the considered compound must have a high Seebeck coefficient, to ensure that the produced voltage by a small temperature gradient is the largest possible, and a large electrical conductivity, to have a large current flowing through the thermocouple with as little dissipation as possible. Moreover, it is also necessary that the compound has a low thermal conductivity in order to maintain the temperature gradient across the material.

Now that we clarified the relation between the transport coefficients and the TE efficiencies through ZT_A, we can describe the different strategies to optimize this quantity.

6.5 Optimizing the thermoelectric properties of materials

In regards to the previous considerations, improving the TE performance of a given compound is achieved by increasing its Z factor or equivalently its adimensional ZT_A. The numerator in Equation (6.31), $S^2\sigma$, is also called the power factor (PF) and should be as large as possible. The denominator is the sum of the lattice and electronic contribution to the thermal conductivity κ, and should be minimized to maximize ZT.

Often, the electrical and thermal conductivities are related. In the case of metals, the *ratio* between electronic thermal conductivity κ_e and electrical conductivity σ follows the Wiedemann-Franz law [188]:

$$\frac{\kappa_e}{\sigma} = \frac{\pi^2 k_B^2}{3\,e} T = LT \tag{6.35}$$

In the above expression, e is the electron charge, k_B is the Boltzmann constant, L is the Lorenz constant , and T is the temperature. The consequence of the Wiedemann-Franz law is that, at a given temperature, the ratio κ_e/σ is constant, and increasing σ is concomitantly followed by an increase in κ_e. This behaviour can be extrapolated for doped semiconductors, resulting in the difficulty to optimize these two coefficient in an opposite fashion. Most of the time, the lattice contribution κ_l to the thermal conductivity dominates: several strategies have been proposed to reduce κ_l, usually by increasing phonon scattering through nanostructures (defects, "rattling" atoms, interfaces, *etc.*).

There has been a tremendous amount of progress in increasing the Figure of Merit in the past years, with many conceptual strategies and ideas proposed by theoretical works. One of the most popular strategies has been proposed by Hicks and Dresslhaus [189]: it consists in confining electrons in quantum wells, such as atomic planes, or even in 1-dimensional crystals such as nanowires [190]: the effect of confinement is to increase the Figure of Merit, beyond what has been obtained from the best bulk TEs. However, such an increase is difficult to achieve in experiments. Recently, with the development of layered nanostructures, two-dimensional electron systems (2DES) have been created and confined between insulating layers in STO-based heterostructures [191], enhancing significantly the thermopower.

In spite of intensive research, there is a lack of good TE compounds with $ZT > 1$, and the best ones are not necessarily featuring the low dimensional aspect advised by Hicks and Dresselhaus. Amongst the best ones, Bi_2Te_3 still remains one of the most powerful TEs since its discovery [192] with a Figure of Merit as high as 1 (and $S^2\sigma \approx 40-50\ \mu\mathrm{Wcm^{-1}K^{-2}}$ at room temperature). Recent developments led to the discovery of new compounds with even better ZT, such as Bi_2Te_3/Sb_2Te_3 superlattices ($ZT = 2.4$, as reported in Reference [193]) and, more recently, SnSe, with $ZT = 2.6$, the highest value ever reported in the litterature [194, 195]. More examples of recently discovered high ZT compounds are given in Figure 6.8. These achievements are mainly related to the low thermal conductivity of these structures. Indeed, record low values of $\kappa_l \approx 0.22 - 0.5\ \mathrm{W\ m^{-1}K^{-1}}$ have been reported [193, 196].

In order for thermoelectricity to become competitive against other, current energy sources, the Figure of Merit should at least reach a value of 3, so that the maximum efficiency goes up to at least 30% (Figure 6.7). However, as shown in Figure 6.8, $ZT > 3$ has yet to be achieved. Alongside the efforts to find compounds with low κ_l, a lot of efforts also focus on the electronic transport aspect of thermoelectricity.

Indeed, a large part of research focuses on improving the PF. A large PF implies a large voltage generation during the conversion process. If one desires to recover wasted heat, then the PF is the key quantity to optimize. However, even the optimization of the power is a tricky task, since S and σ requires conflicting dynamics of the charge carriers, which can be easily observed from the expressions of S and σ in a simple free-carriers-like picture [197] (typical of degenerate semiconductors, with parabolic band dispersion):

$$S = \frac{8\pi^2 k_B^2}{3eh^2}\, m^*\, T \left(\frac{\pi}{3n}\right)^{2/3} \tag{6.36}$$

$$\sigma = ne\mu \tag{6.37}$$

$$\mu = \frac{e}{m^*}\tau \tag{6.38}$$

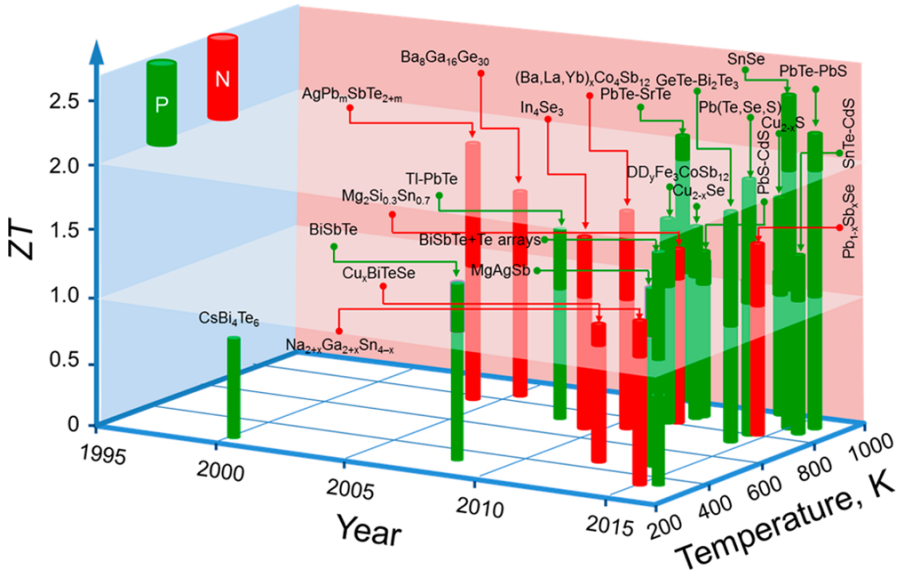

FIGURE 6.8: Figures of merit ZT of the best thermoelectric compounds, sorted with respect to their p-type or n-type performance at a given temperature, and by year of discovery. Adapted from Reference [197].

where m^* is the effective mass of the majority carriers, n is the carrier density, μ is the mobility and τ the relaxation time. For anisotropic structures, the effective mass is anisotropic and should be ascribed as a tensor, related to the curvature in the reciprocal space of the band structure along the different directions:

$$m^*_{\alpha\beta} = \left[\frac{1}{\hbar^2}\frac{\partial^2 \epsilon_{\mathbf{k}}}{\partial k_\alpha \partial k_\beta}\right]^{-1} \tag{6.39}$$

In this simple picture, on one hand, S decreases with increasing n, whereas σ increases with increasing n. On the other hand, S increases with increasing effective mass m^* of the carriers, whereas σ decreases with increasing m^*, with reduced mobility. This means that, for a given electronic structure, there is always an optimal density of majority carriers yielding the highest PF at a given temperature. The conflicting dynamics of the carriers also imply that it is difficult to optimize the band structure to concomitantly increase both S and σ.

One proposed strategy to increase the PF is to increase the number of band extrema near the band edges [197], as well as improving the band degeneracy by exploiting symmetry properties. This is typically achieved by alloying: with a good *ratio* between the parents compounds, the energy difference between the band edges of the individual components can be reduced, increasing the energy degeneracy and raising the PF above the values of the individual compounds. This is the so-called "band convergence" strategy, and constitutes a first effort in engineering directly the band structure to improve the PF [198].

Mahan and Sofo [199] proposed that the best energy distribution to improve the TE properties is a Dirac delta function $\delta\epsilon$. However, this is not achievable in a real material, but can be approached with a high and narrow peak in the electronic density of state. Moreover, the carriers should have high velocities in the direction of applied field. On the contrary, the contribution from a broader energy distribution background

is detrimental to the TE properties. Mahan and Sofo proposed that electrons from f orbitals could satisfy this criterion, as achieved in $YbAl_3$, yielding high PF at low temperature, notwithstanding this PF would decreases drastically at higher temperature. Other families of compounds, such as PbTe, PbSe, PbS, and SnTe [200] or the iron-based full-Heusler Fe_2YZ [25, 201] have also been proposed to have low-dimensional Fermi surfaces, with a pipe-like character, yielding high PFs.

Another strategy to modulate m^* is through the introduction of resonant states within the valence/conduction band, originating from the coupling between electrons/holes of a dilute impurity with those of the conduction/valence band of the host materials, and resulting in the apparition of a peak in the density of state. Such peaks are usually associated with localized states, with weak dispersion in the reciprocal space [202], and can improve the Seebeck coefficient if the Fermi level is in the vicinity of the peak itself [203]. This strategy however also reaches its limit at higher temperatures, where the relaxation time of acoustic phonon scattering is shorter than the relaxation time of resonant impurity scattering.

The shortcomings of the aforementioned strategies highlight the difficulty to balance properly the electronic structure to optimize the PF. The association of seemingly conflicting characteristics associated with high S and σ can however be found in some compounds, by exploiting the highly anisotropic character of certain orbitals, such as $3d$ orbitals, which can be found in transition-metal based semiconductors [25, 200]. Of course, this list of proposed strategies is not exhaustive. The curious readers are encouraged to read interesting introductory reviews highlighting the challenges in the field in the following References [196, 197, 204, 205].

In the following Chapters, we will focus on different, specific cases of $3d$ orbitals engineered thermoelectricity: first, we will study the TE properties of calcium cobaltite $Ca_3Co_3O_9$, which is one of the most studied and promising oxide compounds for TE applications, and how theoretical considerations can be used to further assess its TE properties. We will also discuss the inherent issues related to oxides superlattices. Then we will focus on the topic of iron-based full-Heusler compounds Fe_2YZ, which have been predicted to yield good TE properties, with PFs amongst the highest ever reported. We will show how these high PFs are related to their peculiar electronic band structure, and how they can be reached *via* doping and the challenges of achieving experimentally these predicted performances. All of these compounds are first and foremost semiconductors or insulators, but by defects engineering, it is possible to exploit the properties of their $3d$-states populations.

Chapter 7

Thermoelectric properties of layered-oxides

The present Chapter focuses on the thermoelectric properties of layered-oxides. Specifically, we will discuss how first-principles calculations can provide insights on how to improve the thermoelectric properties in these compounds.

First, we will present the different reasons for the growing interest in oxides for thermoelectric applications. Then the discussion will focus on misfit-layered calcium cobaltite $Ca_3Co_4O_9$ (which we shall refer as CCO in the following). Specifically, we use the theoretical predictions to highlight the highly anisotropic character of its single-crystal transport properties, originating from its layered structure, and which is difficult to grasp from experiments. We will discuss how this anisotropy may impact the thermoelectric performance. Finally, we will discuss about other attempts at engineering low-dimensional transport in other layered-oxides based on $SrTiO_3$, and present the different challenge facing the optimization of the power factor in these materials. Some of the results presented in this Chapter have been published in two articles, one specifically on calcium cobaltite [206] and one on $SrTiO_3$-based heterostructures [207].

7.1 Layered-oxides as thermoelectrics, why such interest ?

In general, most oxides have their transition metal atoms in their common oxidation degrees, remaining stable at high temperatures. Moreover, their strong ionic character, with narrow conduction band width arising from weak orbital overlaps, lead to localized electrons with low mobilities and therefore bad conductivity. Nevertheless, as discussed in Chapter 6, low mobilities are also associated with high effective mass, and high thermopower. Hence, oxides cannot be expected to be inherently bad thermoelectric compounds.

Interest started to gather around oxides when it was discovered that the layered oxide Na_xCoO_2 ($x = 0.5$), consisting of alternating layers of CdI_2-type CoO_2 layers and Na layers stacked on top of each other, with a Seebeck coefficient of $S \approx 100$ μVK^{-1} at 300 K and $ZT \approx 0.75$ at 1000 K [208]. These unexpected good thermoelectric properties motivated the search for other oxides, with similar or better properties. Following this discovery, a lot of focus was put on cobalt-based layered oxides, such as misfit-layered

calcium cobaltite $Ca_3Co_4O_9$ or $Bi_2Sr_3Co_2O_y$ [208, 209]. Research also started to focus on perovskite-based superlattices, such as as $SrTiO_3/SrRuO_3$ superlattices, which are predicted to have good thermoelectric properties if doped with holes [210].

The aforementioned compounds are *p*-type thermoelectrics. However, thermoelectric devices also requires *n*-type compounds to realize the thermocouples. Amongst the different *n*-type oxides, $SrTiO_3$ is known to have good room temperature thermoelectric properties if heavily doped with donors. Let us also cite Al-doped ZnO ($Al_{0.02}Zn_{0.98}O$) having satisfying thermoelectric performances ($ZT = 0.3$ at 1000 K) [211].

We remark that all the aforementioned *p*-type oxides thermoelectrics have layered structures. The main advantage of these materials is that they present substructures with different individual transport properties: it is indeed quite difficult to engineer and control the electronic and lattice properties simultaneously with a simple crystal, and these complex crystals are therefore considered as better options for controlling separately the electronic and thermal transport. Moreover, such structures are expected to realize the phonon-glass electron-crystal (PGEC) strategy proposed by Slack [187, 212], by decoupling the thermal and electrical conductivities between different sublattices, and favouring phonon scattering through the boundaries between them, as well as engineering low-dimensional transport system as proposed by Hicks and Dresselhaus [189, 190].

Finally, beyond thermoelectricity, oxides have a panel of interesting properties for application, such as their stability in oxidizing and corrosive environment at high temperature, their resistance to oxidation in the air, the availability of their constituent as well as their lack of toxicity compared to the more conventional thermoelectrics. With these considerations, CCO appears as a promising candidate.

7.2 Misfit-layered calcium cobaltite

CCO is a misfit-layered compound consisting of two subsystems, Ca_2CoO_3 and CoO_2, alternating along the $\vec{c}$ crystallographic axis (Figure 7.1). The subsystems are different in composition, structure, magnetic, electronic and transport properties. The CoO_2 subsystem has a CdI_2-type structure whereas the Ca_2CoO_3 subsystem has a rocksalt-like (RS) structure. Both subsystems present CoO_6 irregular octahedra, as shown in Figure 7.1. CCO is a misfit and incommensurate compound. This structural property is related to the fact that the two subsystems have different b parameters. Their *ratio* is irrational and very close to the "golden" *ratio*:

$$\frac{b_1}{b_2} \approx \frac{1+\sqrt{5}}{2} = \varphi = 1.61803398... \tag{7.1}$$

This characteristic incommensurability make the structure aperiodic along $\vec{b}$, while it is periodic along $\vec{a}$ and $\vec{c}$. The compound displays several magnetic phases with respect to temperature [209, 213, 214], with the presence of an incommensurate spin density wave at low temperature in the CoO_2 subsystem coexisting with a ferrimagnetic phase. The electronic population around the Fermi energy E_F originates mainly from the Co t_{2g} orbitals in the CoO_2 layers.

Experiments have shown that the compound has an in-plane Seebeck coefficient reaching 125 μVK^{-1} at room temperature [209, 215, 216], which is promising for a high

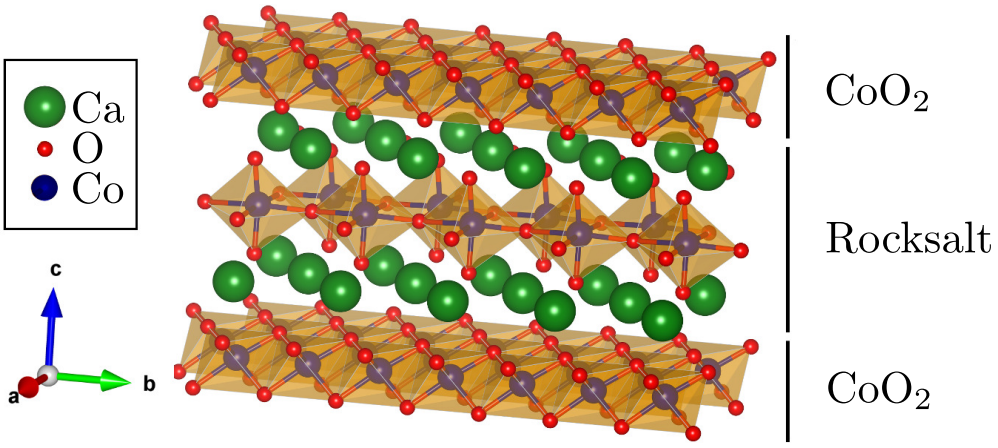

FIGURE 7.1: Calcium cobaltite $Ca_3Co_4O_9$. The RS subsystem is incommensurate with the CoO_2 subsystem. CoO_6 octahedra are highlighted in both subsystems.

room-temperature PF. In addition to its promising thermopower, CCO is stable at high temperatures, above 1000 K [209, 213, 214, 217–219]. The single-crystal transport properties are highly anisotropic, as expected from the layered structure. Experiments mostly focused on the transport properties in terms of in-plane and out-of-plane coefficients. The details of the single-crystal transport tensor component have not been yet discussed to our knowledge.

In contrast to experimental studies, theoretical studies [220–223] are less numerous. It has been reported that standard DFT calculations within the LDA fail to reproduce the experimental electronic structure of CCO around the Fermi energy [217, 218, 221]. This issue is circumvented with DFT+U, which better describes the strong correlation effects in oxides [221].

The objective of the present Section is to discuss the structural, magnetic, electronic and thermoelectric properties of CCO with an alternative approach to DFT+U, the hybrid functional formalism. We aim to address the anisotropic character of the thermoelectric properties, and detail how such properties evolve with temperature and as a function of carrier density. The theoretical results will be compared with the available experimental data, and we will also address the diversity in the experimental data with respect to the single-crystal properties and how these properties average for polycrystalline samples.

7.2.1 Technical details

DFT calculations were performed with the CRYSTAL code [37]. We selected the available basis sets from References [224, 225]. A pseudopotential is used for the Ca atoms, described in the Appendix of [224]. We worked with the B1 Wu-Cohen [42] (B1-WC) hybrid functional (some calculations were also performed with the usual simple local density approximation [226](LDA) for comparison). Magnetic properties are evaluated in the collinear approximation.

A $6 \times 3 \times 3$ Monkhorst-Pack [43] mesh of special k-points is used for the relaxation of the structure. The energy convergence criterion for the self-consistent resolution of the Kohn-Sham problem is fixed to 10^{-7} Ha. For the structural relaxation, we fixed a threshold of 3×10^{-4} Ha/Bohr on the root-mean square values of energy gradients and

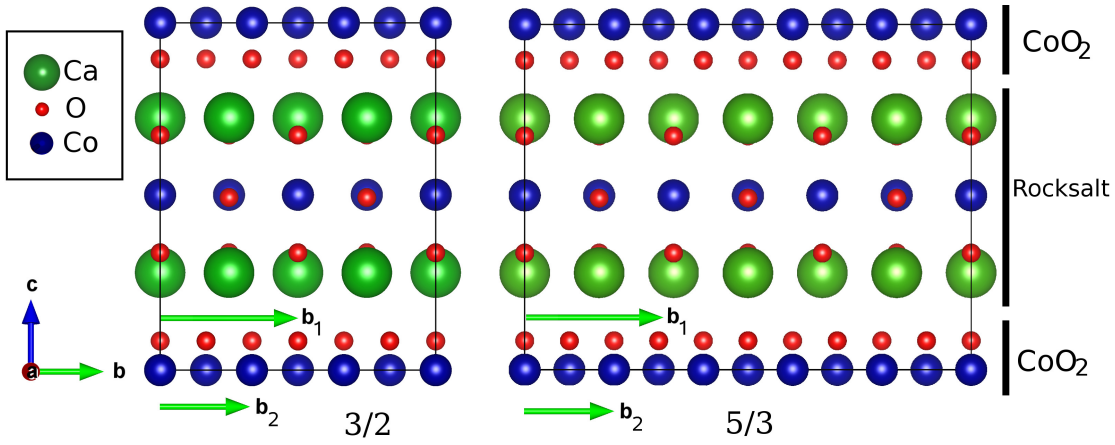

FIGURE 7.2: Two supercells are used to model the misfit character of CCO. Two rational approximants were used: 3/2 (left) and 5/3 (right), respectively with 42 atoms and 66 atoms.

of 1.2×10^{-3} Bohr on the root-mean square values of atomic displacements. The level of accuracy in evaluating the Coulomb and exchange series is defined with five threshold parameters [44], which were fixed to 7, 7, 7, 7 and 14.

The structure is relaxed with different magnetic orderings (Table 7.1), and in contrast to the previous DFT+U study by Rébola *et al.*, we relax the structure from antiferromagnetic configurations as well. After finding the ground-state, the electronic structure is refined at the fixed optimized geometry, with a $12 \times 6 \times 6$ k-mesh. The energy criterion is kept unchanged.

The transport and thermoelectric properties are calculated from the ground-state electronic band structure within the Boltzmann transport theory, using the constant relaxation time approximation. The electronic band structure is computed with a dense uniform mesh of 6492 k-points in the irreducible Brillouin zone. With the resulting first-principles eigenenergies $\epsilon_{i\mathbf{k}}$, we can feed the BoltzTraP code [32] to estimate the Seebeck and the electrical conductivity tensors.

Within the CRTA, the Seebeck coefficient S does not depend on the relaxation time τ; however, the electrical conductivity σ does. Our approach to estimate τ will be detailed in Section 7.2.5.

In order to model this compound and study its bulk properties using periodic boundary conditions, a supercell approximation is required. The golden *ratio* is identified as the limit of the rational fraction between consecutive Fibonacci numbers; Rébola *et al.* therefore proposed that these numbers can be used to build supercells with b_1/b_2 close to the exact *ratio* [221]:

$$b_1/b_2 \quad \approx \quad \varphi = \lim_{n \to +\infty} \frac{F(n+1)}{F(n)} = 1.61803398\ldots \tag{7.2}$$

The first values in this sequence are 3/2 , 5/3, 8/5 $\ldots \to \varphi$. Following this idea, we consider in this work the first two rational approximants : a 3/2 (= 1.5) approximant corresponding to 2 unit cells of rocksalt and 3 unit cells of CoO_2 (Figure 7.2, left), and a 5/3 (= 1.667) approximant, corresponding to 3 unit cells of rocksalt and 5 unit cells

	Start			***Final***	
Label	**CoO_2**	**RS**	**Label**	**CoO_2**	**RS**
FM1	↑↑	-	FEM	∼	↑↑
FM2	-	↑↑	FEM	∼	↑↑
FM3	↑↑	↑↑	FEM	∼	↑↑
AFM1	-	↑↓	FIM	∼	↑↓
AFM2	↑↓	-	FIM	∼	↑↓
AFM3	↓↓	↑↑	FEM	∼	↑↑

TABLE 7.1: Initial magnetic configurations (*start*) in each subsystem between first-neighbours Co, before relaxation. ↑↑ refers to a ferromagnetic state; ↑↓ refers to an antiferromagnetic state. After structural relaxation (*final*), the magnetic moments in the CoO_2 subsystem are very small ("∼"), and in the rocksalt layer (RS), a quasiferromagnetic or quasiferrimagnetic ordering (ground-state) appears.

of CoO_2 (Figure 7.2, right). The identified space group of the built supercells is Pm. These supercells will be referred to using the corresponding rational approximant.

In the following Section, we detail the results of our first-principles calculations, for both 3/2 and 5/3 supercells and for both functionals. We label the different cases as LDA - 3/2, B1-WC - 3/2 and B1-WC - 5/3 according to the supercells and functionals. Then different metastable phases are identified depending of the initial spin configurations. The initial configurations FM1, FM2, FM3 and AFM3, as described in Table 7.1, all relax to the same magnetic phase, where the Co in the CoO_2 layer hold very small magnetic moments, and where the Co in the Ca_2CoO_3 layers have a quasi-ferromagnetic ordering (*i.e.* the same orientation of spin, but slightly different magnetic moments). We label it FEM. One the other hand, the configurations AFM1 and AFM2 relax to a lower energy phase, which we accordingly refer to as the ground state, where the Co in the CoO_2 layer hold very small magnetic moments and the Co in the Ca_2CoO_3 layers have a ferrimagnetic ordering (*i.e.* alternating orientation of spins with slightly different magnetic moments). We label it FIM.

In all cases the FIM phase is more stable, with a gain of energy ΔE (per atoms in the whole cell) with respect to the FEM phase ($\Delta E = E_{\mathrm{FIM}} - E_{\mathrm{FEM}}$) of -1.60 meV/at. for LDA - 3/2, -1.50 meV/at. for B1-WC - 5/3 and -4.15 meV/at. for B1-WC - 5/3. We see that the 5/3 approximant further stabilizes the FIM phase *versus* the FEM phase. In the following Section, we report and compare the results with the available data in the literature. We discuss the structural, magnetic, electronic properties and the thermoelectric properties of the FIM ground state. In specific cases, we also report results of the FEM magnetic phase.

7.2.2 Structural parameters

Several groups [209, 227, 228] confirmed that CCO is a misfit-layered oxide combining two monoclinic subsystems into a unique crystal structure with lattice parameters a (4.83 Å), c (10.84 Å), and β (98.13°), and two different b parameters for each subsystem: the first subsystem with $b_1 = 4.56$ Å consists of a triple rocksalt-type layer Ca_2CoO_3, and

the second subsystem consists of a CdI_2-type CoO_2 layer with $b_2 = 2.82$ Å. The relaxed lattice parameters are summarized in Table 7.2 and compared with experimental data.

First, we focus on the FIM phase and discuss the structure of the 3/2 supercell, within LDA and B1-WC. As usual, LDA slightly underestimates lattice parameters, respectively, by -1.4% and -0.5%. The β parameter is also underestimated by -0.3%. The relative error on b_1 is by far the largest, being around -5.4% for each calculation. The relative error on b_2 is around $+2.0\%$. The B1-WC calculation yields for the β parameter a result very close to the experimental value (error of -0.2%). The a parameter is underestimated by -0.1% while the c parameter is overestimated by $+0.7\%$. On the other hand, the relaxed b_2 and b_1 parameters show larger deviations from the experimental values, respectfully overestimated by $+1.5\%$ and underestimated by -6%.

The errors on b_1 and b_2 are expected to originate from the misfit character of CCO and most likely appear for the 3/2 approximant which is far from the value of the golden ratio, thus forcing the two layers to fit within the same unit cell: this puts the rocksalt layer under compression and the CoO_2 planes under tension. The similarity between the LDA and B1-WC results further confirms that the bad estimation of b_1 and b_2 is not a problem coming from the functional, but rather is inherent to the 3/2 approximant. However, the errors on the a and c parameters are reduced with the hybrid approach.

Then, we report the B1-WC results with the 5/3 supercell. One can see that the optimized values are overall closer to the experimental values. We have errors of -0.01% on β, -0.18% on a, -2.27% on b_2, $+0.72\%$ on b_1 and $+0.33\%$ on c. The biggest errors are still on the b parameters. In contrast to the 3/2 approximant, the 5/3 approximant put the CoO_2 planes under compression and the rocksalt planes under tension. However, these results are much closer to the experimental data than our previous calculations with the 3/2 approximant. In terms of volume, the LDA systemically underestimates the volume of the unit cell, which is consistent with the usual trend of the LDA. The B1-WC functional lowers the relative error on the volume to -0.649% for the FIM. This suggests that the 5/3 approximant, studied within the B1-WC functional, is a good option to study CCO.

The averaged atomic positions in fractional coordinates are listed in Tables 7.3 (LDA) and 7.4 (B1-WC) in comparison with the experimental results of Miyazaki *et al.* [227]. Our results are generally in good agreement with the experimental fractional coordinates. However, the fractional coordinates of O2 in the rocksalt subsystem along the $\vec{a}$ axis are far from the experimental value for the 3/2 approximant. Again these errors may likely originate from the rational approximant model. The 5/3 approximant greatly reduces the errors on the fractional coordinates. In Table 7.3 and 7.4, the quantity Δ, defined as the sum over the squares of the relatives errors of the fractional coordinates with respect to experiments, allows a quantitative appreciation of theses errors. It can be observed that $\Delta^{[x/a]}$ for our LDA - 3/2 or B1-WC - 3/2 slightly increases compared to LDA+U results of Reference [221]. However $\Delta^{[z/c]}$ is comparable to these previous results. The $\Delta^{[z/c]}$ values for B1-WC - 5/3 are the same as the LDA+U value; $\Delta^{[x/a]}$ is reduced by a fraction of two.

Results for the FEM phase are also displayed in Tables 7.2, 7.3 and 7.4. The differences on the volume are a bit larger in the FEM than in the FIM phase, however the Δ values for the FEM phase are slightly inferior to the FIM values. The similarity between the FIM and FEM results suggests that the magnetic ordering in the RS subsystem does not play a major role in the structural properties of CCO.

$\mathbf{E_{xc}}$ & **approx.**	**a**(Å)	$\mathbf{b}_2$(Å)	$\mathbf{b}_1$(Å)	**c**(Å)	β(°)	ΔV (%)
LDA - 3/2 (FIM)	4.762	2.876	4.314	10.789	97.837	−3.611
LDA - 3/2 (FEM)	4.746	2.876	4.314	10.795	97.777	−3.868
B1-WC - 3/2 (FIM)	4.827	2.863	4.295	10.919	97.933	−1.582
B1-WC - 3/2 (FEM)	4.820	2.863	4.295	10.921	97.918	−1.703
B1-WC - 5/3 (FIM)	4.821	2.756	4.593	10.876	98.118	−0.649
B1-WC - 5/3 (FEM)	4.819	2.743	4.572	10.881	98.125	−1.107
LDA+U - 3/2 [221]	4.75	2.83	4.24	10.65	98.20	−6.749
PBE+U - 3/2 [221]	4.81	2.89	4.34	10.86	98.11	−1.531
LDA+U - 5/3 [221]	4.75	2.75	4.58	10.54	98.34	−5.426
PBE+U - 5/3 [229]	4.88	2.82	4.71	10.86	98.22	2.838
PBE+U - 5/3 [223]	4.91	2.82	4.71	10.73	98.3	2.211
Exp. [227] (300 K)	4.83	2.82	4.56	10.84	98.13	-

TABLE 7.2: Experimental [227] and optimized lattice parameters for the FIM and FEM phases. The estimation of relative errors with respect to the experimental unit cell volume, in the rational approximant model, is also displayed, for the ground state and the FEM phase. DFT+U results from References [221, 223, 229] were included for comparison.

In summary, we reviewed the structural parameters of CCO within the rational approximant model, comparing results obtained with LDA+U and B1-WC approaches. Errors in the lattice parameters or atomic positions likely arise from the 3/2 rational approximant, independently of the functional. The errors for the 5/3 rational approximant within B1-WC are comparable or eventually slightly improved compared to LDA+U. At this stage, the hybrid functional formalism appears as a reasonable alternative to the DFT+U method for CCO.

7.2.3 Magnetic structure

It has been found that, below 19 K, a long-range incommensurate spin-density wave in the CoO_2 layers coexists with a ferrimagnetic phase. Several magnetic transitions have been identified, which have been associated with significant changes in the Seebeck coefficient and the electrical resistivity [209, 213, 214].

The effective magnetic moments for each cobalt atom in both subsystems are given in Table 7.5, after performing full relaxation.

In the same way as in the previous Section, we discuss first the magnetic properties observed in the 3/2 supercell, within LDA and B1-WC, for the FIM phase. It can be observed that, the magnetic moments within LDA are mainly localized in the rocksalt subsystem. The average magnetic moment per Co μ_{tot}^{ave} is estimated around 0.749 μ_B/Co, which is relatively far from experimental measurements [209] (1.3 μ_B/Co). It can be argued that, as the rocksalt subsystem hold a non-zero effective magnetic moment (−0.047 μ_B), our calculation tends to reproduce the ferrimagnetic state proposed for calcium cobaltite below 19 K [213, 215]. In comparison, the B1-WC functional yields effective magnetic moments for Co atoms belonging to the CoO_2 subsystem close to

$\mathbf{E_{xc}}$ **& approx.**	**Subsys.**	**Atom**	**[x/a]** [221]	$\mathbf{[x/a]_{exp}}$ [227]	$\mathbf{[x/a]_{FIM}}$	$\mathbf{[x/a]_{FEM}}$	**[z/c]** [221]	$\mathbf{[z/c]_{exp}}$ [227]	$\mathbf{[z/c]_{FIM}}$	$\mathbf{[z/c]_{FEM}}$
LDA - 3/2	CoO_2	Co	0.000	0.000	0.000	0.000	0.000	0.000	0.000	0.000
		O1	0.365	0.363	0.365	0.365	0.093	0.084	0.090	0.090
		O2	−0.365	−0.364	−0.365	−0.365	−0.093	−0.104	−0.090	−0.090
	RS	Ca1	0.175	0.182	0.182	0.180	0.268	0.281	0.271	0.272
		Ca2	0.318	0.312	0.321	0.319	−0.268	−0.273	−0.271	−0.272
		Co	−0.203	−0.298	−0.297	−0.295	−0.500	−0.495	−0.500	−0.500
		O1	−0.312	−0.282	−0.295	−0.298	0.335	0.338	0.337	0.336
		O2	0.212	0.183	0.308	0.302	0.500	0.497	0.500	0.500
		O3	−0.207	−0.163	−0.193	−0.196	−0.335	−0.323	−0.337	−0.336
	Δ		0.213		0.503	0.468	0.027		0.027	0.026

TABLE 7.3: Ground state average atomic positions in the CoO_2 and Ca_2CoO_3 subsystems in the rational approximant model, for the LDA functional. The data from Reference [221] is computed from LDA+U calculations. Results for both FIM and FEM phases are included. The quantity Δ is defined as the sum over the squares of the relative errors on the fractional coordinates.

$\mathbf{E_{xc}}$ & approx.	Subsys.	Atom	[x/a] [221]	$[x/a]_{exp}$ [227]	$[x/a]_{FIM}$	$[x/a]_{FEM}$	[z/c] [221]	$[z/c]_{exp}$ [227]	$[z/c]_{FIM}$	$[z/c]_{FEM}$
B1-WC - 3/2	CoO_2	Co	0.000	0.000	0.000	0.000	0.000	0.000	0.000	0.000
		O1	0.365	0.363	0.364	0.364	0.093	0.084	0.091	0.092
		O2	−0.365	−0.364	−0.364	−0.364	−0.093	−0.104	−0.091	−0.092
	RS	Ca1	0.175	0.182	0.179	0.179	0.268	0.281	0.266	0.266
		Ca2	0.318	0.312	0.321	0.321	−0.268	−0.273	−0.266	−0.266
		Co	−0.203	−0.298	−0.297	−0.295	−0.500	−0.495	−0.500	−0.500
		O1	−0.312	−0.282	−0.294	−0.294	0.335	0.338	0.340	0.340
		O2	0.212	0.183	0.292	0.290	0.500	0.497	0.500	0.500
		O3	−0.207	−0.163	−0.192	−0.192	−0.335	−0.323	−0.340	−0.340
	Δ		0.213		0.389	0.377	0.027		0.029	0.029
B1-WC - 5/3	CoO_2	Co	0.000	0.000	0.000	0.000	0.000	0.000	0.000	0.000
		O1	0.364	0.363	0.362	0.362	0.093	0.084	0.093	0.093
		O2	−0.364	−0.364	−0.362	−0.362	−0.093	−0.104	−0.093	−0.093
	RS	Ca1	0.174	0.182	0.176	0.179	0.268	0.281	0.271	0.271
		Ca2	0.316	0.312	0.320	0.323	−0.268	−0.273	−0.270	−0.270
		Co	−0.206	−0.298	−0.302	−0.297	−0.500	−0.495	−0.498	−0.498
		O1	−0.313	−0.282	−0.202	−0.203	0.335	0.338	0.341	0.340
		O2	0.206	0.183	0.205	0.206	0.500	0.497	0.500	0.500
		O3	−0.205	−0.163	−0.160	−0.158	−0.335	−0.323	−0.341	−0.340
	Δ		0.192		0.097	0.097	0.029		0.027	0.027

TABLE 7.4: Ground state average atomic positions in the CoO_2 and Ca_2CoO_3 subsystems in the rational approximant model, for the B1-WC functional. The data from Reference [221] is computed from LDA+U calculations. Results for both FIM and FEM phases are included. The quantity Δ is defined as the sum over the squares of the relative errors on the fractional coordinates.

zero and an average magnetic moment of 2.65 μ_B/Co in the RS subsystem. The average magnetic moment (1.05 μ_B/Co) in the whole system is now closer to the experimental value 1.3 μ_B/Co, confirming better agreement of the B1-WC functional. We can argue that the ferrimagnetic ordering and the resulting magnetic moment in the rocksalt subsystem due to Co atoms (−0.135 μ_B) is in line with the ferrimagnetic phase observed below 19 K [213, 215]. The increase of magnetic moment going from LDA to B1-WC can be attributed to the better treatment of the exchange energy expected within the hybrid functional formalism. It must be noticed that as we performed our spin-polarized calculations within the collinear approximation and within periodic systems, it is impossible to obtain, at our level of approximation, the incommensurate spin-density wave in the CoO_2 subsystem as observed in experiments [213, 215] .

The B1-WC - 5/3 calculation yields similar results, with μ_{tot}^{ave} = 1.013 μ_B/Co, which is marginally lower than the B1-WC - 3/2 result, and still close to the value measured by Masset *et al.* (1.3 μ_B/Co) [209]. Once again, all the magnetic moments are located within the rocksalt subsystem, which holds a ferrimagnetic coupling between the Co atoms, with a non-zero total effective magnetic moment (0.658 μ_B) slightly larger than the value obtained with the B1-WC - 3/2 calculation, and thus tends to reproduce the ferrimagnetic state observed in the Ca_2CoO_3 below 19 K [213, 215]. In the 5/3 approximant, some Co in the CoO_2 subsystem also have a weak effective magnetic moment. One can notice that a single cobalt (Co5-2) possesses a high magnetic moment of 0.789 μ_B. This specific atom is located in the CoO_2 layers ($z/c = 0.5$) and its oxygen cage is more distorted than those around the other cobalt atoms in the CoO_2 subsystem: for the other Co atoms, the average oxygen-cobalt distance d_{Co-O} is 1.888 Å, whereas for this specific atom, d_{Co-O} = 1.856 Å. This distortion, which appears to the 5/3 approximant which compresses the CoO_2 layers as reported in the previous section, could explain the mixed valences Co^{3+} and Co^{4+} in the CoO_2 subsystem, and the change of occupancy in the t_{2g} resulting from different distortions between the different octahedra, which results in a net magnetic moment for this atom. These results are therefore in good agreement with the mixture of Co^{3+} and Co^{4+} proposed by experiments [209, 213, 214] and confirmed by Yang *et al.* [230].

The magnetic properties within the FEM phase are similar to those of the FIM phase: while we do not discuss the properties in detail, the atomic magnetic moments are close in magnitude to those in the ground state. LDA tends to underestimate the modulus of the atomic magnetic moments of the Co atoms in the rocksalt subsystem in comparison to what is obtained with the B1-WC functional. In contrast, the individual magnetic moments of the Co atoms in the CoO_2 subsystem are overestimated within LDA in comparison to the B1-WC results. Similarly to the FIM ground state and for the same reason, the Co5-2 atom in the CoO_2 layer holds a higher spin than the other cobalt atoms in this sublattice.

For comparison, in the DFT+U studies of Rébola *et al.* [221], the structure was relaxed only in ferromagnetic configurations. Baran *et al.* [223] computed several magnetic configurations for CCO in PBE+U (with a 5/3 supercell), but did not report details of the magnetic structure.

In a nutshell, from the relative energy between the FIM and the FEM phase, their structural properties and their magnetic properties, and the low temperature magnetic configuration described in References. [213, 214], it can be argued that the FIM appears consistently in all respects as the best match to the experimental data. Taking this into

consideration, the use of the hybrid functional scheme seems justified as it predicts this phase to be more stable.

7.2.4 Electronic properties

High-resolution photo-emission spectroscopy experiments performed by Takeuchi *et al.* [217, 218] showed that the electronic population near the Fermi energy comes from the $3d$ orbitals of the cobalt atoms in the CoO_2 layers, which means that the transport properties actually come from the CoO_2 layers, such as in the usual CoO_2-layered thermoelectric oxides, and that the charge carriers are holes. This was confirmed by other research groups [215, 230].

The first DFT calculations were performed by Asahi *et al.* [220] within the LDA. However, their results were in contradiction to the aforementioned experiments since the electronic contributions around the Fermi energy E_F were mainly coming from the rocksalt subsystem. The failure of this study was recently pointed out to come from the strong electronic correlations that are neglected in this framework. It was shown that a LDA+U method is sufficient to recover the experimental observations around the Fermi energy [221]. This LDA+U study highlighted the splitting of the Co $3d$ orbitals in the CoO_2 subsystem, with the t_{2g} orbitals being occupied, whereas the e_g orbitals are not.

Densities of state for the FIM phase are plotted around the Fermi energy in Figure 7.3, for each functional and approximant. Results from the FEM phase are also displayed. As one can see, our LDA calculation suggests that calcium cobaltite is a metal, as determined by Asahi *et al.* [220] with the same functional. Nevertheless, as explained previously, the LDA is known to fail in predicting the density of state around the Fermi energy. The B1-WC results yield semiconductor behaviour, with sizeable differences between the 3/2 and the 5/3 approximants. For the 3/2 structure, one spin channel presents a gap of 1.3 eV, whereas the other spin channel displays a much smaller gap of 0.1 eV and a very small DOS for the first conduction band. The 5/3 structure presents a gap of 0.5 eV for the spin-up channel, and a gap of a 0.83 eV for the spin-down channel.

The density of state for the FEM phase are also displayed in Figure 7.3: the overall shape of the DOS does not change much with the magnetic phase, and the LDA - 3/2 (FEM) result is metallic whereas the B1-WC - 3/2 (FEM) DOS shows more or less the same gap as the ground state. However, the B1-WC - 5/3 (FEM) result is quite different: the band gap of the spin-up channel is about 0.25 eV, while the band gap of the spin-down channel is about 1.06 eV. The gap is thus halved in comparison to the ground state. It is important to note that, with the B1-WC functional, for both the FIM and the FEM phases, CCO is found to be a semiconductor. This contrasts with the DFT+U results of Rébola *et al.* which present a small but finite density of state at the Fermi energy. The photo-emission experiments of Takeuchi *et al.* revealed the opening of a band gap at low temperature [217, 218], and our results are more consistent with this observation.

To get insight into the electronic structure, and to compare with to the photo-emission results of Takeuchi *et al.* regarding the role of the $3d$ orbitals of Co atoms in the conduction properties, we plot the ground state partial density of state projected into $3d$ orbitals of Co for both the CoO_2 and rocksalt subsystems (Figure 7.4), resolved in the local axis oriented along the octahedra in the two different subsystems.

LDA - 3/2 (FIM)			
CoO_2	$\mu_s(\mu_B)$	**RS**	$\mu_s(\mu_B)$
Co1-1	−0.04	Co1-1	1.89
Co1-2	−0.02	Co1-2	1.73
Co2-1	−0.02	Co2-1	−1.84
Co2-2	−0.04	Co2-2	−1.84
Co3-1	−0.04		
Co3-2	−0.03		
Average	−0.03		−0.01
$\sum \mu_s$	−0.20		−0.05
$\langle \overline{M} \rangle$	0.03		1.82

LDA - 3/2 (FEM)			
CoO_2	$\mu_s(\mu_B)$	**RS**	$\mu_s(\mu_B)$
Co1-1	−0.04	Co1-1	2.07
Co1-2	−0.04	Co1-2	1.77
Co2-1	−0.04	Co2-1	1.90
Co2-2	−0.04	Co2-2	1.90
Co3-1	−0.04		
Co3-2	−0.05		
Average	−0.04		1.91
$\sum \mu_s$	−0.24		7.63
$\langle \overline{M} \rangle$	0.04		1.91

B1-WC - 3/2 (FIM)			
CoO_2	$\mu_s(\mu_B)$	**RS**	$\mu_s(\mu_B)$
Co1-1	0.00	Co1-1	2.87
Co1-2	0.00	Co1-2	2.33
Co2-1	0.00	Co2-1	−2.67
Co2-2	0.00	Co2-2	−2.67
Co3-1	0.00		
Co3-2	0.00		
Average	0.00		−0.03
$\sum \mu_s$	0.00		−0.13
$\langle \overline{M} \rangle$	0.00		2.64

B1-WC - 3/2 (FEM)			
CoO_2	$\mu_s(\mu_B)$	**RS**	$\mu_s(\mu_B)$
Co1-1	0.00	Co1-1	2.87
Co1-2	0.00	Co1-2	2.30
Co2-1	0.00	Co2-1	2.65
Co2-2	0.00	Co2-2	2.65
Co3-1	0.00		
Co3-2	0.00		
Average	0.00		2.62
$\sum \mu_s$	0.00		10.48
$\langle \overline{M} \rangle$	0.00		2.62

B1-WC - 5/3 (FIM)			
CoO_2	$\mu_s(\mu_B)$	**RS**	$\mu_s(\mu_B)$
Co1-1	0.00	Co1-1	2.33
Co1-2	0.00	Co1-2	2.83
Co2-1	0.00	Co2-1	2.83
Co2-2	0.02	Co2-1	−2.29
Co3-1	0.02	Co3-1	−2.29
Co3-2	0.00	Co3-2	−2.76
Co4-1	0.00		
Co4-2	0.02		
Co5-1	0.02		
Co5-2	0.79		
Average	0.09		0.11
$\sum \mu_s$	0.86		0.66
$\langle \overline{M} \rangle$	0.09		2.55

B1-WC - 5/3 (FEM)			
CoO_2	$\mu_s(\mu_B)$	**RS**	$\mu_s(\mu_B)$
Co1-1	0.00	Co1-1	2.87
Co1-2	0.00	Co1-2	2.64
Co2-1	0.00	Co2-1	2.64
Co2-2	−0.05	Co2-1	2.25
Co3-1	−0.05	Co3-1	2.25
Co3-2	−0.01	Co3-2	2.84
Co4-1	−0.01		
Co4-2	−0.06		
Co5-1	−0.06		
Co5-2	−0.54		
Average	−0.08		2.58
$\sum \mu_s$	−0.78		15.50
$\langle \overline{M} \rangle$	0.08		2.58

TABLE 7.5: Atomic magnetic moments of Co atoms belonging to the CoO_2 and rocksalt subsystem (computed within LDA and B1-WC functionals and with the 3/2 and the 5/3 rational approximants) with the sum, the mean and the average over the modulus $\langle \overline{M} \rangle$ in each subsystem. Results of the FEM phase are included.

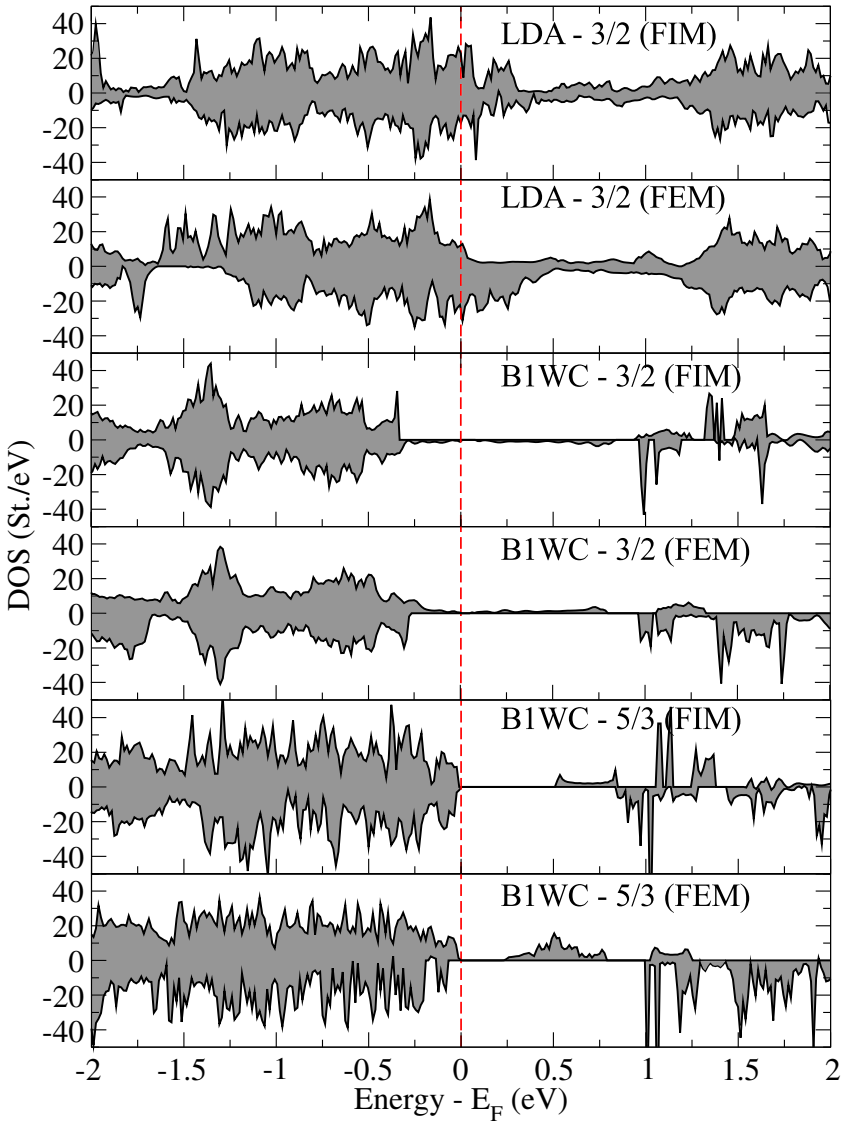

FIGURE 7.3: Electronic densities of state of $Ca_3Co_4O_9$ for each approximant and functional, for both magnetic phases. The Fermi energy E_F is shown with the vertical dashed lines

Within the LDA - 3/2 approximation (Figure 7.4, top), the contribution around the Fermi energy comes from the 3*d* orbitals from both subsystems. However, the main contribution around E_F comes from the rocksalt subsystem, which is in good agreement with the LDA calculations of Asahi *et al.* and Rébola *et al.* [221], but in contradiction to the experimental results of Takeuchi *et al.* [217, 218]. Still, the splitting [222] of the Co 3*d* orbitals in the CoO_2 into t_{2g} (blue plots in Figure 7.4) and e_g orbitals (around 1.2 eV) is well reproduced : the d_{xy}, d_{yz} and d_{xz} orbitals are mainly occupied. The d_{z^2} and $d_{x^2-y^2}$ are mainly unoccupied. An asymmetry between the t_{2g} states can be observed, in agreement with the experiments of Klie *et al.* [231] and the quantum chemistry calculations of with Soret and Lepetit [222], with the d_{xy} states presenting a small unoccupied DOS.

The failure of the LDA motivated the investigation within the hybrid functional formalism. In our B1-WC - 3/2 results (Figure 7.4, middle), it turns out that the main energetic contributions near the Fermi energy are from the 3*d* orbitals of Co atoms in

the CoO_2 subsystem and no contribution of the $3d$ orbitals of Co atoms in the rocksalt subsystem is found, contrary to what is obtained in the LDA and in agreement with the experiments of Takeuchi *et al.* [217, 218]. However, in contrast to the results of Rébola's *et al.* [221], we find a near-zero contribution of the Co $3d$ orbitals in the CoO_2 subsystem at the exact Fermi energy. As one can see, the density of state below the Fermi energy mainly originates from the t_{2g} bands, while the e_g orbitals lies about 3.3 eV above the Fermi energy, and are mainly unoccupied as predicted by the crystal field theory. The t_{2g} orbitals are close to E_F of about 0.5 eV and therefore should contribute to the transport properties. As in the LDA result, the splitting [222] of the $3d$ orbitals of Co in the CoO_2 into t_{2g} and e_g orbitals is once again obtained (around 3.5 eV): the d_{xy} and d_{xz} orbitals are almost fully occupied, the d_{yz} is not fully occupied, and the d_{z^2} and $d_{x^2-y^2}$ are mainly unoccupied.

Finally, we focus on the B1-WC results with the 5/3 approximant. The density of state for the majority spin channel has a gap of about 0.5 eV above the last occupied band, which makes CCO a semiconductor. If we look at the partial density of state projected into Co $3d$ orbitals for both subsystems (Figure 7.4, bottom), one can see that the results are similar to the B1-WC - 3/2 calculation, except that this time, there is an even stronger contribution of the Co $3d$ orbitals from the CoO_2 subsystem which contributes to the Fermi energy, whereas there is no contribution from the Co in the RS subsystem. Similar splitting between the Co $3d$ orbitals as in the previous results can be observed. In all of our calculations, the Co $3d$ from the CoO_2 layers display a bandwidth that is compatible with the aforementioned photo-emission experiments [217, 218] and with the previous DFT+U calculations [221].

We are not presenting the projected DOS for the FEM phase. However, it was checked that they globally follow the same trends with respect to the rational approximant and the exchange-correlation functional as the FIM ground state.

We suggest that CCO modelled with the 5/3 rational approximant and the B1-WC hybrid functional appears as a good option to compute the thermoelectric properties. The choice of the 5/3 supercell size is also motivated by the fact that the DFT+U studies [221] did not underline significant changes with a better approximant for a given functional. Therefore, we present the thermoelectric properties computed from the band structure obtained within B1-WC with the 5/3 approximant.

7.2.5 Thermoelectric properties

The Seebeck (S) and electrical conductivity tensors (σ) are computed from Boltzmann transport theory, within the constant relaxation time approximation. These properties are involved in the overall thermoelectric power factor, $PF = S^2\sigma$, which should be as large as possible in order to increase the figure of merit $ZT = S^2\sigma/\kappa$, where κ is the thermal conductivity.

Due to the anisotropic structure of CCO, it is expected that the thermoelectric properties are anisotropic as well, which has been confirmed by experiments, several of them mainly focusing on the in-plane and out-of-plane properties [209, 232–235]. For simplicity, the following discussion will focus on the diagonal components of S, σ and PF, specifically the ones responsible for the in-plane properties, which are expressed in a Cartesian basis where $\vec{x} \,//\, \vec{a}$, $\vec{y} \,//\, \vec{b}$, and $\vec{z} = \vec{x} \times \vec{y}$.

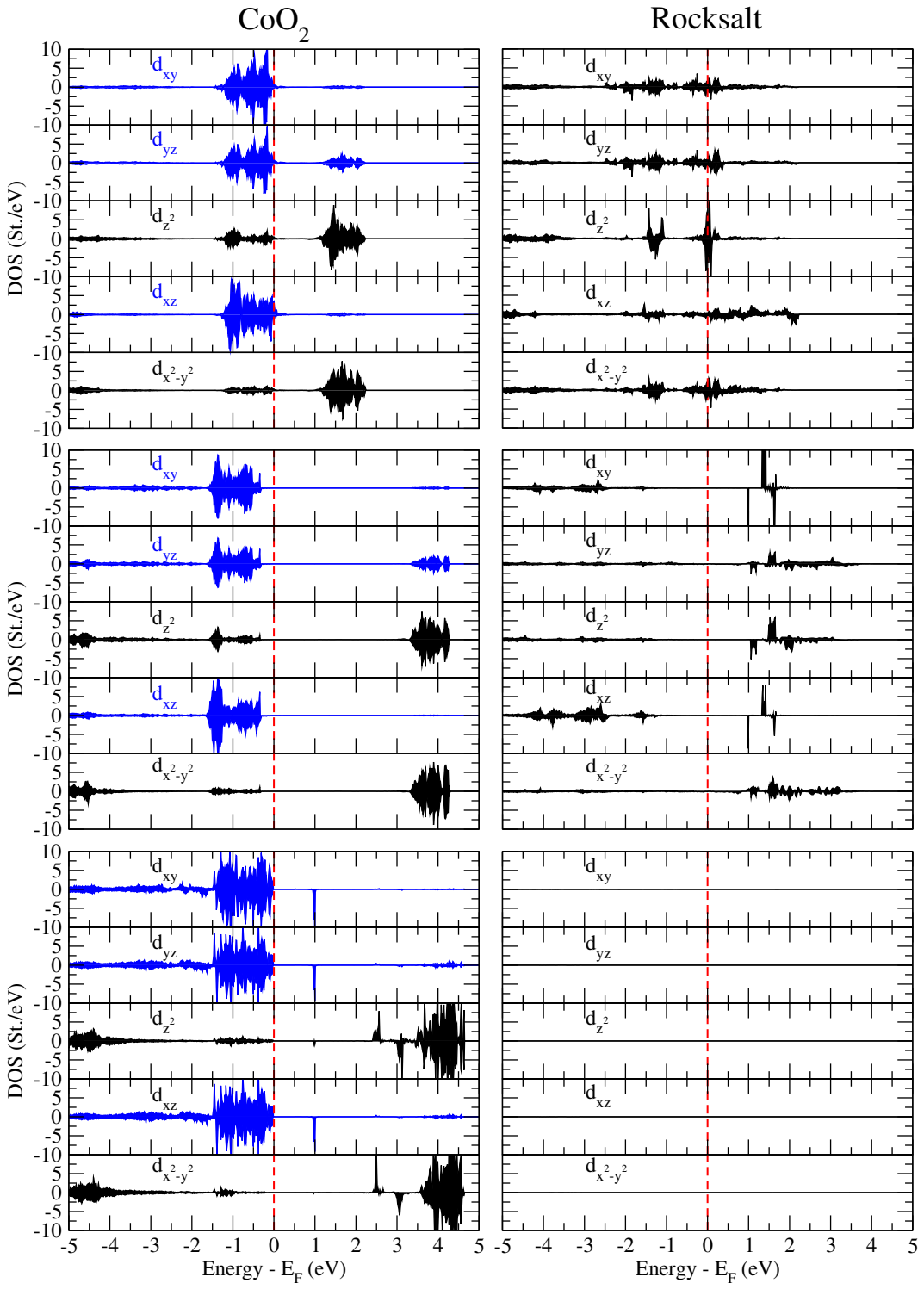

FIGURE 7.4: Spin-up (positive values) and spin-down (negative values) partial density of state projected into 3*d* orbitals of Co atoms in the CoO_2 subsystem and in the RS subsystem, for the FIM ground state. The blue lines are for the t_{2g} orbitals; the black ones are for the e_g orbitals.

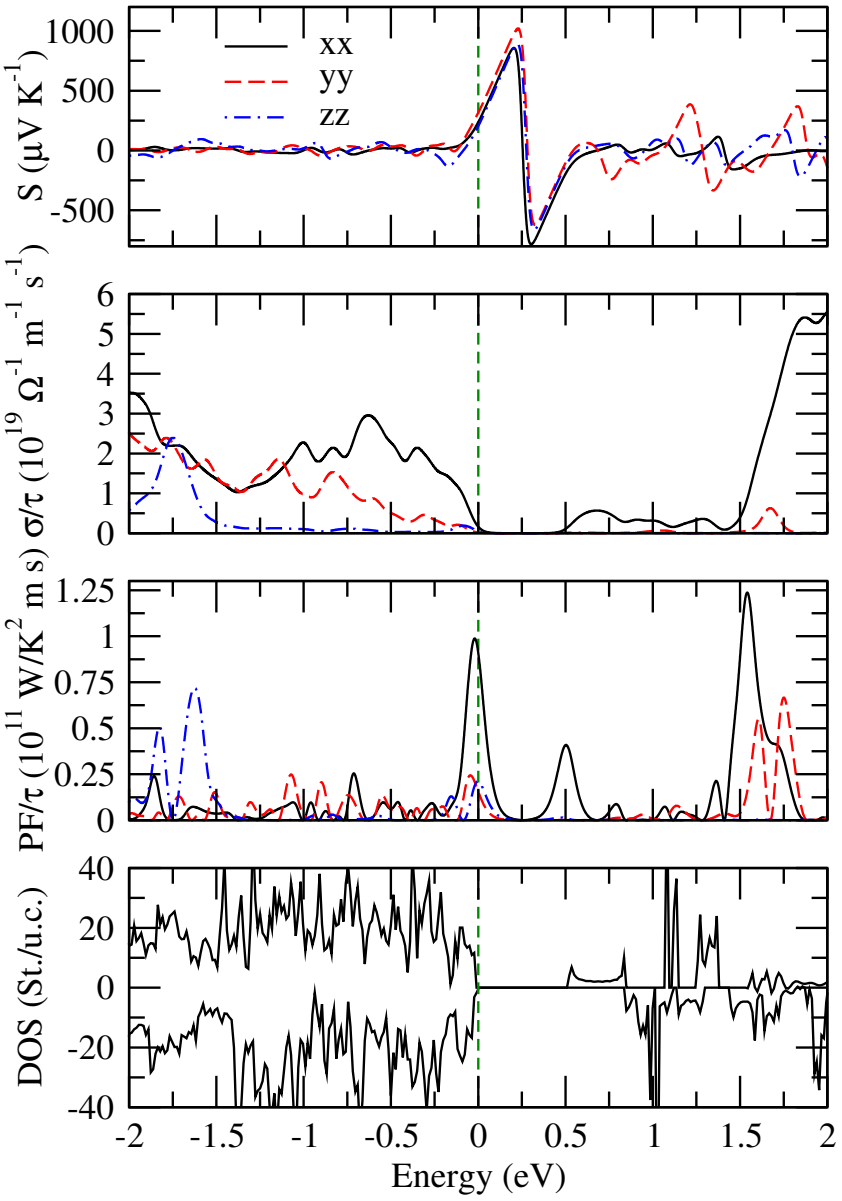

FIGURE 7.5: Diagonal components of the Seebeck tensor and electrical conductivity tensor (over the relaxation time) with respect to the chemical potential, at 300 K. The density of state is also plotted for direct comparison. The Fermi energy is plotted as a dashed line.

In Figure 7.5, the diagonal components of the Seebeck tensor S, the electrical conductivity σ/τ and the power factor $S^2\sigma/\tau$ are plotted with respect to the chemical potential μ, at a fixed temperature of 300 K. The total density of state is also displayed. The Seebeck components are slightly anisotropic at 300 K. Moreover, our calculations of the intrinsic Seebeck coefficients are positive, indicating that the majority charge carriers are holes, as observed experimentally [232, 236]. The electrical conductivity is highly anisotropic, qualitatively consistent with experiments [209, 233–235, 237] and the layered structure of CCO. The power factor in the $\vec{a}$ (xx) direction in the p-type region shows a very large peak, implying a very directional behaviour of the thermoelectric properties. The maximum of this peak is close to $\mu = 0$.

In the following, we mainly discuss the transport properties within the (001) plane,

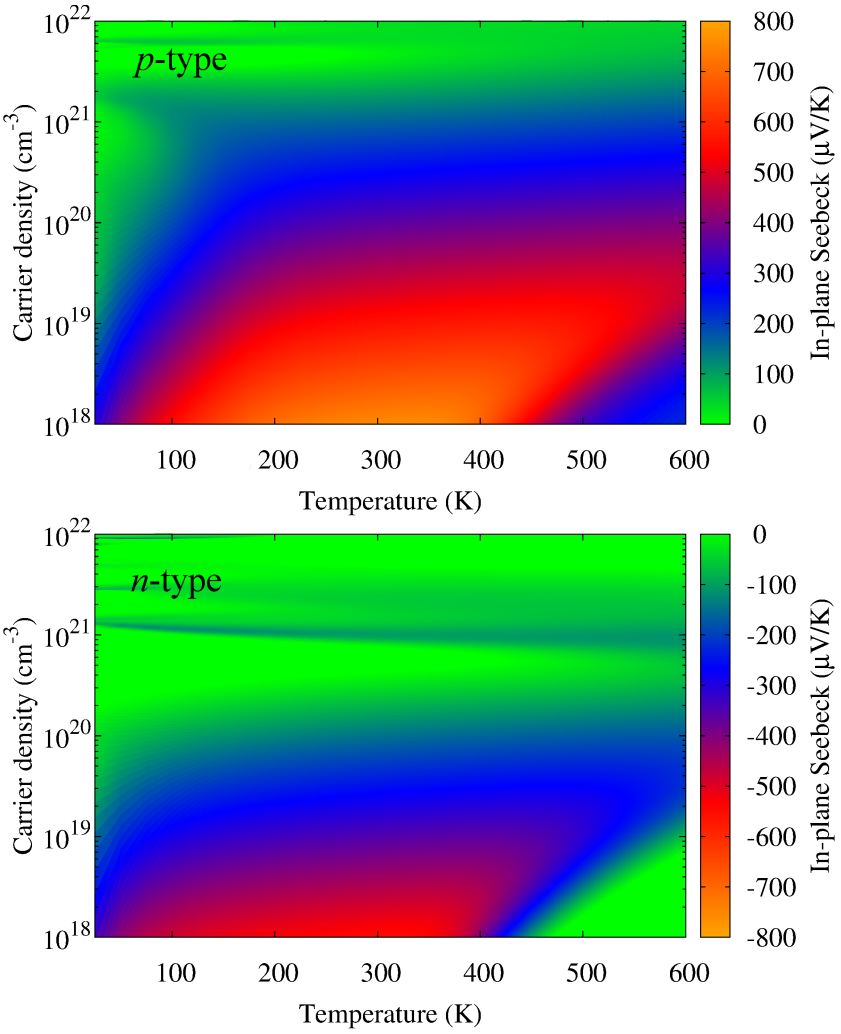

FIGURE 7.6: Maps of calculated in-plane Seebeck coefficient $S_{//}$ with respect to carrier density and temperature.

as most studies focused on the thermoelectric properties along the layers of the structure. We perform the arithmetic average between the xx and yy components from our calculation, providing a rough estimation of the effective in-plane thermoelectric coefficient $S_{//} = S^{\dagger}_{//} = \frac{1}{2}(S_{xx} + S_{yy})$ (*cf.* Appendix B for the definition of $S^{\dagger}$). In Figures 7.6, 7.7 and 7.7, the in-plane Seebeck coefficient $S_{//}$, electrical conductivity $\sigma_{//}/\tau$ ($\sigma_{//} = \frac{1}{2}[\sigma_{xx} + \sigma_{yy}]$) and power factor $\mathrm{PF}_{//}$ are mapped with respect to the temperature and with respect to carrier density n_h (for p-type) and n_e for (n-type). $S_{//}$ increases with the temperature, but at higher hole densities, it saturates at high temperatures. This is qualitatively consistent with measurements [234] performed with several types of CCO samples (single crystals, ceramics, thin films) and with the decrease of S as $\mathrm{n_h}$ increases. Experimentally, the in-plane Seebeck coefficients range from 0 to 170 μV/K as the temperature increases from 0 K to 600 K. Analysis of the p-type map show that this occurs mainly for fixed hole density ranging from 1.0×10^{21} to 1.8×10^{21} cm^{-3}. Further comparison with experiments will follow.

We now focus on the electrical conductivity (Figure 7.7). In the same fashion as we did for the Seebeck coefficient, we estimate the in-plane conductivity from the individual xx and yy components of the tensors. In the case of a p-type doping, a change

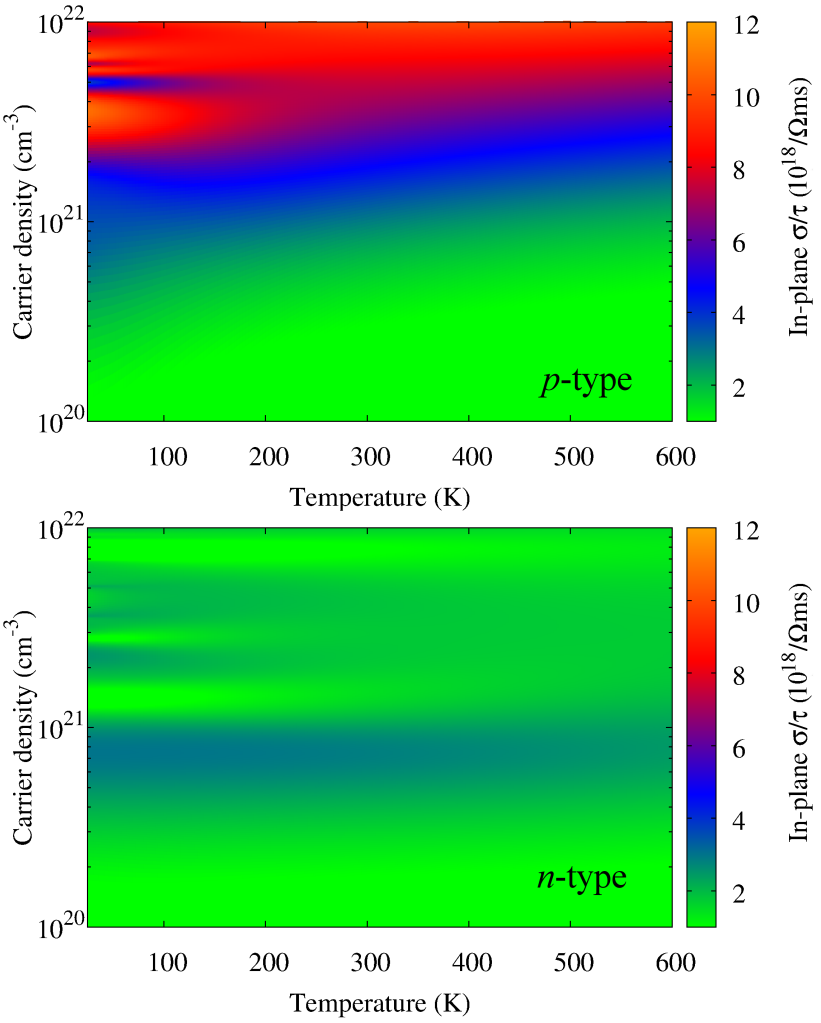

FIGURE 7.7: Maps of calculated in-plane electrical conductivity $\sigma_{//}/\tau$, with respect to carrier density and temperature.

from semiconductor-like ($\sigma_{//}$ increases with T) to metallic-like ($\sigma_{//}$ decreases with T) behaviour of the conductivity can be observed in the range of hole density defined previously, with $\sigma_{//}$ reaching a maximum slightly above 100 K. As the carrier density increases, this change of behaviour eventually disappears, leaving either a metallic-like behaviour or, for hole densities close to 5.0×10^{21} cm^{-3}, a semiconductor-like behaviour. For n-type doping, the in-plane conductivity is much lower, which can be explained by the very low value of σ_{yy} in the n-type region, as shown in Figure 7.5.

Finally, in terms of the power factor (Figure 7.8), we show that for p-type doping values between 4.7×10^{20} cm^{-3} and 2.0×10^{21} cm^{-3}, the power factor is maximized at high temperatures (above 0.06 mW/m K^2 at 600 K). On the other hand, n-type doping is not as effective, with a very narrow carrier density range from 7.8×10^{20} to 1.1×10^{21} cm^{-3} raising the power factor to 0.025 mW/m K^2 at the high temperatures (above 400 K).

In order to compare the temperature dependence of the thermoelectric properties with experimental results, it is necessary to know the carrier density associated with these properties. These can be estimated from Hall measurements (taken from Reference [232])

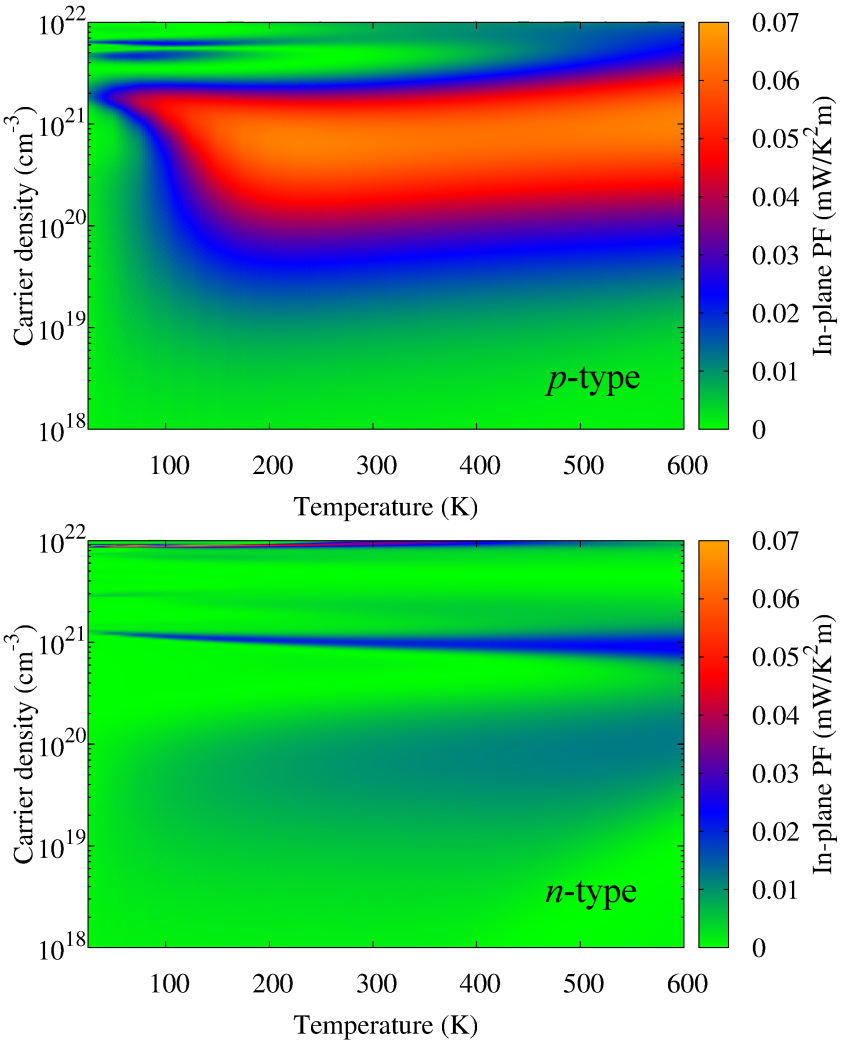

FIGURE 7.8: Maps of calculated in-plane power factor $PF_{//}$ ($\tau = 8.0 \times 10^{-16}$ s), with respect to carrier density and temperature.

by using the following semi-classical formula:

$$R_H = \frac{1}{nq} \tag{7.3}$$

where R_H is the Hall coefficient, n is the charge carrier concentration and q is the charge. We estimate hole densities ranging from 2.56×10^{21} cm^{-3} to 8.15×10^{20} cm^{-3} as temperature increases. This range is slightly larger than the one previously mentioned for which the thermopower has the same order of magnitude as the experimental values. It should be kept in mind, however, that, in the best case, the carrier density and measurements of the thermoelectric properties from experiments should come from the same sample; unfortunately, the carrier density was not reported in any of the cited References.

It is found in Figure 7.9 that, for a fixed hole density around 1.4×10^{21} cm^{-3}, which is in the range of densities extracted from Reference [232], the behaviour of $S_{//}$ is qualitatively consistent with experimental measurements [209] (performed on single-crystal samples), suggesting that the number of charge carriers does not change much with respect to

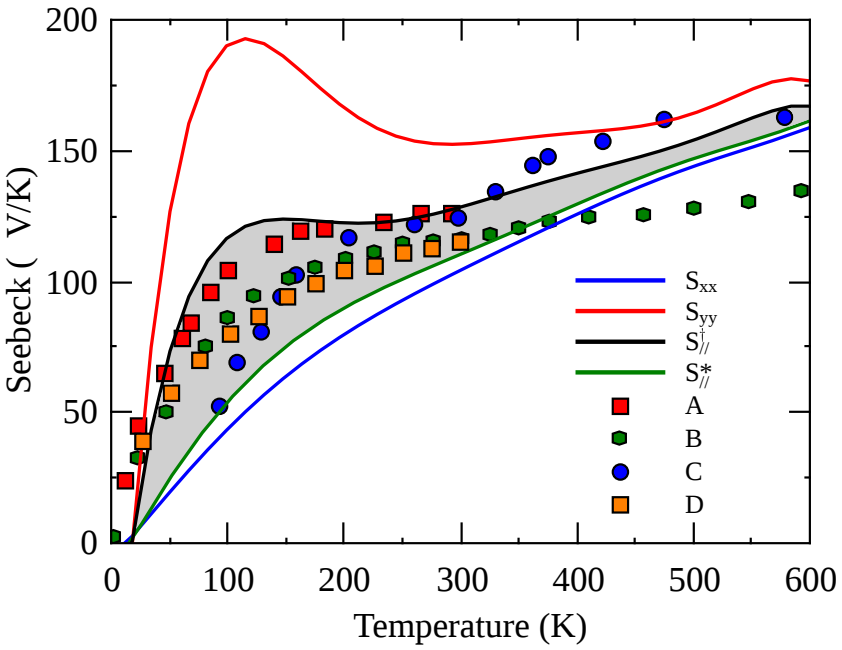

FIGURE 7.9: Calculated in-plane Seebeck coefficient $S_{//}$, up to 600 K, for $n_h = 1.4{\times}10^{21}$ cm^{-3}; the experimental values from References [209] (A), [216] (B), [237] (C), and [238] (D) are included for comparison. $S^{*}_{//}$ and $S^{\dagger}_{//}$ are calculated with two different schemes as explained in Appendix B.

temperature, in contrast to the Hall measurements. If the carriers mainly originates from impurities, the temperature does not have a strong effect on the number of carriers, unless they are excited across the band gap. $S_{//}$ reaches 168 μVK^{-1} at 600 K, which is also in good agreement with the aforementioned measurements. The apparent flat region observed experimentally for the in-plane Seebeck coefficient can be explained by the anisotropy of the Seebeck tensor. Most experiments report the in-plane Seebeck coefficient, but not the individual components of the tensors. If we look at the evolution of S_{xx} and S_{yy} with temperature (Figure 7.9), it can be observed that, along $\vec{b}$, the Seebeck coefficient (S_{yy}) varies in a non-monotonous way, reaching a maximum around 125 K. Depending on the sample, and the distribution of orientation of its grains (single crystal for References [209, 237], polycrystal for References [216, 238]), one can therefore expect different results.

To facilitate the comparison of the resistivity with experiments, we plot in Figure 7.10 the temperature dependence of $\rho_{//}$, at $n_h = 1.4 \times 10^{21}$ cm^{-3} as we did for the Seebeck coefficient. τ is estimated by fitting our relaxation-time-dependent result $\rho \times \tau$ to the experimental results from Reference [216]. We obtain $\tau = 8.0 \times 10^{-16}$ s. $\rho_{//}$ shows different behaviours: $\rho_{//}$ decreases with temperature below 100 K like an insulator, reaches a minimum around 125 K, then increases with the temperature, like a metal. We confirm therefore the transition observed in Figure 7.7. If we compare those results with the available experimental data, it can be argued that $\rho_{//}$ is qualitatively consistent, as $\rho_{//}$ displays an insulator-to-metal change of behaviour, with the transition occurring slightly below 100 K [209, 233]. The experimental data and their diversity suggest an important size effect for the resistivity, which makes the comparison with our results further difficult.

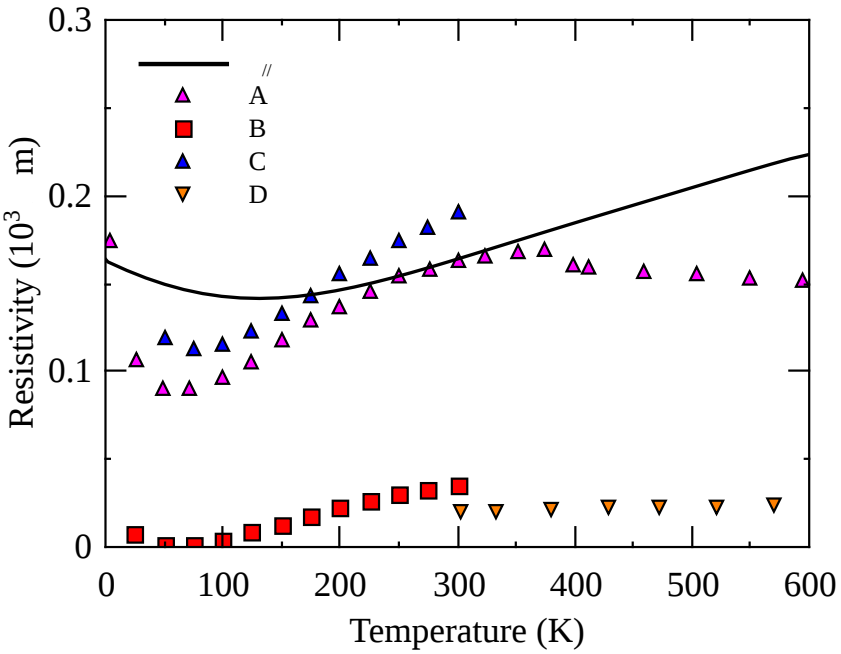

FIGURE 7.10: Calculated $\rho_{//}$ with $\tau = 8.0 \times 10^{-16}$ s, up to 600 K, for $n_h = 1.4{\times}10^{21}$ cm^{-3}, and experimental results from References [216] (A), [232] (B), [233] (C), and [237] (D), for comparison.

It is worth noticing that as we are working in the CRTA, scattering mechanisms at low temperature due to impurities or vacancies are not taken into account, which may explain why the transition is not as sharp as observed in experiments. Similarly to the Seebeck coefficient, the in-plane electrical resistivity seems to be dependent on the structure of the sample; indeed, a wide range of $\rho_{//}$ values has been reported according to the type of sample, and comparisons with experiment are then rather complicated. It has been reported that a sudden change of behaviour of thermoelectric properties occurs around 400 K, which is expected to come from a phase transition [216]. This is also not taken into account in our calculations. As highlighted in Figure 7.5, the electrical conductivity displays a much larger anisotropy than the Seebeck tensor.

It can be expected that this anisotropy of the single-crystal conductivity affects the overall thermoelectric properties, depending on the sample and the growth technique. Indeed, in the case of polycrystals or ceramics, the measurement of the in-plane transport properties is conditioned by the orientation of the individual crystallites. In Appendix B, we address this issue, deriving two models for averaging the Seebeck coefficient corresponding to different extreme orderings of the crystallites. The way we defined $S_{//} = S^{\dagger}_{//}$ corresponds to an extreme case where the transport across the grains of different orientations is in series. We also define a new quantity, $S^{*}_{//}$ which corresponds to an average S for the case where transport across the grains of different orientations is in parallel. Figure 7.9 shows the quantity $S^{*}_{//}$, at fixed $n_h = 1.4{\times}10^{21}$ cm^{-3}. This model does not fit the experimental data as well as the simple arithmetic average of the component ($S^{\dagger}_{//}$). Depending on the homogeneity of the samples, one model might be more adequate than the other, and an actual polycrystal can be expected to fall between the two models. It is worth noticing that such models make strong hypotheses, and do not take into account the anisotropy of the thermal conductivity which affect locally the temperature gradient responsible for the thermoelectric properties.

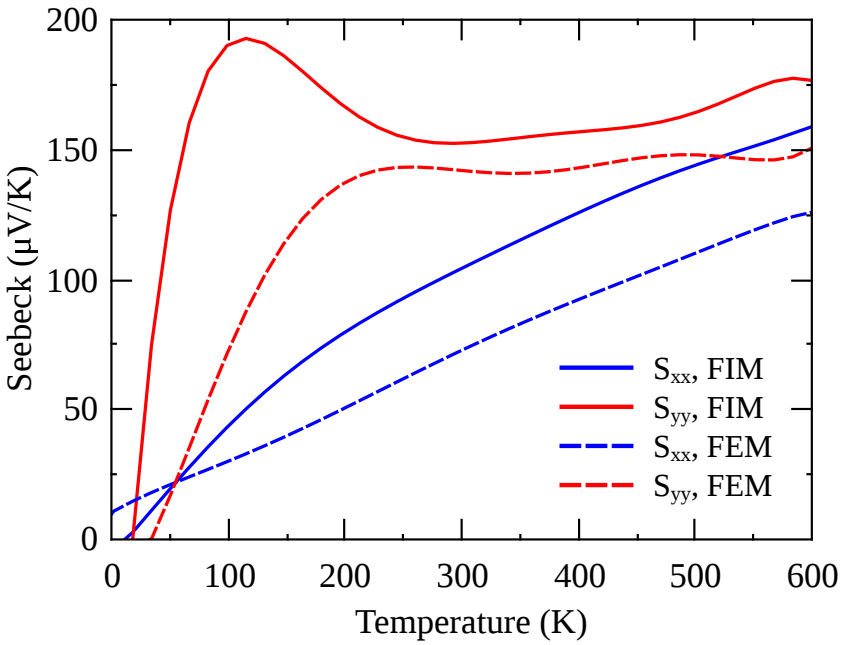

FIGURE 7.11: Calculated S_{xx} and S_{yy} from the ground state band structure and the FEM phase, up to 600 K, for $n_h = 1.4{\times}10^{21}$ cm^{-3}.

In order to check the role of the ground state band structure in contrast to the FEM band structure, we plot in Figure 7.11 the xx and yy components of the Seebeck tensor for the FEM phase, at fixed hole density $n_h = 1.4{\times}10^{21}$ cm^{-3}. The behaviours of the curves for the FEM phase are different from those derived from the ground state, particularly in the case of S_{yy}, which decreases from 100 to 250 K after a steep increase, while S_{yy} grows monotonously until 200 K and then remains flat. The properties follow similar trends above 250 K, but the Seebeck coefficients derived from the FIM ground state remains closer to the experimental data.

At our level of approximation, the global behaviour of $\rho_{//}$ and $S_{//}$ with temperature is qualitatively reproduced within the FIM configuration, although not including any magnetic transitions. This observation, associated with the similar properties computed from the FEM phase at temperature above 250 K, indicates that magnetism does not seem to play a major role in the evolution of the thermoelectric properties at high temperature. However, the descriptions of S_{xx} and S_{yy} at lower temperature does not match between the FIM ground state and the FEM phase. In other words, we suggest that the electronic band structure and excitation of carriers through thermal smearing are the main factors responsible for the evolution of $\rho_{//}$ and $S_{//}$ with temperature.

7.2.6 Summary

From first-principles calculations, we computed the structural, magnetic and electronic properties of $Ca_3Co_4O_9$ within two rational approximant models. We performed DFT calculation within LDA and the hybrid B1-WC functional for the exchange-correlation term in the Kohn-Sham Hamiltonian in order to properly model the electronic population of the Co $3d$ orbitals in the CoO_2 and the Ca_2CoO_3 (rocksalt) sublattices. Our results suggest that the best match to the available experimental data in terms of these

properties is obtained within the B1WC hybrid functional and the 5/3 rational approximant.

The ground state is found to be insulating and have very small magnetic moments in the CoO_2 subsystem, whereas the rocksalt subsystem display a ferrimagnetic behaviour, with unequal antiferromagnetically aligned moments, which is consistent with the magnetic structure observed below 19 K [213, 214]. The main electronic contribution to the density of state around the Fermi energy comes from the Co $3d$ orbitals in the CoO_2 subsystem, in agreement with photo-emission experiments [217, 218]. The broken symmetry of the t_{2g} orbitals is responsible for unoccupied states from the d_{xy} orbitals, which is qualitatively consistent with chemical quantum calculations [222].

From the electronic band structure, we computed the Seebeck and electrical resistivity tensors within the Boltzmann transport theory and the constant relaxation time approximation. The behaviour of the in-plane properties are qualitatively consistent with experiments as reported in the litterature: the Seebeck coefficient rises up to 125 μVK^{-1} at 300 K, and the linear behaviour *versus* temperature above 300 K is well reproduced, reaching 168 μVK^{-1}. $\rho_{//}$ presents a transition from an insulating-like behaviour to a metallic-like behaviour around 125 K, which is also observed experimentally, albeit at lower temperature. These results have been obtained with a model which does not include the magnetic transitions usually associated with the changes in S and ρ. This suggests a minor role of the magnetic properties, further confirmed by the results on the FEM phase who follows similar trends at temperatures above 250 K. Therefore, we suggest that the transition from semiconductor to metallic behaviour at low temperature may not be driven by a magnetic transition, but is driven by the specific features of the ground state electronic band structure.

7.3 $SrTiO_3$-based layered oxides

At the beginning of this Chapter, $SrTiO_3$ has been presented as one of the best candidate for thermoelectric applications. Indeed, if doped with donors, STO can reach $ZT \approx 0.4$, either in film form ($SrTi_{0.8}Nb_{0.2}O_3$ at 1000 K) or in bulk form ($Sr_{1-3x/2}La_xTiO_3$ at 973 K) [125, 239]. In term of power factor, the measured value reaches ~ 3 mW/m K^2 at room temperature, amongst the highest reported values for conventional thermoelectrics. In contrast, the in-plane PF of hole-doped CCO is two order of magnitude lower. Moreover, the realization of a 2-dimensional electron gas in STO-based heterostructures, which is expected to improve the thermoelectric properties as argued by Hicks and Dresselhaus [189, 190], motivates further the study of STO-based heterostructures. In the present Section, we review from first-principles the impact of nanostructuring on the thermoelectric properties, after summarizing briefly why $SrTiO_3$ is a good prototypical thermoelectric in bulk form. A more detailed description of these systems is provided in Reference [207].

7.3.1 Thermoelectric properties of bulk $SrTiO_3$

Let us first discuss about the single-crystal thermoelectric properties of bulk STO. Figure 7.12 displays the room temperature thermoelectric and transport coefficients of cubic STO with respect to the chemical potential, as well as the band structure, calculated

with the B1-WC hybrid functional. The relaxation time was fitted to experimental value of the conductivity in n-type doped STO ($n \sim 10^{21}$ cm^{-3}) [125]: $\tau = 4.3$ fs. Within the Boltzmann transport theory and the CRTA, the maximum value of PF predicted for n-type STO is $\mathrm{PF}_{n,\max} = 1$ mW/m K^2, with associated carrier density $n_e = 6.9 \times 10^{20}$ cm^{-3}, which can be achieved either by La-doping ($Sr_{1-x}La_xTiO_3$, as reported in Reference [125]) or Nb-doped ($SrTi_{1-x}Nb_xO_3$, as reported in References [240, 241]). In addition, we calculated the power factor of reduced $SrTiO_{3-\delta}$ using a $3\times3\times3$ supercell containing one oxygen vacancy (similarly as reported in Chapter 3). According to experiments [67], oxygens vacancies act as donor in STO, with transport properties comparable to La-doped STO. With the density of carriers provided by the vacancy in our simulation, we expect a density of $n_e = 1/(3a)^3 \approx 6.3 \times 10^{21}$ e^-/cm^{-3}, which is close to the density required for optimal power factor as calculated from the pristine band structure. As shown in Figure 7.12.(d), the chemical potential is right at the maximum of power factor, with a value ($\mathrm{PF}_{n,\max} = 0.75$ mW/mK^2, close to the peak of power factor calculated for $Sr_{1-x}La_xTiO_3$ at the same level of approximation [207]) slightly reduced compared to the one estimated from the rigid band approximation[1]. This suggests that tailoring the density of V_O in STO may be yet another strategy to improve its thermoelectric properties.

The peak of power factor found in heavily-doped n-type cubic STO is related to the nature of the bottom of the conduction band, which is formed of three degenerate bands with a Ti t_{2g} orbital character. Each t_{2g} band is associated with an effective mass tensor $m^*_{\alpha\beta}$, with two light diagonal components and one heavy mass diagonal component: for d_{xy}, $m^*_{xx} = m^*_{yy} = m^*_L = 0.4\ m_e$ and $m^*_{zz} = m^*_H = 6.1\ m_e$ as calculated from DFT. The masses for the d_{xz} and d_{yz} bands can be trivially deduced from the cubic symmetry. It can be seen from Figure 7.12 that the peak of power factor coincides with a chemical potential falling in the middle of the flat part of the Ti t_{2g} bands along $\Gamma \rightarrow X$. This highlights that a good combination of carriers with large, anisotropic effective mass can indeed lead to a large power factor, and that low and high carriers mobilities can be found within a single d band. The cubic symmetry imposes a band multiplicity of 3 for the t_{2g} bands, yielding isotropic transport from the contribution of 3 anisotropic bands.

For n-type doped $SrTiO_3$, the Fermi surface in the IBZ associated with these Ti t_{2g} bands can be seen as a combination of three orthogonal intersecting ellipsoids, when the Fermi level is close to the minimum; or as three orthogonal tubes when the Fermi level is deeper in the conduction band. These surfaces are displayed in Figure 7.13: one corresponding to the doping for which the PF is maximum, the other to $n_e = 1.7 \times 10^{21}$ cm^{-3}, highlighting the tubular shape for chemical potentials deeper in the conduction band. The Ti t_{2g} bands therefore realize the shape of Fermi surface predicted to yield high power in bulk thermoelectrics [200]. Each tube/ellipsoid contributes to a two-dimensional transport channel with high mobility carriers in the transverse plane. The large surface of the tube/ellipsoid guarantees that a large amount of carriers are involved in the transport processes.

In addition to the tubular surface, there are closed, quasi-spheric surfaces inside the tubes, related to the dispersive states of the Ti t_{2g} bands around Γ. These enclosed surfaces also contribute to transport, albeit in an isotropic way.

[1] In principle, as the conductivity is measured in doped samples, it would be more rigorous to fit the conductivity calculated from a doped structure. In such a case, the relaxation time τ would be slightly higher.

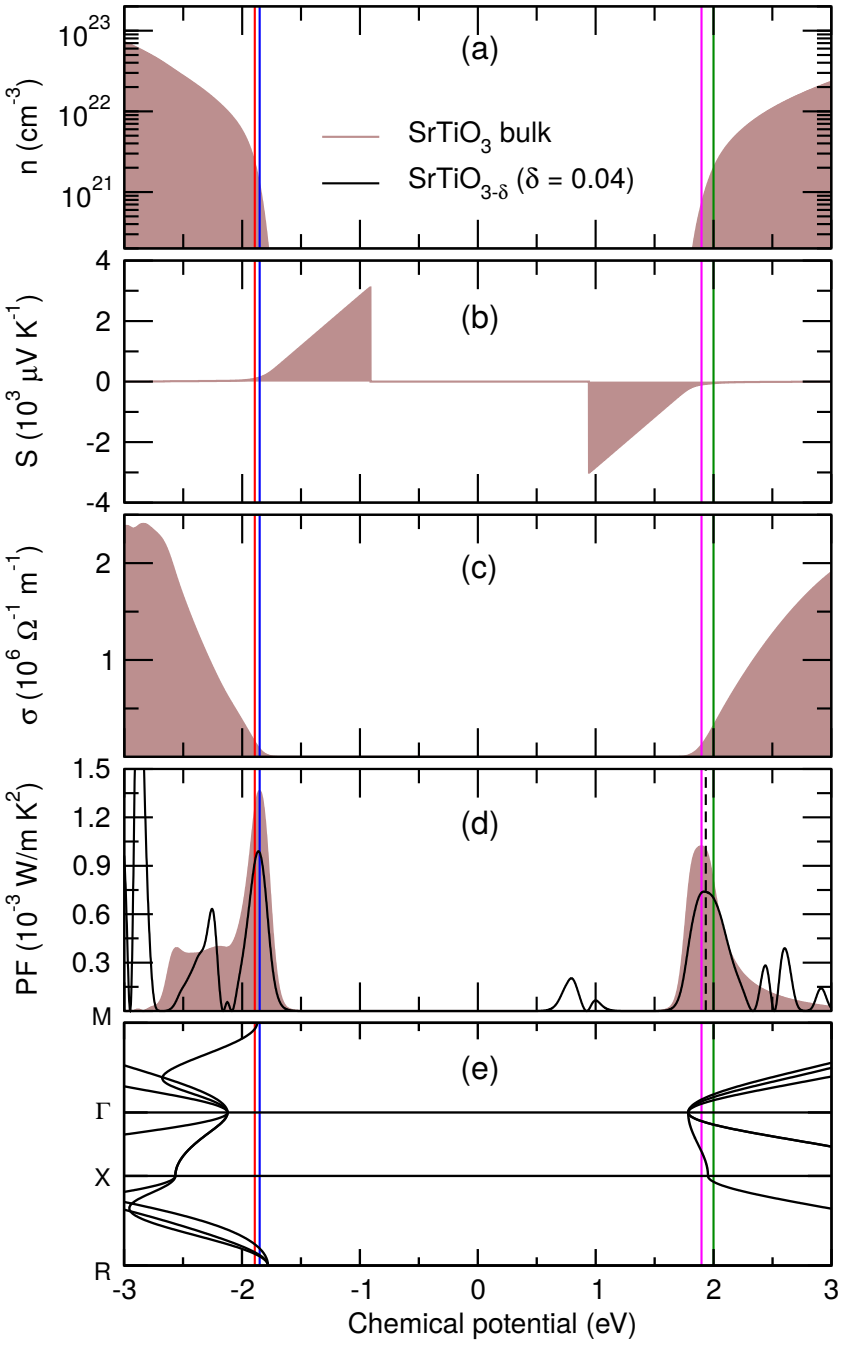

FIGURE 7.12: Thermoelectric properties of cubic STO calculated with the B1-WC functional, at 300 K. From top to bottom: (a) Carrier densities corresponding to the position of the Fermi level; (b) Seebeck coefficient; (c) Electrical conductivity; (d) power factor and (e) the corresponding band structure resolved along the path $M \to \Gamma \to X \to R$. In addition, (d) includes the chemical dependence of reduced $SrTiO_{3-\delta}$, calculated with a $3 \times 3 \times 3$ supercell containing 1 V_O. The vertical dashed line is the Fermi level of this phase. For specific values of the chemical potential, represented in colour: the magenta line corresponds to the Fermi level yielding the maximum n-type power factor ($n_e = 6.9 \times 10^{20}$ cm^{-3}), whereas the green line corresponds to the position of the Fermi level for an arbitrary n-type doping ($n_e = 1.7 \times 10^{21}$ cm^{-3}), slightly deeper in the conduction band. The blue line corresponds to the Fermi level yielding the maximum p-type power factor ($n_h = 1.2 \times 10^{21}$ cm^{-3}), whereas the red line corresponds to the position of the Fermi level for an arbitrary p-type doping ($n_e = 2.2 \times 10^{21}$ cm^{-3}). The used relaxation time is $\tau = 4.3$ fs.

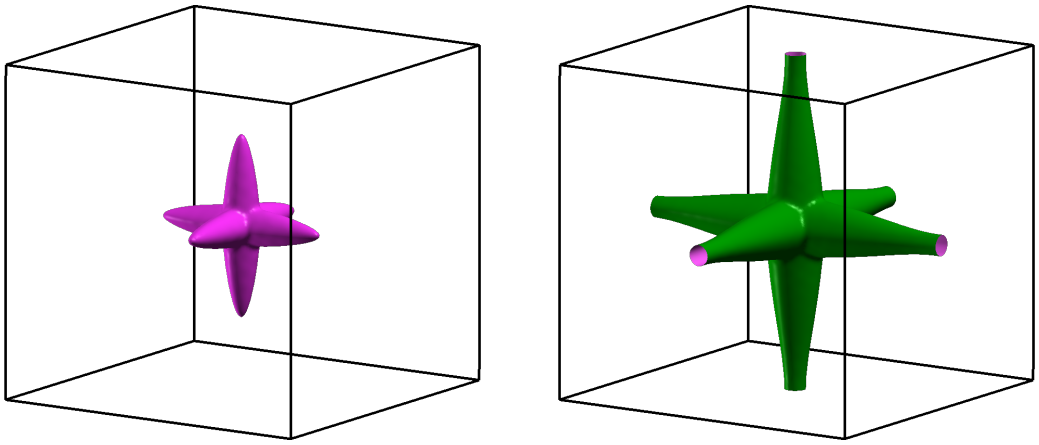

FIGURE 7.13: Fermi surfaces of n-type STO plotted in the IBZ centred around Γ, with electron densities $n_e = 6.9 \times 10^{20}$ cm^{-3} (left) and $n_e = 1.7 \times 10^{21}$ cm^{-3} (right).

The calculated value of the power factor is slightly underestimated compared to the aforementioned experimental result. DFT calculations [207] on $Sr_{1-x}La_xTiO_3$ show that the perturbation (arising from doping) on the band structure is not significant enough to reduce the power factor, ruling out the non-validity of the rigid band approximation in this case.

The underestimation of the calculated power factor compared to the experimental value can be attributed to the strong electron-phonon coupling interaction in STO: from optical conductivity measurements, a factor of 3 larger of the measured inertial effective mass $m^*_{I,\text{exp}}$ is obtained in contrast to the DFT calculated average effective mass m^*_I [242]:

$$\frac{1}{m^*_I} = \frac{1}{3}\left(\frac{2}{m^*_L} + \frac{1}{m^*_H}\right) \rightarrow m^*_I \approx 0.6 \sim \frac{1}{3} m^*_{I,\text{exp}} \tag{7.4}$$

As the DFT calculations purposely ignore such interactions, which relate to the polaronic nature of electronic transport in STO [160], this translates into a smaller value of the relaxation time.

In terms of p-type thermoelectric properties of STO, which can be tailored with acceptor doping to shift the chemical potential toward the O $2p$ bands, there is a similar peak of PF on the left side of the energy spectrum, $\text{PF}_{p,\text{max}} \sim 1.4$ mW/m K^2, slightly higher than the peak for n-type doping. However, to reach the peak value, it requires a hole density $n_h = 1.2 \times 10^{21}$ cm^{-3}, twice higher than the density required to reach the n-type peak. The Fermi surface associated with this hole density is plotted in Figure 7.14, on the left side. Note that in this Figure, and in contrast to Figure 7.13, the IBZ is centred around the R point. It can be seen that, around the R point, the overall look of the surface is similar to the Fermi surface for the peak for the n-type peak, albeit with a larger surface. For a chemical potential deeper in the valence band, it can be seen that the Fermi surface also has a tubular shape, which arises from the weak dispersion along $M \rightarrow R$, which is not explicitly shown in Figure 7.12 (e) but nevertheless can be deduced by the proximity in energy for O $2p$ bands ($\Delta E \sim 0.1$ eV) at the M and R points.

Given the promising values of power factor for bulk STO, which are close to the value found in Bi_2Te_3 ($\sim 2-4$ mW/m K^2 at 300 K [243–245]), it is an ideal candidate to assess if these properties can be improved through nanostructuring, by engineering the band structure and improving the low-dimensional aspect of the electronic transport.

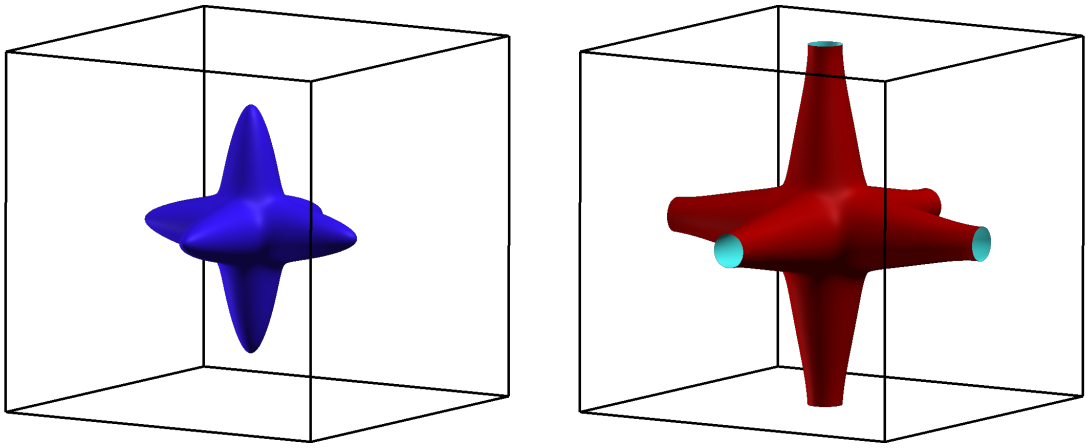

FIGURE 7.14: Fermi surfaces of p-type STO plotted in the IBZ centred around R, with hole densities $n_h = 1.2 \times 10^{21}$ cm^{-3} (left) and $n_h = 2.2 \times 10^{21}$ cm^{-3} (right).

Indeed, by incorporating STO within other compounds in a layered fashion, interface between the STO and other compounds are expected to increase the confinement of the carriers, resulting into a higher anisotropy of the bands and a therefore a higher power factor compared to the bulk phase.

7.3.2 Thermoelectric properties of $SrTiO_3$-based heterostructures

The thermoelectric properties of a few-selected STO-based superlattices have been studied in the context of a collaboration with researchers from NITIM, Cluj-Napoca, published in Reference [207] and compared to the thermoelectric properties of bulk STO, within DFT and with the hybrid functional B1-WC, and at the same level of approximation as the study in the previous Section. Hence, between the different calculations, the relaxation time τ is supposed to remain the same in the heterostructures as in bulk STO. The different investigated STO-based superlattices (shown in Figure 7.15) are:

- $(SrTiO_3)_m/(KNbO_3)_1$ ($m = 1$, 5, Fig. 7.15.(a) and (b)) and $(SrTiO_3)_m/(LaVO_3)_1$ ($m = 1$, 5, Fig. 7.15.(c) and (d)) superlattices.
- Sr_2TiO_4 (Fig. 7.15.(e)) and $Sr_3Ti_2O_7$ (Fig. 7.15.(f)) compounds, with the $AO\,[ABO_3]_m$ Ruddlesden-Popper structure.

In addition to these STO-based nanostructures, the Ruddlesden-Popper Sr_2CoO_3F is also studied within different magnetic orderings (Figure 7.15.(g), (h), (i) and (j)) and compared to bulk STO.

The general observation is that, for all these heterostructures, the power factor is not improved over that of bulk STO, as can be observed in Figure 7.16, which shows the thermoelectric power factor components either in the plane of the interfaces (xx) as well as the out-of-plane components (zz), at 300 K. These are important results which may highlight other requirements for high power factor, which are missed in the nanostructures.

Indeed, all the heterostructures present highly anisotropic bands at their CBM, with a large anisotropy in their effective masses. Despite this feature, the power factor is not

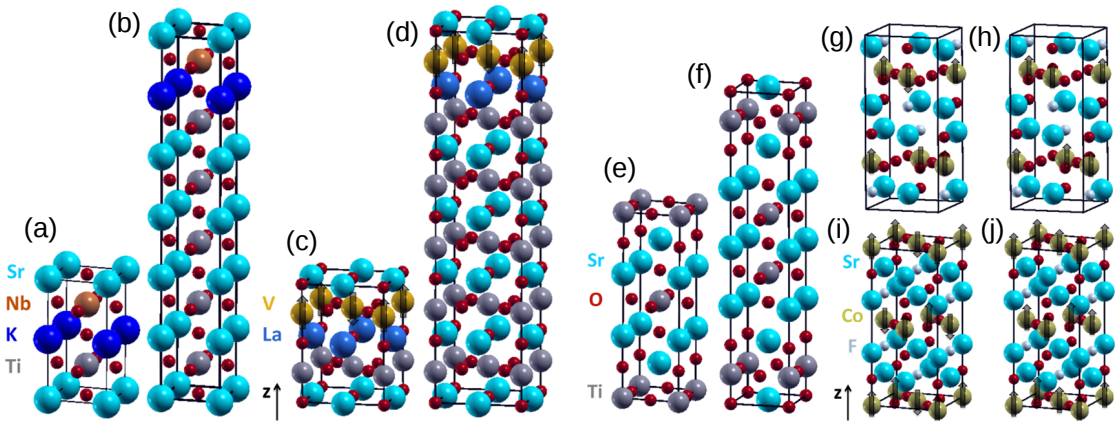

FIGURE 7.15: (a and b) $(SrTiO_3)_m/(KNbO_3)_1$ ($m = 1, 5$) nanostructures; (c and d) $(SrTiO_3)_m/(LaVO_3)_1$ ($m = 1, 5$) nanostructures (with in-plane antiferromagnetic spin order, shown by arrows); (e) Sr_2TiO_4 structure; (f) $Sr_3Ti_2O_7$ structure; (g, h, i and j) Sr_2CoO_3F structure with different spin ordering: (g) antiferromagnetic order on Co and one F atom in apical position, (h) ferromagnetic order on Co and one F atom in apical position, (i) antiferromagnetic order on Co and two F atoms in apical position, and (j) ferromagnetic order on Co and two F atoms in apical position. The spin is shown by arrows. Adapted from Reference [207].

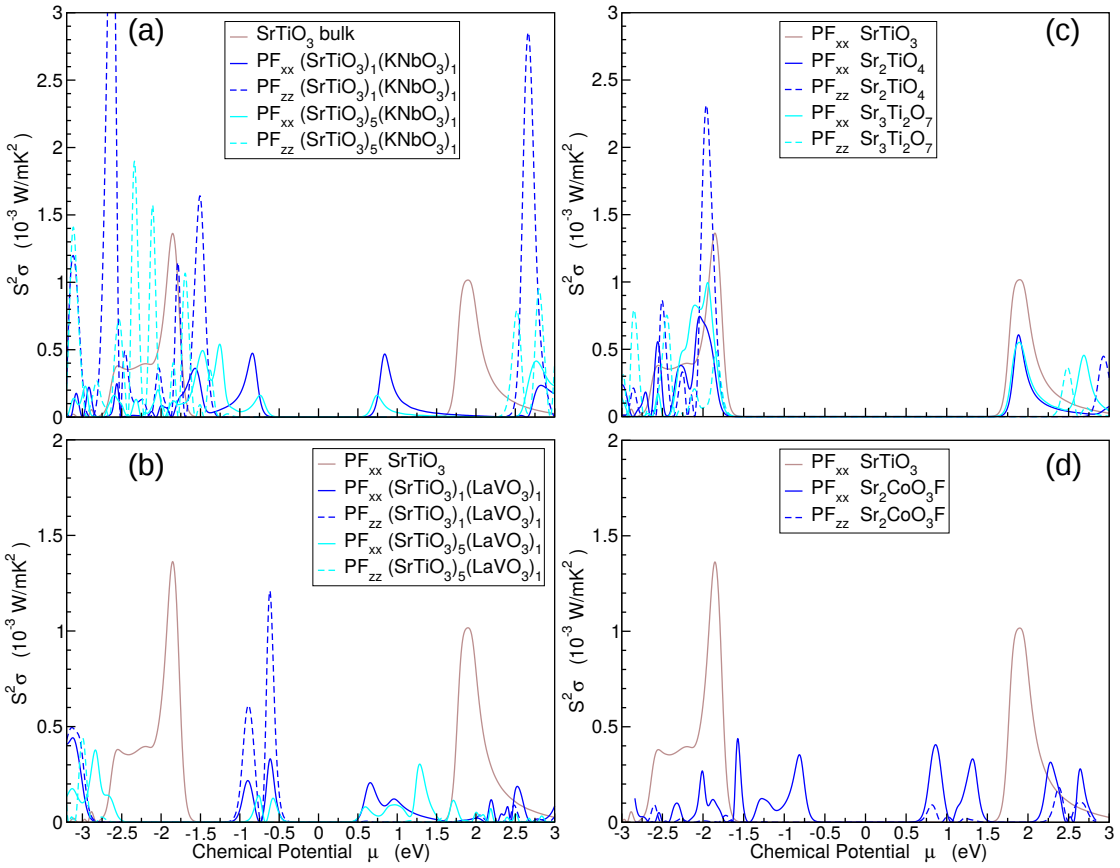

FIGURE 7.16: Power factor (estimated at 300 K within B1-WC, $\tau = 4.3$ fs) dependence on chemical potential of (a) $(SrTiO_3)_m/(KNbO_3)_1$; (b) $(SrTiO_3)_m/(LaVO_3)_1$ superlattices ($m = 1, 5$); (c) Sr_2TiO_4 and $Sr_3Ti_2O_7$; and (d) Sr_2CoO_3F. Adapted from Reference [207].

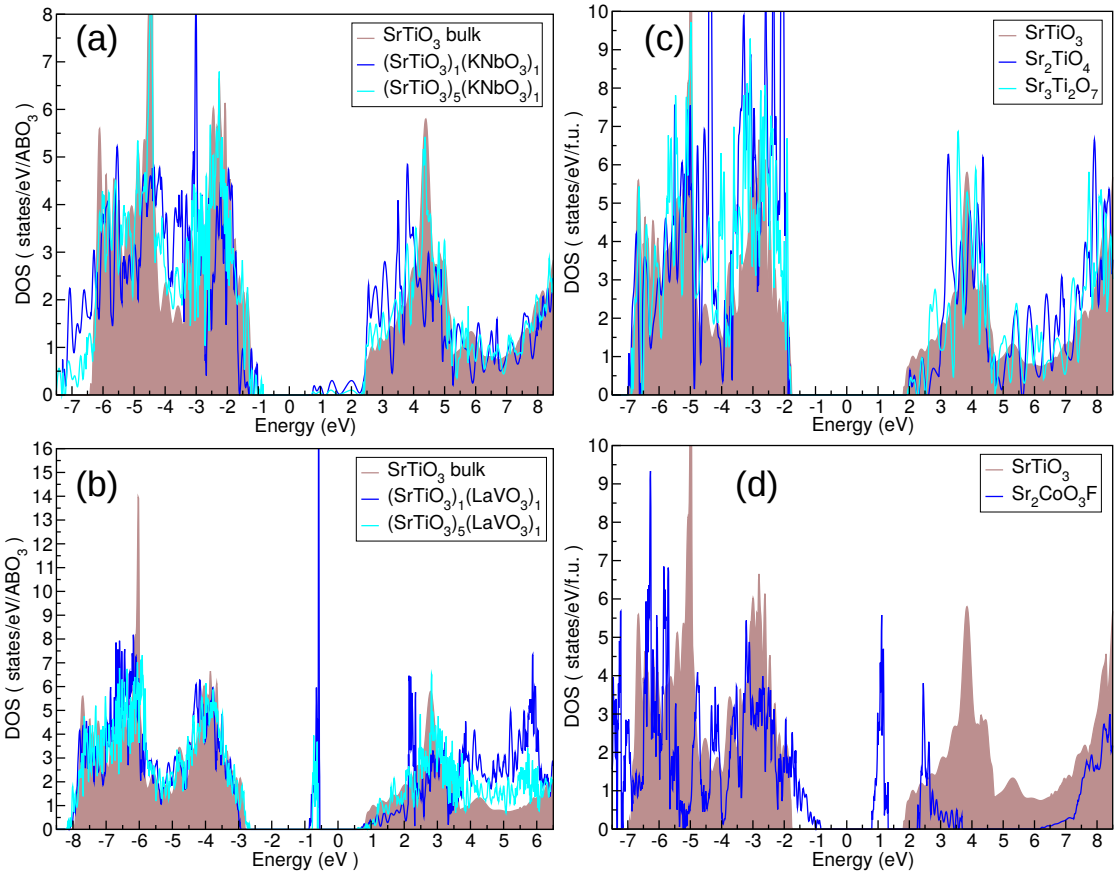

FIGURE 7.17: Densities of state, calculated with the B1-WC functional, of (a) $(SrTiO_3)_m/(KNbO_3)_1$; (b) $(SrTiO_3)_m/(LaVO_3)_1$ superlattices ($m = 1, 5$); (c) Sr_2TiO_4 and $Sr_3Ti_2O_7$; and (d) Sr_2CoO_3F. Adapted from Reference [207].

improved over the value found for bulk STO. It is found, for the STO-based nanostructures and the Ruddlesden-Popper structures, that the states in the vicinity of the CBM associated with the peaks of power have smaller spectral weights (proportional to the DOS) than in bulk STO, as shown in Figure 7.17. This leads to smaller carrier pocket volumes in the IBZ, and therefore a lower amount of carriers involved in transport, and ultimately a decreased power factor. The low weight of the band edge carrier is typical of interfaces, where band bending occurs and on-site as well as inter-site band splitting occurs close to the interfaces, with reduced spectral weight compared to their value in the bulk parent compound.

For the Sr_2CoO_3F structure, the power factor is also lower than in bulk STO, albeit for different reasons: the Co t_{2g} states involved in the n-type transport have large weights, but smaller anisotropy ratio $m_H^*/m_L^* = 3.7$ compared to bulk STO ($m_H^*/m_L^* = 15.3$). Hence, for the largest power factor in $3d$-orbitals based thermoelectrics, the electronic structure should combine a large anisotropy ratio m_H^*/m_L^*, as well large spectral weights.

7.3.3 The specific case of the $SrTiO_3/LaAlO_3$ interface

The specific nanostructures addressed in the previous section, like the parent compounds, are band insulators. Therefore, the power factor for their pristine phase is zero, and in principle, to achieve the highest power factor, they should be doped, generally *via*

chemical substitution. Yet, we have seen that it is possible to achieve electron doping of STO without chemical substitution while achieving a low-dimensional electron system in the $SrTiO_3/LaAlO_3$ (STO/LAO) system with the TiO_2/LaO n-type interface. We shall therefore address briefly this case.

First, we should mention that thermopower measurements combined with the application of a gate voltage is an extremely useful technique to probe the electronic structure of the STO/LAO interface at low temperature [246]. It has also be evidenced that at low temperature, below 50 K, there is a large enhancement of the thermopower, attributed to phonon-drag effects enhanced by confinement near the interface [247].

In term of performances for applications, the thermoelectric properties of STO/LAO heterostructures have also been studied at higher temperatures, with the hope of finding increased thermoelectric properties compared to bulk STO [240, 241]. However, no significant improvement of the thermopower was reported compared n-type STO.

Filippetti *et al.*, from first-principles calculations and using a tunable band model (Figure 7.18), provide a general framework to understand the lack of improvement of the thermoelectric properties [241]. They argue that any improvement of the thermopower due to confinement is counteracted by the splittings of the different t_{2g} states: on-site band splitting $d_{xy} - (d_{xz}, d_{yz})$ as well as inter-site band splitting between band of same nature. Such splittings are also expected to occur in chemically doped STO layered-systems [191, 248], albeit to a much smaller extent, which is why the rigid band picture (and accounting mass renormalization due to the electron-phonon coupling) yields a satisfying estimation. In a strong doping regime, as in the fully-compensated scenario, the splittings are the largest, and result in a reduction of the thermopower. For the lowest densities however, the splittings will be smaller, but sufficient to counteract any gain of thermopower from the low dimensionality. While the study of Filippetti *et al.* focused on the LAO/STO interface, their conclusions can be reasonably extended to other oxides nanostructures with similar Ti t_{2g}-based 2DES. The t_{2g} splittings related to metallic band occupancy also further enhance the loss of spectral weight already observed in the insulating nanostructures discussed in the previous Section, and highlight further challenges in optimizing the thermoelectric properties of layered oxides.

7.4 Conclusions

In this Chapter, we have studied and discussed the thermoelectric properties of various layered oxide compounds. We first focused on the different properties of calcium cobaltite $Ca_3Co_4O_9$, which has an incommensurate layered structure and whose properties are not properly reproduced by *ab initio* calculations based on semi-local functionals for the exchange-correlation, and we showed how the hybrid functional formalism overcomes these shortcomings and properly model the electronic population of the Co $3d$ orbitals in the CoO_2 and the Ca_2CoO_3 (rocksalt) sublattices. We then discussed the anisotropy of the single-crystal transports tensors, related to the layered structure, and we propose to analyse the averaged in-plane thermoelectric properties dependence with respect to the temperature as well as doping. Finally, we rationalized the evolution of the measured properties with temperature, highlighting the overall good agreement between our calculated results and the experiments.

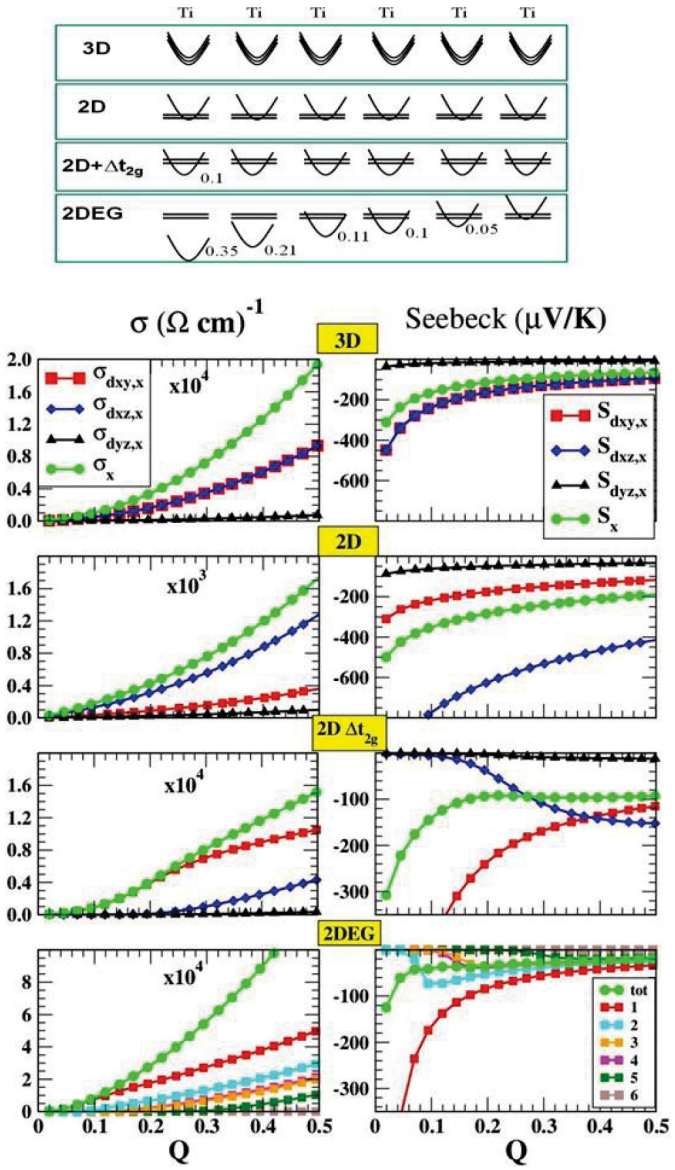

FIGURE 7.18: Total and band-by-band t_{2g} σ_{xx} (left panels) and S_{xx} (right panels) as a function of the total charge at the LAO/STO interface, calculated using a multiband model [241], according to different band splitting scenarii: from top to bottom, (a) the 3D case; (b) the 2D t_{2g}-degenerate case; (c) the 2D case plus a $d_{xy} - (d_{xz}, d_{yz})$ band splitting of 0.1 eV; (d) the 2D case with intersite d_{xy} bands split according to *ab initio* calculations for $Q = 1/2$. Adapted from Reference [241].

Then, we addressed the thermoelectric properties of layered-STO compounds. In its bulk form, STO has good thermoelectric properties if doped with donors, providing electrons to partially occupy the Ti t_{2g} states at the bottom of the conduction band. We also showed that reduced $SrTiO_{3-\delta}$ have similar thermoelectric features as chemically doped STO (either through La- or Nb- doping). According to popular expectations, incorporating STO as nanostructures in other oxides insulators should improve the thermoelectric performance. However, it is found that the layered nanostructures present new DOS features in the vicinity of the conduction band, with lower weights, which counteract on the increase of anisotropy expected to improve the thermopower [200]. All the investigated nanostructures have their power factor peaks in the vicinity of the CBM lowered in comparison to bulk STO. These results suggest that in addition to high anisotropy in effective masses, large weight are also necessary to increase the thermoelectric power factor.

Finally, in the light of the analysis of the $LaAlO_3/SrTiO_3$ interface done in the previous Chapters, we also address the thermoelectric properties of the 2DES close to the TiO_2/LaO n-type interface. Indeed, the achievement of the 2DES in the STO system is achieved without chemical doping, and moreover the electron system self-localizes close the interface, forming a thin metallic layer. Hence, the LAO/STO interface realizes simultaneously a low dimensional system and confinement with large anisotropic effective masses, which according to solid theoretical considerations should improve the thermoelectric properties [189, 190, 199, 200]. However, these expectations were not met, as no improvement was found when comparing the thermoelectric properties of the conducting LAO/STO interface compared to n-type STO.

We summarize the work of Reference [241], establishing the relation between the loss of thermopower due to band splitting counteracting the increase expected from confinement. The band profile at the LAO/STO depends on the carrier density, as discussed in Chapter 4. Therefore, the usual analysis done in the rigid band approximation, in which the thermoelectric properties at a given temperature is analysed with respect to the position of the chemical potential assuming that the electronic band structure is not perturbed by doping, cannot be done for LAO/STO.

This remarkable failure of the rigid band approximation also questions the predictions calculated from the pristine band structure. The thermoelectric properties calculated from the band structure of $SrTiO_{3-\delta}$ are nonetheless close to the rigid band estimation, and similar as the case where the properties are calculated from the band structure of $Sr_{1-x}La_xTiO_3$ [207], in agreement with experiments [67]. This work demonstrates that first-principles calculations combined with the Boltzmann transport theory can be used to predict the thermoelectric properties of materials, as well as to provide arguments to rationalize the different observations in experiments. Furthermore, first-principles calculations may be used to provide guidelines to improve the thermoelectric properties of known systems.

Chapter 8

Tailoring low-dimensional transport in Fe-based Heusler compounds

In the preceding Chapter, we have seen that the large thermoelectric power factor of oxides find their origin from their transition metal $3d$ states in the vicinity of the band gap, and can be exploited by shifting the chemical potential toward these states. In the specific case of STO, the carriers in the Ti t_{2g} band yielding large power factor is characterized by anisotropic effective masses, with a flat energy dispersion along the $\Gamma \rightarrow X$ direction in the IBZ. This specific feature of the band structure translates into a elongated Fermi surface along that direction. In the present Chapter, we focus on a specific family of transition metal ternary compounds, the iron-based full-Heusler compounds Fe_2YZ, which presents similar energy features as the oxides discussed in the preceding Chapters, and have been proposed as potential good thermoelectrics. We address the effect of electron doping *via* chemical substitution from first-principles. Finally, the findings of a collaboration with experimentalists from the University of Genoa focusing on $Fe_2TiSn_{1-x}Sb_x$ phases are reported and discussed.

8.1 A brief introduction to Heusler compounds

The Heusler class of compounds is known to display a large variety of properties and physical phenomena. Their large panel of properties make them promising for applications such as photovoltaics, spintronics, magnetocalorics, and thermoelectrics [249, 250]. These ternary compounds exists in two subcategories, the half-Heusler family (with denomination XYZ) and the full-Heusler family (with denomination X_2YZ). In the following, the discussion will be about the iron-based Fe_2YZ compounds. These compounds crystallize in the $L2_1$ structure, consisting of four face-centred cubic sublattices stacked in the (111) direction, as shown in Figure 8.1; in the 16-atoms conventional cell, the atoms occupy the following Wyckoff positions: $Fe_1(\frac{1}{4}, \frac{1}{4}, \frac{1}{4})$, $Fe_2(\frac{3}{4}, \frac{3}{4}, \frac{3}{4})$, $Y(0, 0, 0)$ and $Z(\frac{1}{2}, \frac{1}{2}, \frac{1}{2})$. The identified space group is $Fm\overline{3}m$.

One of the most studied compounds within this family is Fe_2VAl, which notably gathered interest for thermoelectric applications. Fe_2VAl is a narrow-gap semiconductor,

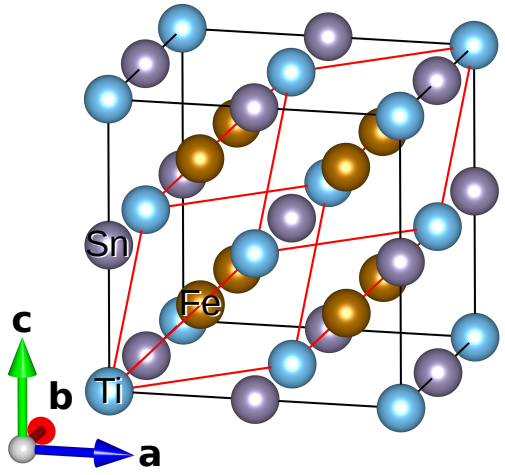

FIGURE 8.1: $L2_1$ crystal structure: red (black) line highlights the primitive (conventional) *fcc* cell.

with a lattice parameter of 5.761 Å [251], and with values for the electronic gap extracted from experiments varying between 100 and 300 meV, depending on the type of experiments [252–254]. These observations are in agreement with the observed decrease of the resistivity with increasing temperature, as illustrated on Figure 8.2.(a). Yet, in spite of such characteristics, photoemission spectroscopy experiments [255–257] detected the presence of a small, finite density of state at the Fermi level. This small density of state has led some groups to describe Fe_2VAl as a semi-metal, motivated by the small overlap between Fe t_{2g} and V e_g states across an indirect band gap as predicted by DFT calculations done within the LDA and GGA [258]. These discrepancies between experiments and the presence of the small DOS at the Fermi level have later been characterized not as intrinsic features of pristine Fe_2VAl, but from defects in the sample in the form of off-stoichiometry [259, 260], antisite defects [261] or weak localization [257]. These results are also supported by first-principles calculations [24], which report the opening of the band gap between the Fe t_{2g} and V e_g states by better treating the exchange-correlation effects typically badly described by the usual semi-local functionals (LDA, GGA).

In terms of magnetic properties, pristine Fe_2VAl is non-magnetic, according to the Slater-Pauling [249, 250, 262, 263] function:

$$M = (N - 24)\ \mu_B \tag{8.1}$$

where M is the unit cell magnetization and N the number of valence electrons within the unit cell. For pristine Fe_2VAl, N is equal: $2 \times (8) + 5 + 3 = 24$, so that $M = 0\ \mu_B$. Any deviation from stoichiometry induces spontaneous magnetic moments [264, 265], which are also reproduced by first-principles calculations based on supercell setups incorporating defects, such as excess Fe or V [266], as well as antisite defects [24].

The presence of defects in real samples, associated with in-gap states, may also explains the scattering between the different reported thermopowers in the literature, as shown in Figure 8.2.(b). The strong sample dependence, with both positive and

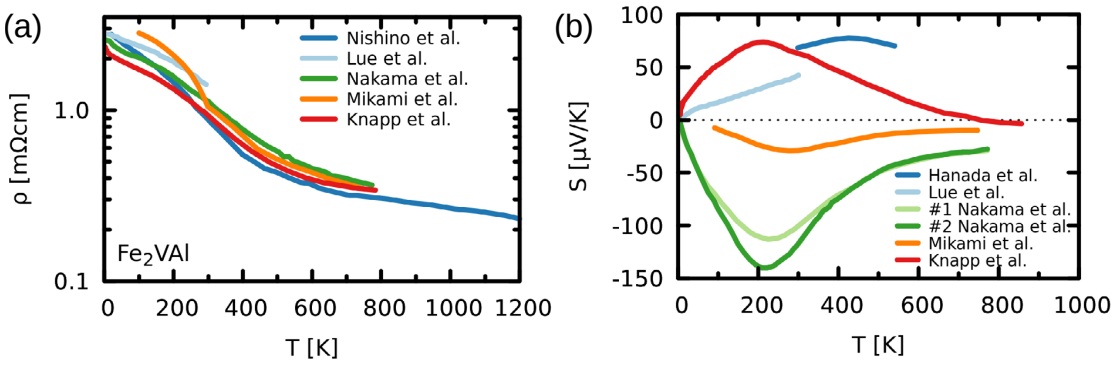

FIGURE 8.2: (a) Temperature dependence of the electrical resistivity of Fe_2VAl as measured from experiments [256, 268–271]. (b) Temperature dependence of the Seebeck coefficient of Fe_2VAl as measured from experiments [268–272]. Adapted from [273].

negative Seebeck coefficients, highlight the strong sensitivity of Fe_2VAl on carrier doping. The thermopower measurements also provide information on the nature of pristine Fe_2VAl: using the semimetal band structure calculated from semi-local functionals, Do *et al.* reports that no thermopower above $\pm 50\ \mu VK^{-1}$ can be predicted from first-principles for stoichiometric Fe_2VAl [258], in contradiction with experiments, as shown in Figure 8.2. With n-type doping, there is a reported measured power factor PF $= 5.4$ mW/m K^2 for $Fe_2VAl_{1-x}Si_x$ ($x = 0.1$) in the $300 - 400$ K temperature range [267] and PF $= 6.8$ mW/m K^2 for for off-stoichiometric $Fe_2V_{1+x}Al_{1-x}$ ($x = 0.05$) [255]. With p-type doping, and within the same temperature range, a value PF $= 4.2$ mW/m K^2 for $Fe_2V_{1+x}Al_{1-x}$ ($x = -0.03$) has also been reported [255]. These values of power factor are within the same order of magnitude as Bi_2Te_3-based thermoelectrics in the same temperature range. However, in terms of thermal conductivity, it is in one order of magnitude larger than Bi_2Te_3-based compounds for stoichiometric Fe_2VAl, leading to thermoelectric Figure of Merit $ZT \approx 0.14$, as measured for $Fe_2VAl_{0.9}Si_{0.07}Sb_{0.03}$ [268]. Nevertheless, the large power factor, characterizing a large voltage generation during the conversion process, is promising enough for waste heat recovery application.

The large power factors found in Fe_2VAl, as well as the benefits in term of lack of toxicity and high stability make the compound an ideal candidate for larger scale applications, similarly to the oxides discussed in the previous Chapter.

Another iron-based full-Heusler compound that is gathering growing interest is Fe_2TiSn. This compound specifically shares a lot of properties with Fe_2VAl. It crystallizes in the stable $L2_1$ structure, and is non-magnetic as well, in agreement with the Slater-Pauling picture. It is a semiconductor with a band gap arising from large Fe $d-d$ hybridization, with Fe t_{2g} states constituting the valence band maximum and Fe e_g states constituting the conduction band minimum [201, 274, 275]. In the same fashion as Fe_2VAl, it has been suggested that magnetism in Fe_2TiSn arises from disorder [276, 277], which is also expected to induce in-gap states. In addition to these properties, it is expected, from the predictions of first-principles calculations [201], that n-type doped Fe_2TiSn displays an even larger power factor than Fe_2VAl. Despite this promising aspect of Fe_2TiSn, and in contrast to Fe_2VAl, there is yet no report of n-type conductivity: the literature only contains reports of p-type conductivity, even when doped with donors. This peculiar aspect of Fe_2TiSn will be a topic of discussion, in the later part of this manuscript.

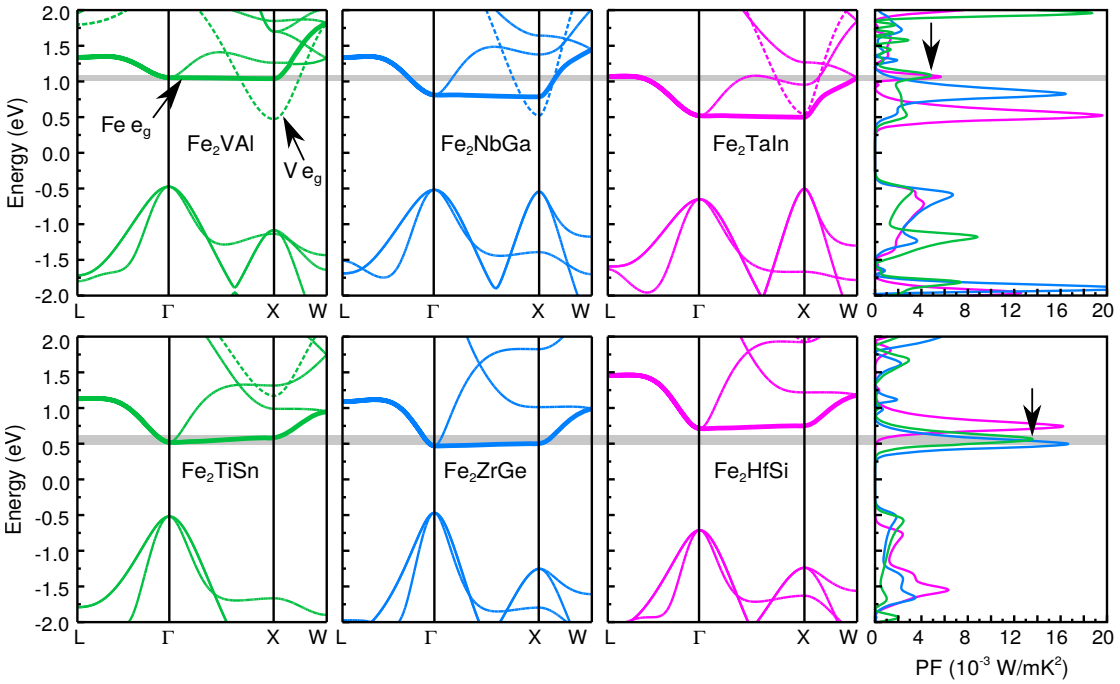

FIGURE 8.3: Electronic band structures and thermoelectric power factors with respect to chemical potential, estimated from first-principles at 300 K, for Fe_2VAl, Fe_2NbGa, Fe_2TaIn, Fe_2TiSn, Fe_2ZrGe and Fe_2HfSi. The bold line indicates the band of Fe e_g character, while the dashed line indicates the band of Y e_g character. On the power factor plots, the arrows show the maximum of power factor peak for Fe_2VAl and Fe_2TiSn. Adapted from Reference [25].

Why is there a growing interest in these full-Heusler compounds for thermoelectric applications, aside the promising power factor found in Fe_2VAl ? Interest basically sparkled from a theoretical study [25] focusing on the electronic properties Fe_2YZ compounds, expected to be non-magnetic based on the Slater-Pauling argument, with the same spirit as a high-throughput study: a large panel of configurations, yielding zero net magnetic moments and presenting an electronic band gap, was screened from first-principles. The result of this study can be summarized as follows: the large power factors calculated for these compounds in the vicinity of the band gap is due to the Fe e_g states which present a highly anisotropic band dispersion, nearly flat in the $\Gamma \rightarrow X$ direction in the IBZ, but highly dispersive in the other directions, as shown in Figure 8.3; this feature is quite reminescent of dispersion the Ti t_{2g} bands in bulk STO. At first glance, it is also much flatter in the $\Gamma \rightarrow X$ direction than the Ti t_{2g} bands in bulk STO, simply by looking at the difference of energy between Γ and X points: 62 meV for Fe_2TiSn, for example, while 170 meV for STO. The relaxation time, estimated by fitting the calculated electrical resistivity $\rho\tau$ to the experimental value of 0.65 mΩ cm for $Fe_2VAl_{1-x}M_x$ (M = Si, Ge) at doping $x = 0.03$ at 300 K [278, 279], has a value of 3.4×10^{-14} s, which is basically one order of magnitude higher than the relaxation time usually found in oxides ($\sim$ 1 fs), which is also expected to increase the mobility of the carriers, as expected from a free-electron-like picture (Equation (6.38)).

As shown in Figure 8.3, the flat Fe e_g band is not necessarily at the bottom of the conduction band. In the specific case of Fe_2VAl, the V e_g band constitutes the CBM, while the Fe e_g is 0.6 eV above the CBM. Hence, shifting the chemical potential toward the Fe e_g via chemical substitution is not possible. Moreover, the dispersive V e_g is

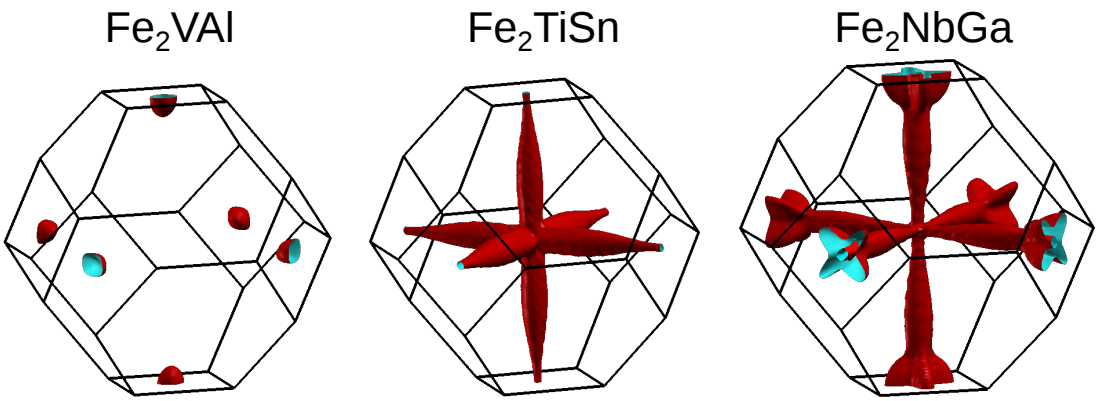

FIGURE 8.4: Fermi surfaces associated with optimal n-type doping, corresponding to the chemical potentials maximizing the power factor at 300 K as displayed in Figure 8.3 for Fe_2VAl, Fe_2TiSn and Fe_2NbGa. Recomputed by the author from the inputs of Reference [25].

detrimental to the power factor, and should be moved above the flat band to yield large power factor. Looking at the other Heusler candidates in Figure 8.3, one can see that all the other candidates, with a Fe e_g CBM, present a large peak of power factor reaching up to $14-20$ mK/mK^2 at room temperature, which is 4 to 5 times larger than the power factor found in Bi_2Te_3-based compounds. These peaks of power factor can be reached with proper n-type doping, with electron densities around $\sim 10^{21}$ cm^{-3}. These peaks of power factor are associated with Fermi surface featuring the tubular (or pipe-like) shapes, as shown in Figure 8.4 for the specific cases of Fe_2VAl, Fe_2TiSn and Fe_2NbGa. The n-type doped Fe_2YZ compounds therefore realize the requirements described by Mahan and Sofo [199, 200] for large power factor. It is also remarkable that the lobes around the X points for the Fe_2NbGa Fermi surfaces (arising from the Nb e_g band), do not have an ellipsoidal shape, but also present a small directional character, with foldings increasing the overall surface, and leading to a large effective density of carriers involved in the transport properties.

8.2 Doping-induced magnetic instabilities in full-Heusler compounds and impact on the thermoelectric properties

In the previous Chapter, the discussion focused on layered-oxides, and the special case of STO-based nanostructures whose thermoelectric properties are not improved over bulk STO, despite featuring the same band feature with enhanced anisotropy. In the specific case of LAO/STO heterostructure, the failure of the rigid band approximation (with explicit dependence of the band profile with respect to carrier density) makes its use questionable when addressing the thermoelectric properties of materials from a theoretical point of view. Given the observed physical phenomena emerging from defects for Fe_2VAl and Fe_2TiSn, and in particular, in the light of the Slater-Pauling rule (Equation (8.1)), any deviation from stoichiometry is expected to gives rise to magnetism and to alter the band structure significantly, further questioning the validity of the rigid band approximation.

It is consequently legitimate to further study these compounds. In this Chapter, we study a few selected Fe_2YZ compounds, by incorporating the donor species in a supercell setup, as done in the previous Chapters to model defects in LAO/STO systems, and to evaluate the effect of chemical substitution on the band structure, and how the overall thermoelectric properties are affected by these changes.

8.2.1 Computational details

DFT calculations were performed using the B1 Wu-Cohen [42] (B1-WC) hybrid functional, as implemented in the CRYSTAL code [37, 44], and the generalized gradient approximation (GGA) with the Perdew-Burke-Ernzerhof flavour for the exchange-correlation functional [10] including a Hubbard-like U correction.

Within the hybrid functional framework, we explored the effects of chemical substitution in $Fe_2YZ_{1-x}A_x$ compounds, which shall be referred to as Fe_2YZ_A in the following, with $A = Si, P, Ge, Sb$ at densities $x = 0, 1/48, 1/32, 1/16$. The geometry of the supercells used for these compositions is shown in Figure 8.6. These compounds have been chosen for two reasons: first, they are all predicted to be thermodynamically stable, as shown in Figure 8.5. On the other hand, the profile of the CBM in Fe_2TiSi, Fe_2TaGa and Fe_2NbGa are intermediate between Fe_2TiSn and Fe_2VAl in term of the relative positions between the Fe e_g and Y e_g bands.

The basis set used in the following study are the same as in Reference [25] and are taken from Reference [280] for Fe, [281] for Ti, [40] for Sn (976-3111(631d) with the outermost Gaussian exponent $sp = 0.1053$), Sb, Nb (976-31(631d)) , Al (88-31 with the optimized outermost Gaussian exponent $sp = 0.1$) and Ta, [282] for V and Ge, [283] for Ga, and [284] for Si. The outermost two sp and one d gaussian exponents of Fe, and V, and the outermost sp exponent of Al were optimized in Fe_2VAl. Their respective values are: 1.155, 0.2817, 0.2439, 0.8335, 0.1151, 0.338, and 0.1. An effective core pseudopotential has been considered for the specific case of Ta, whereas all the other elements are treated at the all-electron level.

Spin-polarization is considered: an initial magnetic moment of 1 μ_B/u.c. is imposed to the unit cell during the first 3 steps of the self-consistent cycle. Different Monkhorst-Pack [43] meshes of special k-points have been used: i) a $9\times9\times9$ mesh for the structural relaxation of the undoped unit cells; ii) a $5 \times 5 \times 5$ mesh for the structural relaxation of the doped supercells; iii) a $10 \times 10 \times 10$ mesh for the computation of the electronic properties; and iv) a $32 \times 32 \times 32$ mesh for the computation of the thermoelectric properties. The energy convergence criterion is set to 10^{-9} Ha. For relaxation, we fix a threshold of 3×10^{-4} Ha/Bohr on the root-mean square values of energy gradients and of 1.2×10^{-3} Bohr on the root-mean square values of atomic displacements. A temperature smearing of the Fermi surface is set to 3.2×10^{-4} Ha. We report the relaxed lattice parameters in Table 8.1. Within B1-WC, the lattice parameters are slightly underestimated ($\sim -3\%$). Fixing the lattice parameter to the experimental values does not significantly alter the band gaps. For the rest of the discussion, we will only consider the fully-relaxed systems.

Within the DFT+U formalism, we explored, at the same time, the effect of extra carriers injected in the pristine phases, bypassing the insertion of atomic impurities, to disentangle the electronic from the ionic and bonding contributions. This effect is also studied

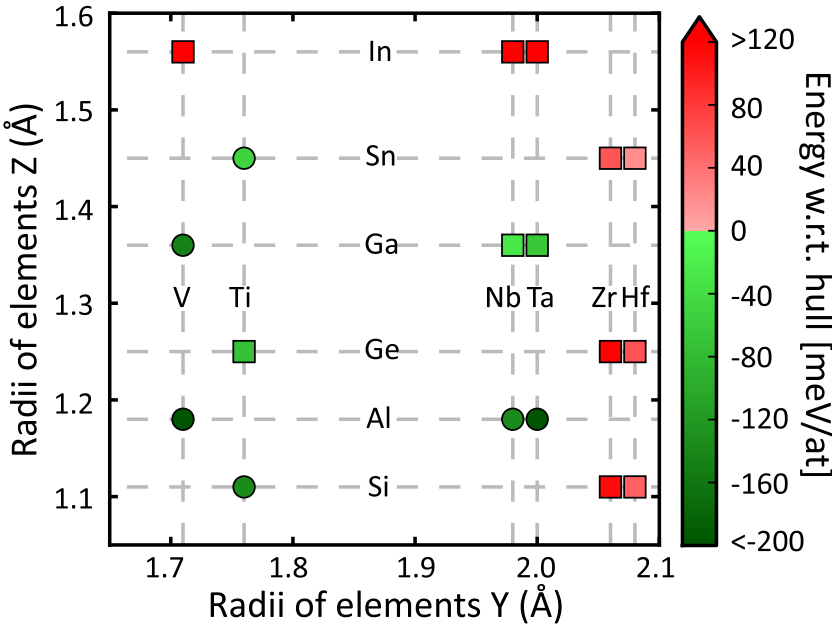

FIGURE 8.5: Map of the thermodynamic stability of Fe_2YZ compounds (as measured by the energy with respect to hull) computed at 0 K as a function of the Y and Z atomic radii. A negative number (inverse energy above hull, green colour) corresponds to a stable phase and a positive number (energy above hull, red colour) to an unstable one. Circles (respectively squares) correspond to compounds (respectively not) previously synthesized. Adapted from Reference [25].

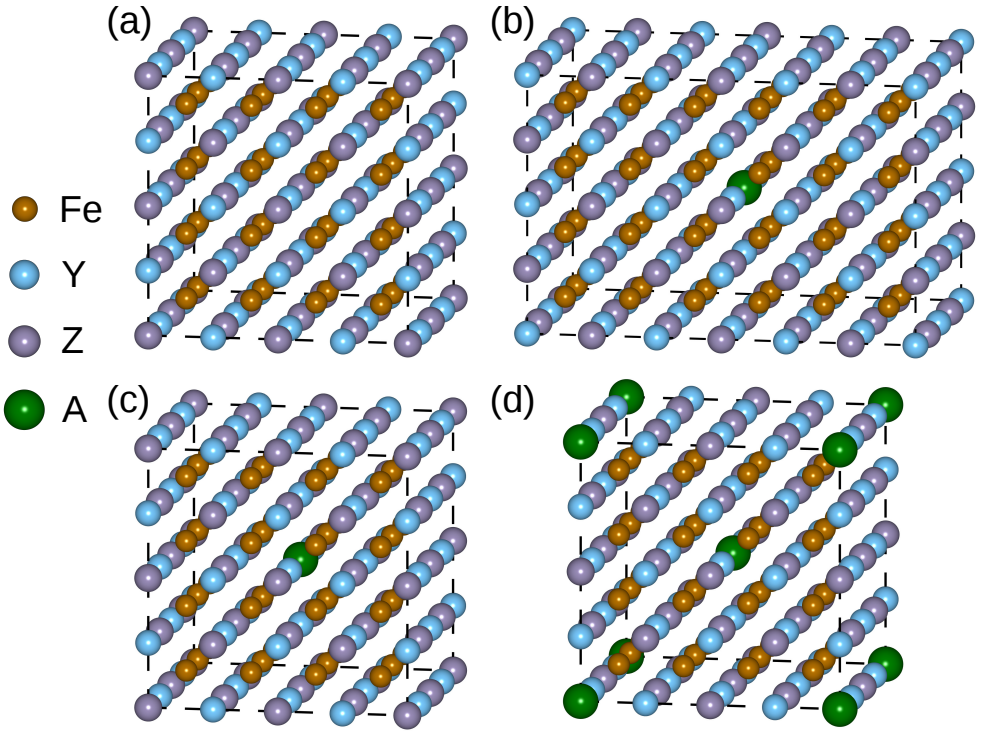

FIGURE 8.6: Supercells for the $Fe_2YZ_{1-x}A_x$ compounds, for (a) $x = 0$, (b) $x = 1/48$, (c) $x = 1/32$ and $x = 1/48$.

Fe_2YZ	U_{Fe}	U_Y	E_g^U	E_g^{Hy}	a^U (Å)	a^{Hy} (Å)	a_{EXP} (Å)	Ref.
Fe_2TiSn	5.09	2.62	1.29	1.04	6.069	5.912	6.074	[290]
Fe_2TiSi	5.02	2.47	1.41	1.51	5.714	5.562	5.720	[291]
Fe_2VAl	5.02	4.86	1.09	0.94	5.733	5.579	5.761	[251]
Fe_2TaGa	5.02	1.28	1.35	0.70	5.929	5.723	-	-
Fe_2NbGa	5.03	1.55	1.02	1.01	5.934	5.720	-	-
X_2YZ	U_X	U_Y	E_g^U	E_g^{Hy}	a^U (Å)	a^{Hy} (Å)	a_{EXP} (Å)	Ref.
Ru_2ZrSn	2.90	1.09	0.17	-	6.479	-	-	-
+ SOC	2.88	1.03	0.15	-	6.479	-	-	-
Os_2HfSn	2.67	0.99	0.59	-	6.484	-	-	-
+ SOC	2.82	0.25	0.14	-	6.483	-	-	-

TABLE 8.1: Self-consistently determined U (in eV) for the transition metal atoms (Fe and Y sites) in the studied X_2YZ compounds; obtained energy gap (E_g, in eV) and relative optimized lattice parameters for the DFT+U (^{U}) and B1-WC (^{Hy}) calculations and experimentally available lattice parameters.

in similar compounds to Fe_2YZ, based this time on $4d$ and $5d$ electrons, Ru_2ZrSn and Of_2HfSn. The DFT+U simulations using the ABINIT code [285] were performed within the PBE [286] flavour of the generalized gradient approximation (GGA). We make use of the U correction in order to treat the electronic correlations on the transition metal atoms d orbitals [287] and we self-consistently determined the Hubbard-like U correction using the linear response formalism [12], with 5.0×10^{-2} eV degree of convergence on the U values, corresponding to a lattice parameter optimization tolerance of the order of 10^{-3} Å. We used projected augmented-wave (PAW) pseudopotentials [288] taken from the JTH table [289] and in order to achieve a satisfactory degree of convergence ($\sim$ 0.01 meV energy differences), the plane wave expansion has been truncated at a cutoff energy of 653 eV and the integrations over the Brillouin Zone were performed considering 20^3 uniform Monkhorst-Pack grid [43]. In this framework, we obtain (see results shown in Tab. 8.1): *1)* lattice parameters in perfect agreement with available experiments ($\Delta a < 0.5$ %); *2)* similar static and dynamic charges on each atomic site with respect to B1-WC calculations (not shown) and *3)* band structures comparable to B1-WC [25]. However, for Fe_2TiSi and Fe_2TiSn the relative position between the Fe and Ti e_g bands is inverted with respect to B1-WC as a consequence of the two different methods. For this reason, we decided to set $U_{Ti} = 5.6$ eV to obtain a band arrangement similar to B1-WC. In addition, the effect of the spin-orbit coupling (SOC) has been checked on the $4d$ and $5d$ transition metals computing again the self-consistent U values, the equilibrium lattice parameters and the electronic properties. These results are also reported on Table 8.1.

The transport properties have been computed in the constant relaxation time approximation within the semi-classical Boltzman approach using BoltzTraP [32] using the eigenvalues extracted from the DFT calculations. The constant relaxation time $\tau = 3.4 \times 10^{-14}$ s is taken from Reference [25], estimated by fitting the calculated resistivity to experiments [278, 279] as described in the precedent Section.

8.2.2 Donor density effects

With the objective to explore and analyse the effect of chemical substitution on the electronic properties, we first focus our study on Fe_2TiSn_{Sb}. Figure 8.7 displays the total and atom-projected DOS for Fe_2TiSn_{Sb} at different dopant concentrations as well as for the undoped case. First and foremost, we analyse the DOS for the non-magnetic (NM) phase for $x = 1/32$ (Figure 8.7.(b)). In this phase, the donor electron density is 6×10^{20} cm^{-3}. The donor electrons are favoured to occupy the Fe states at the CBM, due to their weak bonding with their belonging nuclei. Hence, the Sb atoms act as shallow donors [292, 293], with the donor state resonant inside the conduction band, above the minimum. From Effective Mass Theory [294–296], a small energy shift of the CBM is expected, so that only a slight change in the DOS occurs with respect to the pristine phase. The binding energy of the donor level E_D^b with respect to the CBM and the spatial extension a_D of the related wave function can be expressed as:

$$E_D^b = \frac{m^*}{m}\frac{hc\ R_\infty}{\varepsilon_r^2} \tag{8.2}$$

$$a_D = \frac{m}{m^*}\varepsilon_r\ a_B \tag{8.3}$$

where m (m^*) is the mass (effective mass) of the additional electron, ε_r is the crystal dielectric constant (= 36, calculated within the B1-WC), R_∞ is the Rydberg constant with $hc\ R_\infty = 13.61$ eV and $a_B = 0.53$ Å, the Bohr radius. For Fe_2TiSn, the inertial effective mass $m_I^* = 0.45\ m_e$ (calculated from Equation (7.4) based on the components of $m_{\alpha\beta}^*$ calculated within the B1-WC). We estimate E_D^b and a_D:

$$E_D^b(m_I^*) \approx 5 \text{ meV and } a_D(m_I^*) \approx 42 \text{ Å} ; \tag{8.4}$$

These results are in agreement with the predictions seen in Figure 8.7.(b): the shallow donor mechanism induce a defect level practically incorporated in the conduction band, causing a shift of the Fermi level toward the CBM, as reproduced by a rigid-band-like picture.

However, when we allow for spin-polarization, this picture is strongly modified: a ferromagnetic (FM) half-metallic phase is energetically favoured, inducing in-gap states (see Figure 8.7.(c)). At x = 1/48, those states are mostly isolated and of Fe e_g character (Figure 8.7.(c)). The exchange-splitting is 0.46 eV, with magnetic moments $\mu_{Fe} = 0.28\ \mu_B$ on the Fe atoms surrounding the impurity (schematically shown in Figure 8.8). The moment on the next-nearest neighbours (Ti) is one order of magnitude smaller, and anti-aligned with Fe; on even further atoms (Sn) negligible moments are observed, signature of a strong localization of the magnetization density. At larger Sb concentration of 1/32 and 1/16 (Figure 8.7.(d) and (e), respectively) the in-gap states start overlapping with the CBM and the exchange-splitting decreases to 0.27 eV ($\mu_{Fe} = 0.22\ \mu_B$) and 0.31 eV ($\mu_{Fe} = 0.23\ \mu_B$), respectively. For the whole range of doping, the integrated magnetization density sums to 1 μ_B per each Sb atom, corresponding to the integrated DOS of the additional occupied state up to E_F. The FM transition drives the doped compound to a half-metallic ground state, and highlights a behaviour completely missed in rigid band approximation. Similar results have been obtained in Fe_2TiSn_{As} (not shown), attesting that this behaviour is independent of the dopant specie.

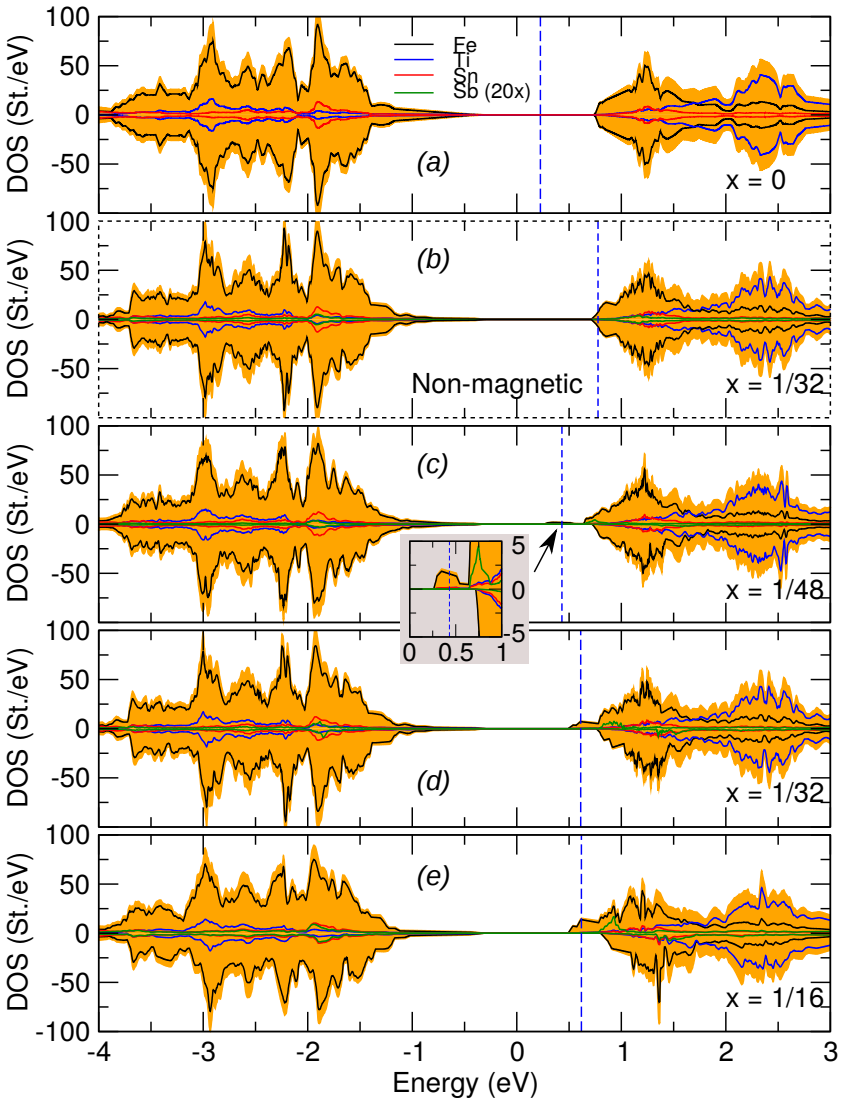

FIGURE 8.7: Density of state of Fe_2TiSn_{Sb} compounds (x = 0, 1/48, 1/32, 1/16), with the atomic contributions (the Sb contributions are 20 times magnified), normalized to the x = 1/16 supercell. The positive (negative) values are for majority (minority) spin states. The Fermi level is given in dashed lines. The small arrow indicates the near-isolated in-gap level for x = 1/48, also illustrated in the inset.

8.2.3 Chemical effects

The rigid band approximation is violated when accounting for explicit doping in Fe_2TiSn_{Sb} given the large exchange-splitting.

It might be questioned if this behaviour is generic to the whole series of Fe_2YZ compounds. From the different band structures shown in Figure 8.9 ($x = 1/32$ and $x = 1/16$), we observe that a magnetic instability is present in Fe_2TiSn_{Sb}, Fe_2TiSi_P and Fe_2TaGa_{Ge} (with magnetization energies $\Delta E = E_{NM} - E_{FM}$ between 1 and 5 meV/f.u. stabilizing the FM phase) but absent in Fe_2NbGa_{Ge} and Fe_2VAl_{Si}. As illustrated in Figure 8.9 ($x = 0$), the distinct behaviours can in fact be linked to the electronic band structure of the host matrix, and in particular to the relative positions of the Fe and Y e_g bands at the CBM. For Fe_2TiSn and Fe_2TiSi the e_g bands of Ti lie well above those of

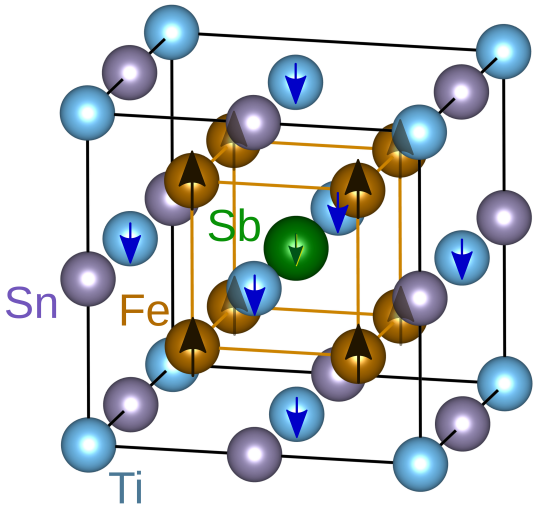

FIGURE 8.8: Schematic arrangement of the doped Fe_2TiSn_{Sb} magnetic moments surrounding the Sb impurity.

Fe. Under doping, the extra electrons populate the flat band associated to Fe e_g states showing half-metallic exchange-splitting. At the opposite, in Fe_2NbGa and Fe_2VAl the e_g bands of Nb and V lie well below those of Fe. The extra electrons populate therefore the highly dispersive Y e_g band and no magnetic transition is observed. Fe_2NbGa is in an intermediate situation with Fe and Ta e_g states closer in energy so that at the investigated doping concentrations both are occupied. The system exhibits a magnetic instability but the difference of energy between FM and NM phases is smaller than for Fe_2TiSn and Fe_2TiSi.

In this band structure analysis, the role of the occupancy of the Fe e_g states, at the origin of the magnetic instability observed in Fe_2TiSn_{Sb}, is highlighted. For the case of doped Fe_2VAl, we show that the rigid band approximation remains valid, therefore the relaxation time estimated from experiments [278, 279] is likely to be a good estimation in regards to conductivity.

8.2.4 Origin of the magnetic instability

From the above, it appears that a magnetic instability takes place when doping electrons start populating the localized Fe e_g states. In order to validate this explanation and explore further the origin of the magnetic instability, we performed a simple computer experiment. Considering Fe_2TiSn as an arbitrary reference compound, we artificially tuned the amplitude of the U_{Ti} parameter (from 0.0 to 5.6 eV) in order to modify the relative position of Fe and Y (Ti) e_g levels and properly mimic the distinct band structures of the whole set of Fe_2YZ compounds reported in Figure 8.9, but without explicitly changing the cations. The different e_g band arrangements are illustrated in Figure 8.10(a-d) (top row) and then used as hosts for electron doping (adding electrons compensated by a positive background). The spin-projected DOS at E_F and the total cell magnetization as a function of the carrier concentration are reported in Figure 8.10(a-d) (bottom row). In order to determine the doping windows where itinerant electron magnetism (typical of intermetallic alloys [249, 297]) is eventually expected to dominate [298–300], the Stoner criterion [300, 301] is also evaluated : a FM state is favoured when the product between

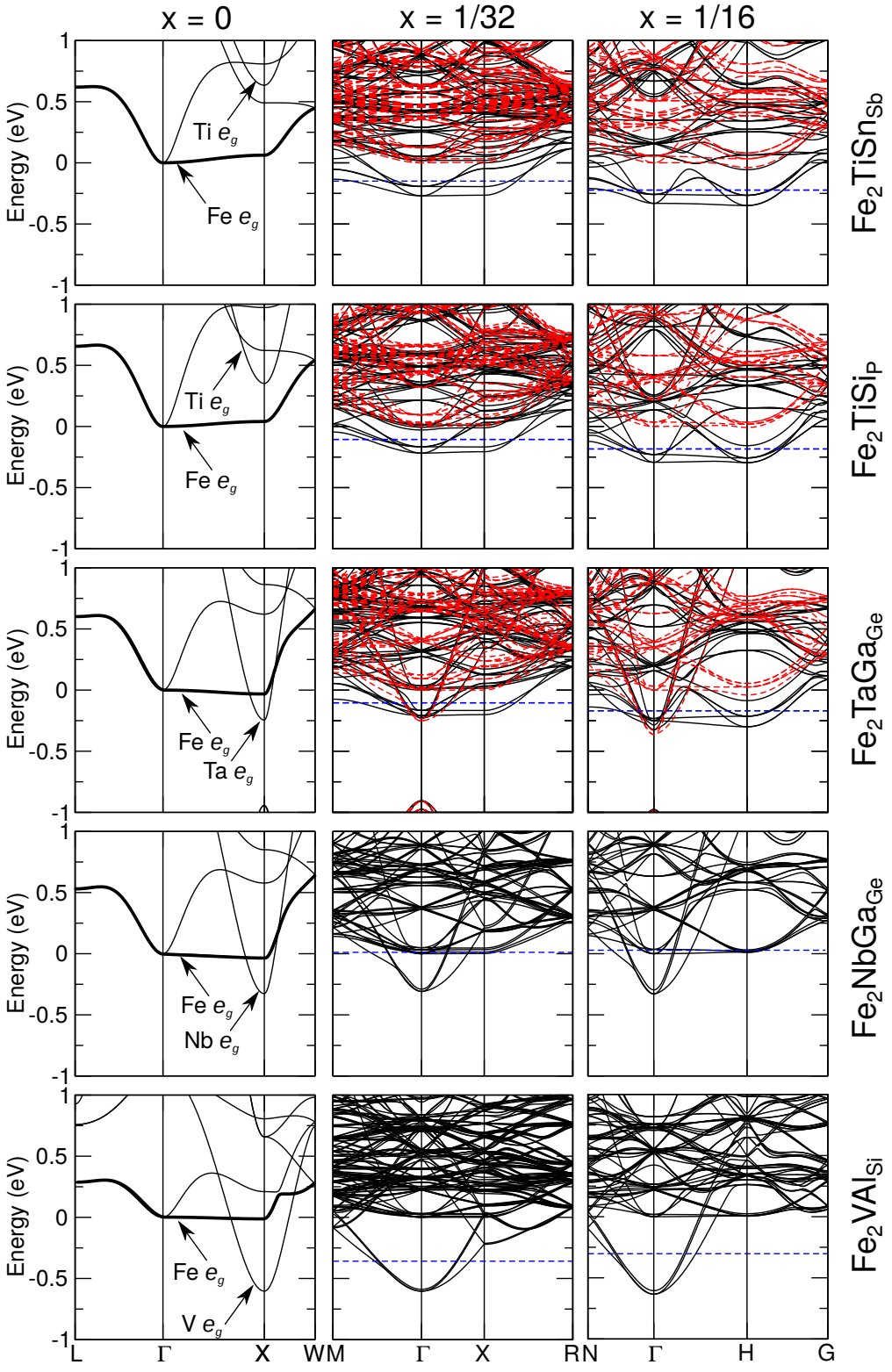

FIGURE 8.9: Spin-resolved Fe_2YZ_A B1-WC band structures in the associated irreducible Brillouin Zone ($Fm\bar{3}m$, $Im\bar{3}m$ and $Pm\bar{3}m$, respectively, for x = 0, 1/32 and 1/16). The black (red) curves are for the majority (minority) spin states. Blue dashed line: E_F; the zero energy is set to the bottom of the Fe e_g band at Γ. Red dashed lines: minority spin channel.

the non-magnetic DOS at E_F and the energy needed to flip a spin (ΔE_{ex}) is larger than one:

$$St \quad = \quad \mathrm{DOS(E_F)} \times \mathrm{\Delta E_{ex}} > 1 \tag{8.5}$$

The band structures in Figure 8.10(a-d) properly reproduce the different regimes identified in Fig.8.9. When the Y e_g states lie below the Fe e_g states (panels a-b), the system is NM at small carrier concentrations (*i.e.* when doping electrons occupy exclusively Y e_g states) and then becomes FM when the Fermi energy touch the Fe e_g states. This also coincides with $St > 1$ so that the appearance of magnetism might be compatible with a Stoner instability. However, when the Fe e_g states lie below the Y e_g states (panels d), doping electrons occupy directly Fe e_g states and the system is always magnetic, independently of the Stoner criterion. When the Y e_g states minimum is below but close to the e_g states, the system is initially NM and becomes FM as soon as these states are occupied. This points out that, although different regimes might exist depending on the value of St, appearance of magnetism is not necessarily the result of a Stoner instability but rather intrinsic to the Fe $3d$ (e_g) states which are strongly localized and experience robust magnetic exchange interactions.

This means that in compounds like Fe_2TiSi or Fe2TiSn, a magnetic ground state cannot be avoided, even at small carrier concentrations such that $St < 1$. It suggests also that substituting the strongly localized $3d$ orbitals of Fe by the more delocalized $4d$ or $5d$ orbitals of Zr or Hf might delay the appearance of magnetism. To proof this, we considered Ru_2ZrSn and Os_2HfSn. As illustrated in Figure 8.10(e-f), in these cases magnetism is no more intrinsic to the occupancy of the d-states: it results from a Stoner instability and appears only when $St > 1$, leaving a wide set of carrier concentrations for which the system remains non magnetic.

For heavy cations, one could expect that the spin-orbit coupling (SOC) (neglected for Fe above) might play an important role, and we further include it in the Ru and Os calculations. As can be seen in Figure 8.10(e), it has no significant effect in the case of Ru_2ZrSn. For Os_2HfSn however, it changes the band structure more substantially, and suppresses the magnetic instability in the whole range of carrier concentrations explored in Fig. 8.10.(f)

8.2.5 Thermoelectric properties

Having demonstrated the appearance of a magnetic instability under doping, it is now important to clarify its consequences on transport and TE properties. To this end, we compare the evolution of the PF as a function of the chemical potential, μ. Our calculations rely on Boltzmann transport theory and the rigid band approximation using either the electronic band structure of the pristine phase or that of the doped system in the NM and eventually FM configurations. For the purpose of comparison, in the latter cases, the zero of μ was defined in order to align deep energy levels on those of the pristine phase. Ideally, calculations at each μ should rely on the band structure at the related carrier concentration. Still, comparing here full curves obtained from the rigid band structure at different carrier concentrations allows us to probe the quality of the rigid band approximation.

The results for two representative cases, Fe_2TiSn_{Sb} and Fe_2NbGa_{Ge} (x = 1/16 at 300 K), are shown in Figure 8.11.(a) and (b) respectively. A vertical line locates the position E_F

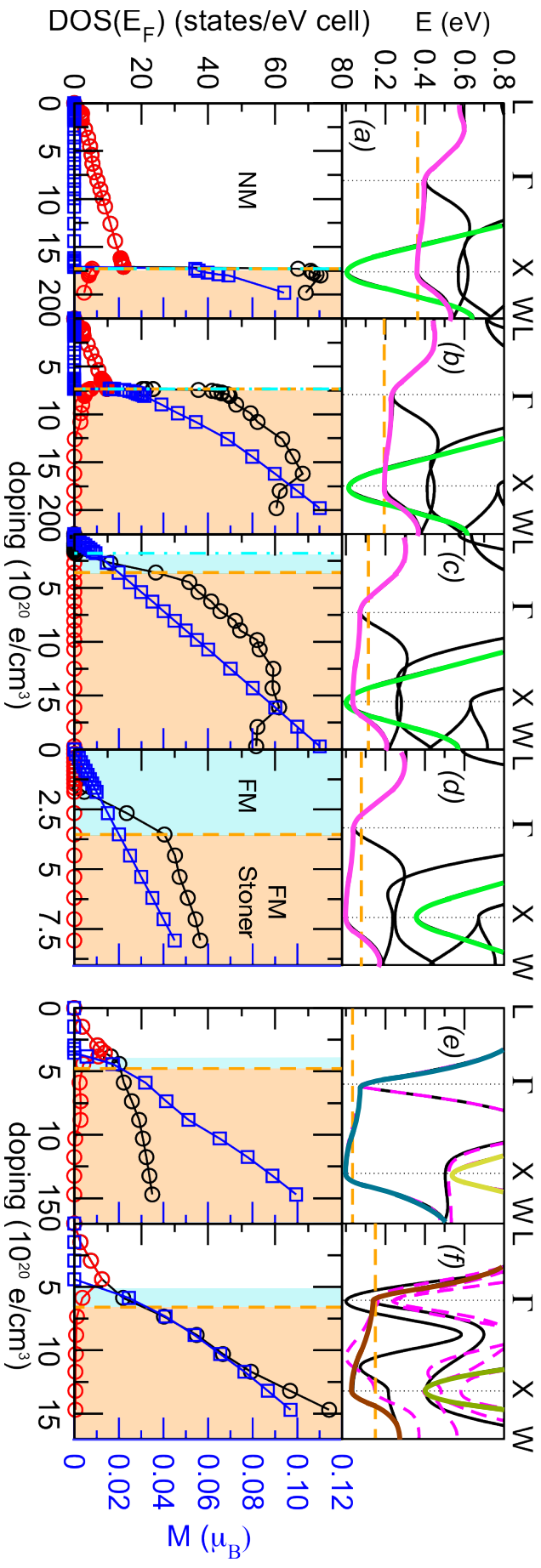

FIGURE 8.10: Top row: Fe_2TiSn band structures at different U_{Ti}: (a) 0.0, (b) 1.4, (c) 2.6 and (d) 5.6 eV and for Ru_2ZrSn (e) and Os_2HfSn (f) (dashed-line magenta bands include SOC). Bottom row: the black (red) circles refer to the up (down) spin-projected DOS at E_F; blue squares to the total magnetization; cyan double-dot dashed line: critical doping needed to populate the Fe e_g level; orange dashed line: critical doping for which $St > 1$.

when considering the band structure of a doped system. For Fe_2NbGa_{Ge}, which remains NM at $x = 1/16$, the shape of the PF remains almost unchanged when using the band structure of the pristine or explicitly doped phase, with just a slight reduction of the main peak by a factor 1.3. This confirms that, as already shown in Figure 2, doping does not significantly affect the band structure so that the rigid band approximation provides a realistic estimate of PF in that case. This remains true for Fe_2TiSn_{Sb} when considering the NM phase. However, when considering the band structure of the FM ground state at $x = 1/16$, the PF changes drastically and the main peak shifts and drops by a factor of 4.3. This highlights that the exchange-splitting is strongly detrimental to the PF. This can be related to the sensitivity of S to the modifications of band structure and chemical potential: although the number of additional carriers is fixed in both case (one electron per site), fewer states in a range of k_BT around E_F contribute to transport, causing the decrease of S. Such an effect cannot be anticipated when considering the pristine phase and the rigid band approximation.

In Figure 8.11.(c), we report the temperature dependence of the PF for various doped Fe_2YZ_A systems at dopant concentration $x = 1/16$, using the band structure under explicit doping and for the magnetic ground state. Although the values are reduced compared to those previously reported [25], relatively large PF can still be observed. The largest values are for Fe_2NbGa_{Ge} (which remains NM) and Fe_2TaGa_{Ge} (which is at the limit of FM). But, even the PF of Fe_2TiSi_P, although significantly reduced by the FM instability, remains sizeable and larger than that of Fe_2VAl_{Si}, confirming the interest of Fe_2YZ compounds for TE applications.

As previously discussed, substituting Fe by Ru or Os is a way to delay, or even suppress, the emergence of the detrimental magnetic instability, enlarging the doping region in which the system remains NM. In Figure 8.11.(d), we report the PF of hypothetical Ru_2ZrSn and Os_2HfSn at 300 K. For Ru_2ZrSn, relying on the band structure of the pristine phase we predict a large PF of 16.1 $\times 10^{-3}$ W/m K^2. This result is confirmed from calculations with the band structure at a carrier concentration of 2.5 $\times 10^{20}$ cm^3 and remains valid in the NM regime. At larger carrier concentrations around n = 10.0 $\times 10^{20}$ cm^3, the PF is significantly reduced when reaching the FM regime. For Os_2HfSn, SOC can no longer be neglected and suppresses the magnetic instability in the whole range of studied carrier concentrations. In that case, although the band structure is significantly modified by SOC, the PF can still reach extremely large values of 22.3×10^{-3} W/m K^2 (up to 45.5×10^{-3} W/m K^2 when neglecting SOC - not shown). Although Zr and Hf are expensive and likely not a scalable solution for TE applications, this confirms that larger PF can be achieved using $4d$ and $5d$ elements [302].

8.2.6 Summary

With B1-WC and DFT+U first-principles approaches, we demonstrate that it is sometimes necessary to go beyond the rigid band approximation to properly assess the properties of a doped system. From one hand, our findings confirm the results obtained by Bilc *et al.* [25] regarding potential candidates for TE applications and, on the other hand, we unveil that such materials, owning "flat-and-dispersive" $3d$ bands, are prone to undergo electronic-driven magnetic phase transitions, which invalidates the rigid-band approximation. We discover that the consequent loss of carriers contributing to transport, in certain cases is not dramatic, since it still maintains power factors larger than

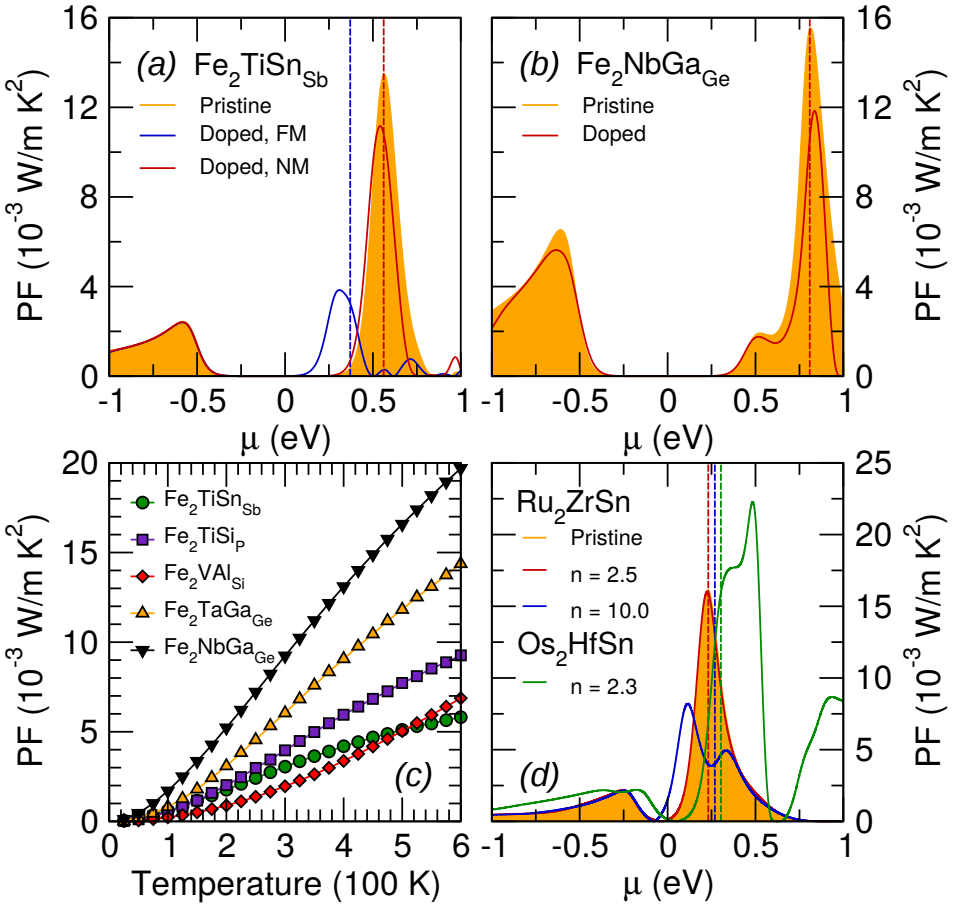

FIGURE 8.11: On the top, spectral PF with respect to μ, at 300 K, in the rigid band approximation, and for explicitly doped (a) Fe_2TiSn_{Sb} and (b) Fe_2NbGa_{Ge} with x = 1/16. On the bottom: (c) panel, PF of Fe_2YZ_A compounds for x = 1/16 with respect to temperature (note that for the high temperatures, near 600 K, the constant relaxation time overestimates the PF [25]) and (d) PF of artificially doped Ru_2ZrSn and Os_2HfSn (n values are expressed in 10^{20} cm^{-3}). The vertical dashed lines are the respective E_F of the doped phases.

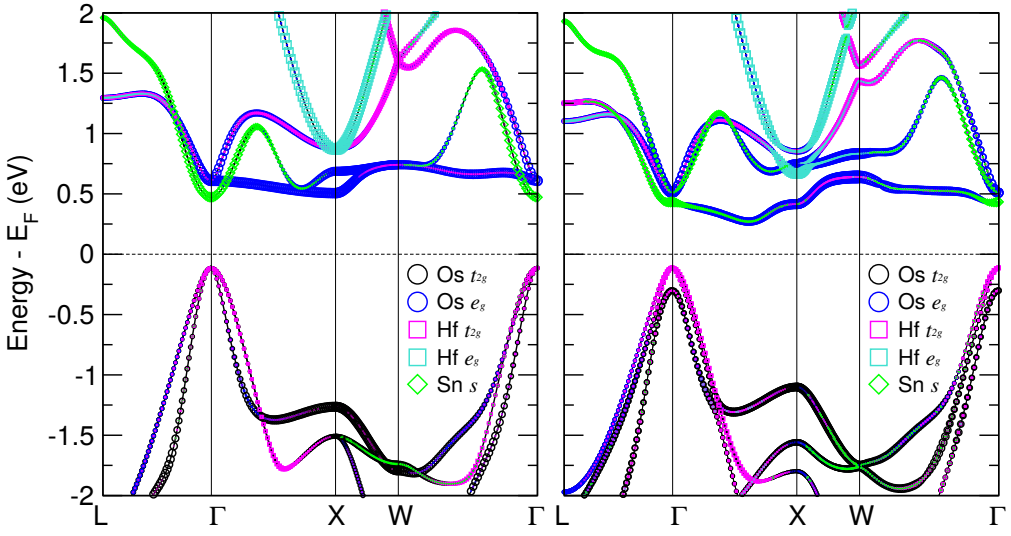

FIGURE 8.12: Os_2HfSn orbital-weighted band structures calculated from DFT+U (a) without SOC interaction and (b) with SOC interaction.

other prototypical TE systems (PF $\sim 3-7$ mW/m K^2 at 300 K in Fe_2VAl [278, 279] or $\sim 4-5$ mW/m K^2 in PbTe [303]).

8.3 Thermoelectric properties of chemically substituted $Fe_2TiSn_{1-x}Sb_x$ compounds

At this stage, there remains a lack of experimental investigations on the thermoelectric properties of doped Fe_2YZ (Fe_2VAl aside). Amongst the most stable Heusler phases, Fe_2TiSn has been considered as the most promising candidate. A collaboration with experimentalists from the University of Genova opened the opportunity the present the first experimental study of the thermoelectric properties $Fe_2TiSn_{1-x}Sb_x$. Contrasting results compared to n-type doped Fe_2VAl will be presented and rationalized with first-principles calculations. The following results have been published as an article [304]; the experimental results presented in this Section are realized by the co-authors of the manuscript.

8.3.1 Experiments

Polycrystalline samples of Fe_2TiSn, $Fe_2TiSn_{0.9}Sb_{0.1}$, $Fe_2TiSn_{0.8}Sb_{0.2}$ are prepared starting from pure elements (99.9 wt% purity for Fe and Sn, 99.99 wt% purity Ti, and 9.999 wt% Sb) weighted in stoichiometric quantities. The metals, in small pieces, are first pressed together to form a pellet and then arc melted in a high-purity argon atmosphere, after the fusion of a Ti-Zr alloy as a getter. The buttons are remelted several times after turning them upside-down, in order to ensure a good homogenization. After melting, the samples are wrapped in Ta foils, closed in silica ampoules under vacuum, and annealed. The annealing conditions are chosen after some preliminary tests on the undoped compound, treated at temperatures between 600 °C and 800 °C for a time varying between 7 and 30 days. A thermal treatment at 700 °C for 8 days is then applied to all samples as a compromise between results in terms of phase purity and homogeneity and an overly long annealing time.

Both as-cast and annealed samples are characterized by x-ray powder diffraction and microscopic techniques. X-ray diffraction analysis is carried out by means of a powder diffractometer in reflection mode (Bragg-Brentano geometry, Ni-filtered Cu K_α or Fe-filtered Co K_α radiations, silicon as an internal standard, $a = 5.4308$ Å). Intensity data for Rietveld refinements are collected in $10-110°$ 2ϑ range, with $0.02°$ in ϑ steps and counting times of $15-20$ s/step. The structural fits are done by means of the FULLPROF program [305]. The homogeneity of the samples is checked by a scanning electron microscope–energy dispersive system (EDS) (Leica Cambridge S360, Oxford X-Max20 spectrometer, with software Aztec). After standard micrographic preparation, the specimens are graphitized and analysed at a working distance of 25 mm, with acceleration voltage 20 kV.

Magnetic susceptibility $\chi(T)$ is measured in a commercial superconducting quantum interference device (SQUID) magnetometer by Quantum Design from 1.8 to 300 K in magnetic fields $50-100$ Oe. Electrical resistivity (ρ), magnetoresistivity, and Hall resistance (R_H) measurements by four-probe technique are performed in a physical properties

measurement system (PPMS) by Quantum Design at temperatures from room temperatures down to 10 K and in magnetic fields up to 90 000 Oe. The Seebeck (S) effect and thermal conductivity (κ) are measured with the PPMS thermal transport option in continuous scanning mode with a 0.4 K/min cooling rate.

8.3.2 Computational details

The hybrid functional calculations are performed with the same technical details as in the previous Section (convergence threshold criteria, smearing of the Fermi surface and basis sets). This time, we compute the properties of pristine Fe_2TiSn by using a Monkhorst-Pack [43] of special k points of $9 \times 9 \times 9$, ensuring a total energy convergence of $\sim$ 0.01 meV to perform the relaxation of the structure. A refined $18 \times 18 \times 18$ mesh is used to refine the electronic structure after relaxation. For the thermoelectric properties, we use the BoltzTraP code to compute the Seebeck coefficient S and Hall coefficient R_H from the Boltzmann Transport Theory within the constant relaxation time (τ) approximation. Within this approximation, scattering mechanisms are ignored and both S and R_H are independent of τ.

Possible native point defects are also studied in a $2 \times 2 \times 2$ cubic supercell (128 atoms) containing one defect (with density of about 6×10^{20} cm^{-3}). Ti and Sn neutral vacancies (referred to as V_{Sn} and V_{Ti} in the text) are modelled by the means of ghost atoms, *i.e.*, the associated cores and electrons are removed from the cell, but the basis set associated to the original atom remains on the site to properly model the electron density within the vacancy [44]. Regarding the antisite defects, we build two systems by switching the position of nearest-neighbours Ti-Fe (Ti_{Fe})and Sn-Fe Sn_{Fe}. The electronic structure of the supercells is estimated at the fixed pristine geometry (a) using a $5 \times 5 \times 5$ k grid, since the geometrical relaxation of the atoms surrounding the defect is not expected to change the donor/acceptor nature of these defects.

8.3.3 Results for undoped Fe_2TiSn samples annealed at different temperatures

The results of both x-ray diffraction (XRD) and microscopy evidence that the Fe_2TiSn phase with the Heusler $L2_1$ structure already forms in the as-cast sample, in agreement with known data on ternary Fe-Ti-Sn phases in the literature [306] as well as the thermodynamic stability predicted by theory (Figure 8.5). The x-ray powder diffraction pattern of the as-cast samples is displayed in Figure 8.13. The compositional variability analysed from EDS shows a compositional variability within $\sim$1 wt % in the undoped samples, with an slight excess of Fe and a slight defect of Ti with respect to the ideal stoichiometry 2 : 1 : 1. In addition to the formation of the Fe_2TiSn phase, extra phases are present in small percentages ($<$ 5 wt %), typically Sn and/or Ti finely dispersed in the matrix, but also binary or ternary phases: in particular, the as-cast sample contains traces of Sn and Ti. The analysis of the annealed samples show traces of FeSn and Sn (annealed at 600 °C) or other ternary phases $(Fe, Ti)Sn_2$ and $Fe_2(Ti, Sn)$ (annealed at 800 °C) in addition to small traces of Sn and Ti. Amongst all samples, the one annealed at 700 °C only contains traces of Sn as an extra phase, and is therefore the most homogeneous. Consequently, the temperature of 700 °C is chosen for the thermal treatment of the Sb-doped samples. A more detailed analysis of the samples discussed here are available [307].

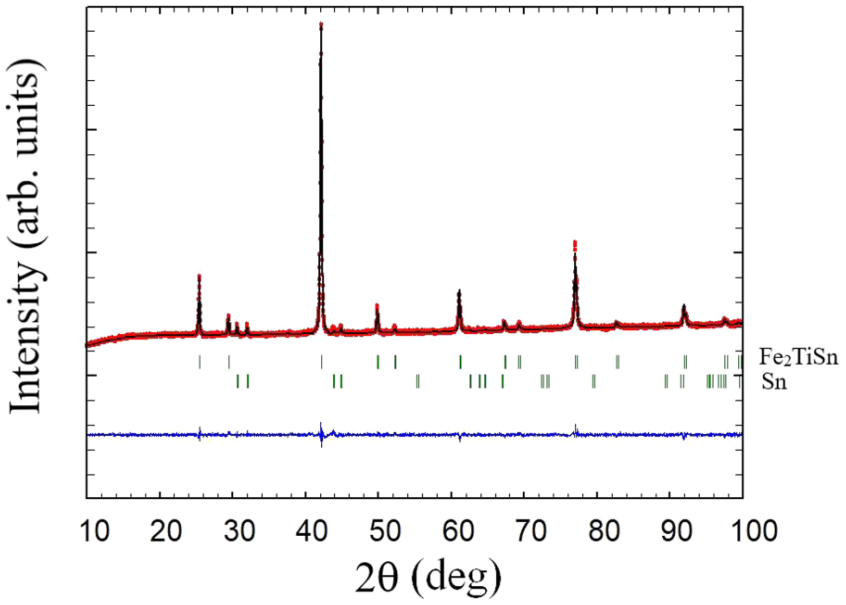

FIGURE 8.13: Rietveld refinement plot of the as-cast Fe_2TiSn sample. Red, black, and blue lines correspond to experimental, calculated, and difference (observed minus calculated) curves, respectively. Vertical bars represent Bragg positions of reflection peaks. The sample contains elemental Sn as secondary phase (4 wt %). $R_B = 2.31$ (main phase Fe_2TiSn), $R_{wp} = 2.03$, $\chi^2 = 1.53$.

The temperature dependences of the resistivity, carrier density and mobility measured in the undoped samples (with the different thermal treatments) are given in Figure 8.14. In all cases, two or three pieces of the prepared lump are measured and compare, as a test of homogeneity. The absolute values are affected by a significant uncertainty of about 20%, related to the estimation of the geometrical factors due to the irregular shape of the different pieces. Yet, the dependence of the measured properties as a function of temperature highlight the mechanisms involved in transport. In Figure 8.14, the resistivity exhibits either a gapless bad metallic behaviour, with a positive temperature derivative $d\rho/dT$ above 100 K (in the as-cast sample) or a small gap semiconducting behaviour with a negative temperature derivative $d\rho/dT$ above 100 K (in the annealed samples). The temperature dependence is quite weak, in contrast with the larger negative temperature derivative $d\rho/dT$ expected from a semiconductor with a $\sim$1 eV band gap, as predicted from first-principles. In Reference [308], the small gap semiconducting behaviour is ascribed to Fe-Ti antisite disorder. The overall shape of the curves are consistent with the literature data on Fe-deficient samples [309] or sample with excess Fe and deficient Ti stoichiometry [310, 311]. The comparison with the available literature suggests that achieving an exact determination of stoichiometry in Fe_2TiSn is rather difficult. Nevertheless, the energy dispersive x-ray (EDX) analyses indicate $\sim$1 at % Fe excess and $\sim$1 at % Ti deficiency, in good agreement with the report of Reference [308]. The carrier density extracted from Hall effect measurements (using a single-band model) are plotted as a function of temperature in Figure 8.14.(b). The evolution with temperature is weak, unlike that of an undoped semiconductor. Below 50 K, the carrier density increase of one order of magnitude with decreasing temperature, more visibly for the as-cast and 600 °C samples. In the temperature regime above 50 K, the density values remain around 10^{21} cm^{-3}. Moreover, increasing the annealing temperature slightly decreases the carrier density in the studied temperature range. The positive sign of the Hall signal points to hole-type carriers. Finally, the carrier mobilities displayed in

Figure 8.14.(c), extracted from the inverse product of the resistivity and carrier density, have values ranging from a few to tens of $cm^2\ V^{-1}\ s^{-1}$, as well as a trend of increasing mobility with increasing annealing temperature. This suggests a possible healing effect of annealing on microstructural or substitutional disorder.

Following the analysis of Reference [312], the degree of atomic disorder can be estimated from the relative height of XRD peaks: the ration of (111) to (220) peak intensities is used as a measure of Ti-Sn antisite disorder, and Ti or Sn vacancies; the *ratio* of the (200) to (220) peak intensities is used as a measure of disorder in the Fe site. It is found that both *ratios* I_{111}/I_{220} and I_{200}/I_{220} increase monotonically and almost double with increasing annealing temperature up to 800 °C. Hence, the XRD analysis confirms our expectations from the analysis of carrier mobilities with annealing temperature, and its healing effect on disorder.

The magnetoresistivity $(\rho(H) - \rho(H = 0))/\rho(H = 0)$ curves, measured at selected temperatures for the as-cast sample and the sample annealed at 700 °C, the latter being representative of the trends observed in all the annealed samples, are shown in Figure 8.15. For the as-cast sample, an almost vanishing magnetoresistivity lower than 0.6% at 90 000 Oe is observed, while in the annealed samples a sizeable negative contribution is observed at low temperature. Below 50 K, the magnetoresistivity curves have a cusplike shape, suggestive of a weak localization mechanism, while at intermediate temperatures of $100 - 150$ K the negative few percent magnetoresistivity may be of magnetic origin.

We now address the thermoelectric properties of the Fe_2TiSn samples. The temperature dependence of the Seebeck coefficient S, thermal conductivity κ, thermoelectric figure of merit ZT, and power factor $PF = S^2\sigma$ are plotted in Figure 8.16. The sign of the Seebeck coefficient is positive for all samples, in the studied temperature range, as expected from the hole nature of the carriers determined from Hall effect measurements. The Seebeck curve of the as-cast sample (Figure 8.16.(a)) increases monotonically, almost linearly, with increasing temperature, as expected from a metal with constant carrier density, while the curves of the annealed samples exhibit a broad maximum in the range $200 - 250$ K, which tends to shift to higher temperatures as the annealing temperature increases. These shapes are reminiscent of typical semiconducting samples. From our analysis of the Seebeck curves, we deduce that the hole carrier involved in transport have a degenerate or metallic character in the case of the as-cast sample, while they have a thermally activated character in the annealed samples, consistent with the resistivity curves shown in Figure 8.14.(a). The thermal conductivity curves shown in Figure 8.16 are characterized by a maximum slightly below 100 K, which mark the crossover between the low-temperature regime (with increasing κ as the temperature increases by excitation of phonon modes), and the high-temperature regime where phonon-phonon scattering counter-balances the further activation of phonon modes. The sharpness of the peak is a strong argument in favour of the good structural quality of the samples, as such a peak would be easily smoothed by any type of disorder limiting the phonon mean-free-path. The room temperature values of the thermal conductivity are in the range of a few $W\,K^{-1}m^{-1}$. The thermoelectric figure of merit ZT curves shown in Figure 8.16.(c): values in the range of $10^{-3} - 10^{-2}$ are reached at room temperature. As a result of the behaviour of S with temperature, the ZT curve of the as-cast sample is smaller in the temperature range below 200 K, but monotonically increases with temperature up to room temperature; in the annealed samples however display a maximum below 300 K. The behaviour of S curves also affects the power factor, shown in Figure 8.16.(d): for the

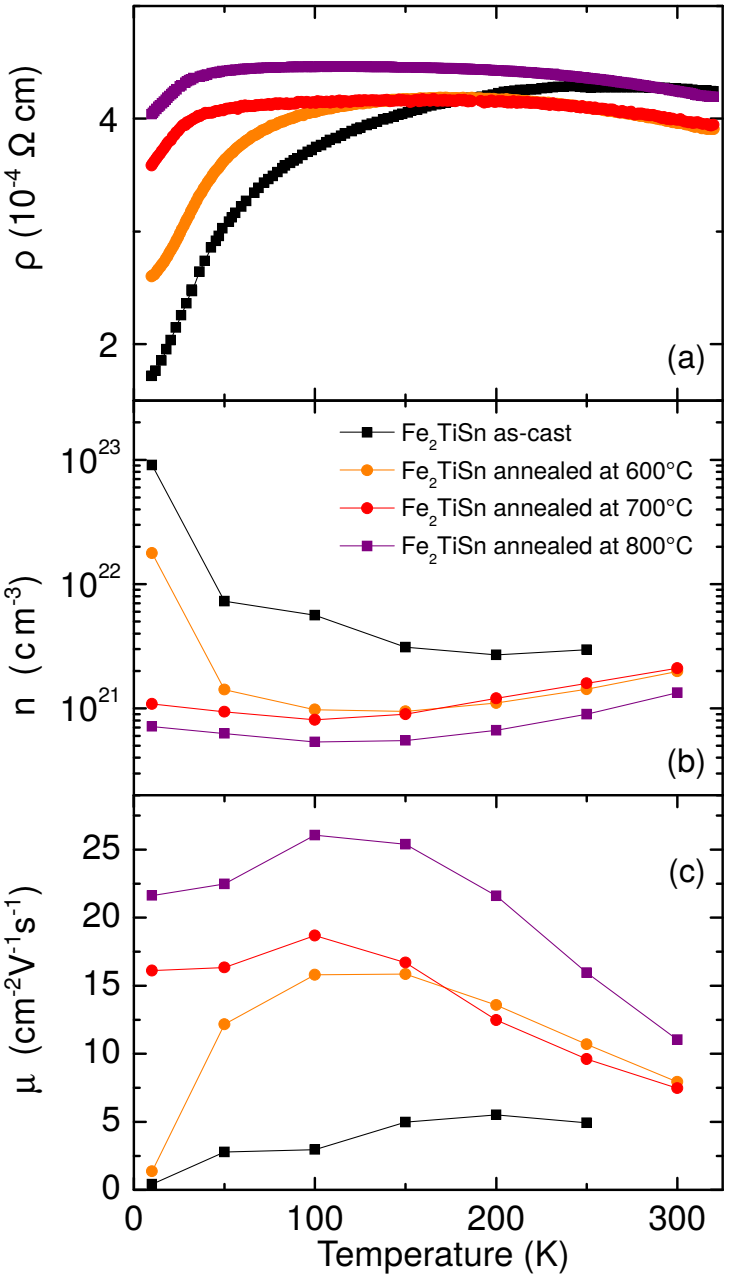

FIGURE 8.14: Temperature dependence of (a) the resistivity of Fe_2TiSn samples with different heat treatments. (b) carrier densities of the extracted from Hall effect measurements. (c) mobilities of the same samples.

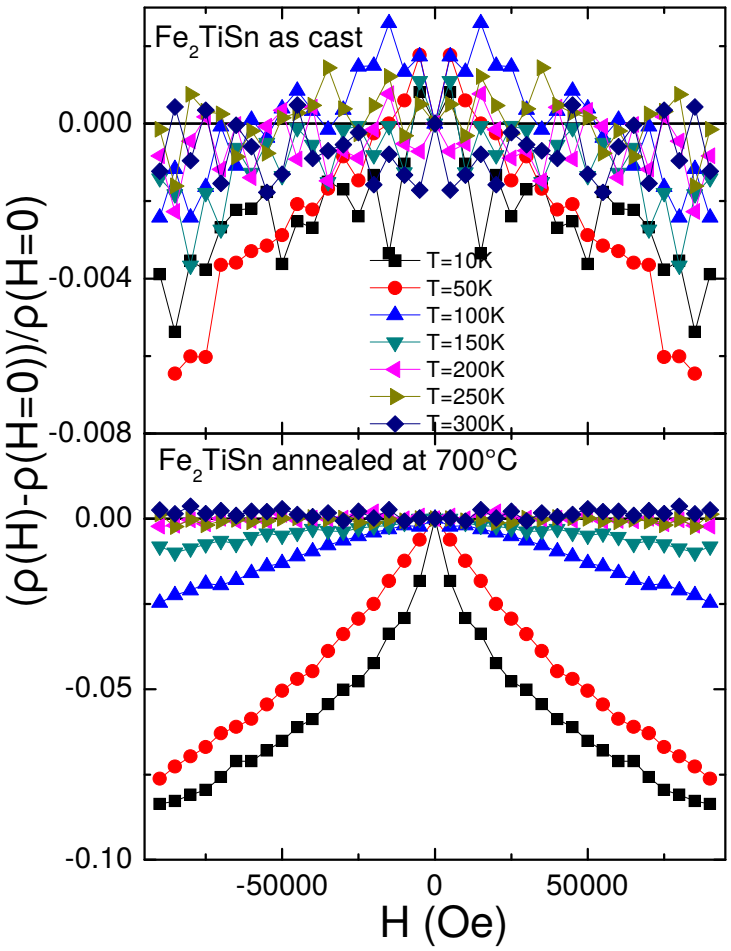

FIGURE 8.15: Field dependence of magnetoresistivity of Fe_2TiSn as-cast (upper panel) and annealed (lower panel) samples.

as-cast sample, there is a monotonic growth of the power factor over the whole studied temperature range, whereas in the annealed samples a maximum is present below 300 K. Noteworthy, the sample annealed at 800 °C displays the largest power factor of about $\sim 10^{-4}$ W/mK^2, in the range $200-250$ K. This value remains smaller than the reported $\sim 1.5\times10^{-4}$ W/mK^2 at 300 K recently measured in undoped Fe_2TiSn samples sintered by spark plasma sintering under a pressure of 50 MPa at 800 °C for 5 minutes [313].

Finally, we report in Figure 8.17 the temperature dependence of the magnetic susceptibility $\chi(T)$ for all the samples in the low-field regime ($50-100$ Oe). The magnetic signal is ten times smaller from the as-cast sample compared to the annealed samples, hence the curves are rescaled for clarity and plotted on the right-hand axis. The small magnitude of the as-cast magnetic signal is consistent with the absence of any magnetic contribution in the magnetoresistivity, as seen in Figure 8.15, top. A ferromagnetic ordering appears below 260 K, well visible in the as-cast sample, and still present in the annealed samples (even though it is not visible in the scale of Figure 8.17. The shape of $\chi(T)$ of the as-cast sample is in good agreement with previous reports [290, 314]. A further ferromagnetic ordering appears in the annealed samples, below 50 K, and could possibly be associated with the regime crossover observed in the resistivity and carrier density curves at the same temperature, as shown in Figure 8.18. The presence of these magnetic contribution in both magnetotransport and susceptibility measurements

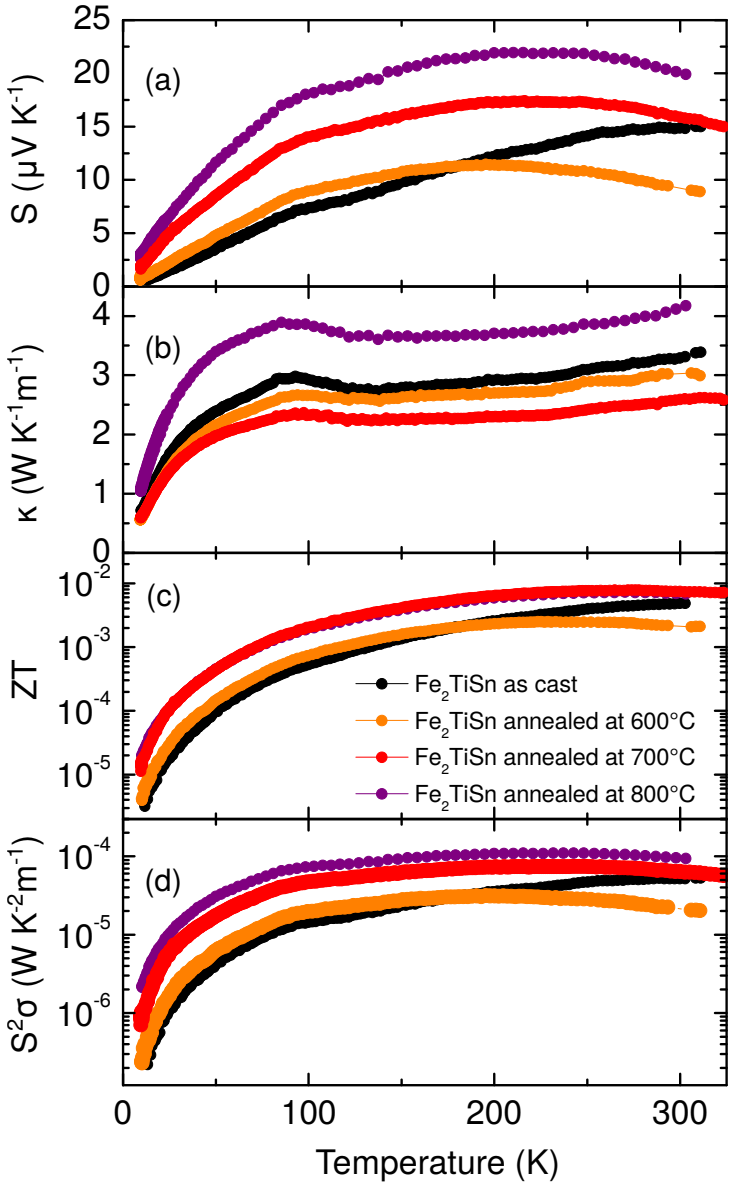

FIGURE 8.16: Temperature dependence of (a) Seebeck coefficients, (b) thermal conductivities, (c) thermoelectric figures of merit, and (d) power factors of the different samples.

suggests that it may be a characteristic of the main phase rather than the secondary phases.

After consideration of uncertainty regarding geometrical factor, we can summarize the following regarding the effect of increased annealing temperature:

1. the carrier density slightly decreases;
2. the mobility of the carriers increases;
3. the Seebeck coefficient is larger in the low-temperature regime (below $100-200$ K);
4. a magnetic contribution appears at low temperature;
5. the power factor and thermoelectric figure of merit ZT increase in the low temperature regime, below 200 K.

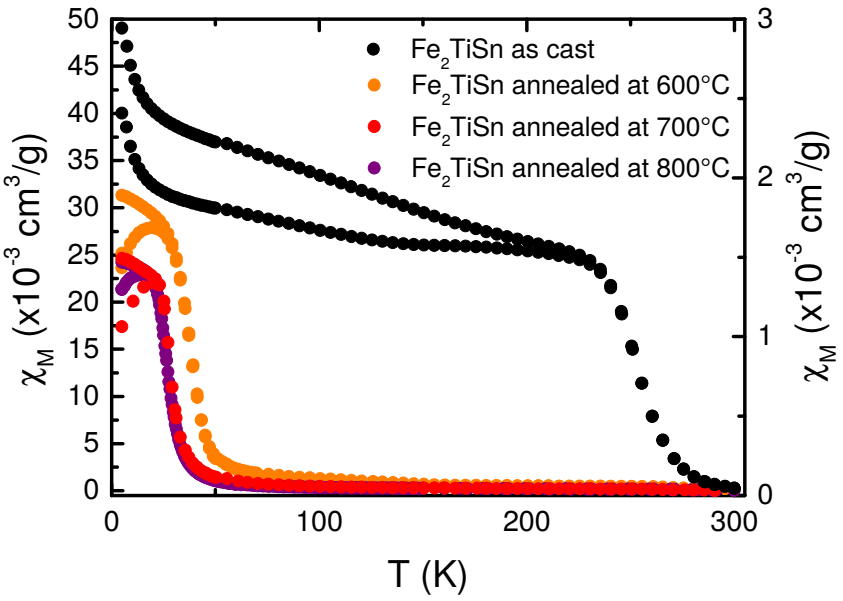

FIGURE 8.17: Zero-field-cooled and field-cooled magnetic susceptibility $\chi(T)$ curves of Fe_2TiSn samples prepared with different heat treatments. For the as cast sample, the magnetic signal is 10 times magnified and plotted separately on the right-hand axis.

We further remark that, due to the linear increase of its $S(T)$ curve, the as-cast sample has a room-temperature figure of merit comparable with the values measured for the annealed samples.

Clearly, the properties unveiled from these experiments for undoped Fe_2TiSn contrast at first glance with the predictions of the first-principles calculations. The analysis of the Sb-doped samples may clarify these observations.

8.3.4 Results for Sb-doped Fe_2TiSn samples

In view of preparing $Fe_2TiSn_{1-x}Sb_x$ samples, we need to consider the growth conditions of the undoped samples whose properties are as close as possible to the predictions from theory. The ideal undoped Fe_2TiSn compound to start from should have a carrier density as low as possible, and exhibit no atomic site disorder and magnetic ordering. However, all the undoped samples exhibit high carrier densities of $\sim 10^{21}$ cm^{-3}, and a magnetic behaviour below 50 K is clearly visible, even in the annealed samples. In addition, the weak temperature dependence of the resistivity and the p-type character of all undoped samples disagree with the electronic structure predicted from theory, with a well defined band gap. Before clarifying the origin of such anomalous properties by simulating atomic defects in *ab initio* calculations, we explore the effect of Sb doping. We consider the following points:

1. the annealed samples have low carrier densities. In order to emphasize the effect of donor doping, low carrier density in undoped Fe_2TiSn samples is a primary requirement;
2. the annealed samples all display the largest S, power factors and figures of merit ZT;

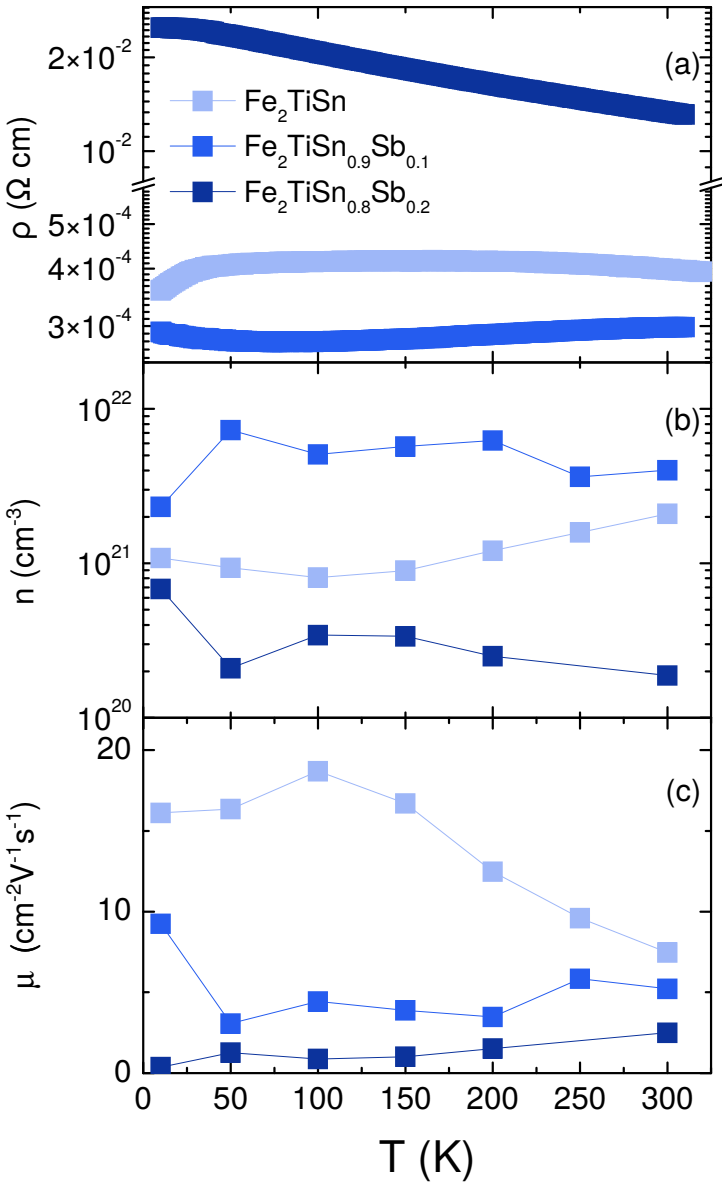

FIGURE 8.18: Temperature dependence of (a) resistivities, (b) carrier densities extracted from Hall effect measurements, and (c) carrier mobilities of $Fe_2TiSn_{1-x}Sb_x$ ($x = 0$, 0.1 and 0.2) samples annealed at 700 °C.

3. it can be expected that with doping, the semiconducting-like shape of the $S(T)$ curve of annealed samples (with a maximum in the $200-250$ K temperature range) is turned into a metalliclike, monotonically increasing $S(T)$ curve, thus improving the thermoelectric properties at room temperature and above, which is the ideal range of temperature for applications;
4. as mentioned in the previous Section, a higher phase purity is detected in the SEM-EDS analyses for the sample annealed at 700 °C as compared to the others.

After these considerations, Sb-doped samples (with Sb concentration $x = 0.1$ and 0.2) have been prepared following the temperature annealing protocol at 700 °C for 8 days.

We can now analyse the electronic transport properties of Sb-doped Fe_2TiSn and compare them with the properties of the undoped samples, all annealed at 700 °C. The

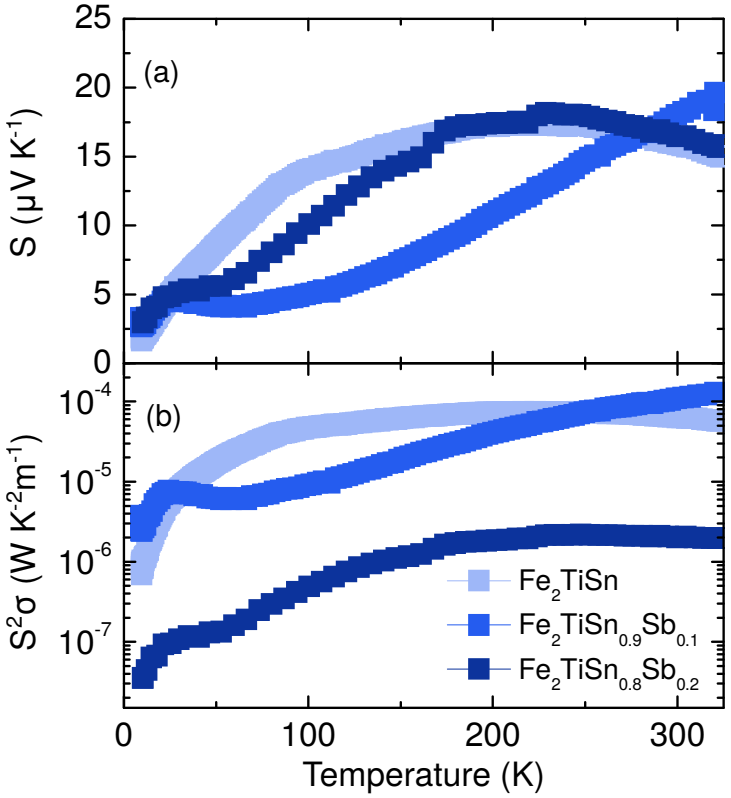

FIGURE 8.19: Temperature dependence of (a) Seebeck coefficients, and (b) power factors of $Fe_2TiSn_{1-x}Sb_x$ ($x = 0$, 0.1 and 0.2) samples annealed at 700 °C.

temperature dependence of the resistivity, carrier density and mobility are plotted in Figure 8.18.(a), (b) and (c) respectively. For the resistivity $\rho(T)$ curves, it is observed that with respect to the bad-metal behaviour of the undoped sample exhibit weak temperature dependence, 10% Sb-doping decreases the resistivity and induces a mild metallic behaviour, while 20% Sb-doping increases the resistivity by a factor of ∼50 and induces a semiconducting behaviour in the whole temperature range, with $\rho(T)$ decreasing as the temperature increases.

Consistently, as shown in Figure 8.18.(b), the hole carrier density increases by almost an order of magnitude from undoped to 10% Sb-doped samples, while for the 20% doped sample the carrier density is decreased back below the value of the undoped sample. As Sb dopants are monovalent donors in Fe_2TiSn, Sb-doping is expected to introduce electron-type charge carriers; hence the increase in hole carriers measured in the 10% doped sample is unexpected in a rigid band approximation approach.

It should be mentioned that the effect of Sb-substitution in Fe_2TiSn on the resistivity has previously been studied (up to $\leqslant 5\%$) in the temperature range $300 - 850$ K, but a negligible effect was found [308]. Fully substituted Fe_2TiSb is predicted to be a half-metal, with 100% spin polarization [315]. The mobility of carriers, shown in Figure 8.18.(c), decreases monotonically with doping.

The magnetoresistance of 10% and 20% doped samples (not shown) display negative contributions of a few percent in magnitude, with the same shape as those found in the annealed undoped samples in Figure 8.15.

To get insights on the effect of Sb-doping on the thermoelectric properties, the temperature dependence of the Seebeck coefficient and the power factor of undoped and doped samples are given in Figure 8.19.(a) and (b), respectively. In the top panel, we can compare the evolution of the Seebeck coefficient with respect to temperature for $x = 0$, 0.1 and 0.2. The maximum of S present for the undoped sample disappears with 10% doping, the curve instead exhibits a more monotonic increase with temperature, expected from metals with nearly constant carrier density. At room temperature, the value of the thermopower in the 10% doped sample exceeds that of the undoped sample.

In contrast, the 20% doped sample has an $S(T)$ curve shape similar to the undoped sample, in agreement with the semiconducting behaviour of the resistivity curve $\rho(T)$ (Figure 8.18.(a)). In terms of power factor, the 10% doped sample exhibits a behaviour of increasing curve with increased temperature above 60 K, yielding a crossover of the two curves for the undoped and 10% doped samples at room temperature. Slightly above room temperature, the power factor of the 10% doped sample is more than twice the value of the undoped sample. For the 20% doped sample, the power factor is severely decreased, by two orders of magnitude.

It must be mentioned that a lower density of Sb impurity results in minor effect on the high-temperature thermoelectric properties (5%, from Reference [308]).

8.3.5 Theoretical results

As discussed beforehand, Fe_2TiSn is found to be a nonmagnetic semiconductor with a band gap of 1.04 eV, as shown in Figure 8.7. This is in agreement with the Slater-Pauling rule [262, 263], but contrasts with the measured high hole density and the low Seebeck coefficient of the undoped samples, as shown in Figures 8.14.(b) and 8.16.(a). It must be noted that similar discrepancies have already been found and explored in Fe_2VAl, as mentioned at the beginning of this Chapter, and which have been attributed to antisite defects and disorder rather than being an intrinsic property of the pristine phase [24].

In order to investigate and clarify the differences between experiments and simulations occurring in Fe_2TiSn, we estimate the influence on the electronic properties of such natives defects as antisites and vacancies, whose presence is evidenced even in the undoped samples by the structural analyses. The simulated electronic DOS, calculated for a $2 \times 2 \times 2$ cubic supercell with on (a) Ti_{Fe}, (b) Sn_{Fe}, (c) V_{Ti}, and (d) V_{Sn} defect, are shown in Figure 8.20, on the panels on the left. From here, we observe the following:

1. All the defects act as acceptor dopant, shifting the Fermi level toward the valence band;
2. in-gap states appear with respect to the pristine phase;
3. the spin degeneracy is removed.

These results suggest that the as-cast undoped Fe_2TiSn samples are actually p-type doped due to the formation of defects, and they consistently justify the bad-metal behaviour of the resistivity, as evidenced in Figure 8.14.(a), as well a the possible magnetic ordering appearing at low temperature (Figures 8.15 and 8.17), and the hole-like transport (Figures 8.14 and 8.16). To further develop our point, we show in Figure 8.20.(e)

and (f) the room-temperature Seebeck coefficient and the carrier density as a function of chemical potential (μ) computed from the eigenenergies of pristine Fe_2TiSn.

Following the rigid-band approach, *i.e.*, due to the presence of acceptor defects, μ rigidly shifts toward the valence band, we recognize that the experimental hole density measured by the Hall effect at 300 K, $n_{300\ \mathrm{K}} \approx 10^{21}$ cm^{-3}, identifies μ inside the valence band (as displayed in Figure 8.20.(f), for which the corresponding calculated S is 12 μVK^{-1}, in agreement with the measurements shown in Figure 8.16).

Upon Sb substitution on Sn sites, providing additional electrons to the system, μ shifts to higher energies and, at the extreme value of $x = 0.2$, the experimental density of carriers decreases by about 1 ordor of magnitude ($n_{300\ \mathrm{K}} \approx 2 \times 10^{20}$ cm^{-3}), consistent with the approach of μ to the band gap and the appearance of an experimental semiconducting-like regime, evidenced by the decrease of the resistivity with the temperature observed from the 20% doped sample (Figure 8.18.(a)) coming from the compensated hole carriers. In the same rigid-band picture, we would expect μ at intermediate doping (such a $x = 0.1$) to fall in-between the region defined by $x = 0$ and $x = 0.2$ [light blue area in Figures 8.20.(e)−8.20.(g)]; however, this expectation contrasts with the experimental evidences of large carrier density ($n_{300\ \mathrm{K}} \approx 4 \times 10^{21}$ cm^{-3}), lower (larger) resistivity, and slightly larger (slightly lower) carrier mobilities with respect to the $x = 0$ ($x = 0.2$) case.

This discrepancy might point out limitation of the rigid-band approximation, which does not account for possible difference in the density of state arising from the formation of defects, as instead evidenced from our simulations. In this way, in the following discussion, a possible defect-induced DOS feature is proposed to be responsible for the experimental observations.

8.3.6 Discussion

We need to consider first the effect of annealing. We observe that annealing increases the carrier mobility, while slightly decreasing hole carrier concentration. Additionally, the relative heights of XRD peaks I_{111}/I_{220} and I_{200}/I_{220} increase with annealing temperature, suggesting increasing atomic order. From theoretical calculations, we attribute the large hole carrier density to atomic disorder. The carrier mobility is certainly limited by atomic disorder as well. Therefore, all these effects point to a healing effect of annealing on atomic disorder, and contribute to the improvement of homogeneity and phase purity in the samples.

We can now address the effect of Sb doping. The comparison of the experimental results and the *ab initio* calculations suggests a twofold effect of Sb-doping: on one hand, it fills bands with electron-type charge carriers, and on the other hand it is responsible for increased atomic disorder, which introduces hole-type charge carriers. The increased atomic disorder associated with doping is consistent with the progressive suppression of carrier mobility with increased doping, even if the relative heights of XRD peaks I_{111}/I_{220} and I_{200}/I_{220} do not show any trend with increased doping.

In the 10%-doped sample, hole doping prevails, resulting in lower and metallic resistivity, the monotonically increasing $S(T)$ curve with increasing temperature, and the enhancement of the thermoelectric power factor at room temperature. In the 20%-doped sample

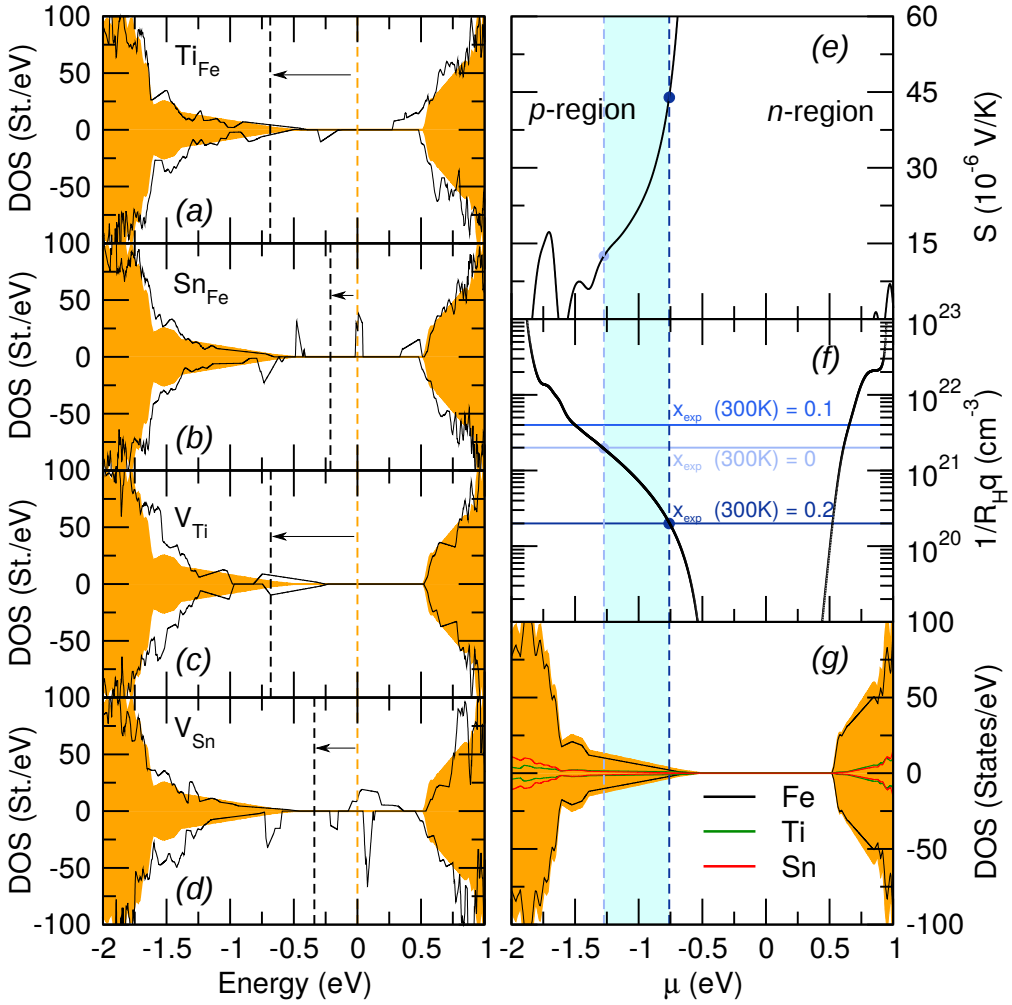

FIGURE 8.20: Theoretical results from DFT and Boltzmann transport theory calculations on Fe_2TiSn. On the left column, the electronic DOS is shown, computed for a $2 \times 2 \times 2$ cubic supercell of Fe_2TiSn containing one (a) Ti_{Fe} , (b) Sn_{Fe} , (c) V_{Ti} , and (d) V_{Sn} defect. The orange background refers to the pristine DOS, and the vertical dashed lines indicate the Fermi level associated with each DOS, with arrows highlighting their shift caused by the impurity. On the right column, we show the (e) chemical potential dependence of the Seebeck coefficient at 300 K, (f) the associated carrier density estimated by the inverse Hall coefficient (with the hole density identified from Hall measurements for $x = 0$, 0.1, and 0.2, highlighted within horizontal lines), and (g) the computed pristine atomic-projected DOS. The experimental carrier densities at 300 K for $x = 0$ and $x = 0.2$ are used to define a chemical potential interval (light blue region) falling inside the valence band.

however, the level of disorder is such that it yields much larger resistivity (with a semiconducting behaviour with increased temperature), decreased carrier density and a $S(T)$ curve shape with a broad maximum in the range $200 - 250$ K, and severe suppression of the thermoelectric power factor.

These properties may possibly be explained in terms of disorder-induced Anderson localization [102]. As an alternative mechanism involving the transport and thermoelectric data measured in the Sb-doped samples, we also suggest that increasing the concentration of Sb impurities compensates part of the hole carriers whose presence is induced by native defects, antisites [312] and/or vacancies [316] already present in the undoped Fe_2TiSn phase, which act as p-type dopants as shown in Figure 8.20 (panels on the left).

Moreover, the competition between the donor electrons and the defect-induced holes makes the system deviate from the monotonic behaviour (expected in a rigid-band picture as a function of the doping level x) if we assume that the doping process shifts the chemical potential through a DOS peak, otherwise absent in the pristine structure, which lies close to the maximum of the valence band at intermediate Sb concentrations.

Hence, for $x = 0.1$, the carrier density increases by 1 order of magnitude with respect to the undoped samples (Figure 8.18.(b)), although, due to the strongly localized nature of those defect states, the carrier mobility decreases (Figure 8.18.(c)) and consequently the sample resistivity decreases only slightly, with a weak temperature dependence in the studied range of temperature. This scenario consistently explains the experimental behaviour of all studied transport properties (resistivity, carrier density, mobility, and Seebeck coefficient) and explain the recovery at higher Sb concentration of a semiconducting-like character as predicted for pristine Fe_2TiSn.

This concludes our analysis of Sb-doped Fe_2TiSn. Despite similar features in term of electronic properties between Fe_2TiSn and Fe_2VAl, it is worth comparing these compounds in terms of the role of doping in improving thermoelectric performances. The large power factor predicted on Fe_2TiSn is for strong n-type doping ($n_e \approx 10^{21}$ cm^{-3}). Similarly to Fe_2VAl [271], Fe_2TiSn forms as p-type doped and the atomic disorder affects significantly the electronic states near the band-gap edges. These states have significant orbital character from Fe and V(Ti) atoms. From our knowledge, Fe_2TiSn has not been yet experimentally made as an n-type doped material, unlike Fe_2VAl [255, 279, 317]. It is therefore reasonable to expect that atomic site disorder plays a stronger role in Fe_2TiSn than in Fe_2VAl. Furthermore, Chaudhuri et al. [312] report that the hole concentration increases with Sb doping and, concomitantly, the concentration of antisite defects decreases with Sb doping. This may be explained if the samples contain significant vacancy defects which also act as p-type dopants and whose concentration increases with Sb doping. Regarding the vacancy defects in Fe_2TiSn, their presence at a concentration significantly larger with respect to Fe_2VAl and the associated Fermi-level pinning by atomic defects (both vacancies and antisite) may be the important difference between Fe_2TiSn and Fe_2VAl. Indeed, by comparing the data for the undoped samples, undoped Fe_2VAl has a dominant p-type transport character, with a high hole concentration of about 4.8×10^{20} cm^{-3} [318], while from our data, undoped Fe_2TiSn forms as p-type doped with a high hole concentration of about 2×10^{21} cm^{-3} at 300 K; the difference with Fe_2VAl is thus about one order of magnitude, and explains why hole compensation in donor-doped Fe_2VAl can be reached with donor density $x = 0.03$ [278, 279], an order of magnitude below the donor density required to compensate the holes in our Sb-doped Fe_2TiSn samples. We can expect that a large fraction of these holes originates from

vacancies, whose concentration has been estimated up $\sim 10^{20}$ cm^{-3} in Fe_2TiSn samples grown by the optical floating zone technique [316]. In summary:

1. In Fe_2TiSn, the resonant and in-gap electronic states generated by vacancy and antisite defects (which are usually magnetic defects) can pin the Fermi level near the top of the valence band, making n-type doping inefficient.
2. Anderson localization and hopping-type conduction, as well a magnetic (ferromagnetic) order may be stronger in Fe_2TiSn than Fe_2VAl.

8.4 Conclusions

In this Chapter, we studied from first-principles the effect of n-type doping on the electronic and thermoelectric properties properties of Fe_2YZ full-Heusler compounds. Our study suggests that these compounds may experience robust magnetic interactions when doped with electrons, undergoing a magnetic phase transition that is detrimental to the thermoelectric power factor, which is decreased with respect to estimations obtained from the rigid band approximation. We propose different strategies to avoid such magnetic instabilities, by either tuning the hybridization between the Y e_g band and the Fe e_g bands, or by switching to $4d$ and $5d$-based compounds, where the larger state overlaps and weaker localization decreases the strength of the exchange mechanisms.

Nevertheless, this questions the use of the rigid band approximation in high-throughput approaches predictions [319, 320] and motivates to always go beyond the simple picture provided by the pristine phases to properly evaluate the thermoelectric properties of doped materials. The increase of computational power, as well as the development of theoretical methods, provide bright perspectives for the theoretical study of more realistic structure.

Beyond this theoretical work on the broad Fe_2YZ family, we also had the opportunity to study the electronic and thermoelectric properties of Sb-doped Fe_2TiSn samples from experiments: polycrystalline Fe_2TiSn, $Fe_2TiSn_{0.9}Sb_{0.1}$ and $Fe_2TiSn_{0.8}Sb_{0.2}$ samples prepared by arc melting are investigated to explore the possibility of exploiting transport properties the "flat-and-dispersive" e_g conduction band, predicted to be at the origin thermoelectric of a large power factor from first-principles [25]. The different samples present a sizeable amount of atomic disorder, which results in p-type transport and depressed thermoelectric properties.

By comparing the experimental transport properties and *ab initio* calculations accounting for the existence of different antisite defects and vacancies, we sustain and show the origin of the measured p-type character of the transport in undoped Fe_2TiSn, as well as the origin of its magnetic ordering at low-temperature and, on the other hand, we also provide an explanation for the change witnessed in Sb n-type doped Fe_2TiSn samples, resulting in a compensated semiconductor.

Specifically, in the Sb-substituted samples annealed at 700 °C, it is observed that 10% substitution increases the hole carrier density, inducing a weakly metallic behaviour, whereas 20% substitution lowers the carrier density and increase the resistivity by a factor of ∼50, restoring a semiconducting behaviour as in the undoped sample. This

behaviour is interpreted in terms of competition between electron doping by band filling, and hole doping associated to atomic disorder.

Particularly, we propose that the non-monotonic effect of Sb doping on transport can be explained by considering that the doping process acts in an already *p*-type doped (and not rigorously pristine) crystalline environment, and is affected by the DOS of the host material encountering its feature induced by the presence of defects states near the top of the valence band.

We conjecture alternatively that in the 10% doped sample, the effect of defect-induced hole doping prevails over electron doping, while in the 20% doped sample, Anderson localization yielded by disorder eventually prevails on both electron and hole doping.

In terms of thermoelectric properties, the measured Seebeck coefficient exhibits a maximum at around $200 - 250$ K for the undoped and 20%-doped samples, while it increases monotonically with increasing temperature for the metallic 10%-doped sample. For the same sample, the room temperature power factor has a value about 0.13 mW/m K^2, about 2 order of magnitude lower than the optimal power factor estimated from the rigid band approximation, 25 times lower than the optimal power factor predicted by accounting the magnetic instability highlighted in the previous Section, yet still improve by more than a factor of two the value of the power factor measured in the undoped sample at the same temperature.

This work, as joint effort combining experiments and theory, shows that it is possible to improve the power factor by chemical doping in Fe_2TiSn. Yet, the nature of real samples must be taken into account when designing possible substitution. Currently, the detrimental effect of atomic site disorder on electronic and thermoelectric properties dominates at high doping level, and this disorder should be minimized as much as possible.

Chapter 9

Summary, concluding remarks and perspectives

This work has been devoted to study from first principles complex structures presenting transition metal with $3d$ orbitals featuring a low-dimensional aspect in term of electronic transport. The originality of our study is that we model the exchange-correlation energy through the B1-WC hybrid functional in our DFT calculations, overcoming the spurious description of the properties associated with highly localized orbitals such as the $3d$ ones typically associated with local and semi-local functionals.

The first half of this manuscript is devoted to the interface between $LaAlO_3$ and $SrTiO_3$, hosting a two-dimensional electron gas at the origin of the conductivity of the interface between these two band insulators. After demonstrating that the B1-WC hybrid functional reproduce quantitatively the properties of the parent bulk compounds, we focus on two of the most popular hypotheses about the origin of the charge at the interface, the polar catastrophe scenario, written in terms of a Zener breakdown (with no atomic reconstruction) or in terms of a polarity-driven surface redox reaction where oxygen vacancies are stabilized at the LAO surface and provide carriers to the interface. Even today, there remains some confusion in the community about these two mechanisms and their validity, despite the large amount of studies available in the literature. Our study aim at clarifying in a quantitative way the relevance of these mechanisms, as we model them at the same level of approximation using beyond standard DFT calculations. We determine that oxygen vacancies at the LAO surface are stabilized for a LAO thickness below the critical thickness required for Zener breakdown, providing a theoretical argument against the possibility of pure Zener breakdown in experiments. In addition to clarifying some aspects witnessed in real samples such as the oxygen partial pressure dependence of the sheet resistance, the surface redox model is also in better agreement with the insulator-to-metal phase transition witnessed at the interface between STO and the $La_{1-x}Sr_xAl_{1-x}Ti_xO_3$ alloy, predicting the threshold thicknesses with respect to the composition x at a better quantitative level in contrast to pure Zener breakdown. Of course, all our results are tributary of the approximations inherent to our methodology, but the overall better agreement with experiment constitutes an argument against the Zener breakdown hypothesis, beyond the lack of experimental evidence of mobile holes at the LAO surface for example.

In addition, we studied the effect of quantum confinement of within the STO substrate, highlighting its dependence on carrier density and size effects by reducing the host

STO thickness. Finally, the electronic properties of STO/LAO structures capped with STO have been investigated to understand the role of the capping layer in reducing the LAO critical thickness, against expectations from polarity-driven mechanisms: the origin of the 2DES remains attributed to electric-field driven surface redox reactions, but facilitated through the chemistry of the STO surface. In this picture, we also expect the coexistence of two spatially separated 2DES in the thick LAO limit.

For the second half of the manuscript, we investigated the thermoelectric properties of layered oxides, namely calcium cobaltite and STO-based superlattices, and make a case against the possibility of improving them through nanostructures and improved carrier mass anisotropy. Despite the improved anisotropic character of the $3d$ states near the band gap, interfacial effects lead to smaller spectral weight of these states with an overall negative impact on the thermoelectric power factor.

Finally, exporting the low-dimensional transport concept from STO-based systems, we investigate the effect of electron doping on iron-based Fe_2YZ Heusler compounds, going beyond the rigid band approximation of prototypical *ab initio* studies. We identify two obstacles to improve the thermoelectric properties: on one hand, the Fe e_g states expected to yield high power factors experience robust magnetic transitions when populated with electrons, related to its low-dimensional Fermi surface, and losing the large thermoelectric power factor expected from the rigid band approximation. On the other hand, experiments performed on doped samples of $Fe_2TiSn_{1-x}Sb_x$ highlight the dominant effect of native defects, such as vacancies and disorder, limiting the possibility to achieve n-type transport in Fe_2TiSn.

In conclusions, we have presented a theoretical study based on density functional theory of different structures featuring transport based on $3d$ orbitals, exploiting their intrinsic anisotropy to achieve low dimensional electron systems. In the present work, we made a point to always remain critical of the theoretical results and to always keep in mind the available experimental data to address the limit of our models. For the STO/LAO systems, we are ultimately limited in the way that we model defects, as it involves a large number of atoms and electrons in the simulation cells. However, with the ever-increasing computational power of supercalculators, combined with the developments of *second principles* numerical tools, we can expect the shortcomings of the first-principles to be avoided, including the effects of multiple defects for example. For STO/LAO systems, some discrepancies remain to be clarified, such as the discrepancy between the densities estimated from spectroscopy or Hall effect measurements, or the exact nature of the transport in capped $STO(001)/LAO_m/STO_n$ systems: so far, the existence of hole in the capping layer has only be reported by a handful of groups. As for the Heusler compounds, beyond thermoelectricity, the possibility of tunable magnetism make them good candidates for spin-caloritronics applications. For the particular case of Fe_2TiSn, the difficulty to achieve n-type transport needs to be clarified: the role of native p-type defects is expected to dominate the transport in these compounds, yet a clear understanding of the stability of these defects remains elusive. Our findings only provide a fraction of answers to these issues, while laying further prospects in these research domains.

Appendix A

Chemical potential of oxygen

We calculate the chemical potential of oxygen at finite temperature and pressure from the thermodynamic model, inspired by the developments of References [45, 46]. Considering the environment as a gas reservoir of N particles at pressure p and temperature T, the chemical potential is given by the derivative of the Gibbs free energy:

$$\mu = \left(\frac{\partial G}{\partial N}\right)_{T,p} = \frac{G}{N} \tag{A.1}$$

As G is a potential function depending on p and T, we can write, using the Maxwell relations:

$$dG = \left(\frac{\partial G}{\partial T}\right)_p dT + \left(\frac{\partial G}{\partial p}\right)_T dp = -S\, dT + V\, dp \tag{A.2}$$

From the ideal gas equation of state ($pV = Nk_BT$), the partial derivative of $G(p,T)$ with respect to p is:

$$\left(\frac{\partial G}{\partial p}\right)_T dp = V = \frac{Nk_BT}{p} \tag{A.3}$$

In turn, a finite change of pressure from p_0 to p results in:

$$G(p,T) - G(p_0,T) = \int_{p_0}^{p} \left(\frac{\partial G}{\partial p}\right)_T dp = Nk_BT\, ln\frac{p}{p_0} \tag{A.4}$$

Combining the first Equation and the last one, we have:

$$\mu_{O_2}(p,T) - \mu_{O_2}(p_0,T) = k_BT\, ln\frac{p}{p_0} \tag{A.5}$$

Hence we have:

$$\mu_O(p,T) = \frac{1}{2}\mu_{O_2}(p,T) = \mu_O(p_0,T) + \frac{1}{2}k_BT\, ln\frac{p}{p_0} \tag{A.6}$$

From the knowledge of temperature-dependant $\mu_O(p_0,T)$ at fixed pressure p_0 and Equation A.6, one can calculate the chemical potential μ_O at given p and T using tabulated values for the O_2 standard enthalpy H_0 and entropy S_0 (at $T_0 = 298$ K and $P_0 = 1$ atm)

through:

$$\mu_{\mathrm{O}}(p_0, T) = \frac{1}{2}\left([H_0 + \Delta H(T)] - T\,[S_0 + \Delta S(T)]\right) \tag{A.7}$$

where $\Delta H(T) = C_p(T - T_0)$ and $\Delta S(T) = C_p\, ln\, \frac{T}{T_0}$. For typical growth conditions for the STO/LAO heterostructures, we use $p = 3.0 \times 10^{-8}$ atm (oxygen partial pressure p_{O_2}) and temperature $T = 1123$ K [88]. As for the standard values H_0, S_0 and heat capacity C_p, we use values from the NIST-JANAF thermochemical Tables [321]:

$$\begin{aligned} H_0 &= 0 \text{ kJ mol}^{-1} \\ S_0 &= 205 \text{ J mol}^{-1}\text{K}^{-1} \\ C_p &= 29.39 \text{ J mol}^{-1}\text{K}^{-1} \end{aligned}$$

With these data, we find:

$$\begin{aligned} H(T = 1123 \text{ K}) &= 24.24 \text{ kJ mol}^{-1} \\ S(T = 1123 \text{ K}) &= 38.99 \text{ J mol}^{-1}\text{K}^{-1} \end{aligned}$$

This leads to $\mu_{\mathrm{O}}(p_0,\, T = 1123 \text{ K}) = -1.29$ eV. Finally, at pressure $p = 3.0 \times 10^{-8}$ atm:

$$\mu_{\mathrm{O}}(p, T) = \mu_{\mathrm{O}}(p_0, T) + \frac{1}{2} k_B T\, ln\, \frac{p}{p_0} = -2.13 \text{ eV} \tag{A.8}$$

In the manuscript, we mainly use a rounded value of $\mu_{\mathrm{O}} = -2.0$ eV, which is the same value used in Reference [47] and close to the value used by Bristowe *et. al.* [117] (-1.9 eV). The chemical potential of oxygen with respect to p and T is given in Figure A.1, where are also displayed several growth conditions (p,T) extracted from the literature, allowing us to determine the scattering of μ_{O} across the average value for the different experiments, determined to lie between -2.2 eV and -1.7 eV. The effect of post-growth annealing is to shift the chemical potential toward zero; depending on the annealing conditions, we expect the upper bound of chemical potential to be roughly -1.0 eV.

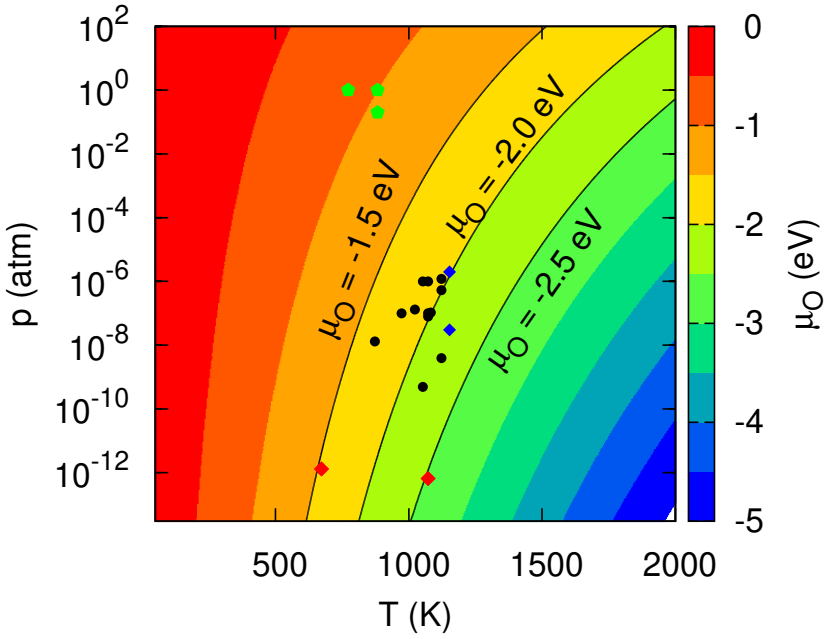

FIGURE A.1: Chemical potential of oxygen $\mu_O(p,T)$, the black dots correspond to growth conditions extracted from the literature [82–84, 140, 141, 240, 322–324]. The two blue lozenges correspond to the growth conditions from Reference [89], for $p = 3\times10^{-5}$ mbar and $p = 2\times10^{-3}$ mbar at $T = 1153$ K. The green triangles correspond to annealing conditions reported in References [141, 171], while the red lozenges correspond to the annealing conditions of bare STO films in ultra-high vacuum [178, 179] with a reported metallic surface.

Appendix B

From single-crystal transport tensors to polycrystalline properties

Comparing the thermoelectric properties of non-textured polycrystalline samples of a material with the properties of single crystals is not a trivial task when the single crystal properties are anisotropic. Indeed, it is expected that, as the transport properties vary locally in such a disordered system, the thermal and electric gradient responsible for the thermoelectric effect also varies locally, which makes the comparison of theoretical results derived from ideal, highly ordered systems much more difficult.

This issue has been addressed from time to time in the literature; however there is no standardized procedure, and the problem becomes quite relevant as the theoretical tools evolve. It is usual to perform an arithmetic average the properties on the single-crystal case along each spatial direction to get a rough estimation of the properties of a macroscopic sample where the crystallites are organized in a completely random direction, as performed in References [325] and [326], for example. A different method has been described in Reference [327], where the authors used a simple circuit model to derive a proper way to estimate the thermoelectric properties of a polycrystal from the single-crystal coefficients. However, as explained in the following, these models are not antagonistic; rather, they complement each other and can be used to assess different types of orderings.

In the model from Reference [327], a thermomodule composed of a single grain (Figure B.2, left), with its Seebeck coefficient S and the conductivity σ, is replaced with the corresponding electromotive force $\mathcal{E}$ and resistivity r. Thus the effective thermopower is the voltage on the module, divided by the temperature difference across the module, ΔT, when the load resistance R_L goes to infinity,

$$\begin{aligned} S_{eff} &= \lim_{R_L \to \infty} \frac{iR_L}{\Delta T} = \lim_{R_L \to \infty} \frac{\mathcal{E}}{r + R_L} \frac{R_L}{\Delta T} \\ &= \frac{\mathcal{E}}{\Delta T} = S \end{aligned} \tag{B.1}$$

The polycrystal model considers that the thermomodule is composed of several grains of three types (Figure B.2, right), with each type having different Seebeck coefficients

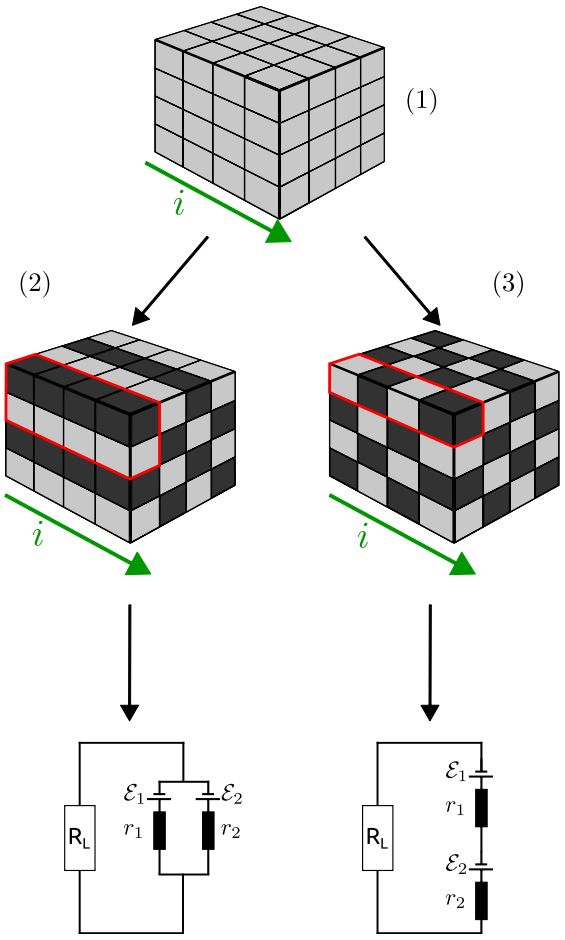

FIGURE B.1: Polycrystal model composed of several grains (1) and possible configurations [(2) and (3)] with two types of grains having different S_k and σ_k. If a current i goes through the thermomodule, the configurations are not equivalent and affect the overall properties of the whole polycrystal. This is illustrated by the equivalent circuits (bottom).

S_k and electrical conductivities σ_k corresponding to the properties of a single crystal in each direction of space. Such a system is modelled as a multi-channels circuit, with the channels connected in parallel [Figure B.1, configuration (2)] and having the corresponding S_k and σ_k (for each kind of grains), and the effective Seebeck coefficient is calculated as

$$S^* = \frac{\sum_{i=x,y,z} S_{ii}\sigma_{ii}}{\sum_{i=x,y,z} \sigma_{ii}} \tag{B.2}$$

This model takes into account the fact that each grain, having a different conductivity σ_k, moderates the electrical potential across the grains. However, the model makes a rather strong assumption that the polycrystal can be represented by a multi-channel parallel circuit, where each channel S and σ matches the components of the corresponding tensor for a single crystal in the three directions, which is not necessarily the case for a random polycrystal [Figure B.1, configuration (3)]. Therefore, we propose another

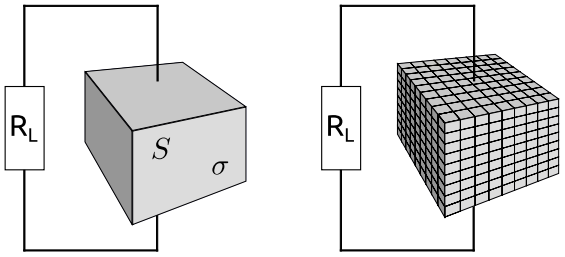

FIGURE B.2: Circuit model for lumped single-crystal thermoelectric material and for a polycrystalline material.

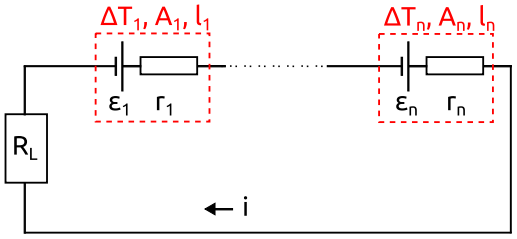

FIGURE B.3: Circuit model with composed of several different grains in series.

model, which consists of a single channel with the different grains in series, with a random distribution of the grains with different S_k and σ_k (Figure B.3). The random distribution of the grains translates in the model to equivalent geometry for each single grain. Additionally, we consider that $\overrightarrow{\nabla} T$ is constant across the material, *i.e.* each individual ΔT_k across each grain is equivalent, such as

$$\sum_{k=1}^{n} \Delta T_k = n\Delta T_1 = n\Delta T_2 = ... = n\Delta T_n = \Delta T \tag{B.3}$$

This would not be true if the thermal transport properties (lattice + electron) are anisotropic as well. However, for the sake of simplicity of the model, we make this hypothesis. The Seebeck coefficient is expressed as:

$$S^{\dagger} = \frac{iR_L}{\Delta T} \tag{B.4}$$

with

$$iR_L = \sum_{k=1}^{n} (\varepsilon_k - i_k r_k) \quad \text{with} \quad i_k = i$$

$$\iff \quad i = \frac{\sum_{k=1}^{n} \varepsilon_k}{R_L + \sum_{k=1}^{n} r_k} \tag{B.5}$$

which, inserted in Equation B.4, gives:

$$\begin{aligned} S^{\dagger} &= \lim_{R_L \to \infty} \frac{\sum_{k=1}^{n} \varepsilon_k}{R_L \left(1 + \frac{1}{R_L} \sum_{k=1}^{n} r_k\right)} \frac{R_L}{\Delta T} \\ &= \frac{\sum_{k=1}^{n} \varepsilon_k}{\sum_{k=1}^{n} \Delta T_1} = \frac{1}{n} \sum_{k=1}^{n} S_k \\ \iff \quad S^{\dagger} &= \langle S \rangle \end{aligned}$$

In this case, the Seebeck coefficient is the arithmetic average of individual S_k over the whole branch. This model can be generalized, for a complete homogeneous polycrystal, to a circuit with multiple channels, all contributing equally to the thermoelectric properties. As said previously, these two models are not antagonistic. $S^{\dagger}$ and S^{*} are the effective Seebeck coefficients for two extreme orderings of the crystallites, which border an infinite range of possible configurations, and therefore, for a given sample, one can expect the measurements to fall between the two extrema.

Appendix C

List of scientific publications

Some of the ideas, results and figures presented in this manuscript have appeared in the following publications:

1. *Thermoelectric properties of the unfilled skutterudite $FeSb_3$ from first-principles and Seebeck local probes*
   Sébastien Lemal, Ngoc Nguyen, Johannes de Boor, Philippe Ghosez, Julien Varignon, Benedikt Klobes, Raphaël P. Hermann, Matthieu J. Verstraete
   Physical Review B 92, 205204 (2015)
   doi:10.1103/PhysRevB.92.205204

2. *First-Principles Modeling of $SrTiO_3$ Based Oxides for Thermoelectric Applications*
   Daniel I. Bilc, Calin G. Floare, Liviu P. Zârbo, Sorina Garabagiu, Sébastien Lemal, Philippe Ghosez
   The Journal of Physical Chemistry C 120, 25678 (2016)
   doi:10.1021/acs.jpcc.6b07634

3. *Thermoelectric properties of layered calcium cobaltite $Ca_3Co_4O_9$ from hybrid functional first-principles calculations*
   Sébastien Lemal, Julien Varignon, Daniel I. Bilc, Philippe Ghosez
   Physical Review B 95, 075205 (2017)
   doi:10.1103/PhysRevB.95.075205

4. *Control of the orbital ordering in manganite superlattices and impact on properties*
   Ayşegül Begüm Koçak, Julien Varignon, Sébastien Lemal, Philippe Ghosez, Marie-Bernadette Lepetit
   Physical Review B 96, 125155 (2017)
   doi:10.1103/PhysRevB.96.125155

5. *Probing Quantum Confinement and Electronic Structure at Polar Oxide Interfaces*
   Danfeng Li*, Sébastien Lemal*, Stefano Gariglio, Zhenping Wu, Alexandre Fête, Margherita Boselli, Philippe Ghosez, Jean-Marc Triscone
   Advanced Science 5, 1800242 (2018)
   doi:10.1002/advs.201800242

6. *Thermoelectric properties of chemically substituted full-Heusler $Fe_2TiSn_{1-x}Sb_x$ (x = 0, 0.1, 0.2) compounds*
   Ilaria Pallecchi, Marcella Pani, Fabio Ricci, Sébastien Lemal, Daniel I. Bilc, Philippe Ghosez, Cristina Bernini, Niccolò Ardoino, Gianrico Lamura, Daniele Marré
   Physical Review Material 2, 075403 (2018)
   doi:10.1103/PhysRevMaterials.2.075403

7. *Tailoring the quantum well states in LAO/STO heterostructures*
   Marco Caputo, Alessio Filippetti, Margherita Boselli, Sébastien Lemal, Alla Chikina, Claudia Cancielleri, Thorsten Schmitt, Stephano Gariglio, Philippe Ghosez, Jean-Marc Triscone and Vladimir N. Strocov
   Submitted, preprint available (*arXiv:1903.10994* [cond-mat.str-el])

8. *Doping-induced magnetic instabilities in full-Heusler compounds*
   Sébastien Lemal*, Fabio Ricci*, Daniel I. Bilc, Matthieu Verstraete and Philippe Ghosez
   Submitted, preprint available (*arXiv:1907.04267* [cond-mat.str-el])

Bibliography

[1] W. Kohn and L. J. Sham, "Self-consistent equations including exchange and correlation effects," *Physical Review*, vol. 140, pp. A1133–A1138, Nov 1965.

[2] J. Halpern, S. Sinex, and S. Johnson, "Chemistry LibreTexts, a 3D Representation of Orbitals." `https://chem.libretexts.org/Bookshelves/General_Chemistry/Map%3A_Chemistry_-_The_Central_Science_(Brown_et_al.)/06._Electronic_Structure_of_Atoms/6.6%3A_3D_Representation_of_Orbitals`, 2019.

[3] R. M. Martin, *Electronic structure : Basic Theory and Pratical Methods*. Cambridge University Press, 2004.

[4] F. Finocchi, "*Density Functional Theory for Beginners, Basic Principles and Practical Approaches*." `http://www.attaccalite.com/wp-content/uploads/2017/04/pdf_DFT4beginners.pdf`, consulted the 05-06-2015, 2011.

[5] S. Blügel, N. Helbig, V. Meden, and D. Wortmann, eds., *Computing Solids: Models, Ab-initio Methods and Supercomputing; Lecture Notes of the 45th IFF Spring School 2014*. Forschungszentrum Jülich, 2014.

[6] M. Born and J. Oppenheimer, "Zur quantentheorie der molekeln," *Annalen der Physik*, vol. 380, p. 457, 1927.

[7] F. Bassani, F. Fumi, and M. P. Tosi, eds., *Highlights of Condensed-matter Theory*. North-Holland, 1985.

[8] S. H. Vosko, L. Wilk, and M. Nusair, "Accurate spin-dependent electron liquid correlation energies for local spin-density calculations - a critical analysis," *Canadian Journal of Physics*, vol. 58, p. 1200, 1980.

[9] J. P. Perdew and A. Zunger, "Self-interaction correction to density-functional approximations for many-electron systems," *Physical Review B*, vol. 23, p. 5048, 1981.

[10] J. P. Perdew, K. Burke, and M. Ernzerhof, "Generalized gradient approximation made simple," *Physical Review Letters*, vol. 77, p. 3865, 1996.

[11] P. Ziesche and H. Eschrig, "Electronic structure of solids '91," 1991.

[12] M. Cococcioni and S. de Gironcoli, "Linear response approach to the calculation of the effective interaction parameters in the LDA+U method," *Physical Review B*, vol. 71, p. 035105, Jan 2005.

[13] J. Harris, "Adiabatic-connection approach to Kohn-Sham theory," *Physical Review A*, vol. 29, pp. 1648–1659, Apr 1984.

[14] A. D. Becke, "Correlation energy of an inhomogeneous electron gas: A coordinate-space model," *The Journal of chemical physics*, vol. 88, no. 2, pp. 1053–1062, 1988.

[15] A. D. Becke, "A new mixing of Hartree-Fock and local density-functional theories," *The Journal of chemical physics*, vol. 98, no. 2, pp. 1372–1377, 1993.

[16] A. D. Becke, "Density-functional exchange-energy approximation with correct asymptotic behavior," *Physical Review A*, vol. 38, pp. 3098–3100, Sep 1988.

[17] C. Lee, W. Yang, and R. G. Parr, "Development of the Colle-Salvetti correlation-energy formula into a functional of the electron density," *Physical Review B*, vol. 37, pp. 785–789, Jan 1988.

[18] D. I. Bilc, R. Orlando, R. Shaltaf, G. M. Rignanese, J. Iniguez, and P. Ghosez, "Hybrid exchange-correlation functional for accurate prediction of the electronic and structural properties of ferroelectric oxides," *Physical Review B*, vol. 77, p. 165107, 2008.

[19] Z. Wu and R. E. Cohen, "More accurate generalized gradient approximation for solids," *Physical Review B*, vol. 73, p. 235116, 2006.

[20] R. Demichelis, B. Civalleri, P. D'Arco, and R. Dovesi, "Performance of 12 DFT functionals in the study of crystal systems: Al_2SiO_5 orthosilicates and al hydroxides as a case study," *International Journal of Quantum Chemistry*, vol. 110, no. 12, pp. 2260–2273, 2010.

[21] R. Demichelis, B. Civalleri, M. Ferrabone, and R. Dovesi, "On the performance of eleven DFT functionals in the description of the vibrational properties of aluminosilicates," *International Journal of Quantum Chemistry*, vol. 110, no. 2, pp. 406–415, 2010.

[22] J. Varignon and P. Ghosez, "Improper ferroelectricity and multiferroism in 2H-$BaMnO_3$," *Physical Review B*, vol. 87, p. 140403, 2013.

[23] N. Bristowe, J. Varignon, D. Fontaine, E. Bousquet, and P. Ghosez, "Ferromagnetism induced by entangled charge and orbital orderings in ferroelectric titanate perovskites," *Nature Communications*, vol. 6, p. 6677, 2012.

[24] D. I. Bilc and P. Ghosez, "Electronic and thermoelectric properties of Fe_2VAl: The role of defects and disorder," *Physical Review B*, vol. 83, p. 205204, 2011.

[25] D. I. Bilc, G. Hautier, D. Waroquiers, G.-M. Rignanese, and P. Ghosez, "Low-dimensional transport and large thermoelectric power factors in bulk semiconductors by band engineering of highly directional electronic states," *Physical Review Lett.*, vol. 114, p. 136601, 2015.

[26] M. Reinle-Schmitt, C. Cancellieri, D. L. D. Fontaine, M. Medarde, E. Pomjakushina, C. Schneider, S. Gariglio, P. Ghosez, J.-M. Triscone, and P. Willmott, "Tunable conductivity threshold at polar oxide interfaces," *Nature Communications*, vol. 3, p. 932, 2012.

[27] P. Delugas, A. Filippetti, V. Fiorentini, D. I. Bilc, D. Fontaine, and P. Ghosez, "Spontaneous 2-dimensional carrier confinement at the n-type $SrTiO_3/LaAlO_3$ interface," *Physical Review Lett.*, vol. 106, p. 166807, Apr 2011.

[28] C. Cancellieri, M. L. Reinle-Schmitt, M. Kobayashi, V. N. Strocov, P. R. Willmott, D. Fontaine, P. Ghosez, A. Filippetti, P. Delugas, and V. Fiorentini, "Doping-dependent band structure of $LaAlO_3/SrTiO_3$ interfaces by soft x-ray polarization-controlled resonant angle-resolved photoemission," *Physical Review B*, vol. 89, p. 121412, Mar 2014.

[29] C. Cancellieri, D. Fontaine, S. Gariglio, N. Reyren, A. D. Caviglia, A. Fête, S. J. Leake, S. A. Pauli, P. R. Willmott, M. Stengel, P. Ghosez, and J.-M. Triscone, "Electrostriction at the $LaAlO_3/SrTiO_3$ interface," *Physical Review Lett.*, vol. 107, p. 056102, Jul 2011.

[30] R. Dovesi, R. Orlando, B. Civalleri, C. Roetti, V. R. Saunders, and C. M. Zicovich-Wilso, "CRYSTAL, a computational tool for the *ab initio* study of the electronic properties of crystals," *Z. Kristallogr.*, vol. 220, p. 571, 2005.

[31] R. Dovesi, V. R. Saunders, C. Roetti, R. Orlando, C. M. Zicovich-Wilson, F. Pascale, B. Civalleri, K. Doll, N. M. Harrison, I. J. Bush, P. D'Arco, and M. Llunell, "CRYSTAL09 user's manual," 2009.

[32] G. K. Madsen and D. J. Singh, "BoltzTraP. A code for calculating band-structure dependant quantities," *Computer Physics Communications*, vol. 175, p. 67, 2006.

[33] D. S. Sholl and J. A. Steckel, *What is Density Functional Theory ?* Wiley-Blackwell, 2009.

[34] M. Kawasaki, K. Takahashi, T. Maeda, R. Tsuchiya, M. Shinohara, O. Ishiyama, T. Yonezawa, M. Yoshimoto, and H. Koinuma, "Atomic control of the $SrTiO_3$ crystal surface," *Science*, vol. 266, no. 5190, pp. 1540–1542, 1994.

[35] G. Koster, B. L. Kropman, G. J. H. M. Rijnders, D. H. A. Blank, and H. Rogalla, "Quasi-ideal strontium titanate crystal surfaces through formation of strontium hydroxide," *Applied Physics Letters*, vol. 73, no. 20, pp. 2920–2922, 1998.

[36] T. Ohnishi, K. Shibuya, M. Lippmaa, D. Kobayashi, H. Kumigashira, M. Oshima, and H. Koinuma, "Preparation of thermally stable TiO_2-terminated $SrTiO_3$ (100) substrate surfaces," *Applied physics letters*, vol. 85, no. 2, pp. 272–274, 2004.

[37] R. Dovesi, R. Orlando, A. Erba, C. M. Zicovich-Wilson, B. Civalleri, S. Casassa, L. Maschio, M. Ferrabone, M. D. L. Pierre, P. D'Arco, Y. Noël, M. Causa, M. Rerat, and B. Kirtman, "CRYSTAL14: A program for the *ab initio* investigation of crystalline solids," *International Journal of Quantum Chemistry*, vol. 114, p. 1284, 2014.

[38] T. Bredow, P. Heitjans, and M. Wilkening, "Electric field gradient calculations for Li_xTiS_2 and comparison with ^{7}Li nmr results," *Physical Review B*, vol. 70, p. 115111, Sep 2004.

[39] S. Piskunov, E. Heifets, R. I. Eglitis, and G. Borstel, "Bulk properties and electronic structure of $SrTiO_3$, $BaTiO_3$, $PbTiO_3$ perovskites: an *ab initio* HF/DFT study," *Computational Materials Science*, vol. 29, no. 2, pp. 165–178, 2004.

[40] M. Towler, "CRYSTAL Resources Page." `http://www.tcm.phy.cam.ac.uk/~mdt26/`. Accessed: 04-05-2015.

[41] X. Cao and M. Dolg, "Segmented contraction scheme for small-core actinide pseudopotential basis sets," *Journal of Molecular Structure: THEOCHEM*, vol. 673, no. 1-3, pp. 203–209, 2004.

[42] D. I. Bilc, R. Orlando, R. Shaltaf, G. M. Rignanese, J. Iniguez, and P. Ghosez, "Hybrid exchange-correlation functional for accurate prediction of the electronic and structural properties of ferroelectric oxides," *Physical Review B*, vol. 77, p. 165107, 2008.

[43] H. J. Monkhorst and J. D. Pack, "Special points for Brillouin-zone integrations," *Physical Review B*, vol. 13, pp. 5188–5192, Jun 1976.

[44] R. Dovesi, V. R. Saunders, C. Roetti, R. Orlando, C. M. Zicovich-Wilson, F. Pascale, B. Civalleri, K. Doll, N. M. Harrison, I. J. Bush, P. D'Arco, M. Llunell, M. Causa, and Y. Noël, "CRYSTAL14 user's manual," 2014.

[45] K. Reuter and M. Scheffler, "Composition, structure, and stability of $RuO_2(110)$ as a function of oxygen pressure," *Physical Review B*, vol. 65, p. 035406, Dec 2001.

[46] J. Osorio-Guillén, S. Lany, S. V. Barabash, and A. Zunger, "Magnetism without magnetic ions: Percolation, exchange, and formation energies of magnetism-promoting intrinsic defects in CaO," *Physical Review Lett.*, vol. 96, p. 107203, Mar 2006.

[47] L. Yu and A. Zunger, "A polarity-induced defect mechanism for conductivity and magnetism at polar-nonpolar oxide interfaces," *Nature communications*, vol. 5, p. 5118, 2014.

[48] V. M. Goldschmidt, "Die gesetze der krystallochemie," *Naturwissenschaften*, vol. 14, no. 21, pp. 477–485, 1926.

[49] N. Miao, N. C. Bristowe, B. Xu, M. J. Verstraete, and P. Ghosez, "First-principles study of the lattice dynamical properties of strontium ruthenate," *Journal of Physics: Condensed Matter*, vol. 26, no. 3, p. 035401, 2013.

[50] M. Koichi and I. Fujio, "*VESTA3* for three-dimensional visualization of crystal, volumetric and morphology data," *Journal of Applied Crystallography*, vol. 44, pp. 1272–1276, Dec 2011.

[51] A. M. Glazer, "The classification of tilted octahedra in perovskites," *Acta Crystallographica Section B: Structural Crystallography and Crystal Chemistry*, vol. 28, no. 11, pp. 3384–3392, 1972.

[52] Y. A. Abramov, V. G. Tsirelson, V. E. Zavodnik, S. A. Ivanov, and I. D. Brown, "The chemical bond and atomic displacements in $SrTiO_3$ from x-ray diffraction analysis," *Acta Crystallographica Section B*, vol. 51, no. 6, pp. 942–951, 1995.

[53] C. J. Howard, B. J. Kennedy, and B. C. Chakoumakos, "Neutron powder diffraction study of rhombohedral rare-earth aluminates and the rhombohedral to cubic phase transition," *Journal of Physics: Condensed Matter*, vol. 12, no. 4, p. 349, 2000.

[54] K. Van Benthem, C. Elsässer, and R. French, "Bulk electronic structure of $SrTiO_3$: experiment and theory," *Journal of applied physics*, vol. 90, no. 12, pp. 6156–6164, 2001.

[55] S.-G. Lim, S. Kriventsov, T. N. Jackson, J. Haeni, D. Schlom, A. Balbashov, P. Uecker, R .and Reiche, J. Freeouf, and G. Lucovsky, "Dielectric functions and optical bandgaps of high-k dielectrics for metal-oxide-semiconductor field-effect transistors by far ultraviolet spectroscopic ellipsometry," *Journal of Applied Physics*, vol. 91, no. 7, pp. 4500–4505, 2002.

[56] A. Filippetti, C. D. Pemmaraju, S. Sanvito, P. Delugas, D. Puggioni, and V. Fiorentini, "Variational pseudo-self-interaction-corrected density functional approach to the *ab initio* description of correlated solids and molecules," *Physical Review B*, vol. 84, p. 195127, Nov 2011.

[57] D. Fontaine, *Origin and properties of the two-dimensional electron gas at the $LaAlO_3/SrTiO_3$ interface: a first-principles hybrid functional study.* PhD thesis, Université de Liège, 2014.

[58] B. Choudhury, K. Rao, and R. Choudhury, "Dielectric properties of $SrTiO_3$ single crystals subjected to high electric fields and later irradiated with x-rays orγ-rays," *Journal of Materials Science*, vol. 24, no. 10, pp. 3469–3474, 1989.

[59] T. Konaka, M. Sato, H. Asano, and S. Kubo, "Relative permittivity and dielectric loss tangent of substrate materials for high-T_c superconducting film," *Journal of Superconductivity*, vol. 4, no. 4, pp. 283–288, 1991.

[60] J. F. Schooley, W. R. Hosler, and M. L. Cohen, "Superconductivity in semiconducting $SrTiO_3$," *Physical Review Lett.*, vol. 12, pp. 474–475, Apr 1964.

[61] W. Gong, H. Yun, Y. Ning, J. Greedan, W. Datars, and C. Stager, "Oxygen-deficient $SrTiO_{3-x}$, $x = 0.28$, 0.17, and 0.08. crystal growth, crystal structure, magnetic, and transport properties," *Journal of Solid State Chemistry*, vol. 90, no. 2, pp. 320–330, 1991.

[62] J. Carrasco, F. Illas, N. Lopez, E. A. Kotomin, Y. F. Zhukovskii, R. A. Evarestov, Y. A. Mastrikov, S. Piskunov, and J. Maier, "First-principles calculations of the atomic and electronic structure of f centers in the bulk and on the (001) surface of $SrTiO_3$," *Physical Review B*, vol. 73, p. 064106, Feb 2006.

[63] T. Tanaka, K. Matsunaga, Y. Ikuhara, and T. Yamamoto, "First-principles study on structures and energetics of intrinsic vacancies in $SrTiO_3$," *Physical Review B*, vol. 68, p. 205213, Nov 2003.

[64] V. E. Alexandrov, E. A. Kotomin, J. Maier, and R. A. Evarestov, "First-principles study of bulk and surface oxygen vacancies in $SrTiO_3$ crystal," *The European Physical Journal B*, vol. 72, no. 1, pp. 53–57, 2009.

[65] C. Mitra, C. Lin, J. Robertson, and A. A. Demkov, "Electronic structure of oxygen vacancies in $SrTiO_3$ and $LaAlO_3$," *Physical Review B*, vol. 86, p. 155105, Oct 2012.

[66] H. L. Zhuang, P. Ganesh, V. R. Cooper, H. Xu, and P. R. C. Kent, "Understanding the interactions between oxygen vacancies at $SrTiO_3$ (001) surfaces," *Physical Review B*, vol. 90, p. 064106, Aug 2014.

[67] H. Muta, K. Kurosaki, and S. Yamanaka, "Thermoelectric properties of reduced and la-doped single-crystalline $SrTiO_3$," *Journal of Alloys and Compounds*, vol. 392, no. 1, pp. 306 – 309, 2005.

[68] J. Mannhart and D. G. Schlom, "Semiconductor physics: The value of seeing nothing," *Nature*, vol. 430, no. 7000, p. 620, 2004.

[69] Z. Hou and K. Terakura, "Defect states induced by oxygen vacancies in cubic $SrTiO_3$: First-principles calculations," *Journal of the Physical Society of Japan*, vol. 79, no. 11, p. 114704, 2010.

[70] W. Meevasana, P. King, R. He, S. Mo, M. Hashimoto, A. Tamai, P. Songsiriritthigul, F. Baumberger, and Z. Shen, "Creation and control of a two-dimensional electron liquid at the bare $SrTiO_3$ surface," *Nature materials*, vol. 10, no. 2, p. 114, 2011.

[71] A. Chikina, F. Lechermann, M.-A. Husanu, M. Caputo, C. Cancellieri, X. Wang, T. Schmitt, M. Radovic, and V. N. Strocov, "Orbital ordering of the mobile and localized electrons at oxygen-deficient $LaAlO_3/SrTiO_3$ interfaces," *ACS nano*, vol. 12, no. 8, pp. 7927–7935, 2018.

[72] C. Lin and A. A. Demkov, "Electron correlation in oxygen vacancy in $SrTiO_3$," *Physical review letters*, vol. 111, no. 21, p. 217601, 2013.

[73] Y. Segal, J. Ngai, J. Reiner, F. Walker, and C. Ahn, "X-ray photoemission studies of the metal-insulator transition in $LaAlO_3/SrTiO_3$ structures grown by molecular beam epitaxy," *Physical Review B*, vol. 80, no. 24, p. 241107, 2009.

[74] P. Tasker, "The stability of ionic crystal surfaces," *Journal of Physics C: Solid State Physics*, vol. 12, no. 22, p. 4977, 1979.

[75] N. Bristowe, P. Littlewood, and E. Artacho, "The net charge at interfaces between insulators," *Journal of Physics: Condensed Matter*, vol. 23, no. 8, p. 081001, 2011.

[76] M. Stengel and D. Vanderbilt, "Berry-phase theory of polar discontinuities at oxide-oxide interfaces," *Physical Review B*, vol. 80, p. 241103, Dec 2009.

[77] D. Vanderbilt and R. D. King-Smith, "Electric polarization as a bulk quantity and its relation to surface charge," *Physical Review B*, vol. 48, pp. 4442–4455, Aug 1993.

[78] A. Ohtomo and H. Hwang, "A high-mobility electron gas at the $LaAlO_3/SrTiO_3$ heterointerface," *Nature*, vol. 427, no. 6973, p. 423, 2004.

[79] N. Nakagawa, H. Y. Hwang, and D. A. Muller, "Why some interfaces cannot be sharp," *Nature materials*, vol. 5, no. 3, p. 204, 2006.

[80] A. Savoia, D. Paparo, P. Perna, Z. Ristic, M. Salluzzo, F. Miletto Granozio, U. Scotti di Uccio, C. Richter, S. Thiel, J. Mannhart, and L. Marrucci, "Polar catastrophe and electronic reconstructions at the $LaAlO_3/SrTiO_3$ interface: Evidence from optical second harmonic generation," *Physical Review B*, vol. 80, p. 075110, Aug 2009.

[81] N. Ogawa, K. Miyano, M. Hosoda, T. Higuchi, C. Bell, Y. Hikita, and H. Y. Hwang, "Enhanced lattice polarization in $SrTiO_3/LaAlO_3$ superlattices measured using optical second-harmonic generation," *Physical Review B*, vol. 80, p. 081106, Aug 2009.

[82] M. Takizawa, S. Tsuda, T. Susaki, H. Y. Hwang, and A. Fujimori, "Electronic charges and electric potential at $LaAlO_3/SrTiO_3$ interfaces studied by core-level photoemission spectroscopy," *Physical Review B*, vol. 84, p. 245124, Dec 2011.

[83] G. Drera, F. Banfi, F. F. Canova, P. Borghetti, L. Sangaletti, F. Bondino, E. Magnano, J. Huijben, M. Huijben, G. Rijnders, D. H. A. Blank, H. Hilgenkamp, and A. Brinkman, "Spectroscopic evidence of in-gap states at the $SrTiO_3/LaAlO_3$ ultrathin interfaces," *Applied Physics Letters*, vol. 98, no. 5, p. 052907, 2011.

[84] F. Pfaff, H. Fujiwara, G. Berner, A. Yamasaki, H. Niwa, H. Kiuchi, A. Gloskovskii, W. Drube, J. Gabel, O. Kirilmaz, A. Sekiyama, J. Miyawaki, Y. Harada, S. Suga, M. Sing, and R. Claessen, "Raman and fluorescence contributions to the resonant inelastic soft x-ray scattering on $LaAlO_3/SrTiO_3$ heterostructures," *Physical Review B*, vol. 97, p. 035110, Jan 2018.

[85] M. Sing, G. Berner, K. Goß, A. Müller, A. Ruff, A. Wetscherek, S. Thiel, J. Mannhart, S. A. Pauli, C. W. Schneider, P. R. Willmott, M. Gorgoi, F. Schäfers, and R. Claessen, "Profiling the interface electron gas of $LaAlO_3/SrTiO_3$ heterostructures with hard x-ray photoelectron spectroscopy," *Physical Review Lett.*, vol. 102, p. 176805, Apr 2009.

[86] G. Berner, S. Glawion, J. Walde, F. Pfaff, H. Hollmark, L.-C. Duda, S. Paetel, C. Richter, J. Mannhart, M. Sing, and R. Claessen, "$laalo_3/srtio_3$ oxide heterostructures studied by resonant inelastic x-ray scattering," *Physical Review B*, vol. 82, p. 241405, Dec 2010.

[87] S. Thiel, G. Hammerl, A. Schmehl, C. Schneider, and J. Mannhart, "Tunable quasi-two-dimensional electron gases in oxide heterostructures," *Science*, vol. 313, no. 5795, pp. 1942–1945, 2006.

[88] M. Huijben, G. Rijnders, D. H. A. Blank, S. Bals, S. V. Aert, J. Verbeeck, G. V. Tendeloo, A. Brinkman, and H. Hilgenkamp, "Electronically coupled complementary interfaces between perovskite band insulators," *Nature Materials*, vol. 5, p. 556, 2006.

[89] R. Pentcheva, M. Huijben, K. Otte, W. E. Pickett, J. E. Kleibeuker, J. Huijben, H. Boschker, D. Kockmann, W. Siemons, G. Koster, H. J. W. Zandvliet, G. Rijnders, D. H. A. Blank, H. Hilgenkamp, and A. Brinkman, "Parallel electron-hole bilayer conductivity from electronic interface reconstruction," *Physical Review Lett.*, vol. 104, p. 166804, Apr 2010.

[90] V. N. Strocov and C. Cancellieri, eds., *Spectroscopy of Complex Oxide Interfaces*. Springer, 2018.

[91] G. Herranz, M. Basletić, M. Bibes, C. Carrétéro, E. Tafra, E. Jacquet, K. Bouzehouane, C. Deranlot, A. Hamzić, J.-M. Broto, A. Barthélémy, and A. Fert, "High mobility in $LaAlO_3/SrTiO_3$ heterostructures: Origin, dimensionality, and perspectives," *Physical Review Lett.*, vol. 98, p. 216803, May 2007.

[92] K. Yoshimatsu, R. Yasuhara, H. Kumigashira, and M. Oshima, "Origin of metallic states at the heterointerface between the band insulators $LaAlO_3$ and $SrTiO_3$," *Physical Review Lett.*, vol. 101, p. 026802, Jul 2008.

[93] M. Basletic, J.-L. Maurice, C. Carrétéro, G. Herranz, O. Copie, M. Bibes, É. Jacquet, K. Bouzehouane, S. Fusil, and A. Barthélémy, "Mapping the spatial distribution of charge carriers in $LaAlO_3/SrTiO_3$ heterostructures," *Nature materials*, vol. 7, no. 8, p. 621, 2008.

[94] O. Copie, V. Garcia, C. Bödefeld, C. Carrétéro, M. Bibes, G. Herranz, E. Jacquet, J.-L. Maurice, B. Vinter, S. Fusil, K. Bouzehouane, H. Jaffrès, and A. Barthélémy, "Towards two-dimensional metallic behavior at $LaAlO_3/SrTiO_3$ interfaces," *Physical Review Lett.*, vol. 102, p. 216804, May 2009.

[95] T. Fix, F. Schoofs, J. L. MacManus-Driscoll, and M. G. Blamire, "Charge confinement and doping at $LaAlO_3/SrTiO_3$ interfaces," *Physical Review Lett.*, vol. 103, p. 166802, Oct 2009.

[96] A. Dubroka, M. Rössle, K. W. Kim, V. K. Malik, L. Schultz, S. Thiel, C. W. Schneider, J. Mannhart, G. Herranz, O. Copie, M. Bibes, A. Barthélémy, and C. Bernhard, "Dynamical response and confinement of the electrons at the $LaAlO_3/SrTiO_3$ interface," *Physical Review Lett.*, vol. 104, p. 156807, Apr 2010.

[97] M. Salluzzo, J. C. Cezar, N. B. Brookes, V. Bisogni, G. M. De Luca, C. Richter, S. Thiel, J. Mannhart, M. Huijben, A. Brinkman, G. Rijnders, and G. Ghiringhelli, "Orbital reconstruction and the two-dimensional electron gas at the $LaAlO_3/SrTiO_3$ interface," *Physical Review Lett.*, vol. 102, p. 166804, Apr 2009.

[98] H. Chen, A. M. Kolpak, and S. Ismail-Beigi, "Fundamental asymmetry in interfacial electronic reconstruction between insulating oxides: An *ab initio* study," *Physical Review B*, vol. 79, p. 161402, Apr 2009.

[99] W.-j. Son, E. Cho, B. Lee, J. Lee, and S. Han, "Density and spatial distribution of charge carriers in the intrinsic n-type $LaAlO_3$-$SrTiO_3$ interface," *Physical Review B*, vol. 79, p. 245411, Jun 2009.

[100] R. Pentcheva and W. E. Pickett, "Charge localization or itineracy at $LaAlO_3/SrTiO_3$ interfaces: Hole polarons, oxygen vacancies, and mobile electrons," *Physical Review B*, vol. 74, p. 035112, Jul 2006.

[101] Z. S. Popović, S. Satpathy, and R. M. Martin, "Origin of the two-dimensional electron gas carrier density at the $LaAlO_3$ on $SrTiO_3$ interface," *Physical Review Lett.*, vol. 101, p. 256801, Dec 2008.

[102] P. W. Anderson, "Absence of diffusion in certain random lattices," *Physical Review*, vol. 109, pp. 1492–1505, Mar 1958.

[103] K. Janicka, J. P. Velev, and E. Y. Tsymbal, "Quantum nature of two-dimensional electron gas confinement at $LaAlO_3/SrTiO_3$ interfaces," *Physical Review Lett.*, vol. 102, p. 106803, Mar 2009.

[104] M. Stengel, "First-principles modeling of electrostatically doped perovskite systems," *Physical review letters*, vol. 106, no. 13, p. 136803, 2011.

[105] N. Reyren, S. Thiel, A. D. Caviglia, L. F. Kourkoutis, G. Hammerl, C. Richter, C. W. Schneider, T. Kopp, A.-S. Rüetschi, D. Jaccard, M. Gabay, D. A. Muller, J.-M. Triscone, and J. Mannhart, "Superconducting interfaces between insulating oxides," *Science*, vol. 317, no. 5842, pp. 1196–1199, 2007.

[106] S. Gariglio, N. Reyren, A. D. Caviglia, and J.-M. Triscone, "Superconductivity at the $LaAlO_3/SrTiO_3$ interface," *Journal of Physics: Condensed Matter*, vol. 21, no. 16, p. 164213, 2009.

[107] A. D. Caviglia, S. Gariglio, N. Reyren, D. Jaccard, T. Schneider, M. Gabay, S. Thiel, G. Hammerl, J. Mannhart, and J.-M. Triscone, "Electric field control of the $LaAlO_3/SrTiO_3$ interface ground state," *Nature*, vol. 456, no. 7222, p. 624, 2008.

[108] A. Brinkman, M. Huijben, M. van Zalk, J. Huijben, U. Zeitler, J. C. Maan, W. G. van der Wiel, G. Rijnders, D. H. A. Blank, and H. Hilgenkamp, "Magnetic effects at the interface between non-magnetic oxides," *Nature Materials*, vol. 6, 2007.

[109] M. Ben Shalom, M. Sachs, D. Rakhmilevitch, A. Palevski, and Y. Dagan, "Tuning spin-orbit coupling and superconductivity at the $SrTiO_3/LaAlO_3$ interface: A magnetotransport study," *Physical Review Lett.*, vol. 104, p. 126802, Mar 2010.

[110] X. Wang, W. M. Lü, A. Annadi, Z. Q. Liu, K. Gopinadhan, S. Dhar, T. Venkatesan, and Ariando, "Magnetoresistance of two-dimensional and three-dimensional electron gas in $LaAlO_3/SrTiO_3$ heterostructures: Influence of magnetic ordering, interface scattering, and dimensionality," *Physical Review B*, vol. 84, p. 075312, Aug 2011.

[111] E. Flekser, M. Ben Shalom, M. Kim, C. Bell, Y. Hikita, H. Y. Hwang, and Y. Dagan, "Magnetotransport effects in polar versus non-polar $SrTiO_3$ based heterostructures," *Physical Review B*, vol. 86, p. 121104, Sep 2012.

[112] L. Li, C. Richter, J. Mannhart, and R. Ashoori, "Coexistence of magnetic order and two-dimensional superconductivity at $LaAlO_3/SrTiO_3$ interfaces," *Nature physics*, vol. 7, no. 10, p. 762, 2011.

[113] J. A. Bert, B. Kalisky, C. Bell, M. Kim, Y. Hikita, H. Y. Hwang, and K. A. Moler, "Direct imaging of the coexistence of ferromagnetism and superconductivity at the $LaAlO_3/SrTiO_3$ interface," *Nature physics*, vol. 7, no. 10, p. 767, 2011.

[114] X. Ariando andWang, G. Baskaran, Z. Liu, J. Huijben, J. Yi, A. Annadi, A. R. Barman, A. Rusydi, S. Dhar, Y. Feng, *et al.*, "Electronic phase separation at the $LaAlO_3/SrTiO_3$ interface," *Nature communications*, vol. 2, p. 188, 2011.

[115] J.-L. Maurice, C. Carrétéro, M.-J. Casanove, K. Bouzehouane, S. Guyard, É. Larquet, and J.-P. Contour, "Electronic conductivity and structural distortion at the interface between insulators $SrTiO_3$ and $LaAlO_3$," *physica status solidi (a)*, vol. 203, no. 9, pp. 2209–2214, 2006.

[116] S. A. Pauli, S. J. Leake, B. Delley, M. Björck, C. W. Schneider, C. M. Schlepütz, D. Martoccia, S. Paetel, J. Mannhart, and P. R. Willmott, "Evolution of the interfacial structure of $LaAlO_3$ on $SrTiO_3$," *Physical Review Lett.*, vol. 106, p. 036101, Jan 2011.

[117] N. C. Bristowe, P. B. Littlewood, and E. Artacho, "Surface defects and conduction in polar oxide heterostructures," *Physical Review B*, vol. 83, p. 205405, May 2011.

[118] J. Lee and A. A. Demkov, "Charge origin and localization at the n-type $SrTiO_3/LaAlO_3$ interface," *Physical Review B*, vol. 78, p. 193104, Nov 2008.

[119] I. Piyanzina, T. Kopp, Y. V. Lysogorskiy, D. Tayurskii, and V. Eyert, "Electronic properties of $LaAlO_3/SrTiO_3$ n-type interfaces: a GGA+U study," *Journal of Physics: Condensed Matter*, vol. 29, no. 9, p. 095501, 2017.

[120] G. Berner, M. Sing, H. Fujiwara, A. Yasui, Y. Saitoh, A. Yamasaki, Y. Nishitani, A. Sekiyama, N. Pavlenko, T. Kopp, C. Richter, J. Mannhart, S. Suga, and R. Claessen, "Direct k-space mapping of the electronic structure in an oxide-oxide interface," *Physical Review Lett.*, vol. 110, p. 247601, Jun 2013.

[121] N. Plumb, M. Kobayashi, M. Salluzzo, E. Razzoli, C. Matt, V. Strocov, K. Zhou, M. Shi, J. Mesot, T. Schmitt, L. Patthey, and M. Radović, "Evolution of the $SrTiO_3$ surface electronic state as a function of $LaAlO_3$ overlayer thickness," *Applied Surface Science*, vol. 412, pp. 271 – 278, 2017.

[122] M. Huijben, D. Kockmann, J. Huijben, J. E. Kleibeuker, A. van Houselt, G. Koster, D. H. A. Blank, H. Hilgenkamp, G. Rijnders, A. Brinkman, and H. J. W. Zandvliet, "Local probing of coupled interfaces between two-dimensional electron and hole gases in oxide heterostructures by variable-temperature scanning tunneling spectroscopy," *Physical Review B*, vol. 86, p. 035140, Jul 2012.

[123] H. Lee, N. Campbell, J. Lee, T. Asel, T. Paudel, H. Zhou, J. Lee, B. Noesges, J. Seo, B. Park, *et al.*, "Direct observation of a two-dimensional hole gas at oxide interfaces," *Nature materials*, vol. 17, no. 3, p. 231, 2018.

[124] A. Kalabukhov, Y. A. Boikov, I. Serenkov, V. Sakharov, J. Börjesson, N. Ljustina, E. Olsson, D. Winkler, and T. Claeson, "Improved cationic stoichiometry and insulating behavior at the interface of $LaAlO_3/SrTiO_3$ formed at high oxygen pressure during pulsed-laser deposition," *EPL (Europhysics Letters)*, vol. 93, no. 3, p. 37001, 2011.

[125] T. Okuda, K. Nakanishi, S. Miyasaka, and Y. Tokura, "Large thermoelectric response of metallic perovskites: $Sr_{1-x}La_xTiO_3$ ($0 \leqslant x \leqslant 0.1$)," *Physical Review B*, vol. 63, p. 113104, Mar 2001.

[126] A. Kalabukhov, R. Gunnarsson, J. Börjesson, E. Olsson, T. Claeson, and D. Winkler, "Effect of oxygen vacancies in the $SrTiO_3$ substrate on the electrical properties of the $LaAlO_3$ interface," *Physical Review B*, vol. 75, p. 121404, Mar 2007.

[127] W. Siemons, G. Koster, H. Yamamoto, W. A. Harrison, G. Lucovsky, T. H. Geballe, D. H. A. Blank, and M. R. Beasley, "Origin of charge density at $LaAlO_3$ on $SrTiO_3$ heterointerfaces: Possibility of intrinsic doping," *Physical Review Lett.*, vol. 98, p. 196802, May 2007.

[128] Y. Li, S. N. Phattalung, S. Limpijumnong, J. Kim, and J. Yu, "Formation of oxygen vacancies and charge carriers induced in the n-type interface of a $LaAlO_3$ overlayer on $SrTiO_3$(001)," *Physical Review B*, vol. 84, p. 245307, Dec 2011.

[129] C. Freysoldt, B. Grabowski, T. Hickel, J. Neugebauer, G. Kresse, A. Janotti, and C. G. Van de Walle, "First-principles calculations for point defects in solids," *Rev. Mod. Phys.*, vol. 86, pp. 253–305, Mar 2014.

[130] N. C. Bristowe, P. Ghosez, P. B. Littlewood, and E. Artacho, "The origin of two-dimensional electron gases at oxide interfaces: insights from theory," *Journal of Physics: Condensed Matter*, vol. 26, p. 143201, mar 2014.

[131] A. Koitzsch, J. Ocker, M. Knupfer, M. C. Dekker, K. Dörr, B. Büchner, and P. Hoffmann, "In-gap electronic structure of $LaAlO_3$-$SrTiO_3$ heterointerfaces investigated by soft x-ray spectroscopy," *Physical Review B*, vol. 84, p. 245121, Dec 2011.

[132] Z. Ristic, R. Di Capua, F. Chiarella, G. M. De Luca, I. Maggio-Aprile, M. Radovic, and M. Salluzzo, "Photodoping and in-gap interface states across the metal-insulator transition in $LaAlO_3/SrTiO_3$ heterostructures," *Physical Review B*, vol. 86, p. 045127, Jul 2012.

[133] S. A. Chambers, M. H. Engelhard, V. Shutthanandan, Z. Zhu, T. C. Droubay, L. Qiao, P. Sushko, T. Feng, H. D. Lee, T. Gustafsson, *et al.*, "Instability, intermixing and electronic structure at the epitaxial $LaAlO_3/SrTiO_3$ (001) heterojunction," *Surface Science Reports*, vol. 65, no. 10-12, pp. 317–352, 2010.

[134] L. Qiao, T. C. Droubay, V. Shutthanandan, Z. Zhu, P. Sushko, and S. A. Chambers, "Thermodynamic instability at the stoichiometric $LaAlO_3/SrTiO_3$ (001) interface," *Journal of Physics: Condensed Matter*, vol. 22, no. 31, p. 312201, 2010.

[135] P. R. Willmott, S. A. Pauli, R. Herger, C. M. Schlepütz, D. Martoccia, B. D. Patterson, B. Delley, R. Clarke, D. Kumah, C. Cionca, and Y. Yacoby, "Structural basis for the conducting interface between $LaAlO_3$ and $SrTiO_3$," *Physical Review Lett.*, vol. 99, p. 155502, Oct 2007.

[136] F. Gunkel, S. Hoffmann-Eifert, R. Dittmann, S. Mi, C. Jia, P. Meuffels, and R. Waser, "High temperature conductance characteristics of $LaAlO_3/SrTiO_3$-heterostructures under equilibrium oxygen atmospheres," *Applied Physics Letters*, vol. 97, no. 1, p. 012103, 2010.

[137] A. S. Kalabukhov, Y. A. Boikov, I. T. Serenkov, V. I. Sakharov, V. N. Popok, R. Gunnarsson, J. Börjesson, N. Ljustina, E. Olsson, D. Winkler, and T. Claeson, "Cationic disorder and phase segregation in $LaAlO_3/SrTiO_3$ heterointerfaces evidenced by medium-energy ion spectroscopy," *Physical Review Lett.*, vol. 103, p. 146101, Sep 2009.

[138] V. Vonk, J. Huijben, D. Kukuruznyak, A. Stierle, H. Hilgenkamp, A. Brinkman, and S. Harkema, "Polar-discontinuity-retaining *a*-site intermixing and vacancies at $SrTiO_3/LaAlO_3$ interfaces," *Physical Review B*, vol. 85, p. 045401, Jan 2012.

[139] D. C. Vaz, E. Lesne, A. Sander, H. Naganuma, E. Jacquet, J. Santamaria, A. Barthélémy, and M. Bibes, "Tuning up or down the critical thickness in $LaAlO_3/SrTiO_3$ through *in situ* deposition of metal overlayers," *Advanced Materials*, vol. 29, no. 28, p. 1700486, 2017.

[140] C. Cancellieri, M. L. Reinle-Schmitt, M. Kobayashi, V. N. Strocov, T. Schmitt, P. R. Willmott, S. Gariglio, and J.-M. Triscone, "Interface Fermi States of

$LaAlO_3/SrTiO_3$ and related heterostructures," *Physical Review Lett.*, vol. 110, p. 137601, Mar 2013.

[141] D. Li, S. Lemal, S. Gariglio, Z. Wu, A. Fête, M. Boselli, P. Ghosez, and J.-M. Triscone, "Probing quantum confinement and electronic structure at polar oxide interfaces," *Advanced Science*, vol. 5, no. 8, p. 1800242, 2018.

[142] M. Caputo, M. Boselli, A. Filippetti, S. Lemal, D. Li, A. Chickina, C. Cancellieri, T. Schmitt, J.-M. Triscone, P. Ghosez, S. Gariglio, and V. N. Strocov, "Artificial quantum confinement in $LaAlO_3/SrTiO_3$ heterostructures," *arXiv preprint arXiv:1903.10994*, 2019.

[143] A. Fête, C. Cancellieri, D. Li, D. Stornaiuolo, A. Caviglia, S. Gariglio, and J.-M. Triscone, "Growth-induced electron mobility enhancement at the $LaAlO_3/SrTiO_3$ interface," *Applied Physics Letters*, vol. 106, no. 5, p. 51604, 2015.

[144] C. Cancellieri, N. Reyren, S. Gariglio, A. Caviglia, A. Fête, and J.-M. Triscone, "Influence of the growth conditions on the $LaAlO_3/SrTiO_3$ interface electronic properties," *EPL (Europhysics Letters)*, vol. 91, no. 1, p. 17004, 2010.

[145] F. Stern, "Self-consistent results for n-type Si inversion layers," *Physical Review B*, vol. 5, pp. 4891–4899, Jun 1972.

[146] A. Fête, *Magnetotransport experiments at the* $LaAlO_3/SrTiO_3$ *interface.* PhD thesis, Université de Genève, 2014.

[147] N. Reyren, S. Gariglio, A. Caviglia, D. Jaccard, T. Schneider, and J.-M. Triscone, "Anisotropy of the superconducting transport properties of the $LaAlO_3/SrTiO_3$ interface," *Applied Physics Letters*, vol. 94, no. 11, p. 112506, 2009.

[148] M. Tinkham, "Introduction to superconductivity," 2012.

[149] S. Gariglio, M. Gabay, and J.-M. Triscone, "Research update: Conductivity and beyond at the $LaAlO_3/SrTiO_3$ interface," *APL Materials*, vol. 4, no. 6, p. 060701, 2016.

[150] A. Janotti, L. Bjaalie, L. Gordon, and C. G. Van de Walle, "Controlling the density of the two-dimensional electron gas at the $SrTiO_3/LaAlO_3$ interface," *Physical Review B*, vol. 86, p. 241108, Dec 2012.

[151] T. Yamamoto and T. Mizoguchi, "Importance of fermi energy for understanding the intermixing behavior at the $LaAlO_3/SrTiO_3$ heterointerface," *Applied Physics Letters*, vol. 105, no. 20, p. 201604, 2014.

[152] A. Reshak, M. Abu-Jafar, and Y. Al-Douri, "Two symmetric n-type interfaces $SrTiO_3/LaAlO_3$ in perovskite: Electronic properties from density functional theory," *Journal of Applied Physics*, vol. 119, no. 24, p. 245303, 2016.

[153] M. Gu, J. Wang, X. Wu, and G. Zhang, "Stabilities of the intrinsic defects on $SrTiO_3$ surface and $SrTiO_3/LaAlO_3$ interface," *The Journal of Physical Chemistry C*, vol. 116, no. 47, pp. 24993–24998, 2012.

[154] C. S. Koonce, M. L. Cohen, J. F. Schooley, W. R. Hosler, and E. R. Pfeiffer, "Superconducting transition temperatures of semiconducting $SrTiO_3$," *Physical Review*, vol. 163, pp. 380–390, Nov 1967.

[155] A. Raslan, P. Lafleur, and W. A. Atkinson, "Temperature-dependent band structure of $SrTiO_3$ interfaces," *Physical Review B*, vol. 95, p. 054106, Feb 2017.

[156] K. Ueno, T. Nojima, S. Yonezawa, M. Kawasaki, Y. Iwasa, and Y. Maeno, "Effective thickness of two-dimensional superconductivity in a tunable triangular quantum well of $SrTiO_3$," *Physical Review B*, vol. 89, p. 020508, Jan 2014.

[157] D. Valentinis, S. Gariglio, A. Fête, J.-M. Triscone, C. Berthod, and D. van der Marel, "Modulation of the superconducting critical temperature due to quantum confinement at the $LaAlO_3/SrTiO_3$ interface," *Physical Review B*, vol. 96, p. 094518, Sep 2017.

[158] V. Strocov, X. Wang, M. Shi, M. Kobayashi, J. Krempasky, C. Hess, T. Schmitt, and L. Patthey, "Soft-X-ray ARPES facility at the ADRESS beamline of the SLS: Concepts, technical realisation and scientific applications," *Journal of synchrotron radiation*, vol. 21, no. 1, pp. 32–44, 2014.

[159] M. P. Seah and W. Dench, "Quantitative electron spectroscopy of surfaces: A standard data base for electron inelastic mean free paths in solids," *Surface and interface analysis*, vol. 1, no. 1, pp. 2–11, 1979.

[160] C. Cancellieri, A. S. Mishchenko, U. Aschauer, A. Filippetti, C. Faber, O. Barišić, V. Rogalev, T. Schmitt, N. Nagaosa, and V. N. Strocov, "Polaronic metal state at the $LaAlO_3/SrTiO_3$ interface," *Nature communications*, vol. 7, p. 10386, 2016.

[161] V. Strocov, "Photoemission response of 2D electron states," *Journal of Electron Spectroscopy and Related Phenomena*, vol. 229, pp. 100–107, 2018.

[162] Z. Wang, S. M. Walker, A. Tamai, Y. Wang, Z. Ristic, F. Y. Bruno, A. De La Torre, S. Riccò, N. Plumb, M. Shi, P. Hlawenka, J. Sánchez-Barriga, A. Varykhalov, T. K. Kim, M. Hoesch, P. D. C. King, W. Meevasana, U. Diebold, J. Mesot, B. Moritz, T. P. Devereaux, M. Radovic, and F. Baumberger, "Tailoring the nature and strength of electron-phonon interactions in the $SrTiO_3$ (001) 2D electron liquid," *Nature materials*, vol. 15, no. 8, p. 835, 2016.

[163] C. Chen, J. Avila, E. Frantzeskakis, A. Levy, and M. C. Asensio, "Observation of a two-dimensional liquid of Fröhlich polarons at the bare $SrTiO_3$ surface," *Nature communications*, vol. 6, p. 8585, 2015.

[164] Z. Wang, Z. Zhong, S. McKeown Walker, Z. Ristic, J.-Z. Ma, F. Y. Bruno, S. Riccò, G. Sangiovanni, G. Eres, N. C. Plumb, *et al.*, "Atomically precise lateral modulation of a two-dimensional electron liquid in anatase TiO_2 thin films," *Nano letters*, vol. 17, no. 4, pp. 2561–2567, 2017.

[165] E. Maniv, M. B. Shalom, A. Ron, M. Mograbi, A. Palevski, M. Goldstein, and Y. Dagan, "Strong correlations elucidate the electronic structure and phase diagram of $LaAlO_3/SrTiO_3$ interface," *Nature communications*, vol. 6, p. 8239, 2015.

[166] A. E. M. Smink, J. C. de Boer, M. P. Stehno, A. Brinkman, W. G. van der Wiel, and H. Hilgenkamp, "Gate-tunable band structure of the $LaAlO_3{-}SrTiO_3$ interface," *Physical Review Lett.*, vol. 118, p. 106401, Mar 2017.

[167] Y. Xie, Y. Hikita, C. Bell, and H. Y. Hwang, "Control of electronic conduction at an oxide heterointerface using surface polar adsorbates," *Nature communications*, vol. 2, p. 494, 2011.

[168] W. Dai, S. Adhikari, A. C. Garcia-Castro, A. H. Romero, H. Lee, J.-W. Lee, S. Ryu, C.-B. Eom, and C. Cen, "Tailoring $LaAlO_3/SrTiO_3$ interface metallicity by oxygen surface adsorbates," *Nano letters*, vol. 16, no. 4, pp. 2739–2743, 2016.

[169] K. A. Brown, S. He, D. J. Eichelsdoerfer, M. Huang, I. Levy, H. Lee, S. Ryu, P. Irvin, J. Mendez-Arroyo, C.-B. Eom, *et al.*, "Giant conductivity switching of $LaAlO_3/SrTiO_3$ heterointerfaces governed by surface protonation," *Nature communications*, vol. 7, p. 10681, 2016.

[170] E. Lesne, N. Reyren, D. Doennig, R. Mattana, H. Jaffrès, V. Cros, F. Petroff, F. Choueikani, P. Ohresser, R. Pentcheva, A. Barthélémy, and M. Bibes, "Suppression of the critical thickness threshold for conductivity at the $LaAlO_3/SrTiO_3$ interface," *Nature communications*, vol. 5, p. 4291, 2014.

[171] A. K. Singh, T.-C. Wu, M.-C. Chen, M.-Y. Song, W.-L. Lee, C.-P. Su, and M.-W. Chu, "Influence of $SrTiO_3$ capping layer on the charge transport at the interfaces of $SrTiO_3/LaAlO_3/SrTiO_3$ (100) heterostructure," *Physical Review Materials*, vol. 2, p. 114009, Nov 2018.

[172] E. Heifets, R. Eglitis, E. Kotomin, J. Maier, and G. Borstel, "First-principles calculations for $SrTiO_3$ (100) surface structure," *Surface science*, vol. 513, no. 1, pp. 211–220, 2002.

[173] I. Tamm, "On the possible bound states of electrons on a crystal surface," *Phys. Z. Sowjetunion*, vol. 1, p. 733, 1932.

[174] M. Saghayezhian, S. M. Rezaei Sani, J. Zhang, and E. W. Plummer, "Rumpling and enhanced covalency at the $SrTiO_3$(001) surface," *The Journal of Physical Chemistry C*, vol. XX, no. X, p. XXXX, 2019.

[175] R. S. Mulliken, "Electronic population analysis on lcao-mo molecular wave functions," *The Journal of Chemical Physics*, vol. 23, no. 10, pp. 1833–1840, 1955.

[176] A. R. Silva and G. M. Dalpian, "Oxygen vacancies at the surface of $SrTiO_3$ thin films," *Journal of Applied Physics*, vol. 115, no. 3, p. 033710, 2014.

[177] N. C. Plumb, M. Salluzzo, E. Razzoli, M. Månsson, M. Falub, J. Krempasky, C. E. Matt, J. Chang, M. Schulte, J. Braun, H. Ebert, J. Minár, B. Delley, K.-J. Zhou, T. Schmitt, M. Shi, J. Mesot, L. Patthey, and M. Radović, "Mixed dimensionality of confined conducting electrons in the surface region of $SrTiO_3$," *Physical Review Lett.*, vol. 113, p. 086801, Aug 2014.

[178] L. Dudy, M. Sing, P. Scheiderer, J. D. Denlinger, P. Schütz, J. Gabel, M. Buchwald, C. Schlueter, T.-L. Lee, and R. Claessen, "In situ control of separate electronic phases on $SrTiO_3$ surfaces by oxygen dosing," *Advanced Materials*, vol. 28, no. 34, pp. 7443–7449, 2016.

[179] S. Cook, M. T. Dylla, R. A. Rosenberg, Z. R. Mansley, G. J. Snyder, L. D. Marks, and D. D. Fong, "The vacancy-induced electronic structure of the $SrTiO_{3-\delta}$ surface," *Advanced Electronic Materials*, vol. 5, no. 1, p. 1800460, 2019.

[180] Y. He, X. Yu, Y. Wang, H. Li, and X. Huang, "Alumina-coated patterned amorphous silicon as the anode for a lithium-ion battery with high coulombic efficiency," *Advanced Materials*, vol. 23, no. 42, pp. 4938–4941, 2011.

[181] C. M. Burt, X. Piao, F. Gaudi, B. Busch, and N. Taufik, "Electric motor efficiency under variable frequencies and loads," *Journal of irrigation and drainage engineering*, vol. 134, no. 2, pp. 129–136, 2008.

[182] M. L. Baglione, *Development of System Analysis Methodologies and Tools for Modeling and Optimizing Vehicle System Efficiency.* PhD thesis, University of Michigan, 2007.

[183] H. Ritchie and M. Roser, "Energy production & changing energy sources." `http://web.archive.org/web/20080207010024/http://www.808multimedia.com/winnt/kernel.htm`, 2019. Accessed: 2019-01-09.

[184] V. Smil, *Energy Transitions: Global and National Perspectives.* BP Statistical Review of World Energy, 2017.

[185] W. van Sark, "Feasibility of photovoltaic − thermoelectric hybrid modules," *Applied Energy*, vol. 88, no. 8, pp. 2785 – 2790, 2011.

[186] "Photography of a Voyager probe, from the NASA." `https://voyager.jpl.nasa.gov/galleries/images-of-voyager/`. Accessed: 10-19-2018.

[187] G. Nolas, J.Sharp, and H.J.Goldsmid, *Thermoelectrics - Basic Principles and New Materials Developments.* Springer Science & and Business Media, 2001.

[188] R. Franz and G. Wiedemann, "Ueber die wärme-leitungsfähigkeit der metalle," *Annalen der Physik*, vol. 165, no. 8, pp. 497–531, 1853.

[189] L. D. Hicks and M. S. Dresselhaus, "Effect of quantum-well structures on the thermoelectric figure of merit," *Physical Review B*, vol. 47, p. 12727, 1993.

[190] L. D. Hicks and M. S. Dresselhaus, "Thermoelectric figure of merit of a one-dimensional conductor," *Physical Review B*, vol. 47, pp. 16631–16634, Jun 1993.

[191] H. Ohta, Y. Mune, K. Koumoto, T. Mizoguchi, and Y. Ikuhara, "Critical thickness for giant thermoelectric Seebeck coefficient of 2DEG confined in $SrTiO_3/SrTi_{0.8}Nb_{0.2}O_3$ superlattices," *Thin Solid Films*, vol. 516, no. 17, pp. 5916–5920, 2008.

[192] D. I. Bilc and P. Ghosez, "Electronic and thermoelectric properties of Fe_2VAl: The role of defects and disorder," *Physical Review B*, vol. 83, p. 205204, 2011.

[193] R. Venkatasubramanian, E. Siivola, T. Colpitts, and B. O'Quinn, "Thin-film thermoelectric devices with high room-temperature figures of merit," *Nature*, vol. 413, p. 597, 2001.

[194] L.-D. Zhao, S.-H. Lo, Y. Zhang, H. Sun, G. Tan, C. Uher, C. Wolverton, V. P. Dravid, and M. G. Kanatzidis, "Ultralow thermal conductivity and high thermoelectric figure of merit in SnSe crystals," *Nature*, vol. 508, p. 373, 2014.

[195] L.-D. Zhao, C. Chang, G. Tan, and M. G. Kanatzidis, "SnSe: a remarkable new thermoelectric material," *Energy Environ. Sci.*, vol. 9, pp. 3044–3060, 2016.

[196] M. G. Kanatzidis, "Nanostructured thermoelectrics: The new paradigm ?," *Chemistry of Materials*, vol. 22, no. 3, pp. 648–659, 2010.

[197] G. Tan, L.-D. Zhao, and M. G. Kanatzidis, "Rationally designing high-performance bulk thermoelectric materials," *Chemical Reviews*, vol. 116, no. 19, pp. 12123–12149, 2016.

[198] Y. Pei, X. Shi, A. LaLonde, H. Wang, L. Chen, and G. J. Snyder, "Convergence of electronic bands for high performance bulk thermoelectrics," *Nature*, vol. 473, p. 66, 2011.

[199] G. D. Mahan and J. O. Sofo, "The best thermoelectric," *Proceedings of the National Academy of Sciences*, vol. 93, no. 15, pp. 7436–7439, 1996.

[200] D. Parker, X. Chen, and D. J. Singh, "High three-dimensional thermoelectric performance from low-dimensional bands," *Physical Review Lett.*, vol. 110, p. 146601, Apr 2013.

[201] S. Yabuuchi, M. Okamoto, A. Nishide, Y. Kurosaki, and J. Hayakawa, "Large Seebeck coefficients of Fe_2TiSn and Fe_2TiSi : First-principles study," *Applied Physics Express*, vol. 6, pp. 025504–1, 2013.

[202] S. Thébaud, C. Adessi, S. Pailhès, and G. Bouzerar, "Boosting the power factor with resonant states: A model study," *Physical Review B*, vol. 96, p. 075201, Aug 2017.

[203] J. P. Heremans, B. Wiendlocha, and A. M. Chamoire, "Resonant levels in bulk thermoelectric semiconductors," *Energy Environ. Sci.*, vol. 5, pp. 5510–5530, 2012.

[204] C. Wood, "Materials for thermoelectric energy conversion," *Reports on Progress in Physics*, vol. 51, no. 4, p. 459, 1988.

[205] G. J. Snyder and E. S. Toberer, "Complex thermoelectric materials," *Nature Materials*, vol. 7, 2008.

[206] S. Lemal, J. Varignon, D. I. Bilc, and P. Ghosez, "Thermoelectric properties of layered calcium cobaltite $Ca_3Co_4O_9$ from hybrid functional first-principles calculations," *Physical Review B*, vol. 95, p. 075205, Feb 2017.

[207] D. I. Bilc, C. G. Floare, L. P. Zarbo, S. Garabagiu, S. Lemal, and P. Ghosez, "First-principles modeling of $SrTiO_3$ based oxides for thermoelectric applications," *The Journal of Physical Chemistry C*, vol. 120, no. 45, pp. 25678–25688, 2016.

[208] I. Terasaki and N. Murayama, "Oxide thermoelectrics," 2002.

[209] A. C. Masset, C. Michel, A. Maignan, M. Hervieu, O. Toulemonde, F. Studer, B. Raveau, and J. Hejtmanek, "Misfit-layered cobaltite with an anisotropic giant magnetoresistance: $Ca_3Co_4O_9$," *Physical Review B*, vol. 62, p. 166, 2000.

[210] P. García-Fernández, M. Verissimo-Alves, D. I. Bilc, P. Ghosez, and J. Junquera, "First-principles modeling of the thermoelectric properties of $SrTiO_3/SrRuO_3$ superlattices," *Physical Review B*, p. 85305, 2012.

[211] M. Ohtaki, T. Tsubota, K.Eguchi, and A. Toxen, "High-temperature thermoelectric properties of $(Zn_{1-x}Al_x)O$," *Physical of Applied Physics*, vol. 79, p. 1816, 1996.

[212] C. Press, ed., *CRC Handbook of Thermoelectrics*. D. M. Rowe, 1995.

[213] J. Sugiyama, J. H. Brewer, E. J. Ansaldo, H. Itahara, K. Dohmae, Y. Seno, C. Xia, and T. Tani, "Hidden magnetic transitions in thermoelectric layered cobaltite $[Ca_2CoO_3]_{0.62}[CoO_2]$," *Physical Review B*, vol. 68, p. 134423, 2003.

[214] J. Sugiyama, C. Xia, and T. Tani, "Anisotropic magnetic properties of $Ca_3Co_4O_9$: Evidence for a spin-density-wave transition at 27 K," *Physical Review B*, vol. 67, p. 104410, 2003.

[215] Y. Miyazaki, K. Kudo, M. Akoshima, and Y. Ono, "Low-temperature thermoelectric properties of the composite crystal $[Ca_2CoO_3]_{0.62}[CoO_2]$," *Japanese Journal of Applied Physics*, vol. 39, p. 531, 2000.

[216] T. Wu, T. A. Tyson, H. Chen, J. Bai, H. Wangf, and C. jaye, "A structural change in $Ca_3Co_4O_9$ associated with enhanced thermoelectric properties," *Journal of physics : Condensed Matter*, vol. 24, p. 455602, 2012.

[217] T. T. *et al*, "Contribution of electronic structure to the large thermoelectric power in layered cobalt oxides," *Physical Review B*, vol. 69, p. 125410, 2004.

[218] T. Takeuchi, T. Kondo, T. Kitao, K. Soda, M. Shikano, R. Funahashi, M. Mikami, and U. Mizutani, "Electronic structure near the fermi level in the $Ca_3Co_4O_9$ layered cobalt oxide," *Journal of Electron Spectroscopy and Related Phenomena*, vol. 144, p. 849, 2005.

[219] D. Kenfaui, D. Chateigner, M. Gomina, J. G. Noudem, B. Ouladdiaf, A. Dauscher, and B. Lenoir, "Volume texture and anisotropic thermoelectric properties in $Ca_3Co_4O_9$ bulk materials," *Materials Today: Proceedings*, vol. 2, pp. 637–646, 2015.

[220] R. Asahi, J. Sugiyama, and T. Tani, "Electronic structure of misfit-layered calcium cobaltite," *Physical Review B*, vol. 66, p. 155103, 2002.

[221] A. Rébola, R. Klie, P. Zapol, and S. Ögüt, "First-principles study of the atomic and electronic structures of misfit-layered calcium cobaltite $(Ca_2CoO_3)(CoO_2)_{1.62}$ using rational approximants," *Physical Review B*, vol. 85, p. 155132, 2012.

[222] J. Soret and M. B. Lepetit, "Electronic structure of the $Ca_3Co_4O_9$ compound from *ab initio* local interactions," *Physical Review B*, vol. 85, p. 165145, 2012.

[223] J. Baran, M. Molinari, N. Kulwongwit, F. Azough, R. Freer, D. Kepaptsoglou, Q. M. Ramasse, and S. C. Parker, "Tuning thermoelectric properties of misfit layered cobaltites by chemically induced strain," *Journal of Physical Chemistry C*, vol. 119, pp. 21818–21827, 2015.

[224] A. Kulkarni, K. Doll, J. C. Schoen, and M. Jansen, "Global exploration of the enthalpy landscape of calcium carbide," *Journal of Physical Chemistry B*, vol. 114, p. 15573, 2010.

[225] E. Ruizand, M. Llunell, and P. Alemany, "Calculation of exchange coupling constants in solid state transition metal compounds using localized atomic orbital basis sets," *Journal of Solid State Chemistry,*, vol. 176, p. 400, 2003.

[226] S. H. Vosko, L. Wilk, and M. Nusair, "Accurate spin-dependent electron liquid correlation energies for local spin-density calculations - a critical analysis," *Canadian Journal of Physics*, vol. 58, p. 1200, 1980.

[227] Y. Miyazaki, M. Onoda, T. Oku, M. Kikuchi, Y. Isuii, Y. Ono, Y. Morri, and T. Kajitani, "Modulated structure of the thermoelectric compound $(Ca_2CoO_3)_{0.62}(CoO_2)$," *Journal of the Physical Society of Japan*, vol. 71, p. 491, 2002.

[228] S. Lambert, H. Leligny, and D. Grebille, "Three forms of the misfit layered cobaltite $[Ca_2CoO_3][CoO_2]_{1.62}$: A 4d structural investigation," *Journal of Solid State Chemistry*, vol. 160, p. 322, 2001.

[229] A. Rébola, R. Klie, P. Zapol, and S. Ögüt, "Phonon and thermal transport properties of the misfit-layered oxide thermoelectric $Ca_3Co_4O_9$ from first principles," *Applied Physics Letters*, vol. 104, p. 251910, 2014.

[230] G. Yang, Q. Ramasse, and R. F. Klie, "Direct measurement of charge transfert in thermoelectric $Ca_3Co_4O_9$," *Physical Review B*, vol. 78, p. 153109, 2008.

[231] R. Klie, Q. Qiao, T. Paulauskas, Q. Ramasse, M. P. Oxley, and J. C. Idrobo, "Examining the structure and bonding in complex oxides using aberration-corrected imaging and spectroscopy," *Physical Review B*, vol. 85, p. 054106, 2012.

[232] P. Limelette, V. Hardy, P. Auban-Senzier, D. Jérome, D. Flahaut, S. Hébert, R. Frésard, C. Simon, J. Noudem, and A. Maignan, "Strongly correlated properties of the thermoelectric cobalt oxide $Ca_3Co_4O_9$," *Physical Review B*, vol. 71, p. 233108, 2005.

[233] S. Bhattacharya, D. Aswala, A. Singh, C. Thinahara, N. Kulkarni, S. Gupta, and J. Yakhmi, "Anisotropic electrical transport studies of $Ca_3Co_4O_9$ single crystals grown by the flux method," *Journal of Crystal Growth*, vol. 277, p. 246, 2005.

[234] H. Ohta, K. Sugiura, and K. Koumoto, "Recent progress in oxide thermoelectric materials: p-type $Ca_3Co_4O_9$ and n-type $SrTiO_3^-$," *Inorganic Chemistry*, vol. 47, p. 8429, 2008.

[235] Y. Huang, B. Zhao, J. Fang, R. Ang, and Y. Sun, "Tunning of microstructure and thermoelectric properties of $Ca_3Co_4O_9$ ceramics by high-magnetic-field sintering," *Journal of Applied Physics*, vol. 110, p. 123713, 2011.

[236] H. Guo, S. Wang, L. Wang, K. Jin, and S. C. et al., "Electrical properties of thermoelectric cobalt $Ca_3Co_4O_9$ epitaxial heterostructures," *Journal of Applied Physics*, vol. 113, p. 113707, 2013.

[237] M. Shikano and R. Funahashi, "Electrical and thermal properties of single-crystalline $(Ca_2CoO_3)_{0.7}$CoO2 with a $Ca_3Co_4O_9$ structure," *Applied Physics Letters*, vol. 82, p. 1851, 2003.

[238] S. Demirel, S. Avci, E. Altin, S. Altin, and M. Yakinci, "Enhanced thermoelectric properties induced by chemical pressure in $Ca_3Co_4O_9$," *Ceramics International*, vol. 40, p. 5217, 2014.

[239] S. Ohta, T. Nomura, H. Ohta, M. Hirano, H. Hosono, and K. Koumoto, "Large thermoelectric performance of heavily nb-doped $SrTiO_3$ epitaxial film at high temperature," *Applied physics letters*, vol. 87, no. 9, p. 092108, 2005.

[240] I. Pallecchi, M. Codda, E. Galleani d'Agliano, D. Marré, A. D. Caviglia, N. Reyren, S. Gariglio, and J.-M. Triscone, "Seebeck effect in the conducting $LaAlO_3/SrTiO_3$ interface," *Physical Review B*, vol. 81, p. 085414, Feb 2010.

[241] A. Filippetti, P. Delugas, M. J. Verstraete, I. Pallecchi, A. Gadaleta, D. Marré, D. F. Li, S. Gariglio, and V. Fiorentini, "Thermopower in oxide heterostructures: The importance of being multiple-band conductors," *Physical Review B*, vol. 86, p. 195301, Nov 2012.

[242] J. L. M. van Mechelen, D. van der Marel, C. Grimaldi, A. B. Kuzmenko, N. P. Armitage, N. Reyren, H. Hagemann, and I. I. Mazin, "Electron-phonon interaction and charge carrier mass enhancement in $SrTiO_3$," *Physical Review Lett.*, vol. 100, p. 226403, Jun 2008.

[243] J. P. Carmo, L. M. Goncalves, and J. H. Correia, "Improved *p*- and *n*-type thin-film microstructures for thermoelectricity," *Electronics Letters*, vol. 45, no. 15, pp. 803–805, 2009.

[244] J. Lee, Y. Kim, L. Cagnon, U. Gösele, J. Lee, and K. Nielsch, "Power factor measurements of bismuth telluride nanowires grown by pulsed electrodeposition," *Physica Status Solidi (RRL) - Rapid Research Letters*, vol. 4, no. 1, pp. 43 – 45, 2010.

[245] J.-H. Kim, J.-Y. Choi, J.-M. Bae, M.-Y. Kim, and T.-S. Oh, "Thermoelectric characteristics of *n*-type Bi_2Te_3 and *p*-type Sb_2Te_3 thin films prepared by co-evaporation and annealing for thermopile sensor applications," *Materials Transactions*, vol. 54, pp. 618–625, 2013.

[246] I. Pallecchi, F. Telesio, D. Li, A. Fête, J.-M. T. Stefano Gariglio, A. Filippetti, P. Delugas, V. Fiorentini, and D. Marré, "Giant oscillating thermopower at oxide interfaces," *Nature Communications*, vol. 6, p. 6678, 2015.

[247] I. Pallecchi, F. Telesio, D. Marré, D. Li, S. Gariglio, J.-M. Triscone, and A. Filippetti, "Large phonon-drag enhancement induced by narrow quantum confinement at the $LaAlO_3/SrTiO_3$ interface," *Phys. Rev. B*, vol. 93, p. 195309, May 2016.

[248] H. Ohta, S. Kim, Y. Mune, T. Mizoguchi, K. Nomura, S. Ohta, T. Nomura, Y. Nakanishi, Y. Ikuhara, M. Hirano, H. Hosono, and K. Koumoto, "Giant thermoelectric Seebeck coefficient of a two-dimensional electron gas in $SrTiO_3$," *Nature Materials*, vol. 6, 2007.

[249] T. Graf, C. Felser, and S. S. Parkin, "Simple rules for the understanding of Heusler compounds," *Progress in Solid State Chemistry*, vol. 39, no. 1, pp. 1 – 50, 2011.

[250] C. Felser and A. Hirohata, eds., *Theory of Heusler and full-Heusler Compounds*, pp. 3–36. Cham: Springer International Publishing, 2016.

[251] Y. Nishino, "Thermoelectric properties of the pseudogap Fe_2VAl system," *Materials Science Forum*, vol. 449-452, no. II, pp. 909–912, 2004.

[252] C.-S. Lue and J. H. Ross, "Semimetallic behavior in Fe_2VAl : nmr evidence," *Physical Review B*, vol. 58, pp. 9763–9766, Oct 1998.

[253] H. Okamura, J. Kawahara, T. Nanba, S. Kimura, K. Soda, U. Mizutani, Y. Nishino, M. Kato, I. Shimoyama, H. Miura, K. Fukui, K. Nakagawa, H. Nakagawa, and T. Kinoshita, "Pseudogap formation in the intermetallic compounds $(Fe_{1-x}V_x)_3Al$," *Physical Review Lett.*, vol. 84, pp. 3674–3677, Apr 2000.

[254] E. I. Shreder, A. D. Svyazhin, and A. A. Makhnev, "Evolution of the electronic structure and optical properties of iron-based Heusler alloys," *Optics and Spectroscopy*, vol. 119, pp. 969–973, Dec 2015.

[255] H. Miyazaki, S. Tanaka, N. Ide, K. Soda, and Y. Nishino, "Thermoelectric properties of Heusler-type off-stoichiometric $Fe_2V_{1+x}Al_{1-x}$ alloys," *Materials Research Express*, vol. 1, no. 1, p. 015901, 2014.

[256] Y. Nishino, M. Kato, S. Asano, K. Soda, M. Hayasaki, and U. Mizutani, "Semiconductorlike behavior of electrical resistivity in Heusler-type Fe_2VAl compound," *Physical Review Lett.*, vol. 79, pp. 1909–1912, Sep 1997.

[257] K. Soda, S. Osawa, M. Kato, H. Miyazaki, and Y. Nishino, *Semiconducting Transport Properties in Off-Stoichiometric $Fe_{2-x}VAl_{1+x}$*, ch. 3, p. 017036. Physical Society of Japan, 2014.

[258] D. Do, M.-S. Lee, and S. D. Mahanti, "Effect of onsite Coulomb repulsion on thermoelectric properties of full-Heusler compounds with pseudogaps," *Physical Review B*, vol. 84, p. 125104, Sep 2011.

[259] Y. Nishino, H. Kato, M. Kato, and U. Mizutani, "Effect of off-stoichiometry on the transport properties of the Heusler-type Fe_2VAl compound," *Physical Review B*, vol. 63, p. 233303, May 2001.

[260] T. Naka, A. M. Nikitin, Y. Pan, A. de Visser, T. Nakane, F. Ishikawa, Y. Yamada, M. Imai, and A. Matsushita, "Composition induced metal-insulator quantum phase transition in the Heusler type Fe_2VAl," *Journal of Physics: Condensed Matter*, vol. 28, no. 28, p. 285601, 2016.

[261] Y. Feng, J. Y. Rhee, T. A. Wiener, D. W. Lynch, B. E. Hubbard, A. J. Sievers, D. L. Schlagel, T. A. Lograsso, and L. L. Miller, "Physical properties of Heusler-like Fe_2VAl," *Physical Review B*, vol. 63, p. 165109, Apr 2001.

[262] J. C. Slater, "The ferromagnetism of nickel. ii. temperature effects," *Physical Review*, vol. 49, pp. 931–937, Jun 1936.

[263] L. Pauling, "The nature of the interatomic forces in metals," *Physical Review*, vol. 54, pp. 899–904, Dec 1938.

[264] K. Soda, H. Murayama, S. Yagi, M. Kato, T. Takeuchi, U. Mizutani, S. Imada, S. Suga, Y. Saitoh, T. Muro, H. Sumi, and Y. Nishino, "Magnetic circular dichroism at Fe and V $L_{2,3}$ thresholds of Heusler-type $Fe_{2-x}V_{1+x}Al$," *Physica B: Condensed Matter*, vol. 351, no. 3, pp. 338 – 340, 2004. Proceedings of The International Symposium on Synchrotron Radiation Research for Spin and Electronic States in d and f Electron Systems.

[265] T. Naka, K. Sato, M. Taguchi, T. Nakane, F. Ishikawa, Y. Yamada, Y. Takaesu, T. Nakama, and A. Matsushita, "Ferromagnetic quantum singularities and small pseudogap formation in Heusler type $Fe_{2+x}V_{1-x}Al$," *Physical Review B*, vol. 85, p. 085130, Feb 2012.

[266] S. Fujii, Y. Ienaga, S. Ishida, and S. Asano, "Roles of excess atoms in electronic and magnetic properties of $Fe_{2+x}V_{1-x}Z$ (Z = Al, Ga)," *Journal of the Physical Society of Japan*, vol. 72, no. 3, pp. 698–704, 2003.

[267] K. H., K. M., N. Y., M. U., and A. S, "Effect of silicon substitution on thermoelectric properties of Heusler-type Fe_2VAl alloy," *Journal of the Japan Institute of Metals and Materials*, vol. 65, no. 7, pp. 652–656, 2001.

[268] M. Mikami, S. Tanaka, and K. Kobayashi, "Thermoelectric properties of sb-doped Heusler Fe_2VAl alloy," *Journal of Alloys and Compounds*, vol. 484, no. 1, pp. 444 – 448, 2009.

[269] C. S. Lue and Y.-K. Kuo, "Thermoelectric properties of the semimetallic Heusler compounds $Fe_{2-x}V_{1+x}M$ (M = Al, Ga)," *Physical Review B*, vol. 66, p. 085121, Aug 2002.

[270] T. Nakama, Y. Takaesu, K. Yagasaki, T. Naka, A. Matsushita, K. Fukuda, and Y. Yamada, "Transport properties of Heusler compounds $Fe_{3-x}V_xAl$," *Journal of the Physical Society of Japan*, vol. 74, no. 5, pp. 1378–1381, 2005.

[271] I. Knapp, B. Budinska, D. Milosavljevic, P. Heinrich, S. Khmelevskyi, R. Moser, R. Podloucky, P. Prenninger, and E. Bauer, "Impurity band effects on transport and thermoelectric properties of $Fe_{2-x}Ni_xVAl$," *Physical Review B*, vol. 96, p. 045204, Jul 2017.

[272] Y. Hanada, R. O. Suzuki, and K. Ono, "Seebeck coefficient of $(Fe, V)_3Al$ alloys," *Journal of Alloys and Compounds*, vol. 329, no. 1, pp. 63 – 68, 2001.

[273] J. M. Tomczak, "Thermoelectricity in correlated narrow-gap semiconductors," *Journal of Physics: Condensed Matter*, vol. 30, no. 18, p. 183001, 2018.

[274] J.-Y. Jong, J. Zhu, M.-G. Jon, Y. Zhou, J. Kim, and J. Yan, "Theoretical investigation of stabilities and physical properties of low cost Fe-based full-Heusler materials," *Journal of Alloys and Compounds*, vol. 693, pp. 462–467, 2017.

[275] D. J. Singh and I. I. Mazin, "Electronic structure, local moments, and transport in Fe_2VAl," *Physical Review B*, vol. 57, pp. 14352–14356, Jun 1998.

[276] A. Jezierski and A. Ślebarski, "Atomic disorder and magnetism in Fe_2TiSn alloys," *Journal of Magnetism and Magnetic Materials*, vol. 223, p. 33, 2001.

[277] A. Ślebarski, J. Deniszczyk, W. Borgiel, A. J. andM. Swatek, A. Winiarska, M. B. Maple, and W. M. Yuhasz, "Electronic structure and thermodynamic properties of the Heusler alloys $Fe_2Ti_{1-x}V_xSn$ alloys," *Physical Review B*, vol. 69, p. 155118, 2004.

[278] Y. Nishino, S. Deguchi, and U. Mizutani, "Thermal and transport properties of the Heusler-type $Fe_2VAl_{1-x}Ge_x$ ($0 \leq x \leq 0.20$) alloys: Effect of doping on lattice thermal conductivity, electrical resistivity, and Seebeck coefficient," *Physical Review B*, vol. 74, p. 115115, Sep 2006.

[279] M. Vasundhara, V. Srinivas, and V. V. Rao, "Electronic transport in Heusler-type $Fe_2VAl_{1-x}M_x$ alloys ($M = B, In, Si$)," *Physical Review B*, vol. 77, p. 224415, Jun 2008.

[280] I. de P. R. Moreira, R. Dovesi, C. Roetti, V. R. Saunders, and R. Orlando, "*Ab initio* study of MF_2 (M = Mn, Fe, Co, Ni) rutile-type compounds using the periodic unrestricted Hartree-Fock approach," *Physical Review B*, vol. 62, pp. 7816–7823, Sep 2000.

[281] T. Bredow, P. Heitjans, and M. Wilkening, "Electric field gradient calculations for Li_xTiS_2 and comparison with ^{7}Li NMR results," *Physical Review B*, vol. 70, p. 115111, Sep 2004.

[282] E. Ruiz, M. Llunell, and P. Alemany, "Calculation of exchange coupling constants in solid state transition metal compounds using localized atomic orbital basis sets," *Journal of Solid State Chemistry*, vol. 176, no. 2, pp. 400 – 411, 2003. Special issue on The Impact of Theoretical Methods on Solid-State Chemistry.

[283] R. Pandey, M. Causa, N. M. Harrison, and M. Seel, "Electronic and thermoelectric properties of Fe_2VAl: The role of defects and disorder," *Journal of Physics: Condensed Matter*, vol. 8, p. 3993, 1996.

[284] A. R. Porter, M. D. Towler, and R. J. Needs, "Muonium as a hydrogen analogue in silicon and germanium: Quantum effects and hyperfine parameters," *Physical Review B*, vol. 60, pp. 13534–13546, Nov 1999.

[285] X. Gonze and *et al.*, "ABINIT: First-principles approach to material and nanosystem properties," *Computer Physics Communications*, vol. 180, no. 12, p. 2582, 2009.

[286] J. P. Perdew, K. Burke, and M. Ernzerhof, "Generalized gradient approximation made simple," *Physical Review Letters*, vol. 77, p. 3865, 1996.

[287] A. I. Liechtenstein, V. I. Anisimov, and J. Zaanen, "Density-functional theory and strong interactions: Orbital ordering in Mott-Hubbard insulators," *Physical Review B*, vol. 52, no. 8, pp. R5467–R5470, 1995.

[288] M. Torrent, F. Jollet, F. Bottin, G. Zérah, and X. Gonze, "Implementation of the projector augmented-wave method in the ABINIT code: Application to the study of iron under pressure," *Computational Materials Science*, vol. 42, p. 337, 2008.

[289] F. Jollet, M. Torrent, and N. Holzwarth, "Generation of projector augmented-wave atomic data: a 71 element validated table in the XML format," *Computer Physics Communications*, vol. 185, pp. 1246–1254, 2014.

[290] A. Ślebarski, "Electron-correlation effects in a disordered Fe_2TiSn Heusler alloy," *Journal of Physics D: Applied Physics*, vol. 39, no. 5, p. 856, 2006.

[291] M. Meinert, M. P. Geisler, J. Schmalhorst, U. Heinzmann, E. Arenholz, W. Hetaba, M. Stöger-Pollach, A. Hütten, and G. Reiss, "Experimental realization of a semiconducting full-Heusler compound: Fe_2TiSi," *Physical Review B*, vol. 90, p. 085127, Aug 2014.

[292] M. P. T. P. N. Butcher, Norman H. March, *Crystalline Semiconducting Materials and Devices*. Springer Science+Business Media, LLC, 1986.

[293] H. Peelaers, E. Durgun, B. Partoens, D. I. Bilc, P. Ghosez, C. G. V. de Walle, and F. M. Peeters, "*Ab initio* study of hydrogenic effective mass impurities in Si nanowires," *Journal of Physics: Condensed Matter*, vol. 29, no. 9, p. 095303, 2017.

[294] A. Baldereschi and R. Resta, eds., *Shallow Impurity Centers in Semiconductors*. Oxford: Elsevier, 1987.

[295] J. M. Spaeth and H. Overhof, *Point Defects in Semiconductors and Insulators*. Springer-Verlag Berlin Heidelberg, 2003.

[296] M. Grundmann, *The Physics of Semiconductors*. Springer-Verlag Berlin Heidelberg, 2006.

[297] C. Felser and A. Hirohata, *Heusler Alloys*. Springer series in Material Science, Springer-Verlag Berlin and Heidelberg GmbH and Co. K, 2016.

[298] K. Buschow and F. de Boer, *Physics of Magnetism and Magnetic Materials*. Springer US, 2003.

[299] T. Moriya, *Spin fluctuations in itinerant electron magnetism*. Springer series in solid-state sciences, Springer International Publishing Switzerland, 1985.

[300] E. C. Stoner, "Collective electron ferromagnetism," *Proceedings of the Royal Society of London A: Mathematical, Physical and Engineering Sciences*, vol. 165, no. 922, pp. 372–414, 1938.

[301] C. M. Teodorescu and G. A. Lungu, "Band ferromagnetism in systems of variable dimensionality," *Journal of Optoelectronics and Advanced Materials*, vol. 10, pp. 3058–3068, Nov 2008.

[302] M. Yin and P. Nash, "Standard enthalpies of formation of selected Ru_2YZ Heusler compounds," *Journal of Alloys and Compounds*, vol. 634, pp. 70–74, 2015.

[303] S. J. R., K. Huijun, U. Ctirad, D. J. James, W. Chun-I, H. T. P., C. Thierry, and K. M. G., "Large enhancements in the thermoelectric power factor of bulk PbTe at high temperature by synergistic nanostructuring," *Angewandte Chemie*, vol. 120, no. 45, pp. 8746–8750, 2008.

[304] I. Pallecchi, M. Pani, F. Ricci, S. Lemal, D. I. Bilc, P. Ghosez, C. Bernini, N. Ardoino, G. Lamura, and D. Marré, "Thermoelectric properties of chemically substituted full-Heusler $Fe_2TiSn_{1-x}Sb_x$ ($x = 0, 0.1, 0.2$) compounds," *Physical Review Materials*, vol. 2, p. 075403, Jul 2018.

[305] J. Rodríguez-Carvajal, "Recent advances in magnetic structure determination by neutron powder diffraction," *Physica B: Condensed Matter*, vol. 192, no. 1, pp. 55 – 69, 1993.

[306] L. Romaka, V. V. Romaka, Y. Stadnyk, and N. Melnychenko, "On the formation of ternary phases in the Ti–Fe–Sn ternary system at 773 K," *Chemistry of metals and alloys*, vol. 6, pp. 12–19, 2013.

[307] M. Pani, I. Pallecchi, C. Bernini, N. Ardoino, and D. Marré, "Synthesis and structural characterization of Sb-doped $TiFe_2Sn$ Heusler compounds," *Journal of Materials Engineering and Performance*, vol. 27, pp. 6314–6321, Dec 2018.

[308] M. L. C. Buffon, G. Laurita, L. Lamontagne, E. E. Levin, S. Mooraj, D. L. Lloyd, N. White, T. M. Pollock, and R. Seshadri, "Thermoelectric performance and the role of anti-site disorder in the 24-electron Heusler $TiFe_2Sn$," *Journal of Physics: Condensed Matter*, vol. 29, no. 40, p. 405702, 2017.

[309] A. Ślebarski, A. Wrona, T. Zawada, A. Jezierski, A. Zygmunt, K. Szot, S. Chiuzbaian, and M. Neumann, "Electronic structure of some Heusler alloys based on aluminum and tin," *Physical Review B*, vol. 65, p. 144430, Apr 2002.

[310] C. Lue and Y.-K. Kuo, "Thermal and transport properties of the Heusler-type compounds $Fe_{2-x}Ti_{1+x}Sn$," *Journal of Applied Physics*, vol. 96, p. 2681, 2004.

[311] M. Nakabayashi, K. Fukuda, H. Kitagawa, Y. Yamada, S. Kubo, and A. Matsushita, "Magnetic and transport properties in Heusler-type Fe_2TiSn compounds," *Physica B*, vol. 329-333, pp. 1134–1135, 2003.

[312] S. Chaudhuri, P. A. Bhobe, and A. K. Nigam, "Possible half-metallicity and variable range hopping transport in Sb-substituted Fe_2TiSn Heusler alloys," *Journal of Physics: Condensed Matter*, vol. 30, no. 1, p. 015703, 2018.

[313] T. Zou, T. Jia, W. Xie, Y. Zhang, M. Widenmeyer, X. Xiao, and A. Weidenkaff, "Band structure modification of the thermoelectric Heusler-phase $TiFe_2Sn$ via mn substitution," *Phys. Chem. Chem. Phys.*, vol. 19, pp. 18273–18278, 2017.

[314] A. Ślebarski, M. B. Maple, E. J. Freeman, C. Sirvent, D. Tworuszka, M. Orzechowska, A. Wrona, A. Jezierski, S. Chiuzbaian, and M. Neumann, "Weak ferromagnetism induced by atomic disorder in Fe_2TiSn," *Physical Review B*, vol. 62, pp. 3296–3299, Aug 2000.

[315] H. Luo, G. Liu, F. Meng, J. Li, E. Liu, and G. Wu, "Half-metallicity in Fe-based Heusler alloys Fe_2TiZ (Z = Ga, Ge, As, In, Sn and Sb)," *Journal of Magnetism and Magnetic Materials*, vol. 324, no. 20, pp. 3295–3299, 2012.

[316] C. Hugenschmidt, A. Bauer, P. Böni, H. Ceeh, S. W. H. Eijt, T. Gigl, C. Pfleiderer, C. Piochacz, A. Neubauer, M. Reiner, H. Schut, and J. Weber, "Quality of Heusler single crystals examined by depth-dependent positron annihilation techniques," *Applied Physics A*, vol. 119, pp. 997–1002, Jun 2015.

[317] H. Matsuura, "Doping effects on thermoelectric properties of the pseudogap Fe_2VAl system," *J. Japan. Inst. Metals*, vol. 66, pp. 767–771, 2002.

[318] M. Kato, Y. Nishino, S. Asano, and S. Ohara, "Electrical resistance anomaly and Hall effect in $(Fe_{1-x}V_x)_3Al$," *J. Jpn. Inst. Met.*, vol. 62, p. 669, 1998.

[319] G. Hautier, "Prediction of new battery materials based on *ab initio* computations," *AIP Conference Proceedings*, vol. 1765, no. 1, p. 020009, 2016.

[320] R. W. McKinney, P. Gorai, V. Stevanovic, and E. S. Toberer, "Search for new thermoelectric materials with low Lorenz number," *J. Mater. Chem. A*, vol. 5, pp. 17302–17311, 2017.

[321] J. M. W., Chase, "NIST-JANAF Thermochemical Tables, Fourth Edition," *J. Phys. Chem. Ref. Data, Monograph*, vol. 9, 1998.

[322] H. Zaid, M. H. Berger, D. Jalabert, M. Walls, R. Akrobetu, N. J. Goble, X. P. A. Gao, P. Berger, I. Fongkaew, W. Lambrecht, and A. Sehirlioglu, "Role of the different defects, their population and distribution in the $LaAlO_3/SrTiO_3$ heterostructure's behavior," *Journal of Applied Physics*, vol. 123, no. 15, p. 155304, 2018.

[323] H. Xue, C. Li, Y. Hong, X. Wang, Y. Li, K. Liu, W. Jiang, M. Liu, L. He, R. Dou, C. Xiong, and J. Nie, "Temperature dependence of the conductive layer thickness at the $LaAlO_3/SrTiO_3$ heterointerface," *Physical Review B*, vol. 96, p. 235310, Dec 2017.

[324] M. Salluzzo, S. Gariglio, D. Stornaiuolo, V. Sessi, S. Rusponi, C. Piamonteze, G. M. De Luca, M. Minola, D. Marré, A. Gadaleta, H. Brune, F. Nolting, N. B. Brookes, and G. Ghiringhelli, "Origin of interface magnetism in $BiMnO_3/SrTiO_3$ and $LaAlO_3/SrTiO_3$ heterostructures," *Physical Review Lett.*, vol. 111, p. 087204, Aug 2013.

[325] A. Reshak and W. Khan, "Electronic structure, optical and thermoelectric transport properties of layered polyanionic hydrosulfate $LiFeSO_4OH$: Electrode for Li-ion batteries," *Journal of Alloys and Compounds*, vol. 591, pp. 362–369, 2014.

[326] J.-H. Lee, G. A. Galli, and J. C. Grossman, "Nanoporous Si as an efficient thermoelectric material," *Nano Letters*, vol. 8, pp. 3750–3754, 2008.

[327] K. Kutorasinski, B. Wiendlocha, S. Kaprzyk, and J. Tobola, "Electronic structure and thermoelectric properties of *n*- and *p*-type SnSe from first-principles calculations," *Physical Review B*, vol. 91, p. 205201, May 2015.